High-intensity laser generated neutrons:
A novel neutron source and
new tool for plasma diagnostics

Dissertation der Fakultät für Physik
der Ludwig-Maximilians-Universität München

vorgelegt von
Stefan Karsch
aus Ebingen

München, den 01.11.2002

1. Gutachter: *Prof. Dr. Dietrich Habs*

2. Gutachter: *Prof. Dr. Theodor W. Hänsch*

Tag der mündlichen Prüfung: *12.12.2002*

Zusammenfassung

Diese Arbeit befaßt sich mit der Erzeugung von Neutronen durch ultrakurze Laserimpulse moderater Energie. Dabei stand einerseits die Entwicklung einer Neutronenquelle im Vordergrund, zu deren Optimierung es der Klärung der zugrundeliegenden Erzeugungsprozesse bedurfte. Die höchsten Neutronenausbeuten liefern Kernreaktionen laserbeschleunigter Ionen. Die Charakterisierung der schnellen Ionen, welche größtenteils auf Neutronenspektroskopie beruht, ist ein wesentlicher Bestandteil dieser Arbeit. In den hier vorgestellten Experimenten gelang es, bis zu 10^8 Neutronen pro Laserschuß zu erzeugen, was einer spezifischen Ausbeute von 10^7 Neutronen pro Joule Laserenergie entspricht. Die gefundenen Skalierungsgesetze lassen für eine Erhöhung der Laserenergie eine weitere Steigerung dieser spezifischen Ausbeute erwarten, was auch durch Experimente anderer Gruppen bestätigt wird.
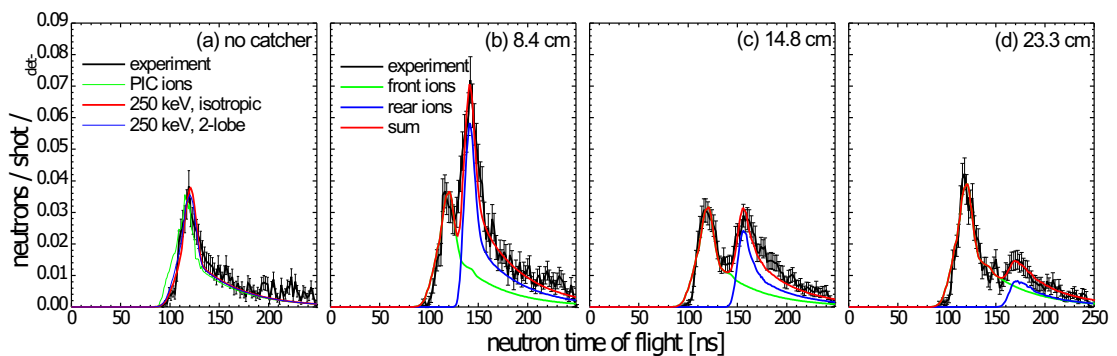
Figure 1: Quantitativer Vergleich von zwei separaten, laserbeschleunigten Ionenpopulationen durch Neutronenspektroskopie an Schwerwassertröpfchen.

Andererseits birgt die Spektroskopie der lasererzeugten Ionen auch ein großes Potential für die Diagnostik von lasererzeugten Plasmen. In Fällen, in denen die lasererzeugten Ionen entweder der Beobachtung unzugänglich sind, weil sie in dichtes Plasma laufen und dort gestoppt werden, oder durch die dort herrschenden starken Felder abgelenkt werden, stellen die Neutronen als Sekundärteilchen oft die einzige Möglichkeit dar, Informationen über die primäre Ionenverteilung zu gewinnen. So wurde in dieser Arbeit Neutronenspektroskopie zur quantitativen Analyse der in das Target laufenden Ionenpopulation angewendet, woraus Ionentemperaturen und -zahlen bestimmt werden konnten. Aufbauend darauf wurde diese Technik dazu eingesetzt, erstmals in einem einzigen Experiment den bisher sehr kontrovers diskutierten Ursprung der lasererzeugten Ionen zu klären. Bisher wurden von anderen Gruppen entweder Ionen direkt aus dem Laserfokus oder von der Targetrückseite

nachgewiesen. Demgegenüber wurden hier durch Neutronenspektroskopie zum ersten Mal beide Mechanismen gleichzeitig beobachtet und quantitativ miteinander verglichen. Dadurch können durch Ausschluß laserbedingter Einflüsse wichtige Erkenntnisse über die Effizienz beider Prozesse im Hinblick auf die Entwicklung einer Laser-Ionenquelle gewonnen werden. Ähnliche Messungen bei wesentlich höherer Laserenergie liefern gute Anhaltspunkte zur weiteren Skalierung dieser Ergebnisse. Für den Fall der Ionenerzeugung im Laserfokus konnten Simulationen mit drei-dimensionalen Particle-In-Cell-Codes (3D-PIC) zur Modellierung der Ionenverteilung im Verbund mit einem im Rahmen dieser Arbeit entwickelten 3-D Monte-Carlo Neutronenerzeugungscodes die experimentellen Ergebnisse recht genau reproduzieren. Damit trugen sie auch zum Aufschluß sowohl über die Ionenverteilung als auch über den ihr zugrundeliegenden Beschleunigungsmechanismus bei. Dabei stellte sich heraus, daß die im allgemeinen verwendete theoretische Beschreibung zumindest für kurze, höchstintensive Pulse unvollständig ist, da dort die Pulsdauer zur Ausbildung einer bisher zur Ionenbeschleunigung postulierten Dipol-Schicht zu kurz ist. Damit ist ein Grundstein gelegt für eine zukünftige Verbesserung der Theorie. Durch die Mitwirkung in einer Kollaboration zur Untersuchung der lasergetriebenen Ionenbeschleunigung konnten die Ergebnisse der Neutronenmessungen mit direkten Ionenmessungen verglichen werden.
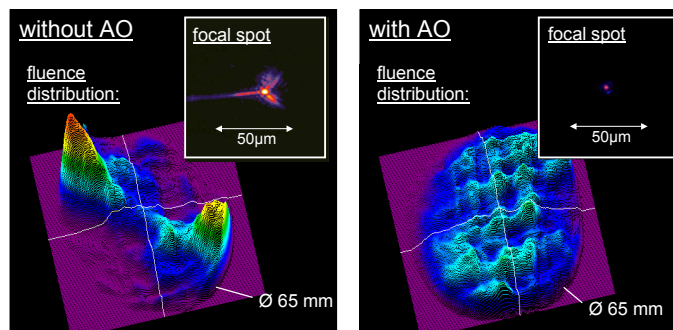
Figure 2: Simultane Verbesserung von Nah- und Fernfeld des ATLAS-Strahls durch Einführung einer neuartigen adaptiven Optik

Schlussendlich war zum erfolgreichen Einsatz des am Max-Planck-Institut für Quantenoptik (MPQ) installierten ATLAS-Lasers die Entwicklung eines adaptiven Optik-Systems zur gleichzeitigen Korrektur des Strahlprofils und der Fokussierbarkeit erforderlich, welches von der Laser-Plasma-Gruppe gemeinsam mit dem Institut für Laser- und Informationstechnologie der Russischen Akademie der Wissenschaften konzipiert und gebaut wurde. Dabei optimiert ein geschlossener Regelkreis die Wellenfront. Das System ist das erste seiner Art zur Korrektur sehr großer Wellenfrontabweichungen und funktioniert mittlerweile im täglichen Betrieb.

Abstract

Within the framework of this thesis the generation of neutrons using ultrashort laser pulses with moderate pulse energy was investigated. On the one hand, the aim was directed towards the development of a neutron source, whose optimization naturally calls for a detailed understanding of the underlying neutron production processes. Since the highest neutron yields are achieved by nuclear reactions of laser-accelerated ions, the characterization of these ions is necessary, which was done mainly by neutron spectroscopy. Using this strategy, neutron yields of up to 10^8 neutrons/ laser shot were demonstrated in the experiments presented here. This is equivalent to a specific neutron yield of 10^7 per Joule of pulse energy. The scaling laws found in this context anticipate a further increase of the specific neutron yield with laser energy, which has recently been proven by a number of groups.
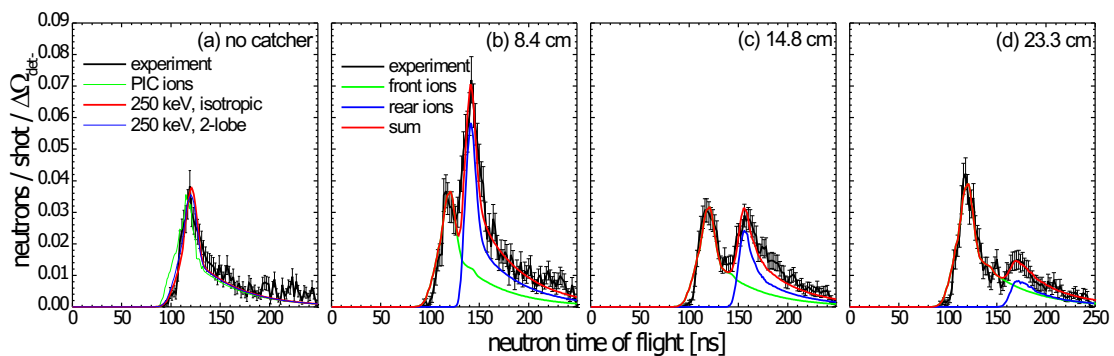
Figure 3: Quantitative and simultaneous comparison of two separate, laser-accelerated ion populations by neutron spectroscopy after irradiating heavy water droplets with 80 fs, 10 TW laser pulses.

On the other hand, the spectroscopy of these laser-generated neutrons offers a great potential as a diagnostics of laser-generated plasmas. In cases where the laser-accelerated ions are either not directly observable, because they run into dense plasma while being stopped there, or are deflected by the strong electromagnetic fields in the plasma, neutrons as secondary particles offer the only possibility of getting information on the ion distribution. In this work, the application of neutron spectroscopy to quantitatively analyze the inward going ion population was demonstrated for the first time. From this data, ion numbers and temperatures could be determined. Using these skills, neutron spectroscopy was applied to clarify the somewhat controversially discussed ion origin in a single experiment. Up to now, other groups reported ion acceleration either exclusively from the laser focus

or from the target rear side. Here, in contrast, by using neutron spectroscopy we could for the first time observe and quantitatively compare both acceleration mechanisms simultaneously. Thus excluding the influence of laser conditions, insight into both mechanisms important for the optimization of a laser-based ion source could be gained. A similar experiment at much higher laser energy provided good information for the scaling of behaviour of these results. For the case of ion acceleration in the laser focus, combining a three-dimensional particle-in-cell code (3D-PIC) to model the ion distribution with a newly developed 3-D Monte-Carlo neutron production code, could reproduce the experimental result quite accurately. This provided further insight into the ion distribution and the underlying acceleration process. A main result of this analysis is the conclusion that the commonly used theoretical description at least in the case of short, highly intense pulses is incomplete, because the pulse duration is too short for the formation of a previously postulated dipole layer for ion acceleration. This insight can serve as a basis for the future improvement of the theory. By being part of a collaboration to investigate laser-driven ion acceleration, the neutron data could be compared to directly measured ion spectra.
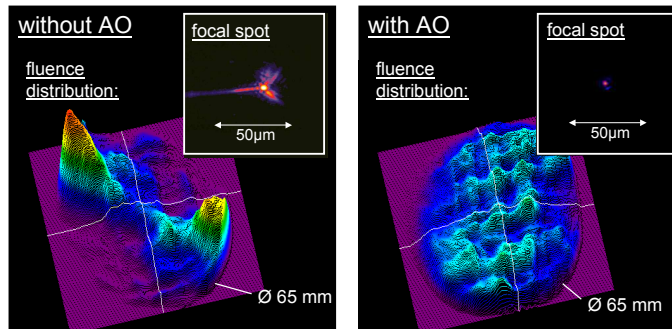
Figure 4: Simultaneuos improvement of near- and far-field of the ATLAS beam by commissioning a novel two-deformable-mirror adaptive optics system.

Finally, in order to successfully operate the ATLAS-laser at the Max-Planck-Institut für Quantenoptik (MPQ) as a tool for neutron production, the development of an adaptive optics system for the simultaneous correction of the beam profile and the focusability became necessary, which was designed and built jointly by the MPQ laser-plasma group and Institut for Laser- and Information Technology of the Russian Academy of Sciences. It uses a closed loop control system to optimize the wavefront. This system is the first of its kind capable of correcting very large wavefront aberrations and is in daily operation in the meantime.

Contents

Chapter 1

Introduction

1.1   Scope of this Work

Since the first application of the chirped-pulse-amplification- (CPA-) principle by
Strickland and Mourou in 1985 [1] to amplify ultrashort and hence broadband
laser pulses from a fs-oscillator to high energies, the last decade has witnessed
ever increasing laser peak powers up to the petawatt (PW) level [2, 3]. While so
far PW powers have been reached only with large kJ glass amplifier chains and
pulse durations of several 100 fs, small table-top Ti:Sapphire laser systems are now
also capable of producing powers in the 10-100 terawatt (TW) regime with much
shorter pulses of durations <100 fs, reaching almost the same focused intensity as
the large glass systems. These developments and the resulting new interest for high
intensity laser applications also have sparked off the development of new amplifi-
cation schemes like optical parametric chirped pulse amplification (OPCPA) [4] as
well as new laser materials like Yb-doped glass for efficient broadband amplifiers.
The recent progress in achieving ever higher focused intensities lead to light fluxes
in the focus of such lasers as high as 10^{21}W/cm^2 at the Lawrence-Livermore PW
laser and up to a few times 10^{20}W/cm^2 for the biggest table-top systems. The Max-
Planck-Institut für Quantenoptik (MPQ) Advanced Ti:Sapphire Laser (ATLAS)
facility routinely reaches intensities up to 2×10^{19}W/cm^2. If such a laser pulse
interacts with matter, in the leading edge of the pulse the electric fields are well
in excess of the inner-atomic fields [5]. Hence, the matter is rapidly field-ionized.
The major part of the pulse therefore always interacts with a plasma. The high
light intensities translate into the strongest electromagnetic fields created so far in
the laboratory, reaching several TV/m and 10^4-10^5 Tesla. These strong oscillating
fields interact primarily with the plasma electrons and force them to oscillate at
the light frequency with relativistic average energies. This leads to a number of

fundamentally new physical phenomena, as can be intuitively understood from Fig. 1.1. It shows the development of the focused intensity of lasers since their
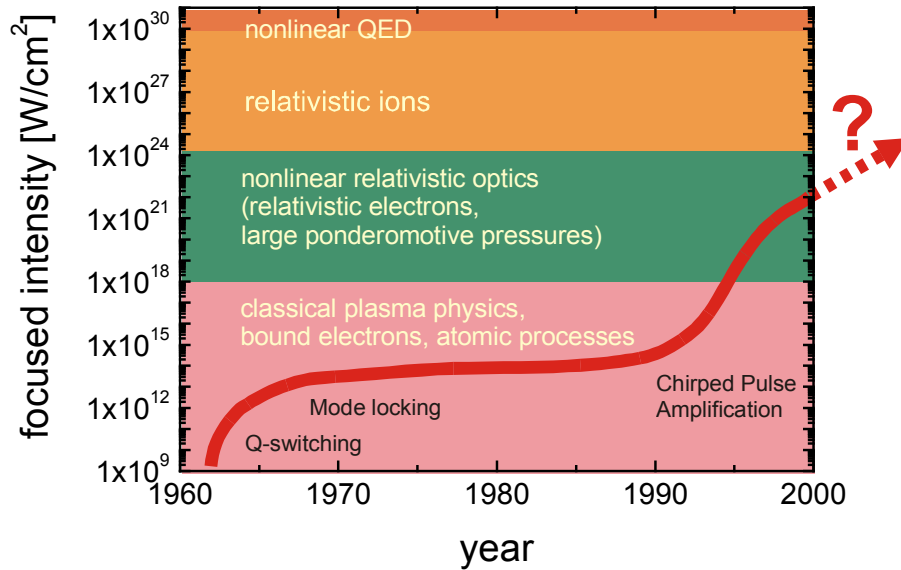
Figure 1.1: The development of laser focused intensity and the different regimes of laser-matter interaction.

invention in 1960, and the regimes of laser-matter interaction that can be reached at these intensities. The step caused by the invention of the CPA technique is particularly striking and illustrates the relative novelty of this field of research. The laser intensities used here place this work well within the realm of nonlinear relativistic optics, with a wealth of new physics to discover.

One well investigated effect in this new regime is the self-focused collapse of the laser beam in an underdense plasma into a very narrow light filament which carries intensities well in excess of the above stated vacuum intensities [6, 7]. Electron acceleration to multi-MeV energies takes place in this channel, and close to the critical density at the edge of an overdense plasma. A number of different mechanisms account for that acceleration, which are not yet fully understood. Electron beam currents in these kind of experiments reach several Alfvén currents (17.6 kA $\beta\gamma$, $\beta = v/c$, $\gamma = \sqrt{1 - \beta^2}^{-1}$), which is the upper limit for a beam current flowing in a plasma before the self-pinching effect of its own magnetic field leads to current reversal [8]. Understanding the transport of such strong electron currents in matter and vacuum in detail poses a great challenge.

One effect of the large electron currents is undisputed: The rapid removal of a total charge of several nC from a volume of the order of a few $(10 \ \mu\text{m})^3$ creates quasistatic electric and magnetic fields of the same strength as the laser fields

(where quasistatic means slowly varying in comparison with the rapidly oscillating laser fields). Plasma ions, which are too inert to follow the laser oscillation, can in turn be accelerated and deflected by the quasistatic fields, and reach multi-MeV energies. These ions carry information about the field distribution in the interaction region, and therefore are interesting candidates for plasma diagnostics. However, the presence of the magnetic and space charge field of the whole target significantly alters and distorts the information carried by the ions when they leave the focal region of the laser. Moreover, those ions that are running into a solid-density target are not accessible to standard ion spectroscopy methods. For these cases, it is convenient to have an alternative probe for the plasma conditions that can carry information unaffected by fields and matter out of the laser interaction zone. Such a probe exists in the form of fusion neutrons. They are generated by the $d(d,n)^3$He fusion reaction in deuterated targets, and their use as a laser-plasma diagnostic is not fundamentally new. The first observations of neutrons generated by nanosecond lasers pulses were presented in the early seventies (e.g. [9]). In the 1990's, large neutron yields were reported from multi-kJ-class fusion laser installations, where they are used as a tool to determine burn fraction of a compressed fusion capsule (for an overview, see [10]). Norreys [11] showed that by reducing the pulse duration to the ∼ps level, the energy requirements for producing high neutron yields were dramatically reduced. Pretzler [12] published the first experimental evidence for fusion neutron generation with ultrashort-pulse table-top-lasers, proving that these systems are capable of driving nuclear physics processes merely by laser light. He achieved a yield of ∼140 neutrons/shot from 200-mJ, 130-fs pulses. In this work, the first high-yield experiments (several 10^4 neutrons/shot) with table-top lasers were conducted, making feasible the use of these neutrons as a diagnostic for short-pulse laser-plasma interaction. Disdier [13] obtained the first experimental emission characteristics of ions running into the target by angular resolved neutron yield measurements. Ditmire and Zweiback [14, 15] have demonstrated efficient neutron emission (10^4 neutrons per shot) from deuterium clusters irradiated by 100-mJ, 30-fs laser pulses with a focused intensity of only 10^{17}W/cm^2. Unfortunately, the scalability of this result to higher laser energies could not yet be proven positively [16]. The same authors also determined the neutron pulse duration to be <500 ps in their setup [17]. With these experimental findings it was shown that a large number of neutrons can indeed be generated by short pulse lasers of moderate size. In contrast, the LLNL PW laser achieved a neutron yield of 3×10^{10} [18], using the same schemes as discussed here. This demonstrates the scalability our results.

The idea of using neutron as a diagnostic is based on the fact that fusion neutrons

from the d(d,n)^{3}He reaction are emitted with a well-defined energy of 2.45 MeV in the center-of-mass (CM) frame of the two reaction partners. Any deviation of the measured neutron energy in the laboratory system from this value corresponds to a moving center of gravity of the two deuterons. If one of these is at rest before the interaction, which is the case for a >100keV beam of ions accelerated into a hot (<1keV) plasma, the measured energy shift corresponds to the initial momentum of the moving deuteron. By measuring the energy spectrum of the neutrons, one can deduce the deuteron distribution and information about the acceleration processes at work in the laser interaction zone. So far, neutron spectroscopy is the only way of probing the ion distribution inside thick, solid targets. In this work, we will describe the first application of neutron TOF spectroscopy as a practicable plasma diagnostics for a variety of different scenarios. In spite of a number of previous publications on this topic, the experiments reported about here are the first related to diagnosing relativistic laser-plasma interaction.

Parallel in time to the development of high-intensity CPA lasers, the application of neutrons in solid state physics, biology, medicine, and material science has been boosted similarly. This has sparked off the need for new neutron sources like the new Munich research reactor FRM II or the European spallation source ESS. All of these reactor or spallation sources are expensive, billion Euro class, large-scale facilities which in the case of reactors are not always easy to establish due to environmentalist and safety concerns. If a cheap, safe, reliable pulsed neutron source based on laser-plasma interaction could be developed, this could relieve the pressure on and in the far future even eliminate the need for those large scale facilities. The wide spectrum of applications calls for neutron sources with different properties. A laser-plasma based source offers many optimization possibilities for a given application. For instance, by choosing the type of reaction and parameters like the target type and geometry, primary particle energy, laser energy etc., the neutron yield, energy, directionality and pulse duration can be varied within broad limits. For instance, when neutrons are produced from laser accelerated ions in the bulk of an irradiated $(CD_2)_n$ target, they are emitted within a few ps from a volume of the order of a few $(10\ \mu)^3$. During the neutron pulse, in a distance of several millimeters from the target, fast neutron fluxes of $10^{19}/(cm^2\ s)$ can be achieved, which is 4 orders of magnitude higher than current continuous research reactors can deliver. Of course, if thermal neutrons are desired by the user, both the short pulse duration and the small source size are lost due the necessary thermalization. Nevertheless, given the rapid progress in neutron research in the last years, it is very likely that upon availability of a laser driven neutron source this community will find a number of applications for it. One such application is radiography and

tomography with fast neutrons. The small size is a a unique property of a laser neutron source, with active volumes in the order of 10^{-3} mm^3 compared to the few cm^3 of conventional sources. Projection neutron imaging can gain a factor of 100 in spatial resolution with such a small source.

1.2   Outline of the Thesis

- Chapter 2, "Theory and Simulations", gives an introduction into the theory of high-intensity laser plasma particle acceleration. Starting with the relativistic motion of a single free electron in the laser field and the resulting ponderomotive acceleration, various collective schemes of electron acceleration will be described briefly. The ultrastrong fields set up by the missing electrons act as a "field rectifier" to generate large, quasistatic fields which in turn accelerate ions. The two most important mechanisms, namely charge separation in the laser focus and Target-Normal Sheath Acceleration (TNSA) are explained a bit more in detail, and for the first case 3-dimensional particle-in-cell (3D-PIC) simulations will be presented.

- Chapter 3, "Neutron Generation and Detection", describes various neutron source reactions useful for laser plasma applications. In a second part, this chapter focuses on the techniques used in this work to detect and characterize the laser generated neutrons, while providing discrimination against the strong γ-ray background from the laser interaction. The time-of-flight technique to measure neutron energies is described briefly along with a activation method to get accurate information of the neutron yield.

- In chapter 4, "Modeling of Neutron Spectra", a 3-D Monte Carlo code for modeling neutron spectra for arbitrary given ion distributions is described. A considerable part of this chapter is devoted to estimate the effect of target preheating by fast electrons on the neutron spectra. Since the energy loss of ions propagating in plasma differs from that in cold matter, this quantity defines the number of fusion partners an ion can encounter per given energy loss. These stopping power modifications scale dynamically with the ion velocity as well as the local target temperature and hence might influence the shape of the neutron spectra. This analysis shows that the influence of this effect is small for the laser conditions considered here, but may play a mayor role at higher laser energy.

- Chapter 5, "Neutron Yield and Spectroscopy at ATLAS", presents results

obtained with the ATLAS laser at MPQ. It first focuses on the yield optimization, in order to reach neutron quantities sufficient for spectroscopy experiments. An investigation of polarization and angle dependence of neutron yields and spectral features gives first insight into the ion acceleration processes involved here. Upon completion of the ATLAS adaptive optics system the laser got reliable enough to perform systematic studies of neutron yield and spectrum with varying laser energy. Trying to understand these results leads to questions about the primary electron acceleration and its dependence of preplasma conditions, which was investigated at the end of this chapter.

- In chapter 6, "Transfer to High Laser Energy at LULI", we try to transfer the knowledge gained on ATLAS to higher laser energies and intensities in order to boost the neutron yield. This was done at the 100TW laser of the Laboratoire Utilisation des Lasers Intenses (LULI) in Palaiseau. Using various source reactions, and a catcher technique to make use of the rear-surface accelerated ions, the yield could be increased by 3-4 orders of magnitude, while scaling the spectroscopy techniques to a single-shot, high-energy laser environment was successfully demonstrated. By analyzing the time-of-flight spectra, new information was gained about the isotope content of an accelerated ion beam, and different source reactions could be distinguished by their neutron spectrum. Finally it was discovered that in the presence of protons, the acceleration of all heavier ion species is strongly suppressed and that by laser-heating the target prior to the shot the protons could be removed and the deuteron fraction in the ion beams substantially raised.

- Considering these problems, in Chapter 7, "Acceleration Processes Revealed by Neutrons", an attempt was made to prepare a target surface free of contaminations by using a droplet jet as target. The experiments were conducted at the Jena 10TW laser. In addition to fusion neutrons from the droplets themself, the installation of a secondary catcher target as it was successfully used at LULI provided neutrons generated by ions accelerated from the droplet rear surface. Thus it was possible to distinguish and quantitatively compare two independent ion acceleration mechanisms in one experiment for the first time. By comparing the experimental findings to the theory described in chapter 2 and 4, quantitive information about the distribution of the accelerated ions is gained. The experiment shows that contrary to the literature [19], even with small lasers the acceleration from the target rear surface by far dominates over the acceleration in the laser focus itself. A comparison with a similar experiment conducted at LULI is presented at the

end of the chapter, which shows that this method is also suited for single shot use.

- In Chapter 8, a summary and conclusion of the reported experimental and theoretical insights are given. Finally, an outlook on continuative work in this field is presented, proposing both experimental and theoretical studies interesting for further advance in this field.

- In Appendix A, "ATLAS Development", the installation and commissioning of the ATLAS adaptive optics system is described. This has been vital for achieving the high intensities and the reproducibility needed for successful neutron production and, by the way, consumed a mayor part of the time for this thesis. Appendix B, "Development of a Thomson Parabola Spectrometer", shortly describes the design of a Thomson parabola spectrometer used to investigate the heavy ion acceleration at the LULI laser

Chapter 2

Theory of Laser Ion Acceleration

The experiments presented here are all concerned with neutron generation by high intensity lasers. A single laser photon is by orders of magnitude not energetic enough to free a neutron from a bound state in the atomic nucleus of a stable isotope, which requires at least $\sim$1.7 MeV (via the $^9\text{Be}(\gamma,\text{n})2\alpha$ reaction). Comparing this energy to a photon energy of $\sim$1 eV), it becomes clear that a direct production (or better freeing) of neutrons by laser light is not feasible. Thus neutrons can only be produced as secondary particles in nuclear reactions triggered by fast particles accelerated from the laser. The following discussion will show how these particles can be accelerated to the necessary energies of a a few 100 keV to several 10 MeV just by the interaction high-intensity light with a plasma. The key to these processes are collective effects in the plasma, with are driven by direct interaction of the laser light with the plasma electrons.

2.1 Laser-Plasma Interaction

In the following, for the time being we will regard the laser beam as a plane, oscillating electromagnetic wave, whose electric and magnetic field components $\vec{E}$ and $\vec{B}$ can be written as:

$$\vec{E}_L = E_0 \hat{y} \cos \phi \qquad (2.1)$$

$$\vec{B}_L = E_0/c \hat{z} \cos \phi \qquad (2.2)$$

Here E_0 is the amplitude, $\hat{y}, \hat{z}$ are the base vectors, $\phi = \omega t - kx$ is the phase, ω the frequency, $k = \omega/2\pi c$ the wave number, and c the speed of light. When such a laser beam interacts with a plasma, its transverse electromagnetic field makes the plasma electrons oscillate with the laser frequency. Electrons oscillate stronger

than the much heavier ions. (*Except for extreme intensities, the light forces on the ions are mediated by the electrons.*) The equation of motion for an electron reads

$$\frac{d\vec{p}}{dt} = \frac{d}{dt}(m\gamma\vec{v}) = -e\left(\vec{E}_L + \vec{v} \times \vec{B}_L\right), \tag{2.3}$$

where $\vec{v}$ and $\vec{p}$ are velocity and momentum of the electron, and c is the speed of light. $d\vec{p}/dt$ is the momentum change with time, and $\gamma = \sqrt{1 - \vec{v}^2/c^2}^{-1}$ is the relativistic Lorentz factor. For non-relativistic velocities the magnetic force term is much smaller than the electric term and can be neglected in the first order. Integrating the equation of motion gives $\vec{p} = -e/\omega\ \vec{E}_L$. By rewriting this expression

$$\vec{v} = \frac{\vec{p}}{\gamma m} = -\frac{1}{\gamma}\frac{e\vec{E}_L}{m\omega c}c, \tag{2.4}$$

it can be seen that the electron motion becomes relativistic, if the dimensionless value

$$\vec{a}_0 = e\vec{E}/m\omega c \tag{2.5}$$

approaches 1. $\vec{a}_0$ is called *dimensionless light amplitude*. It divides different regimes of laser-plasma-interaction. For $\vec{a}_0 \ll 1$ the electron motion is non-relativistic, for $\vec{a}_0 \approx 1$ relativistic and for $\vec{a}_0 \gg 1$ ultra-relativistic. In the relativistic and ultra-relativistic regime the magnetic force cannot be neglected any more. The laser-plasma interaction becomes non-linear and a large variety of new effects emerge. For ions, $\vec{a}_0$ becomes 1 at field strengths that are higher by a factor of m_i/m_e, where m_i and m_e are the ion and electron mass. This means that reaching the relativistic regime requires much higher laser fields for ions than for electrons.

We can now rewrite the electric and magnetic field amplitudes in units of $\vec{a}_0$:

$$E_0 \quad = \quad \frac{\vec{a}_0}{\lambda_L[\mu\mathrm{m}]} \cdot 3.2 \cdot 10^{12}\frac{\mathrm{V}}{\mathrm{m}} \tag{2.6}$$

$$B_0 = E_0/c \quad = \quad \frac{\vec{a}_0}{\lambda_L[\mu\mathrm{m}]} \cdot 1.07 \cdot 10^4\mathrm{T} \tag{2.7}$$

where λ_L is the laser wavelength given in μm. With these fields, we can also write the light intensity in terms of $\vec{a}_0$ as

$$I \quad = \quad |\vec{S}| = \left\langle\left|\vec{E} \times \frac{\vec{B}}{\mu_0}\right|\right\rangle = \frac{\epsilon_0 c}{2}|E_0|^2 \tag{2.8}$$

$$= \quad \frac{\vec{a}_0^2}{\lambda_L^2[\mu\mathrm{m}^2]} \cdot 1.37 \cdot 10^{18}\frac{\mathrm{W}}{\mathrm{cm}^2}, \tag{2.9}$$

with the Poynting Vector $\vec{S}$, and the dielectric and magnetic constants ϵ_0 and μ_0. For laser light with a wavelength of $\lambda_L = 1\mu$m, a_0 becomes > 1 for intensities above 1.37×10^{18}W/cm^2.

It is obvious that the electric field implied by $\vec{a}_0 = 1$ of 1-μm laser light is substantially larger than the inner-atomic field that binds the valence electrons, which is on the order of 10^{10} V/m. Thus, if such a laser pulse interacts with matter, even the rising edge of the pulse is sufficiently intense to rapidly ionize the target atoms and generate a plasma.

2.1.1   Interaction with Single Particles in Vacuum

We will now in brief investigate the effect of these strong fields on single electrons and ions, before we will describe the collective plasma effects leading to efficient particle acceleration in the next section.

Due to the particle mass in equation 2.5 the response of ions to the laser light is much smaller than that of electrons, and the energy transfer from laser light to electrons is much more efficient than to heavier particles. We can conclude that efficient ion acceleration by direct laser light is not feasible. It turns out that in a *plasma*, collective effects can indeed lead to strong space charge fields and subsequent ion acceleration. These fields are generated by accelerating electrons to high energies by the laser field. To understand the underlying mechanisms, however, it is helpful to first consider the motion of electrons in the laser field. The movement of a single electron or ion in these strong fields can be described by the relativistic equation of motion 2.3. Using equation 2.1 and setting $\gamma = 1$ we can quickly solve the remaining differential equation for $\vec{v}$:

$$\vec{v} \overset{(a_0 \ll 1)}{=} \frac{e\vec{E}}{m\omega}\sin(\omega t - kx) = a_0 c \sin(\omega t - kx) \qquad (2.10)$$

This describes a transverse oscillatory ("quiver") motion of the electrons following the oscillations of the laser field. Obviously, after crossing the threshold $\vec{a}_0 = 1$, the non-relativistic description leads to wrong results, and we enter a new regime of relativistic laser-matter interaction.

1. **Mass increase:** If the electron velocity approaches c in every oscillation period, its average mass increases.

2. **Anharmonic motion:** Since the electron mass changes dynamically over one oscillation period, the motion is no longer harmonic. The maximum

quiver amplitude is given by $y_0 = a_0\lambda/2\pi$.

3. **Forward drift:** For v approaching c, the $v \times \vec{B}/c$ term in equation 2.3 cannot be neglected and leads to a bending of the particle trajectory from the pure oscillatory motion in $\hat{y}$ direction into a positive $\hat{x}$- directed drift.

The derivation of the resulting electron motion is straightforward for a box-shaped pulse profile (see e.g. [20]), but for the realistic case of a gaussian laser pulse profile (spatially and temporally) it is more complicated. The easiest way to obtain the quiver motion is to numerically integrate the equation of motion 2.3. In Fig. 2.1 the electron trajectories for two different situations are shown. In the red curve, a single electron is overtaken by a laser pulse with infinite transverse extension, resulting in a quiver motion that increases towards the pulse maximum and then drops back to zero again. During the pulse the electron has drifted into the laser direction, but after the pulse it is in rest, thus having experienced no net energy gain. In the blue curve, the situation is shown for an electron moving in a laser focus of finite width. Since at the maximum transverse elongation of the electron the field strength is less than that on the laser axis, the electron feels less driving force to bring it back to the axis. This leads to a gradual sideways drift out of the high intensity region and a resulting energy transfer to the electron. Thus for a finite field extension, this mechanism leads to electron acceleration by the laser light. Without taking into account the actual trajectories, the net force of
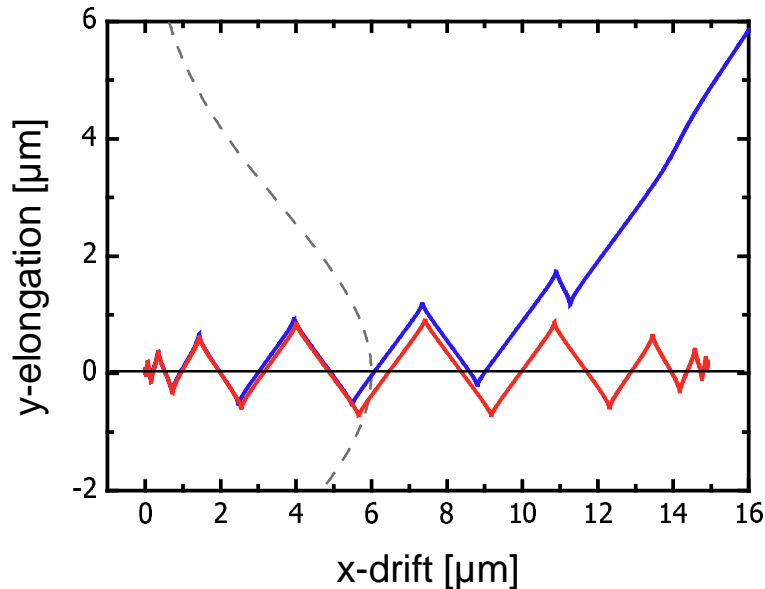
Figure 2.1: Single electron trajectory ("quiver-motion") in a gaussian laser pulse (τ_L=20 fs, $I_L = 3 \times 10^{19}$ W/cm^2) with infinite transverse extension (red) and in a laser focus of 8μm diameter (blue).

the laser pulse on an electron can thus be described by introducing the so-called *ponderomotive potential*

$$U_{pond.} = \frac{m_e c^2}{4\bar{\gamma}} a_0^2 \tag{2.11}$$

where $\bar{\gamma}$ is the cycle-averaged relativistic γ-factor ([21]):

$$\bar{\gamma} = \langle\gamma\rangle \approx \sqrt{1 + a_0^2/2} \tag{2.12}$$

The electrons are accelerated along the steepest gradient of this potential, which can also be understood as the light pressure or ponderomotive force.

From this simple picture, one would expect electron emission only in the laser polarization plane. However, in a more realistic scenario taking into account longitudinal field components in the gaussian beam waist of a laser focus ([22]), electron acceleration occurs in a radially symmetric pattern, and the electrons are expelled from the focus in a large solid angle. The relativistically correct, three-dimensional expression for the momentum change $d\vec{p}/dt$ of a particle in the laser field is given in [22]:

$$\left\langle \frac{d\vec{p}}{dt} \right\rangle = \frac{1}{2m_e \langle\gamma\rangle} \nabla \left\langle |q\mathbf{A}_\perp|^2 \right\rangle \tag{2.13}$$

Here, $q \equiv 1$ is the electron charge and $\mathbf{A}_\perp$ is the transverse component of the 4-vector of the electromagnetic potential ($\mathbf{A} = (e\Phi, \vec{A})$). $\langle\rangle$ denotes averaging over one laser period. This equation shows that electrons are expelled from the region of high laser fields following the potential gradient in both transverse dimensions.

These processes are only efficient for electrons, since ions with their large rest mass are much too inert to be efficiently accelerated. This leads to the conclusion that laser ion acceleration in vacuum is not feasible at presently achievable intensities of $\leq 10^{21} \text{W/cm}^2$.

2.1.2   Interaction in Plasmas

As already mentioned before, the electric field of the laser is several orders of magnitude higher than inner-atomic binding fields, and even the foot of the laser pulse is able to ionize all kind of matter and form a plasma. Therefore, the most part of the pulse always interacts with a certain amount of pre-formed plasma. The dimensions of the plasma depend strongly on the temporal behavior of this rising edge. In most laser systems, a certain amount of short prepulses and a long underlying pedestal is present, which both generate and shape the plasma gradient

in front of a target. Let us assume for the following considerations that the plasma consists only of one singly charged ion species and therefore one electron per ion.

If a laser pulse interacts with a plasma, the electrons start to collectively quiver around the (almost) stationary ions. Since the ion background exerts a spring force on the electrons, the system acts as a driven oscillator, leading to electron density waves in the plasma (plasma oscillations). Their characteristic frequency is given by the *electron plasma frequency*

$$\omega_p = \sqrt{\frac{e^2}{\epsilon_0} \frac{n_e}{\bar{\gamma} m_e}}, \tag{2.14}$$

which depends on the electron density n_e and the cycle-averaged γ factor. If the laser frequency ω_L is lower than ω_p, the plasma electrons can follow the light oscillations and therefore cancel the light propagation. Equation 2.14 thus defines a maximum plasma electron density in which light can still propagate. It is called the *critical density*,

$$n_{cr,rel} = \frac{\omega_L^2 \epsilon_0 \bar{\gamma} m_e}{e^2}, \tag{2.15}$$

and depends on the laser frequency and $\bar{\gamma}$. Plasma densities above and below the critical density are commonly referred to as *overcritical* and *undercritical*, respectively. Note that for relativistic intensities, the critical density scales approximately linear with a_0, so that highly intense laser pulses can penetrate further into a plasma gradient than light of lower intensity. For nonrelativistic intensities, n_{cr} is approx. $1.7 \times 10^{21} \text{cm}^{-3}$ for $\lambda_L = 800$nm. In an undercritical plasma ($n_e < n_{cr}$) light propagates with the phase and group velocities

$$v_{ph} = \frac{c}{n_p}, \quad v_{gr} = cn_p \quad \text{with} \quad n_p = \sqrt{1 - \left(\frac{\omega_p}{\omega_L}\right)^2}, \tag{2.16}$$

where n_p is the plasma refractive index.

Light propagating in an underdense plasma cannot only cause the electrons to quiver relativistically, but also expel electrons from high-intensity regions by the ponderomotive force. This leads to a reduction of the plasma frequency ω_p (equation 2.14) and subsequently to an increase of the plasma refractive index n_p (equation 2.16) in regions of high intensity. In a Gaussian beam profile, for example, where the intensity is highest on the laser axis, this leads to an increase of the refractive index on the axis and consequently to focusing of the laser light. That behavior is called relativistic self-focusing and may strongly enhance the laser intensity compared to the focused intensity in vacuum.

The plasma oscillations can reach very high amplitudes, if the ponderomotive force is strong enough to completely expel electrons out of high-field regions. This

also means that a plasma is able to support very strong electric fields due to space-charge separation, since the typical scale of these electron density fluctuations is on the order of 1 μm. Up to now, these fields belong to a traveling plasma wave, meaning that they are rapidly oscillating. For efficient ion acceleration, however, the fields have to be quasistatic, since, because of their high inertia, the ions need more time to get accelerated. Such quasistatic fields are possible if the electrons are completely removed from region in space. We thus have to identify processes which are able to accelerate many electrons to high energy, leaving behind a region with a strong space-charge potential.

Electron acceleration by the ponderomotive process is possible for electrons in vacuum in a plasma whose density is lower or equal to the critical density. In presence of plasma, additional collective effects may accelerate electrons to even higher energies. We will not describe these mechanisms in detail, since they only play a minor role in our case. For completeness, they are shortly described below:

1. **Ponderomotive Acceleration (PA)** As outlined above, it takes place wherever high intensity light interacts with electrons. These in turn acquire an energy distribution which is quasi-exponential with a temperature given by [23]

$$T_{pond} \;=\; 0.511 \;\cdot\; \left(\sqrt{1 \;+\; \frac{I\lambda^2}{1.37 \times 10^{18} \mathrm{W/cm}^2}} - 1 \right) \mathrm{MeV} \qquad (2.17)$$

   For intensities above $10^{19} \mathrm{W/cm}^2$, the temperature is on the order of $>$1 MeV. This process is highly efficient at the critical surface, since the electron density is highest here. THe PA therefore can produce both many and moderately fast electrons

2. **Wakefield acceleration (WFA)**[24] An intense laser pulse propagating in an underdense plasma excites a strong plasma wave (by expelling electrons with the head of the pulse ponderomotively, thus creating plasma density modulations). In this plasma wave travelling at nearly the speed of light electrons are trapped and "surf" the plasma wave. This process is efficient at low plasma densities around 10^{17} cm^{-3}, and thus is only capable of accelerating comparably few electrons, but to very high energies.

3. **Direct laser acceleration (DLA)** [25] If a high intensity laser pulse propagates in a plasma of sub-critical ($\sim 10^{20}$ cm^{-3}), the relativistic quiver motion of the electrons leads to a mass increase and therefore to a reduction of the plasma refractive index. This leads to the self-focussing of the laser pulse and

a propagation along a μm-sized light channel. By ponderomotive accelera-
tion a large electron current is driven forward, so that a azimutal magnetic
field and radial electric field is formed along the channel. Electrons leaving
the channel (by the ponderomotive force) are bent back into the channel by
these large quasistatic fields. If an electron crosses the channel in the right
phase of the laser light, it can pick up energy from the transverse field and
be bent back again into the channel. If its oscillation period is in phase with
the laser field, it can gain a large amount of energy, so that this mechanism
is favored for very high energy electron production. It requires, however, a
long plasma for the channel to form and the fields to develop, so in our case
it only plays a minor role.

4. **Brunel-mechanism, vacuum heating [26]** When a p-polarized laser pulse
   interacts with a plasma exhibiting a steep density gradient at the critical
   surface, electrons get sucked out of the regions of overcritical density into
   vacuum by the component of the electric field pointing out of the target.
   After the next half-cycle, they are smashed back in by the electric field
   of opposite polarity, having gained a large amount of energy in the half-
   period they were propagating in vacuum. This mechanism cannot accelerate
   electrons to very high energies, and is dominant in steep density gradients.

As a conclusion, in our case only the ponderomotive acceleration is of impor-
tance. It drives many electrons out of the laser focus region to high energies, thus
leaving behind a strong space-charge.

2.2   Ion Acceleration

2.2.1   Ponderomotive Charge Separation

The laser pulse expels electrons from the focus by the ponderomotive force. For
the sake of simplicity, let us assume that the focus region is of spherical shape and
isolated from the surroundings, thus neglecting the conductivity of the target and
any charge flow. The target then represents a spherical capacitor whose the outer
boundary is at infinity, and whose capacity is hence given by

$$C = 4\pi\epsilon_0 R \simeq 1 \text{ fF} \tag{2.18}$$

with the radius of the plasma region $R \simeq 10\mu m$. Since the charge Q in the capacitor is given by

$$Q = eN_e = CU \qquad (2.19)$$

where U is the voltage, $N_e \sim 7 \times 10^9$ electrons can be removed before the target charges up to 1 MV (this electron number is indeed of the same order of magnitude as found typically in experiments). Since the ponderomotive potential of the laser is also 1-2 MV, this puts a limit on the maximum number of electrons to be removed and in turn on the maximum achievable space charge, since the laser is not able to push electrons against a potential drop stronger than that. This means that the space charge potential is limited by the mean electron energy, and therefore is approximately equal to T_{pond} from equation 2.17.

Let us for the moment assume that the laser intensity stays constant during the box-shaped pulse of finite duration. As the laser hits the gradient of the preformed plasma, it starts to accelerate electrons out of its way by the ponderomotive force. It penetrates into the preplasma up to the relativistic critical density (equation 2.15). At the head of the pulse, electrons are removed out of the region of laser light, which leads to a charge displacement in a way that a double layer is formed. Electrons are running ahead of the ions, trailing them behind, so negative charge is running ahead and positive charge behind. The charge separation is counter-balanced by the electrostatic field forming at the boundary layer, and can be estimated by a balance of laser pressure and the ponderomotive force.

$$P_L = \frac{I}{c} = \frac{F_{pond.}}{A} \qquad (2.20)$$

The laser pulse propagates up to the critical electron density n_{cr}, where it is partially absorbed (absorption coefficient α) and reflected. The *light pressure*

$$P = (2 - \alpha)\frac{I}{c} = (2 - \alpha)I_{18} * 3.3 \; GBar \qquad (2.21)$$

displaces electrons into the dense plasma and a double layer is produced. I_{18} denotes the laser intensity in 10^{18}W/cm². The generated electrostatic field $E_{\rm s}$ accelerates ions. It is counterbalanced by the laser *ponderomotive force*

$$F_{\rm p} = e\langle \mathbf{v} \times \mathbf{B_L} \rangle /c, \qquad (2.22)$$

where $\mathbf{B_L}$ is the laser magnetic field and $\langle ... \rangle$ means averaging over one laser period. For relativistically intense lasers, we take $|v| \approx c$, and estimate $E_{\rm s} \approx E_{\rm L}/2$, where $E_{\rm L}$ is the laser field. The characteristic ion energy can be found from the recession velocity u_r of the laser-plasma interface [27, 28, 23]:

$$\left(\frac{u_r}{c}\right)^2 = \left(1 - \frac{\alpha}{2}\right)\frac{mZn_{cr}I_{18}}{1.37Mn_{cr,rel}}, \qquad (2.23)$$

where $n_{cr,rel}$ is the relativistic critical density given by equation 2.15 and n_{cr} is the classical critical density for $\gamma = 1$. The ion energy associated with this velocity is

$$E_{\text{ion}} = Mu_r^2/2 \approx (1 - \alpha/2)m_e c^2 \overline{Z}\sqrt{I_{18}/2.74} \simeq 0.84 MeV \qquad (2.24)$$

for $\alpha = 1$, $\overline{Z} = 1$, $I_{18} = 30$. Peak ion energies can be up to 4 times higher than this due to the reflection from the running shock front [29, 27].

We can now also loosen our restriction of a constant laser intensity by breaking up an arbitrarily shaped pulse into little boxes and arguing along the same lines. The temporal variation of the laser intensity further smears out the ion energy distribution, leading to the broad distributions seen in experiments.

However, the ion energies measured in experiments (see chapter 5, 7) are significantly lower than suggested by equation 2.24, at least for laser pulses with a duration of $\approx$100 fs. This can be attributed to two reasons, as described below:

- The underlying assumption of deriving equation 2.24 is the interaction in a 1-D geometry, and the plasma can only react to the light pressure by moving forward. In 2-D and 3-D, the plasma can also move sideways, which means that the pressure can be released more easily, leading to less forceful acceleration. This is especially important in the case of small laser foci, high intensity and fairly long preplasma gradients, where the pulse bores deeply into the plasma.

- It needs a certain time to form the double layer and a stable acceleration regime. This time is not negligible in comparison to the pulse duration for sub-100 fs pulses. If the laser intensity already declines before the double layer is formed, the acceleration is less efficient

We can also expect that the situation gets more complex the more different ion species and charge states are present in the plasma. The argumentation presented above is therefore only a handy picture to understand the basic principle of ion acceleration by ponderomotive charge separation. Let us summarize the most important features before proceeding.

1. Laser light does not directly accelerate ions, but instead laser-accelerated electrons act as a "field transformer" which converts the rapidly oscillating laser field into quasistatic fields. These fields live long enough to accelerate ions in spite of their high inertia.

2. Ions are accelerated by the electron-ion double sheath forming at the relativistic critical surface, which bends around the head of the laser pulse following its intensity distribution. For small focal spots this leads to an almost hemispherical geometry of the double layer, leading to a large angular spread of the accelerated ions.

3. The maximum potential the ions can be accelerated in is given by the ponderomotive scaling. Thus the maximum kinetic energy of the ions is limited to $\sim T_{pond.}$.

4. In addition to a comparatively small number of high energy ions from this process much more ions are accelerated in the preplasma region before the critical surface to smaller energies by much weaker fields. This explains the two-component ion spectrum seen in most experiments.

All in all, this analytical model is very unsatisfactory since it only makes a quite vague statement about the "typical" ion energy, and this value is largely dependent on the absorption fraction of the laser light in the plasma. If one can identify the typical energy as a temperature of the ion distribution (which of course depends on the shape of this distribution), only that one parameter of the ion distribution is known. As stated above, the validity of this model is restricted to a more or less 1-dimensional situation, and maybe also only to longer ($> 200\ fs$) pulses. The model makes no assumption about the number of accelerated ions nor about their angular distribution.

2.2.2 PIC Modeling

The ion acceleration in the laser focus discussed above hence can not be treated adequately in a simple analytical model, so numerical methods have to be employed. The main goal was to model the 3-D ion momentum space after the laser pulse and compare it to the experimental data. By Alexander Pukhov's courtesy I was able to use his 3D-particle-in-cell (PIC) code VLPL-3D [30] to model the interaction of a relativistically intense laser pulse impinging on a steep (few μm) plasma density gradient in front of a slab of solid material. The code runs on the CRAY T3E-816 supercomputer at the Rechenzentrum Garching and uses 256 processors for the simulations performed for this work. A typical simulation run takes 6 hrs and produces a data output of around 10 GB. The code solves the relativistic equations of motion and Maxwell's equations simultaneously on the nodes of a three-dimensional grid, which samples the space volume ("simulation box")

under observation. The principle of PIC codes in general and especially VLPL are described in detail elsewhere [30] and will not be repeated here.

The simulation box in most of the runs performed for this work was $x = 19.2 \times y = 16 \times z = 16\mu m^3$ in size and consisted of $640 \times 160 \times 160$ cells, leading to a cell spacing of 30 nm in x-direction and 100 nm in y- and z-direction. This ensures that both the skin depth

$$\lambda_s \; = \; (c \; \sqrt{\overline{\gamma}})/\omega_p \approx 130 nm, \tag{2.25}$$

which defines the penetration depth of the light field at the critical surface, and the Debye length

$$\lambda_D = \sqrt{\frac{kT\epsilon_0}{ne^2}} = 130 \text{ nm (for T = 1 MeV)}, \tag{2.26}$$

which determines the length over which charge fluctuations in a plasma are shielded, are resolved at the relativistic critical surface. The laser either propagated into positive x-direction or under 45° to it.

We can now look a bit more in detail into the ion acceleration at the critical surface. In the following simulation a laser pulse with a duration 80 fs was hitting a preformed plasma with a exponential gradient of $3\mu m$ scalelength in front of a target with a maximum density of 16 n_{cr}. The focal spot was Gaussian-shaped in space and time and had a diameter of $4\mu m$. and the intensity $3 \times 10^{19} W/cm^2$, corresponding to the parameters of the Jena 10 TW laser. It is not easily possible to extract the acceleration fields directly from the simulation output, so in the following pictures (see Fig. 2.2) the difference of the electron and ion densities $(n_e - n_i)$ was plotted in a plane perpendicular to the polarization direction of the laser for times of 10, 20, 30, ..., 70 laser cycles (cycle duration 2.7 fs for 800 nm laser wavelength). At t=0, the laser pulse maximum is at -30 μm left of the simulation box, and is moving to the right. Electron excess is coded blue, while ion excess is marked red. Strong fields exist in places where the gradient (blue-red) is steep.

At 10 laser cycles, the laser starts to push electrons into forward direction, and a bow-shaped cusp of high electron density is formed around the head of the laser pulse. This leads to strong acceleration fields, but the ions are still stationary, and the structure is only caused by modifications of the electron density. The onset of modulation in the electron density by the oscillating laser field is already visible behind the head of the pulse. As the pulse propagates further (20 cycles), the rapid electron density modulation is fully developed. Still the ions are virtually immobile. As they start to move and the laser stops at the
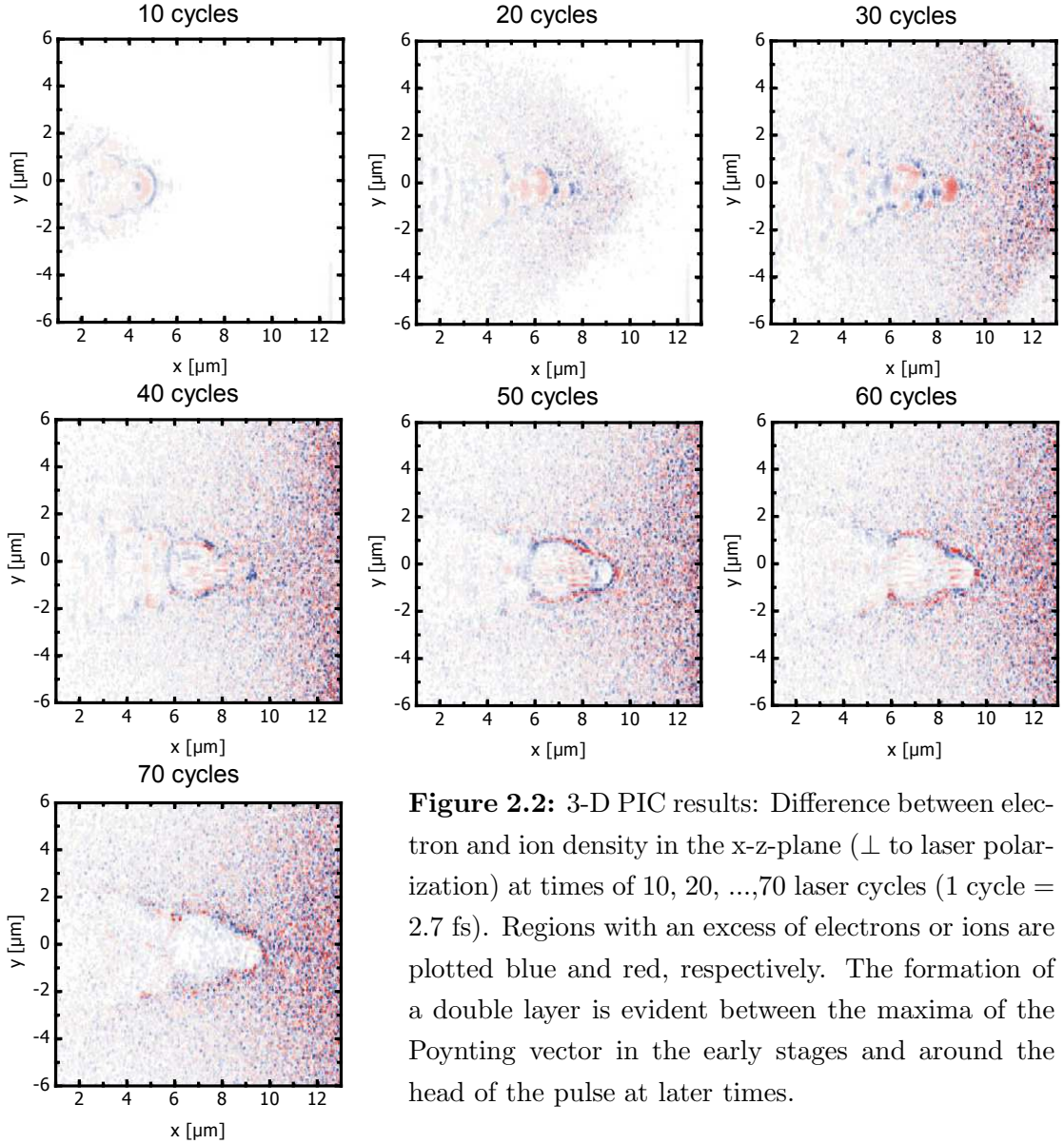
Figure 2.2: 3-D PIC results: Difference between electron and ion density in the x-z-plane ($\perp$ to laser polarization) at times of 10, 20, ...,70 laser cycles (1 cycle = 2.7 fs). Regions with an excess of electrons or ions are plotted blue and red, respectively. The formation of a double layer is evident between the maxima of the Poynting vector in the early stages and around the head of the pulse at later times.

relativistic critical surface (at 30 cycles), the rapid modulation breaks up and a more bowl-shaped electron density enhancement is developed. Note that now at the boundary of disturbed and undisturbed plasma, a very narrow double layer of electrons preceding the ions is formed (40 and 50 cycles), which leads to even stronger fields and efficient ion acceleration. At 60 and 70 cycles, the laser intensity drops so far that now the electrons oscillate back through the ion sheet, and the polarity of the boundary layer is reversed. Since the fastest ions going towards higher plasma density have already outrun the double layer, this reversed polarity causes a backwards acceleration as well. At 70 cycles, the driving force of the laser has vanished and the double layer neutralizes very fast.

In this case, the time between the formation of the double layer and the decrease in laser intensity is very short, so efficient ion acceleration is prevented, and the

ion energies stay far below the value inferred from equation 2.24. Also the pulse bores deeply into the plasma, leading to less forward directed push as in a 1-D case, distributing the available energy among more ions around the circumference of the focal region.

2.2.3   Acceleration in an Underdense Plasma

When the laser propagates through an underdense plasma, as in experiments employing a gas jet target or in the preplasma caused in front of solid targets by early prepulses from the laser (see Chapter 5, Section 5.2), ion acceleration occurs from a mechanism very similar to the above one. As has been studied both experimentally by eg. Pretzler [12] and Krushelnick [31] as well as theoretically (e.g. Pukhov [32]). Similar to the situation described above, electrons are expelled by the laser from the focus region. A number of mechanisms can accelerate electrons in an underdense plasma, such as wakefield-, direct laser (DLA)- and ponderomotive acceleration. Without going into more detail, the effect of this electron acceleration is the creation of a positively charged laser propagation region. This region subsequently Coulomb-explodes and accelerates ions. The main difference to acceleration at the critical surface are the lower quasistatic fields and the purely radial ion emission from the elongated laser propagation channel. Since the laser propagates freely in an underdense plasma, there is no critical surface to be pushed back by the laser. Consequently, the energy and momentum conservation ansatz described above is not applicable here. Instead, the transverse momentum transferred to the electrons is available for the formation of the double layer. Since most electrons are accelerated in forward direction, their transverse momentum is smaller than the longitudinal one.

The various experiments presented here were done with a variety of laser conditions, ranging from 80 fs pulses to 400 fs pulses and focal spot sizes from 3μm to 10μm, respectively. For the 400 fs case a full simulation can presently not be performed because of computer power limitations, since it would have to cover a large volume and a long time. However, for the experiments done at ATLAS (150 fs, 4.5μm focus, 2×10^{19}W/cm^2), and Jena (80 fs, 3μm focus, $3\text{-}4\times10^{19}$W/cm^2), full 3-D runs were performed. The output of the code for different cases is shown in the individual chapters related to a particular experiment.

2.2.4 Target-normal Sheath Acceleration (TNSA) Mechanism

The ion acceleration discussed so far takes place in the laser focus, and is a direct consequence of the ponderomotive displacement of electrons from their original location. It does not depend on where these electrons are moving, but only on the space charge fields set up by this electron removal. In contrast to that, there is another way of accelerating ions, which depends on the buildup of a large density of these displaced electrons in a region separated from the laser field. The process was first suggested by Wilks et al. [33] after the discovery of collimated beams of high energy protons normal to the rear surface of planar and wedge-shaped targets by several groups ([18, 34, 35]. It was named Target-Normal Sheath Acceleration (TNSA) by its inventor, and is now widely accepted by the laser-plasma community, although there still remains some controversy about its role under different experimental conditions. I will quickly describe the basic mechanism of TNSA in the following paragraph.

  Electrons accelerated by the laser (mainly ponderomotively) penetrate the target in forward direction. The first electrons can escape into vacuum, but in doing so they charge up the target, analog to the estimate given in equations 2.18, 2.19. The charging up of the target prevents further electrons from escaping, so that the hot electrons are bound inside and around the target. The hot electrons can be considered as a separate electron population in the target, with only little interaction with the cold background electrons. One consequence of this presence of a hot electron population is that its density does not apruptly drop to zero at the target (rear) boundary. It rather extends into vacuum at a typical scalelength of about one Debye-length, forming a so-called "Debye-Sheath" of hot electrons at the target rear surface.

$$\lambda_D = \sqrt{\frac{kT\epsilon_0}{ne^2}}. \tag{2.27}$$

Here T is the temperature of the hot electron component, and n is the density of these electrons at the target rear surface. For typical conditions found at e.g. the LULI laser or the Livermore Petawatt laser, λ_D is on the order of 1μm. Note that the Debye-Sheath mainly forms at the target rear surface, because the electron momentum is forward directed as dictated by the laser fields. Only if the electrons bounce back in the electrostatic field of the sheath, they can also reach the front surface and set up a second, but weaker sheath there, too. The situation now represents an excess of negative charge in the sheath opposing an excess of positive charge in the bulk of the target, similar to a plate capacitor. In Fig. 2.3 the situ-

ation is depicted schematically for two different times, the left side corresponding to the arrival of the first electrons at the rear surface, and the right side showing the beginning of the ion movement. The electron sheath extending into vacuum
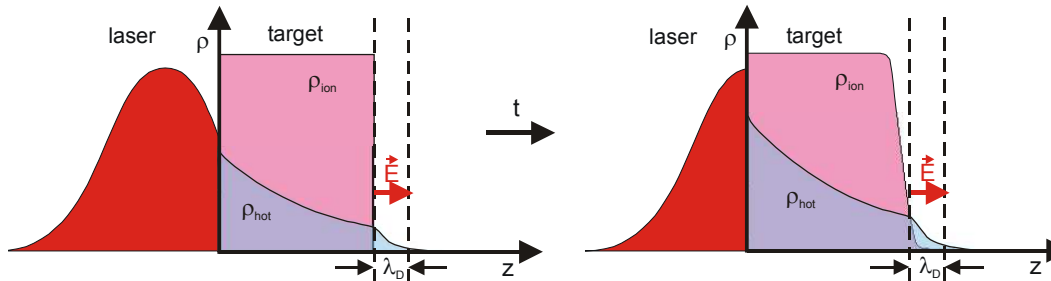
Figure 2.3: Schematics of laser intensity (red), ion density (pink) and hot electron density (blue) for two different times.

acts as a virtual cathode, which can ionize and accelerate target atoms off the rear surface. The electric fields strength caused by this charge imbalance amounts to

$$E_{stat} \approx kT_{hot}/e\lambda_D \tag{2.28}$$

which is on the order of 1 TV/m for typical experimental conditions ($T_{hot} \approx 1-2$ MeV). This field is of the same order of magnitude as the primary laser fields, and therefore is sufficiently strong to ionize light atoms up to He-like electron configurations. As the field rises with increasing electron density and temperature in the rising edge of the laser pulse, it subsequently ionizes atoms up to charge states allowed by barrier suppression ionization threshold in a matter of femtoseconds. As soon as the field strength at the back surface of the target reaches the threshold for single ionization, the free electrons available now are pinning the field at the rear surface to exactly the ionization value, because for each further increase in field strength a new charge pair is generated, which compensates for the field increase. Thus, only in regions behind the rear surface, the field can increase further and ionize the accelerated singly charged ions up to higher charge states. This means that at the rear surface, a sequence of spatially separated field steps is formed, ionizing the ions up to the maximum charge state. For more detail, the reader should refer to [33, 36, 37]. The scaling of the maximum ion energy and temperature is not well understood up to now. For a given ion species (i.e. mass and charge state) it is highly dependent on the other species accelerated as well. Especially protons with their high charge-to-mass ratio can severely inhibit the acceleration efficiency for all other species [36]. The precise process of field inhibition by protons is still work under progress and subject to a number of theoretical and experimental studies.

We have now discussed the two main mechanisms responsible for ion acceleration. These processes represent the first step to efficient neutron production, since they provide the high energy ions needed for triggering the necessary nuclear reactions. As a next step, different nuclear reactions suitable for neutron generation will be presented.

Chapter 3

Neutron Generation and Detection

3.1 Neutron Generation

In the experiments presented in this work, neutrons are not "generated" from vacuum, but are, of course, only freed from a bound state, the atomic nucleus. Free neutrons are not stable, but undergo a weak decay with a half-life of $\sim 614\,s$ into a proton, an electron and an electron-antineutrino. Thus it is not feasible to prepare an ensemble of neutrons without this nuclear binding energy in order to make neutrons from this ensemble readily available. The only viable road to neutron production is to free them from the nuclear potential. The mean energy with which a neutron is bound to the nucleus amounts to ~ 8 MeV. This amount of energy has hence to be spent to free it. On the other hand, this binding energy ensures the stability of the bound neutron. The large value of this binding energy is prohibitive for simply trying to kick the neutron out of the nucleus, if efficient neutron production is desired. Indeed, there are various other types of neutron generation reactions as well.

3.1.1 Reaction Types, Cross-Sections

First, a short overview over the most important reactions useful for laser-induced neutron production is given.

1. **(γ,n) reactions:** If a γ-quantum interacts with an atomic nucleus, it can

be absorbed and its energy will be used to excite the nucleus. In the case
where the excitation energy is higher than the nuclear binding energy, one or
more neutrons (or protons, depending on the nuclear structure) is emitted
from the core. In general, the threshold energy required for this to happen
is the nuclear binding energy for the weakest bound particle, which ranges
from 1.7 MeV in the case of ^{9}Be over ~ 15 MeV for very stable (even-even
paired) light nuclei like carbon to ~ 8 MeV for heavy nuclei. This energy
is not equal to the well known mean binding energy per nucleon (Fig. 3.1)
especially for light elements, since some valence-nuclei might be less tightly
bound. A broad resonance (the giant dipole resonance) in the cross-section
is located at $\approx$ twice this energy. The peak cross-sections for this kind
of reaction range from ~ 2 mbarn in the case of light nuclei (deuterons,
^{9}Be) to ~ 800 mbarn for ^{208}Pb. In a laser-plasma experiment, the number
of γ-photons emitted at these high energies is relatively small due to their
Boltzmann-like spectrum. Hence, (γ,n)-reactions give rise to a moderate
amount of low energy neutrons. Lacking an accurate γ- or electron-, yield-
and temperature-measurement, these neutrons could not be attributed to a
particular source and were therefore not further treated.
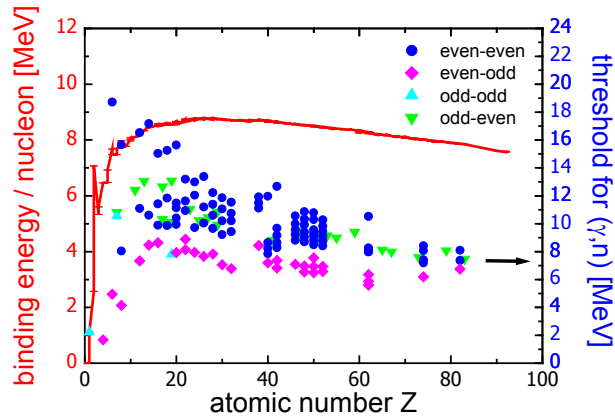
Figure 3.1: Binding energy / nucleon (red line) and the threshold for the (γ,n)-reaction
(dots) for a selected number of stable nuclides as a function of the atomic number Z.
The scale for the threshold values is plotted at the right side. Dots arranged in a
vertical column belong to a series of isotopes of one element. The threshold values are
color coded separately for even-even (blue), even-odd (magenta), odd-odd (cyan) and
odd-even (green) isotopes (data taken from [38]).

In analogy to these (γ,n)-reactions, also the emission of x neutrons can be
triggered in (γ, xn) reactions. Since here roughly x-times the binding en-
ergy has to be transferred to the nucleus, the threshold for these reactions

increases in approximately equidistant steps. This makes these reactions useful for determining the temperature of the hot γ-spectrum.

2. **(p,n), exchange or stripping reactions:** The excitation energy necessary for the emission of a neutron can also be supplied by the interaction of an ion with the nucleus. The simplest projectile is a proton, which can either be captured into an energetically favorable state and release its binding energy or simply knock out a neutron from the nucleus by its momentum transfer. Heavier ions can exchange nucleons with the target and therefore reach an energetically more stable configuration, which can also lead to the freeing of neutrons. In the case of two particles in the exit channel, the neutron spectrum is monoenergetic for a given projectile energy and neutron emission angle. However, since the angle and energy spread of laser-emitted particles is large, only strongly exothermal reactions ($Q \gg E_{proj.}$) will yield roughly monoenergetic neutrons. Which process takes place in a particular case depends on the combination of target, projectile and momentum transfer. The cross-sections for these processes are in the range of 100 mbarn up to one barn and therefore quite large.
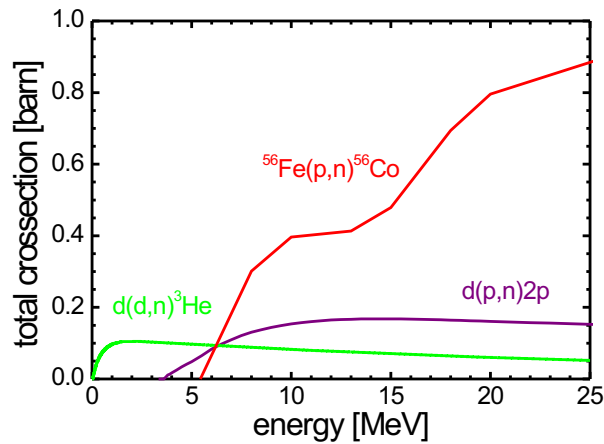
Figure 3.2: Neutron production cross-section for the reactions d(d,n)^{3}He, d(p,n)2p and ^{56}Fe(p,n)^{56}Co [39].

3. **Fusion reactions:** For light nuclei, the fusion reactions can be a source of monoenergetic neutrons, since they sometimes fulfill the necessary criteria of high energy release combined with low threshold. Some of them are a special case of exchange or stripping reactions. As can be seen from Fig. 3.1, light nuclei have a low binding energy per nucleon. By fusing together, they can obtain a higher binding energy, which is equivalent to a net energy release.

Two fusion reactions are particularly important for laser plasma interaction studies:

(a) *d-d fusion:*

$$^2\mathrm{H} + {}^2\mathrm{H} \quad \longrightarrow \quad {}^3\mathrm{He}\,(0.8\mathrm{MeV}) + \mathrm{n}\,(2.45\mathrm{MeV}), \tag{3.1}$$
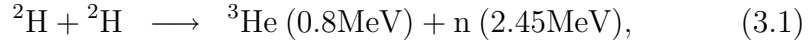
and its equivalent reaction

$$^2\mathrm{H} + {}^2\mathrm{H} \quad \longrightarrow \quad {}^3\mathrm{H}\,(1.0\mathrm{MeV}) + \mathrm{p}\,(3.02\mathrm{MeV}). \tag{3.2}$$
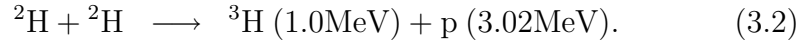
Also two endothermic reactions in a d-d collision shall be mentioned here, but they play only a minor role for the overall neutron production.

$$^2\mathrm{H} + {}^2\mathrm{H} \quad \longrightarrow \quad \mathrm{n} + \mathrm{p} + {}^2\mathrm{H} - 2.22\mathrm{MeV}, \tag{3.3}$$

$$^2\mathrm{H} + {}^2\mathrm{H} \quad \longrightarrow \quad 2\mathrm{n} + 2\mathrm{p} - 4.44\mathrm{MeV} \tag{3.4}$$
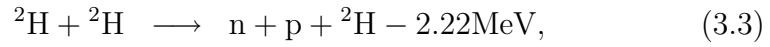
with a threshold of 4.44 MeV and 8.89 MeV, respectively.

(b) *d-T fusion:*

$$^2\mathrm{H} + {}^3\mathrm{H} \quad \longrightarrow \quad \alpha\,(3.52\mathrm{MeV}) + \mathrm{n}\,(14.07\mathrm{MeV}). \tag{3.5}$$
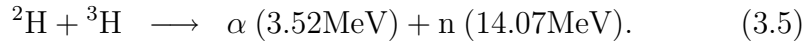
The competing reaction

$$^2\mathrm{H} + {}^3\mathrm{H} \quad \longrightarrow \quad {}^5\mathrm{He} + \gamma + 16.7\mathrm{MeV} \tag{3.6}$$

$$\tag{3.7}$$
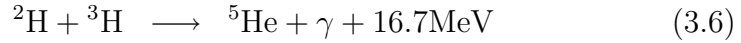
has a very small cross-section due to the stability of the ^{4}He nucleus produced in the first case. Also in this case there exist two endothermal neutron production reactions

$$^2\mathrm{H} + {}^3\mathrm{H} \quad \longrightarrow \quad \mathrm{n} + \mathrm{p} + {}^3\mathrm{H} - 2.22\mathrm{MeV} \tag{3.8}$$

$$^2\mathrm{H} + {}^3\mathrm{H} \quad \longrightarrow \quad 2\mathrm{n} + {}^3\mathrm{He} - 2.99\mathrm{MeV} \tag{3.9}$$
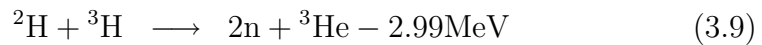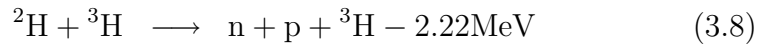
with a threshold of 5.56 MeV and 7.46 MeV, respectively.

The cross-section of the reactions 3.1,3.2,3.5 are plotted in Fig. 3.3. While the first two cross-sections are nearly equal, the tritium cross-section exceeds the others by almost two orders of magnitude. Using laser generated ions of energies below 1 MeV, by switching to d-t fusion reactions the neutron output could be boosted by the same factor.

However, due to the radioactivity of tritium, experiments using the (d,T) fusion reaction were not performed in this work. The reaction 3.2 took place in the experiments too, but it was not looked at. Therefore only reaction 3.1 will be described a bit more in detail.
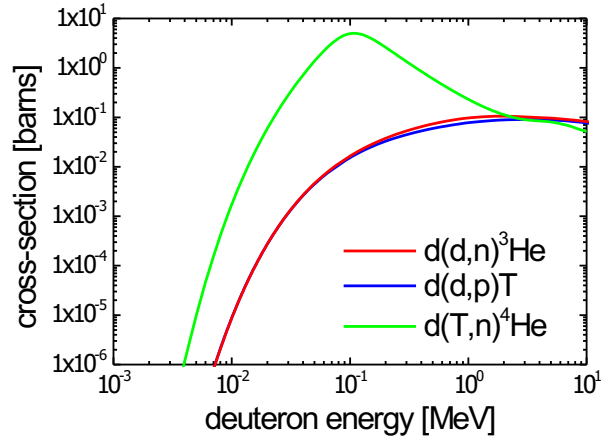
Figure 3.3: Fusion reaction cross-section for the d-d and d-t fusion reactions (data taken from [39])

3.2 Neutron Detectors and Data Aquisition

In order to do neutron spectroscopy, we have to find a suitable detector system that is able to both record the number and energy of the generated neutrons from a rapidly pulsed source. As already suggested by their name, neutrons are neutral particles. Therefore,

1. They cannot be deflected by magnetic fields to separate different neutron energies spatially.

2. They do not ionize matter or cause electron mediated damage, so with conventional particle detectors that either rely on ionization or electronic damage neutrons are hard to detect.

Thermal neutrons can be detected fairly easily by employing a neutron-capture reaction in a number of nuclides with a subsequent exothermal decay of the product nuclide. The cross-sections can run as high as $\sigma \approx 5000$ barns in the case of ^{3}He, making the detection of these thermal neutrons very efficient. This cross-section drops linearly with the time the neutron is within reach of the nuclear forces upon passing an nucleus and therefore scales with $\sigma \propto 1/v_n$, where v_n is the neutron's velocity. For fast neutrons, these capture cross-sections are therefore several order of magnitude smaller than for thermal neutrons, thus reducing the detection efficiency per detector mass significantly. Because of this behaviour, for efficient fast neutron detection the method of choice is the moderation of fast neutrons before detecting them in a thermal neutron detector with high efficiency.

Moderation is the process of slowing down a neutron during a number of elastic scattering events with light nuclei, where the energy of the neutron is partially or fully transferred to the recoil particle. The cross-section for the elastic scattering process is shown in Fig. 3.4 [39, 40]. From this figure it is evident that the scattering
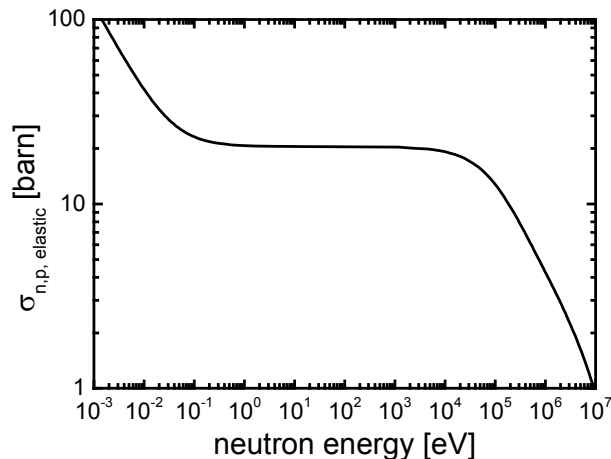
Figure 3.4: (n,p)-elastic scattering cross-section

cross-section for neutrons of a few MeV is strongly dependent on the neutron energy, which is an issue to be considered for the efficiency of detectors thinner than a few neutron mean free paths. The maximum energy $E_{R,max}$ transferred to the recoil particle (which is assumed to be in rest before the collision) in a single scattering event from a neutron of energy E_n is given by [40]

$$E_{R,max} = \frac{4A}{(1+A)^2}(\cos^2 \theta) \ E_n, \tag{3.10}$$

where A is the mass number of the recoil nucleus and θ is the scattering angle in the laboratory frame. For protons ($A = 1$, $\theta = 0$), this maximum energy equals the incident neutron energy. Since the scattering is isotropic (independent of θ) for protons below 10 MeV [40], the probability distribution of the recoil proton's energy and scattered neutron's energy after one scattering event is flat up to the incident neutron energy. On average, in a hydrogenous medium, neutrons therefore loose half of their initial energy in a single collision. This leads to quick thermalization ($\equiv$ slowing down) of neutrons to thermal energies, at which the moderator nuclei will not be able to extract energy from a neutron anymore due to their own thermal motion. Placing a thermal neutron detector into a sufficient amount of hydrogen-containing material (moderator) leads to almost complete thermalization of the fast neutron flux before it reaches the detector. During the moderation the information on the initial energy of the neutron is completely lost, which makes these detectors suitable only for counting (With certain restrictions,

by shaping the moderator properly, the energy response of such a detector can be tailored to a relatively narrow bandwidth).

The moderation approach is employed in the silver activation counters [41] used in this thesis for accurate neutron yield calibration. The slow neutrons are captured in two silver isotopes, and the resulting radioactive isotopes decay after a $\sim$ 25-s halflife to cadmium. This delayed decay signature makes it possible to handle the huge neutron fluxes following the laser pulse without pileup effects, since always enough nuclei are present as capture partners. On the other hand this detector always integrates over a time constant of one halflife. The activation process itself is inherently insensitive to γ-rays. The detector is described in the following section below.

A different approach to fast neutron detection is the counting of single proton recoil events. The energy of the proton is given above in equation 3.10 and is can reach all values between 0 and E_n. For a single event, it is therefore not possible to get information on the neutron energy. This only becomes possible by statistical methods [40] or by a neutron-time-of-flight technique as employed here. The fast neutrons scatter off the protons in matter, causing them to gain energy and ionize the detector material along their track. If this material is a liquid or plastic scintillator, the recoil protons can be counted in a phototube coupled to it. Since the scattering event and the subsequent stopping of the proton are fast processes, this detector can operate with a high temporal resolution, which makes it suitable for time-of-flight spectroscopy. This system is described at the end of this chapter.

Any useful detector system has has to meet the following requirements:

1. **Energy resolution:** While activation methods are ideally suited for measuring the total neutron yield, time-resolved neutron detection can be employed to measure the neutron spectrum. Since neutrons do have mass, different energies also correspond to different velocities. A d-d fusion neutron in the center-of-mass system is generated with an energy of 2.45 MeV, or an velocity of 2.165×10^7 m/s = 0.072c. Therefore spectroscopy can be done using the time-of-flight (TOF) technique, where the time between a well defined start signal (laser shot) and the arrival time of the neutron in the detector at a fixed distance is measured to calculate the neutron's energy.

2. **Background suppression:** Activation techniques inherently are not sensitive to other particles than neutrons, so there is no background problem with

an activation detector. The time-of-flight technique has the added benefit
that the time resolution allows to clearly distinguish between prompt back-
ground signal and delayed time-of-flight neutrons. Also the low duty cycle
of the laser (approx. 5×10^5 helps greatly in suppressing background, since
the detector is only active 100ns before and after the pulse.

3.2.1 Silver Activation Detector and Yield Calibration

In order to perform an accurate yield measurement, silver activation detectors were
loaned from one of our collaborators (see also chapter 6). The design and perfor-
mance of these detectors is described in [41]. They exploit a (n,γ) neutron capture
reaction in the two stable silver isotopes, which both occur at approximately the
same natural abundance:

$$^{107}\text{Ag} \quad \overset{\text{n–capture}}{\Rightarrow} \quad ^{108}\text{Ag},$$
$$^{109}\text{Ag} \quad \overset{\text{n–capture}}{\Rightarrow} \quad ^{110}\text{Ag}.$$
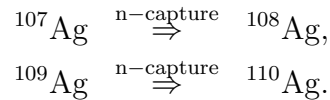
Neutrons entering the detector volume are thermalized in the plastic scintillator
material (see below) and captured in by those isotopes with the large thermal cross-
section of 37 barn and 86 barn for ^{107}Ag and ^{109}Ag, respectively. The generated
silver isotopes on the right-hand side are radioactive and predominantly suffer
a electron-capture- (ec-) decay predominantly to the ground state of ^{108}Cd and
^{110}Cd:

$$^{108}\text{Ag} \quad \overset{2.41\text{min}}{\Rightarrow} \quad ^{108}\text{Cd} + 1.65\,\text{MeV},$$
$$^{110}\text{Ag} \quad \overset{24.6\text{s}}{\Rightarrow} \quad ^{110}\text{Cd} + 2.89\,\text{MeV}.$$
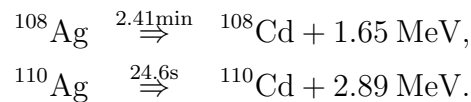
In Fig. 3.5 the (n,γ) cross-sections for these two reactions are plotted against the
neutron energy.

Since almost all ec-decays of the cadmium isotopes go directly to the ground
state of the according silver isotopes, no direct γ-quantum or charged particle is
emitted from the decay. Instead, the k_α x-ray emission can be detected, which is
emitted when the hole in the K-shell created by the capture event is filled by an L-
electron. The half-life of 2.41 min and 26.4 s of ^{108}Ag and ^{110}Ag offer a convenient
way of identifying short neutron pulses entering the detector by measuring the
decay time of the induced radiation. The time delay between the neutron pulse
and the decay events thus acts as a discrimination against the electromagnetic
pulse (EMP) and γ-flash from the laser.
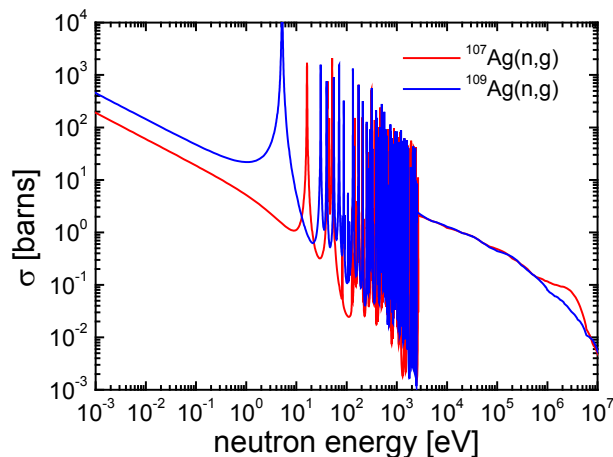
Figure 3.5: Radiative n-capture cross-section $\sigma(n,\gamma)$ in ^{107}Ag and ^{109}Ag (data from [39])

The silver detector itself consists of an active volume of 31 silver foils (101.6 × 203.2 × 0.245 mm, total mass 1.64 kg) placed between 32 NE-110 plastic scintillator sheets (102 × 204.0 × 3.2mm), both embedded in a light-tight aluminum case. The scintillator sheets act as a light guide for the scintillation photons, and are coupled side-on to a lucite light pipe, which in turn is connected to a standard 2" photomultiplier tube. It was connected to a industry standard frequency-to-voltage converter originally intended only for slowly varying signal frequencies, connected to a digital storage oscilloscope. Driving the converter with random signals resulted in large output spikes, which could be dampened in the analysis by applying an FFT low-pass filter to the recorded dataset. Although the efficiency of the silver counters is investigated and stated to be 0.25±0.02 for 2.5 MeV neutrons in [41], no specifications are given for the type of phototubes used in the original work (the tubes were replaced by modern types for this work according to our collaborator). Neither are any informations given about the PMT supply voltage and discriminator settings. However, since the PMT gain and discriminator threshold were carefully optimized before the experiment, we are quite confident that this calibration is approximately valid for our case. Unfortunately, due to a misunderstanding, the detectors were used in a side-on illumination scheme instead of the proper head-on-configuration, which leads to smaller efficiency for high energy neutrons above 4 MeV. Since the thermalization length for 2.5 MeV neutrons is on the order of the transverse extent of the active volume, the orientation should play only a minor role for neutrons around the interesting energy range for this work (from 0.1-4 MeV). An attempt to recalibrate the detectors failed because of the high-energy spectrum of the only available ^{241}Am-Be neutron source, and the unknown efficiency for those in the side-on configuration. A more accurate yield

calibration in principle could be done with a ^{252}Cf neutron source, which exhibits a very similar neutron spectrum as the laser generated d-d fusion neutrons. Otherwise, the energy dependence of the efficiency can be calculated using elaborate neutron scattering and thermalization codes.

The main advantage of this detector is that it (in principle) allows a very accurate absolute determination of the neutron yield, as long as the neutron flux is either high enough to get a measurable signal from a single shot or remains fairly stable over a longer sequence of shots (the latter case will be clarified below). However, due to the thermalization of the neutrons before detection all information on the primary neutron energy is lost.

3.2.2   Time-of-Flight Diagnostics

In order to do spectroscopy, a detector system with energy resolution is needed. Here, the above mentioned proton recoil detector were used in the form of fast liquid and plastic scintillators coupled to fast PMT's. The energy resolution was provided by using them as time-of-flight detectors that measure the time between the laser shot and the arrival of the neutron at a given distance. Additionally, this approach provides separation between promptly emitted γ-rays and electromagnetic pulses (EMP), which can saturate the detector for up to 50 ns after the shot, on the one hand and delayed neutrons on the other hand. A conventional fast plastic scintillating detector employing a fast photomultiplier tube (PMT) has a time resolution on the order of 1-2 ns, so in principle this does not pose a problem. There are two ways of operating such a detector.

1. **Counting mode:** In this mode, the voltage on the photomultiplier tube is chosen such that the signal from one incoming particle drains a large fraction of the charge stored in the PMT's electrodes. This yields a strong signal (typically about 1 nC in ≈2 ns) for each particle. Since the PMT is fully drained by the γ-flash, the voltage supply must be able to recharge the tube in a sufficiently short time to restore its sensitivity. Due to the lack of a correlation of knock-on energy and neutron energy, it is not possible to decide whether a given signal was caused by one or more neutrons. Hence, it has to be made sure that only one neutron at a time can hit the detector, which means that, allowing for statistical fluctuations, only about one neutron per 10 laser shots can reach the detector without causing pileup problems. Using the detector in this mode is the only way of being able to count single

neutrons, but the price that has to be paid is that a TOF spectrum has to be accumulated over a large number of shots. Therefore, this mode was chosen for the ATLAS and Jena experiments, where the neutron yield was low and the shot rate high.

2. **Current mode:** In the current mode, the voltage on the PMT is chosen so that a large number of neutrons do cause an integrated signal, which does not drain the PMT charge. If this integrated signal is deconvolved with a single-particle signal, a time-of-flight spectrum can be obtained directly from one laser shot, provided a sufficient number of neutrons hit the detector. This method was applied for the LULI experiments, where the neutron output was sufficient to detect approximately 1000 neutrons simultaneously.

The setup for the ATLAS experiments is presented here as an example of the detection procedure. The low average neutron count rate in one detector made possible to use a simple CAMAC based nuclear physics data aquisition system that is only able to record a single logical signal per trigger.

As main neutron detectors two arrays of four TOF scintillation counters were used. Each array consisted of one 14-cm diameter by 10-cm thick liquid scintillation counters (NE213) and three 11-cm diameter by 2-cm thick plastic scintillation counters (NE110). The thickness for the thick scintillator was chosen such that the scattering probability for all neutrons in the interesting energy range is always greater than unity (see Fig. 3.6). Since the energy transfer to a recoil proton on the average is half the incident neutron energy (and therefore approximately 1.25 MeV, the energy deposition from the first scattering event is usually high enough to be detected, and the detector response is close to flat for all interesting neutron energies.

While for gamma rays the time resolution of the detector is governed by the photomultiplier's signal rise time (measured to 1.1±0.2 ns), for neutrons the flight time through the scintillator becomes important. For a fusion neutron of 2.45 MeV it takes 4.6 ns for 10 cm flight distance to cross, which presents an additional TOF uncertainty since the location of the scattering event is not known. Therefore the thin scintillators were optimized for fast counting, with only 2 cm thickness, reducing the TOF uncertainty due to fluctuations in scattering location to 0.9 ns. However, this leads to a scattering probability below unity (Fig. 3.6), which varies over the interesting energy range by about a factor of three. This variation has to be accounted for in the data analysis. For the measurements on ATLAS, this is of minor importance since the large majority of counts in the spectra were recorded
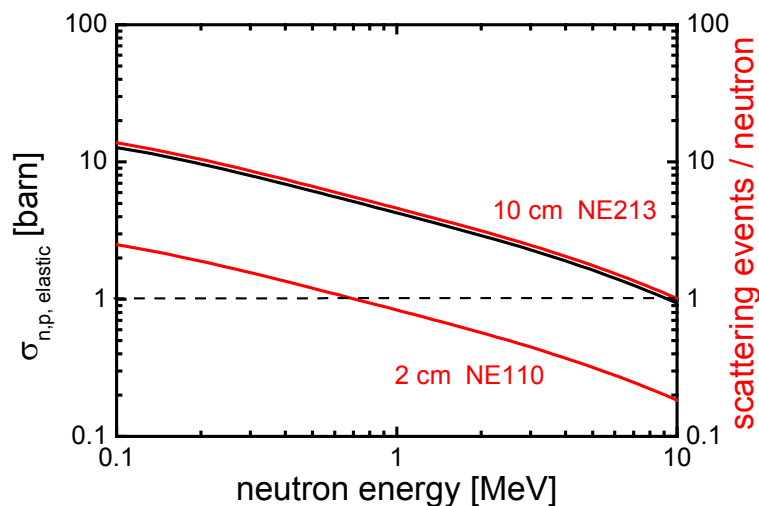
Figure 3.6: (n,p) elastic scattering cross-section in the energy range between 0.1 and 10 MeV, and the number of scattering events/neutron in the 2 cm and 10 cm scintillators.

with the large detector. In the Jena and Luli experiments, which were done with the small detectors only, this effect was taken into account. Overall, depending on discriminator thresholds, the efficiency of the thick detector is a factor of 2-3 higher than for the thin ones. The two detector arrays were encased in a lead shielding with 7.5 cm thickness in front and 5 cm to the sides to shield against γs from the interaction, while neutrons are able to pass (see section "MCNP Scattering Calculations", in chapter 4).

The detector signals are fed into a constant fraction discriminator (CFD), which produces a fast logic signal for the CAMAC time-to-digital-converter (TDC). This unit digitizes the time between the detector signal and a start signal, which is derived from the laser pulse itself. The CAMAC system is read out by a PC running the WinCAMDA [42] software which provides an easy to use, freely programmable readout interface. The data is stored to disk in binary format, which in turn is converted to an ASCII list for further processing.

The prompt gamma signal is seen on almost all shots even inside the lead housing of the detectors. This signal can be used as an in-situ time calibration, which is measured with the same detectors, cable length and electronics, and is therefore independent of changes in the setup. Since the TDCs can only handle one detector signal per start signal, it is necessary accumulate two different TOF spectra with two different start times. One is started before the prompt gamma signal (Start 1) and mainly consists of gamma signals. The second one is started after the gamma pulse (Start 2) and only accumulates the delayed neutron signals (Fig. 3.7).
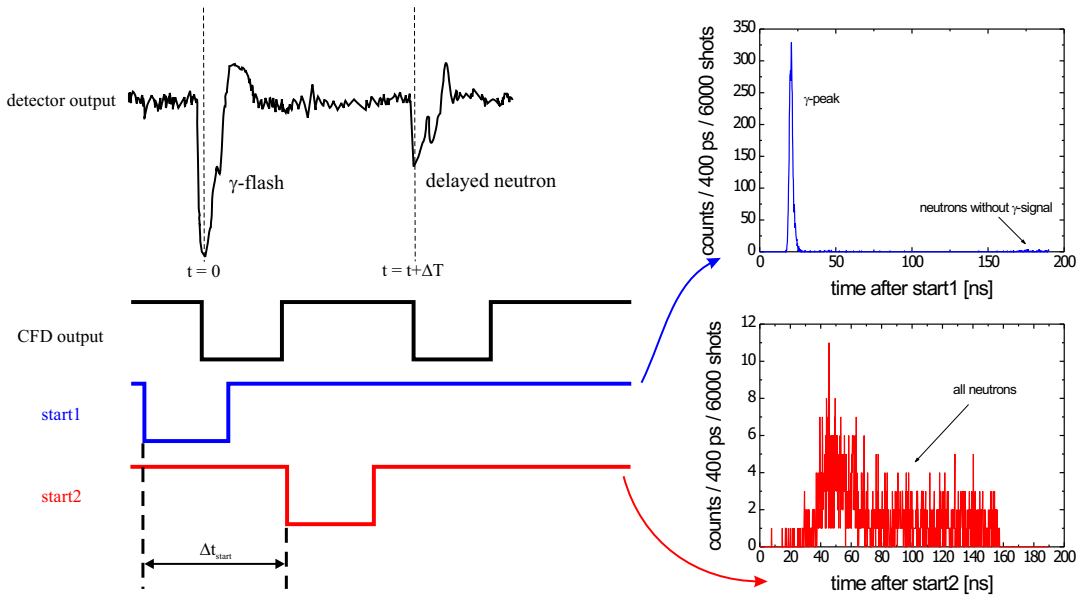
Figure 3.7: Timing schematics and resulting TOF neutron and gamma spectra. The signal from the detector and the resulting logic signal from the CFD is drawn in black, the blue line shows the prompt start signal and the resulting TOF spectrum accumulated from 6000 shots. It is dominated by the prompt gamma signals, but on shots without a gamma signal also some delayed neutron signals are visible (note: only the first signal after the trigger is counted) The red curves show the delayed start signal and a resulting TOF neutron spectrum.

The few neutrons in the Start 1 TOF spectrum can be used as an online check of the delay Δt_{start} between Start 1 and Start 2 when compared to their equivalent signals in the Start 2 spectrum. This makes possible the exact fitting together of the two spectra even without an exact absolute timing calibration. These detector arrays are not well suited for determining the absolute neutron number, since their precise efficiency for 2.45 MeV neutrons is not known. Lacking a calibrated, pulsed source for fast neutrons, it is very difficult to determine an absolute efficiency for the arrays. It was thus decided to use a separate activation detector for the total yield calibration, which is described below.

A cross-calibration of the detection efficiency of the TOF detectors was performed using the silver-activation counter with laser generated neutrons, eliminating the problem of a ill-matched source spectrum or problems from gating the TOF detectors by a random source decay for background suppression. The main difficulty in doing so arose from the fact that the neutron yield during a run is not very stable.
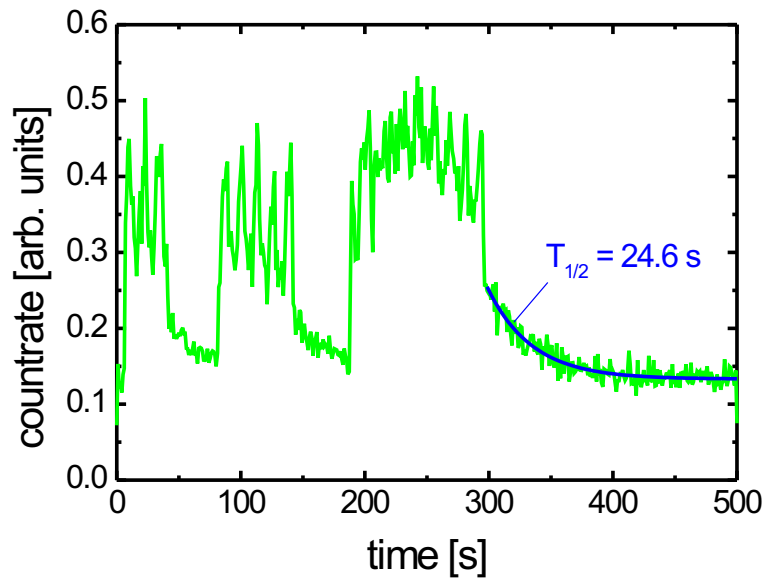
Figure 3.8: Record of the silverdetector count rate during an experimental run

In fact, it is very sensitive on variations of shifts of the target surface relative to the focalplane. These arise from an uneven target surface, wobbling of the rotating target and drifts in the laser focal plane. Moreover, since the target rotates with constant angular velocity and is shifted with constant horizontal velocity, the separation of the laser impacts is not constant, so sometimes the areas ablated by the beam halo overlap, leading to a recession of the surface. All these factors make it difficult to achieve a stable neutron production rate over a run, and in turn the accuracy of the silver detector measurement drops drastically. Fig. 3.8 shows a typical record of the silver detector countrate during a run, which had to be interrupted a couple of times due to laser realignment. It is evident that the count rate is not stable during the irradiation. However, a rough cross-calibration of the TOF detectors is possible with this data, leading to an overall efficiency for the large detectors of 0.6±0.2 and of the small ones of 0.4±0.15. These values are used as the basis for all yield estimates, unless otherwise stated. Since the silver detector was obtained at the end of the experiments at ATLAS, by far not all experiments used the silver detector, but have to rely on the TOF detectors alone. Instabilities in the neutron output play an even stronger role in these, since only the number of shots and the number of neutrons is monitored. As a conclusion, the absolute error of any yield statement is on the order of 50%.

Chapter 4

Modeling of Neutron Spectra

In this chapter, we will extend the theoretical background discussed in chapter 2 to develop the numerical code MCNEUT for simulating and quantifying the experimentally measured neutron spectra. As a basis for these modeling attempts, ion distributions obtained from the PIC simulations in chapter 2 as well as arbitrary user-defined ion distributions were used. As it turns out, one of the main difficulties is the correct treatment of ion stopping in hot plasma, which is different from cold matter stopping and may affect the neutron spectra. The solution of this problem comes down to estimating the target heating by fast electrons from the laser preceding the ions, which is largely dependent on the electron beam characteristics and target conductivity. Especially, electron beam filamentation and space-charge inhibition of the electrons in insulators are not well understood. Currently, this problem is treated both experimentally and theoretically, but the knowledge base up to now is quite slim. The approach presented here to solve this problem is quite simple and effects of target conductivity, filamentation and space charge effects are ignored. For the low laser energies and the comparatively low electron beam current on the ATLAS and Jena lasers, this is a good approximation. But even for higher energy lasers as in the LULI case, the results of this simple method are remarkably close to detailed numerical simulations done by Gremillet [43]. However, the effect on the neutron spectral shape is quite small for the laser parameters in this work. For bigger lasers, in contrast, the effect of abnormal stopping may become large, and in this case it might be even possible to use neutron spectroscopy to probe the target temperature distribution.

The development of MCNEUT was done having in view the $d(d,n)^3He$ fusion reaction as the most commonly used neutron production scheme in this work, but the method can of course be transferred to other reactions as well, given that the

differential cross-section is known.

4.1   d(d,^{3}He)n-Fusion Cross-Section and Kinematics

The most neutron generation experiments performed during this thesis were employing the d(d,n)^{3}He fusion reaction. In order to quantitatively understand the produced neutron spectra, it is necessary to model the contribution to the total fusion output of ions accelerated in all three dimensions.

In a binary reaction of the type A(a,b)B, with A = target nucleus, a = projectile, b = ejectile and B = residual nucleus, for thin targets the energy E_b of the ejectile produced in the laboratory frame under an angle θ to the projectile with the energy $E_{0,a}$ can be written as [44]:

$$E_b(E_{0,a}, \theta) = \frac{m_a m_b E_{0,a}}{(m_a + m_A)(m_b + m_B)}$$
$$\times \left[\cos(\theta) + \sqrt{\frac{m_A m_B E_{0,a} + Q m_B (m_a + m_A)}{m_a m_b E_{0,a}} - \sin^2 \theta} \right]^2 , \qquad (4.1)$$

where m_i is the mass of particle i. (For d-d fusion, $m_a = m_A = m_{deuteron}$, $m_b = m_{neutron}$ and $m_B = m_{^3He}$). Q is the reaction Q-value, which for d-d fusion is 3.26 MeV. Of course, this equation is valid analogue for all binary reactions with the proper choice of the masses and Q. The result of this formula is plotted in Fig. 4.1 for a number of angles θ and deuteron incident energies $E_{0,d}$.

The number of neutrons of a given energy detected within the solid angle $\Delta\Omega$ can be written as

$$N_n(E_n(E_{0,d}, \theta)) = N_d(E_{0,d}, \theta) \cdot \frac{d\sigma}{d\Omega}(E_{0,d}, \theta) \cdot \Delta\Omega \cdot n_d \cdot \frac{dx}{dE_{0,d}}(E_{0,d}) \qquad (4.2)$$

in this case. Here, $N_d(E_{0,d}, \theta)$ is the deuteron energy and angular distribution, θ is the angle between incoming deuteron and outgoing neutron, $\frac{d\sigma}{d\Omega}(E_{0,d}, \theta)$ is the differential fusion cross-section dependent on the current energy of the deuteron and its angle to the emitted neutron, n_d is the deuteron atom density in the target and $\frac{dx}{dE}(E_{0,d})$ is the derivative of the energy dependent deuteron range.
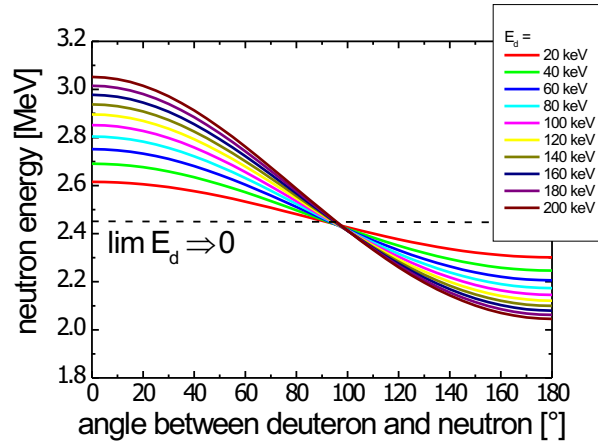
Figure 4.1: Energy-angle dependence of the neutron energies for the d(d,n)^{3}He fusion reaction.

Since the deuterons produced in our experiments were stopped inside the deuterated target in most cases, the assumption of a thin target is not valid anymore. Now, for calculating the momentary fusion probability, the slowing down of the deuteron from its starting energy $E_{0,d}$ to its current energy E_d on its trajectory through the target has to be taken into account. A closed analytical formula cannot be given for that.

The neutron spectrum for thick targets thus has to be calculated in the following way: For a single particle of the fast deuteron distribution, the probability spectrum for detecting a neutron with the energy $E_n(E_d, \theta)$ is given by:

$$P(E_n(E_d, \theta)) = \Delta\Omega \cdot \int_0^{E_{0,d}} \frac{d\sigma}{d\Omega}(E_d, \theta) \cdot n_d(x(E_d)) \cdot \frac{dx}{dE_d}(E_d) \cdot dE_d \qquad (4.3)$$

Now, in a generalized case, $n_d(x(E_d)$ becomes a function of the deuteron position in matter or vacuum (this includes material changes). $\frac{d\sigma}{d\Omega}(E_d, \theta)$ and $\frac{dx}{dE}(E_d)$ are now functions of the momentary energy E_d of the deuteron on its trajectory. The argument $E_n(E_d, \theta)$ on the left side hence has to be evaluated synchronously with the integration variable E_d. Note that in spite of a well defined deuteron starting energy, due to the stopping in matter the neutron energy is not defined, but subject to statistics. Using a possibility spectrum therefore is a correct description for a large number of particles. The neutron spectrum is generated by summation over all deuterons in the distribution:

$$N(E_n) = \sum_{E_d,\theta} N(E_d,\theta) \cdot P(E_n(E_d,\theta)) \qquad (4.4)$$

The cross-section data for the d-d fusion reaction is well known and conveniently available in a tabular format from the DROSG2000 computer code [45], and dx/dE can be inferred from stopping tables evaluated with the program SRIM2000 [46]. In Fig. 4.3 this data is plotted. It is striking that the cross-section is strongly forward peaked, which caused by a transformation of the peanut-shaped (long axis is the propagation axis) cross-section in the center-of-mass (c-m) system into the laboratory system (See Fig. 4.2).
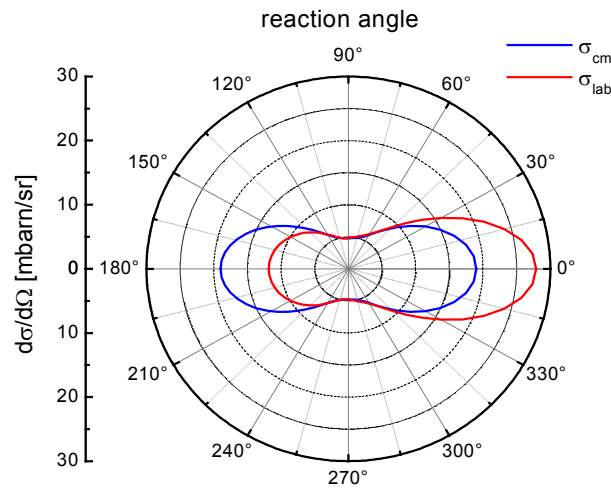
Figure 4.2: Differential cross-section of the d-d fusion reaction for a 1 MeV incident deuteron in the center-of-mass frame (blue line) and laboratory frame (red line). For different deuteron energies, the figure looks quantitatively similar.

This peanut-shaped form can be explained by the stripping nature of the reaction, where the proton of one reactant fuses with the other reactant, while the neutron keeps is original momentum. Since in the c-m system both deuterons are indistinguishable, the cross-section must be mirror-symmetric to a plane in the middle between the deuterons and perpendicular to the propagation axis.

Plugging these functions into equation 4.3 (evaluated for a single ion) yields the number of neutrons/ion for thick targets as a function for E_d and θ. Fig. 4.4 shows the result.

Multiplication with the detector solid angle $\Delta\Omega$ determines the total neutron output / ion seen in the detector. To obtain neutron energy and/or TOF spectra, 4.3 is evaluated for all deuteron energies and starting angles in the input spectrum and the result is plotted against the neutron energies inferred from 4.1. The inverse
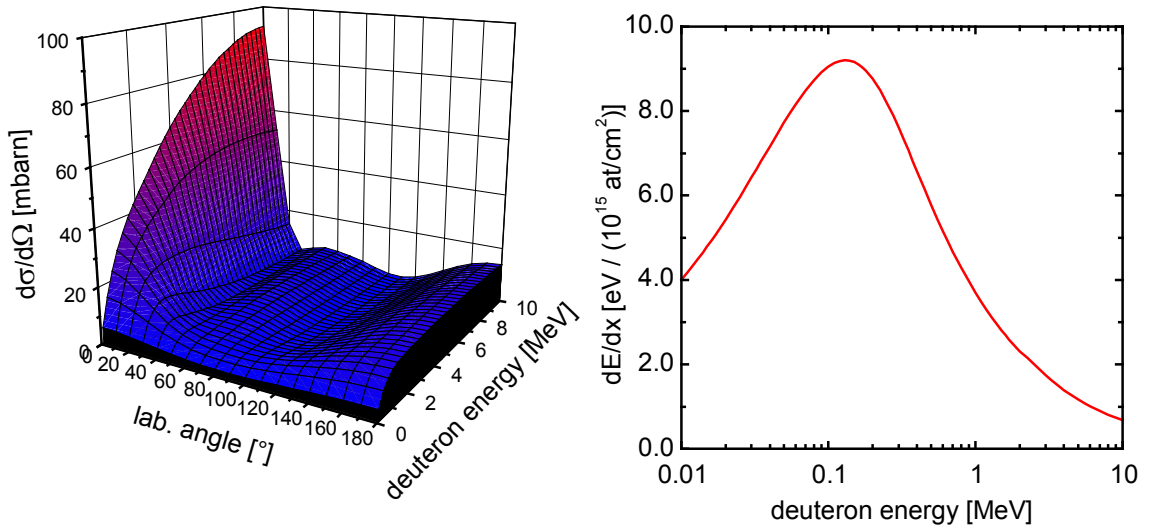
Figure 4.3: Differential d(d,n)³He reaction cross-section from DROSG2000 [45] (left) and energy loss dE/dx of deuterons in $(CD_2)_n$-plastic from SRIM2000 [46](right)
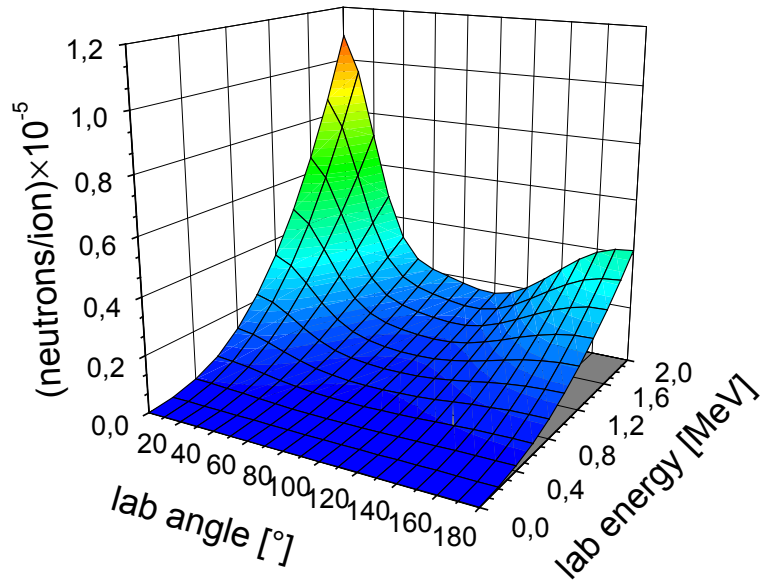
Figure 4.4: $N_n(E_n(E_d, \theta))/ion$

of the stopping power $\frac{1}{dE/dx}$ determines the number of fusion partners a fast ion sees. Also the geometrical extent of the target has to be taken into account, in order to determine the locations where the ions exit and enter the targets and thus be able to calculate their flight path in matter.

4.2 Ion Stopping in Cold Matter and Plasmas

4.2.1 Modifications to Bethe-Bloch

From equation 4.3 it becomes clear that the stopping power is an important input parameter for the data analysis. Unfortunately, the stopping in plasma can be quite different from the stopping power in cold matter, which is given by the Bethe-Bloch formula, or in a more accurate form by the SRIM [46] stopping power tables, which we will use for the numerical simulation. The following consideration is similar to the treatment by Belyaev et al. [47] and was inspired by Jackson [48]. It is a simplification of the results given in [47], in so far that it allows the calculation of the Coulomb logarithm and the stopping power very efficiently over a broad range of ion velocities and plasma temperatures, albeit with a little less precision. Nevertheless, for the purpose of this work, the precision is more than sufficient. For an analytical treatment, we will now focus on the Bethe-Bloch equation. It can be written in the following way [48] (The density correction can be safely neglected, since it does have little effect in the interesting energy region between 10 keV and 10 MeV per nucleon.):

$$\frac{dE}{dx} = NZ_T \cdot \frac{Z_i^2 e^4}{8\pi \epsilon_0^2 m_e v_{ion}^2} \cdot \ln\left(\frac{2\gamma^2 m_e v_{ion}^2}{\hbar \langle \omega_{at} \rangle} - \frac{v_{ion}^2}{c^2}\right) \tag{4.5}$$

The logarithmic term on the right hand side is commonly called the Coulomb logarithm. NZ_T is the number density of electrons in the target material in $[1/\text{cm}^3]$, e the unit charge, m_e the electron mass in [g], v_{ion} the velocity of the incoming particle and γ its relativistic factor. Z_i is the (effective) charge of the incoming charged particle and for protons and deuterons is close to unity. (Because electron transfer from the target to the ion can occur, Z_i is not precisely 1). $\hbar\langle\omega\rangle$ is the mean ionization potential of the target atoms. This formula describes the energy loss of swift, charged heavy particles in a cold target material. In a plasma, however, the stopping power for heavy ions is modified. We have to consider the effects of plasma formation in the target in order to understand the experimental results. In the neutron generation experiments, it is likely that the target material gets ionized by four mechanisms, two of which can be effective even before the accelerated ions pass through matter.

1. **Laser-induced Field Ionization**: The electric field of the laser light is strong enough to ionize atoms very rapidly by barrier-suppression ionization (BSI) [49, 50, 51] BSI driven by laser fields can only take place where these

fields exist. As we will see later, ions travel most of the time outside the regions the laser can reach. As soon as the ions reach overcritical plasma, this ionization mechanism breaks down.

2. **Shock Heating**: Known for a long time from long pulse experiments, this mechanism refers to a shock wave launched by the ablated material during the laser irradiation. It runs into the target with the sound speed of the ions, which is much slower than the ponderomotively accelerated ions. Therefore, this process does not have to be taken into account here.

3. **Collisional Heating**: Hot electrons from the laser focus propagate into the target, where they ionize cold target atoms by binary collisions with shell electrons. This effect can be treated by calculating the electron energy loss in the target. The energy deposited by this process heats and ionizes the target matter and leads to changes in the stopping power For moderate laser energies and electron currents this simple heating model gives quite good results.

4. **Field Ionization in the Target**: For higher laser energies and electron currents, the heating process cannot be treated purely collisional anymore, and collective stopping of the electron beam plays an increasing role. As the beam current approaches and crosses the Alfvén limit (17.6 kA $\beta\gamma$, $\beta = v/c$, $\gamma = \sqrt{1 - \beta^2}^{-1}$), it starts to break up and filament, as has been seen in experiments [52] and model calculations [53, 54]. Tikhonchuk [55] gives a nice analytical description of the basic process. The hot, filamenting current has to be compensated for by a return current of cold background electrons. It can only flow in conducting targets, whereas in insulators strong space charge fields of the order of TV/m are building up rapidly. They are capable of ionizing a large fraction of target atoms up to He-like ions. This mechanism is efficient as well as fast and deserves attention. However, the extent of the affected target volume and the temperatures reached therein strongly depend on the electron beam characteristics, such as divergence and energy. Since these properties are not well known and are still the subject of great experimental and theoretical efforts in the laser-plasma community, field ionization in the target will be neglected here for reasons of simplicity. In the case of the ATLAS and Jena experiments, it should only be of secondary importance since the electron current is limited and not the whole target volume will be affected. However, detailed numerical simulations of this problem can be found in [43]. The results from this detailed work for isotropic electron emission from the focus with temperatures given by the

ponderomotive scaling 2.17 agree quite well with our simplistic model just taking into account collisional effects given below.

In the case of an ionized target, the total energy loss of an ion can be written as (neglecting the contribution of plasma ions):

$$\frac{dE}{dx} = \frac{n_{bound}}{n_{bound} + n_{free}} \cdot \left(\frac{dE}{dx}\right)_{cold} + \frac{n_{free}}{n_{bound} + n_{free}} \cdot \left(\frac{dE}{dx}\right)_{plasma} \tag{4.6}$$

where n_{free} and n_{bound} are the numbers of ionized and bound electrons per atom, and dE/dx_{cold} and dE/dx_{plasma} are the stopping powers of cold matter and plasma. Before we give an estimate of the electron temperatures and the ionization degree in the target, let us consider the modifications to the two stopping power contributions in equation 4.6:

1. **Stopping in cold matter:** The Coulomb logarithm (logarithmic term in equation 4.5) depends on the mean electron frequency in an atom, $\hbar\langle\omega_{at}\rangle$, which can also be interpreted as the mean ionization potential $\langle I_p\rangle$. Therefore, since $\langle I_p\rangle$ is affected by the atom's ionization state Z_{eff}, the appropriate ionization potential $\langle I_p\rangle(Z_{eff})$ has to be used. This leads to a decrease of the stopping power since $\langle I_p\rangle(Z_{eff})$ is increasing with Z_{eff}. The effect, however, is small since the change occurs in the argument of the logarithm.

2. **Stopping in Plasma:**

   (a) *Cold Plasma:* For ion velocities v_{ion} smaller than the electron thermal velocity $v_{th,e}$, the Coulomb logarithm is modified in the following way:

   $$\left[\ln\left(\frac{2\gamma^2 m_e v_{ion}^2}{\hbar\langle\omega_{at}\rangle} - \frac{v_{ion}^2}{c^2}\right)\right]_{cold} \Rightarrow \left[\ln\left(\frac{2\gamma^2 m_e v_{ion}^2}{\hbar\omega_p} - \frac{v_{ion}^2}{c^2}\right)\right]_{plasma} \tag{4.7}$$

   i.e., the mean atomic frequency is replaced by the plasma frequency. It is important to bear in mind that the plasma frequency depends on the square root of the plasma electron density, which in turn is proportional to the mean ionziation state of the target atoms. For weakly ionized matter, this frequency is smaller than $\langle\omega_{at}\rangle$. For instance, at an electron density of $\sim 10^{20}$ cm^{-3}, ω_p approximately equals the frequency of visible light, and the corresponding energy is ~ 1 eV, compared to $\langle I_p\rangle \sim 10$-100 eV. This leads to an increase in stopping power for weakly ionized, cold plasmas. As the ionization state increases, and the electron density approaches solid density ($\sim 10^{24}$ cm^{-3}), ω_p is of the order of ω_{at}.

(b) *Hot Plasma:* For hot plasma, $(v_{th,e} > v_{ion})$ the the stopping power drops rapidly due to an inefficient energy transfer onto the plasma electrons. For a more detailed description, see [48]. This behavior was modeled in this work by replacing the quantity v_{ion}^2 in equation 4.5 by $(v_{ion}^2 + v_{th,e}^2)$ in the nonrelativistic case.

Thus, the modified Bethe-Bloch-equation for stopping in plasma can be written as $(\gamma \approx 1)$:

$$\frac{dE}{dx} \approx N(1 - Z_{eff}) \cdot \frac{Z_i^2 e^4}{8\pi\epsilon_0^2 m_e(v_{ion}^2 + v_{th,e}^2)}$$
$$\times \ln\left(\frac{2m_e(v_{ion}^2 + v_{th,e}^2)}{\hbar\langle\omega_p(Z_{eff})\rangle} - \frac{(v_{ion}^2 + v_{th,e}^2)}{c^2}\right) \tag{4.8}$$

with

$$\omega_p(Z_{eff}) = \sqrt{\frac{NZ_{eff}e^2}{\epsilon_0 m_e}} \tag{4.9}$$

where N is the number of molecules/cm^3.

4.2.2 Electron Temperature and Ionization degree

After having specified the treatment of energy losses in plasma, the influence of target electron temperature and ionization degree can be studied. Since the electron temperature was not measured in the experiments, some work has to be dedicated to find reasonable constraints to this quantity from published data and theoretical considerations.

Estimating the electron temperature is quite straightforward for conducting (i.e. metal) targets. Since the charge transported by the relativistic hot electron beam can be compensated by cold return currents, no large space-charge fields can be sustained by the target. Thus, the target heating can be described by a purely collisional model for electron stopping in cold matter [56], and the internal energy in eV per target atom is simply given by (in the 1-D case):

$$E_i(x) = \frac{j(x)}{n_{at}} \cdot \left(\frac{dE}{dx}(x)\right)_e. \tag{4.10}$$

Here, $j(x)$ is the electron current density in electrons/cm, n_{at} the atom density in atoms/cm^3 and $(dE/dx(x))_e$ the electron energy loss in eV/cm at a given target depth x. The situation gets more complex for non-conducting targets. Here, there are no free electrons available to set up a return current, so a large space-charge field can be built up, acting against a further transport of electrons. This leads

to a varying degree of electric (space-charge) inhibition, depending on the target conductivity, electron beam charge and current density [52, 43]. This effect cannot be modeled easily, but fortunately some measurements exist [56], which allow a very crude extrapolation to the conditions prevailing in the present experiment.

Tikhonchuk's model [55] for field-inhibited electron propagation suggests a smaller electron range in the target, leading to an enhanced stopping for electrons in the target and therefore to a larger energy deposition of the electrons along a given trajectory. However, the estimate presented here agrees pretty well with the numerical results given by Gremillet [52, 43].
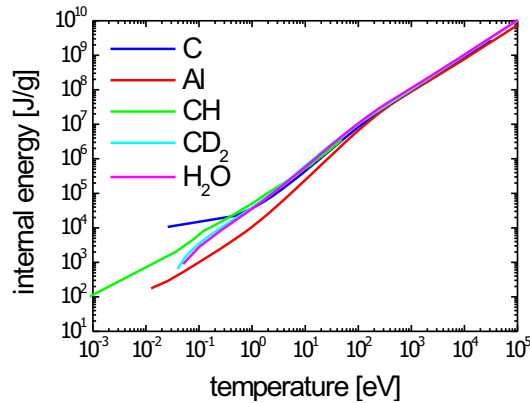
Figure 4.5: EOS curves taken from SESAME [57] for carbon, H_2O, CD_2, and aluminum.

After having determined the local internal energy of the target, its local temperature can be inferred from Equation-of-State (EOS) tables like SESAME [57]. Fig. 4.5 shows the temperature plotted against the internal energy for carbon, water (as substitute for D_2O), CD_2 and aluminum.

From the local temperature, the ionization degree of the target matter was determined using the Thomas-Fermi ionization model [58]. This simple model provides an estimate of the electron temperatures and mean charge states in the target at a time before the ions are penetrating. The values calculated from it are surprisingly close to detailed 3-D calculations done by Gremillet [43].

In Fig. 4.6 typical results for the local electron temperature and effective charge state are shown, along with modeled neutron time-of flight spectra for electron-heated and cold targets. The spectra were simulated with MCNEUT (described below). The laser parameters used in the upper row (corresponding to the Jena experiment in chapter 7) of Fig. 4.6 were E_L=0.6J, I=3×10^{19} W/cm², λ=0.79μm, which assuming a conversion efficiency of η=0.2 leads to 5.2×10^{11} electrons with a temperature of T_e=1.45 MeV. One can see that the temperature in the vicinity

of the focus reaches 40 eV, leading to an ionization degree of 5, corresponding to 50% of all electrons. This amount of heating is sufficient to ionize a large enough fraction of the target material to have an effect on the stopping and therefore the neutron output. However, the main effect is a small increase in stopping power due to the ionization. This in turn leads to a small reduction in neutron output, since a given ion ranges out more quickly and therefore encounters less fusion partners. The spectral shape remains unchanged. The heating is not strong enough to raise the thermal velocity of the bulk electrons to a value sufficient to have a decreasing effect on the stopping power.
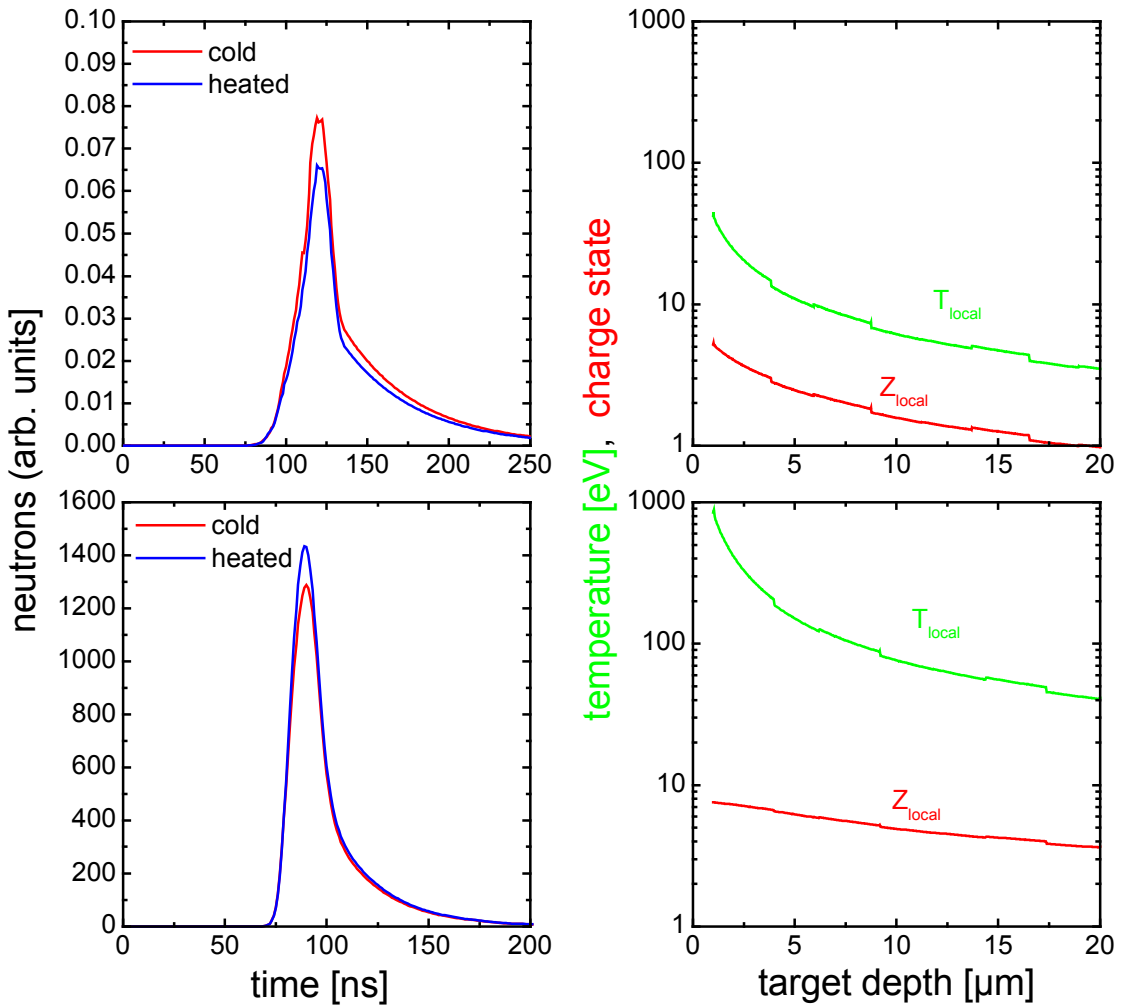
Figure 4.6: Neutron time-of-flight spectra, electron temperature and effective charge state as calculated by the simple model used here. The steps in the graphs are artefacts from the numerical treatment. They are negligible for the overall result. (upper row: Jena case, D_2O droplets, lower row: LULI case, CD_2 target.)

This effect is only encountered for the typical LULI case (described in chapter 6), as displayed in the lower row of Fig. 4.6. The respective parameters were

E_L=15J, I=5$\times10^{19}$ W/cm^2, λ=1.064μm, η=0.3, leading to 10^{13} electrons with T_e=2.81 MeV. This leads to a local electron temperature of $\sim$1 keV, and to almost complete ionization close to the focus. Now the heated target produces a slightly higher neutron output than the cold one, indicating a reduced ion energy loss. Still, the overall effect is small and this consideration shows that the effect of target heating is of minor importance.

4.3   Neutron Scattering

Since neutrons generated in the laser target carry the information about the interaction dynamics encoded in their kinematic shift, it is desirable to measure an undistorted neutron spectrum from the interaction. However, since neutrons are scattered by material present in the vicinity of the neutron source (such as target chamber, mirrors, detector shielding etc.), their flight path is modified by each scattering event. Scattered neutrons reaching the detector do not come straight from the target, and their path length is longer than for unscattered particles. Moreover, in the scattering event the neutrons transfer a part of their energy to the scattering partner, so they always arrive later than unscattered neutron. This leads to a distortion of the TOF spectrum. If the distortion is not corrected for, wrong results for the neutron energy and therefore the ion distribution are obtained. Since for a single neutron the precise location and number of scattering events is unknown (and cannot be measured), one has to rely on statistical methods to correct for the effect of scattering. Therefore, detailed calculations were carried out using the 3D-Monte-Carlo neutron transport code MCNP ([59]) to generate a scattering function which can be used to unfold the measured spectra. The code calculates the neutron transport and scattering in an arbitrary 3D-geometry consisting of any chosen material modeled to resemble the target chamber setup and its surroundings, and calculates the effect on the TOF spectrum. In particular, the effect on the TOF spectrum of monoenergetic neutrons of different energy was investigated (Fig. 4.7). It can be clearly seen that due to scattering a large part of the otherwise sharply peaked neutron spectrum is seemingly shifted to lower energies. To account for this effect, the three curves were interpolated to yield a 2-parameter array (start energy / TOF energy), which is used to unfold the experimental TOF spectra. This treatment yields scattering corrected neutron spectra, which can be directly compared to theoretical models. The MCNP output also directly shows which part of the started neutrons reaches the detector and which part is scattered away or captured, thus providing a scaling factor for
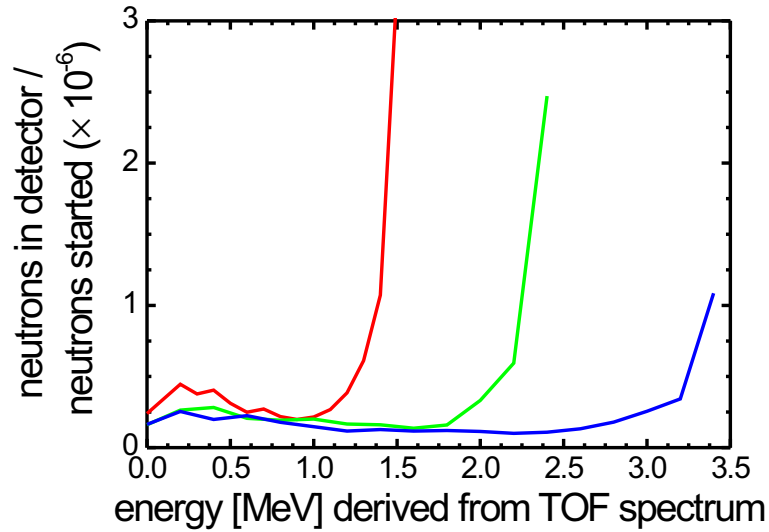
Figure 4.7: Influence of scattering in the experimental setup. The energy spectra of monoenergetic neutrons of 1.5, 2.45 and 3.5 MeV were derived from time-of-flight calculations including the paths of scattered neutrons. The geometry of the experimental setup was modeled with the neutron transport code MCNP [59], including the target chamber, the concrete floor, and the detector lead shielding. The spectra are modeled for a detector distance of 3.75 m at 45° to the laser axis. The detector solid angle was 1.5 msr. The angle of the detector setup has little influence on the result.

the yield calibration. This information, however, was only used to cross-check the independently determined yield from the activation detector.

4.4 The 3D-Monte Carlo Code MCNEUT

Fusion neutrons from laser generated plasmas can be used to diagnose the ion temperature and/or angular distribution inside the plasma. Understanding the ion distribution is not only prerequisite for optimizing the neutron (or ion) source performance, but also a tool for plasma diagnostics. Thus one of the key issues in this work is the attempt to extract information on the ion population from the measured neutron spectra. This is not possible by directly measuring the neutrons' kinematic shift in energy since in all these experiments the fusion target is thick compared to the mean ion range in matter. This leads to ambiguities in the ion energy needed to produce a neutron of certain energy. Using a Monte Carlo method to simulate the neutron production in the geometry of the experiment allows us to determine the ion temperature and rough angular distribution by making reasonable assumption on the ion spectral shape and 3-D emission characteristics.

Such a method was implemented in the code MCNEUT, which furthermore gives an estimate for the fast electron heating of the target and the resulting changes to the energy loss of heavy ions in partially ionized matter. It was written in different versions to treat ion distributions from 3D-PIC output as well as arbitrary model distributions and neutron source reactions. Targets that can be modeled include planar targets, wire and droplet targets and presently only planar catchers. However, the neutron production kernel and the geometry setup is generalized.

4.4.1 General

MCNEUT tracks ions through the given experimental geometry and calculates neutron TOF and energy spectra measured in the detector. The probability for detecting a neutron in the detector with a solid angle $\Delta\Omega$ generated by fusion of a single ion with the energy $E_{0,i}$ is given as

$$P_n(E_{0,i}, \alpha_i) = \Delta\Omega \cdot \int_{E_{0,i}}^{0} \frac{d\sigma}{d\Omega}(E_i, \alpha_i) \cdot n_d(x(E_i)) \cdot \frac{dx}{dE_i} \cdot dE_i. \qquad (4.11)$$

Here α_i is the angle between the ion trajectory and the neutron (and therefore the detector), $\frac{d\sigma}{d\Omega}$ is the differential reaction cross-section, $n_d(x(E))$ is the local deuteron atom density at the position $x(E)$ an ion with the energy E has in the target, and $\frac{dx}{dE}$ is the derivative of the energy dependent ion range $x(E)$.

To obtain a neutron spectrum, it is necessary to treat the above expression differentially for each energy E_i in the slowing down process of the ion and calculate the neutron energy and time of flight delay for the current E_i and α_i. If the ion reaches a material boundary, one has to take care of changes in stopping, and for jumps of α_i due to crossing of large vacuum gaps as between the jet and the catcher target. Angular straggling at the end of the ion range is neglected, since the contribution to the neutron output is maximal at high ion energies, where straggling is still weak. Scattering in the target chamber and the detector shielding is implemented from a simulation of the actual experimental setup with MCNP [59].

Technically, the code starts ions accelerated in the laser focus according to a predefined angular and energy distribution $P_{ang}(\theta, \phi) \cdot P_e(E_i)$, which can be either given analytically or read from a PIC code output file. Here θ is the angle of the ion trajectory with the positive laser axis and ϕ denotes the angle of the ion to an axis perpendicular to the polarization plane in the plane normal to the laser axis. (See Fig. 4.8.)
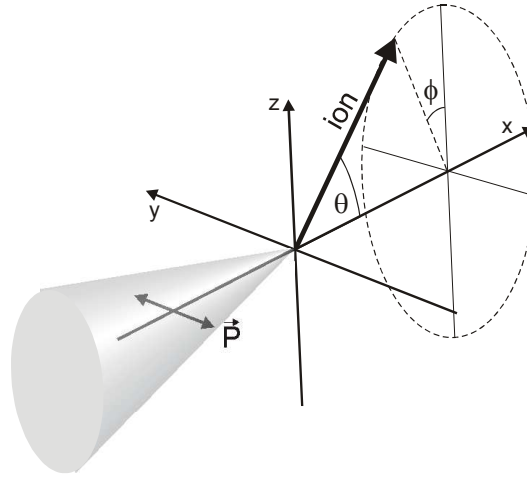
Figure 4.8: Definition of axes and angles in MCNEUT

For droplet or wire targets the source point can be randomly scanned over the target surface to take into account an unstable laser spot. This changes $d(\theta)$, which is the thickness of material an ion emitted at an angle θ to the laser axis travels through, and therefore has an influence on the spectral weight of ions at certain angles θ. For ions accelerated off the rear target surface, the target thickness can be set to zero; so all ions will directly proceed to the catcher without interaction in the primary target.

An ion from the first energy bin in the input spectrum is started with a direction given by a Monte-Carlo sampling of the input angular distribution. In a first step, the length of the ion's trajectory through the target is calculated. Each ion is slowed down in equidistant energy steps ΔE along its trajectory through matter, and moves on a distance Δx for each step as determined by the inverse of its stopping power $\frac{dx}{dE}$, as given by modified SRIM ([46]) stopping tables (see section 4.2.1 and 4.4.2). The areal density of fusion partners on its trajectory is then given by $N_{d,cold} = \rho_d \cdot \Delta x$. The differential (d,d)-fusion cross-section $d\sigma/d\Omega(E_i,\alpha)$ tabulated by DROSG2000 ([45]) is interpolated for the current ion energy E_i and the angle between the ion direction and the detector direction α. It is multiplied with the number of cold fusion partners, $N_{d,cold}$, to yield a total fusion probability of the ion while it travels with the energy E_i. This probability is then weighted with the total number of ions in the input energy bin and added to the neutron energy bin and/or time-of-flight bin in the output file that is calculated from the reaction kinematics for α and E_i. This treatment yields a whole probability spectrum from one ion. Note that the annihilation of the neutron due to fusion is neglected, since the binary fusion event is replaced by the fusion probability. The error arising from this treatment is small, since the total fusion probability for a MeV deuteron

stopping in CD_2 is of the order of 10^{-4}. If the deuteron has sufficient energy to reach the back surface of the target, its exit energy (E_{flight})is recorded and the distance to the catcher target (Δl_{t-c}) is calculated to determine the ion time-of-flight delay Δt_{ionTOF}. The further treatment of the ion is similar to inside the target, except that the detector solid angle is computed with the distance between detector and the location of the ion impact on the catcher, and the stopping is adjusted to the catcher material, which can be different from the target. The neutron time of flight is also computed with this new distance and includes the contribution of Δt_{ionTOF}. This procedure is repeated with a few hundred deuterons of the same input energy bin to sample specified angular distribution, before the next energy bin is treated in the same way. The output generated by the code is a file with energy and time-of-flight neutron spectra as seen in the detector normalized to the total ion number in the input spectrum and a file of points in three dimensions which represent the locations of ions exiting the target and/or entering the catcher.

4.4.2   Implementation of Electron Heating

For treating the electron heating, it was assumed that the electrons from the laser focus stream into the target in a 2π solid angle. The temperature of the electrons is determined by the ponderomotive scaling 2.24 given by Wilks [23] and the number of electrons corresponds to a given fraction of laser energy converted to fast electrons. This number is not accurately known and depends largely on pre-plasma conditions and laser incidence angle [60, 61, 18] In this work, the conversion efficiency was assumed to be 0.2 - 0.3.

4.4.3   Main Routine

The results of the above heating calculation is used as an input for the following main routine, which calculates the actual energy-and angle-dependent neutron generation probability. The values for $T_e(L)$ and $Z_{eff}(L)$ are used to modify the stopping power tables.
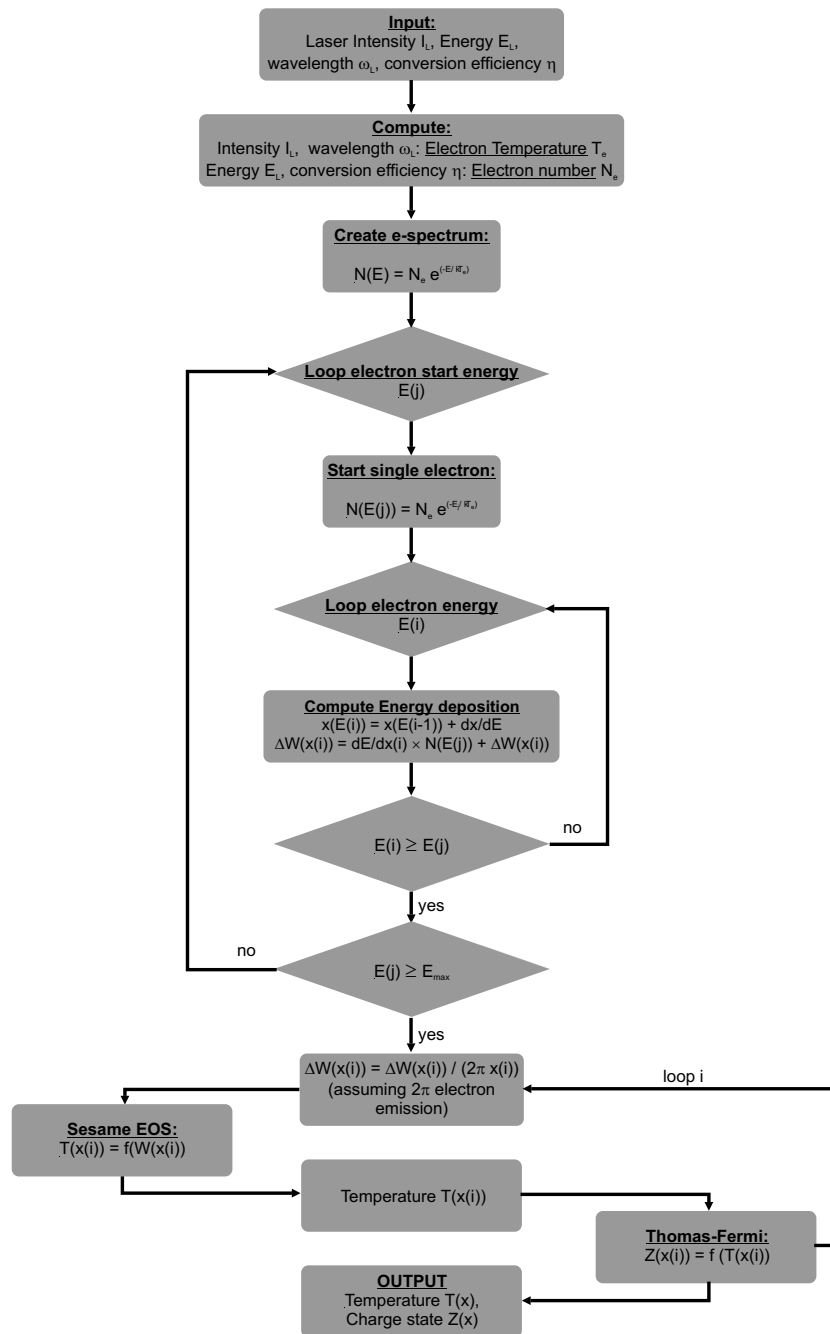
Figure 4.9: Flowchart of the electron heating treatment

4.4.4 Output

The main output from MCNEUT is an ASCII file with neutron energy and time-of flight spectra, which can be directly imported and plotted in a data analysis software. Its header contains information on the detector solid angle, direction to the laser axis and laser incidence angle. Additionally, files containing the individual ion momentum components, angles to the laser axis and optionally its position at a
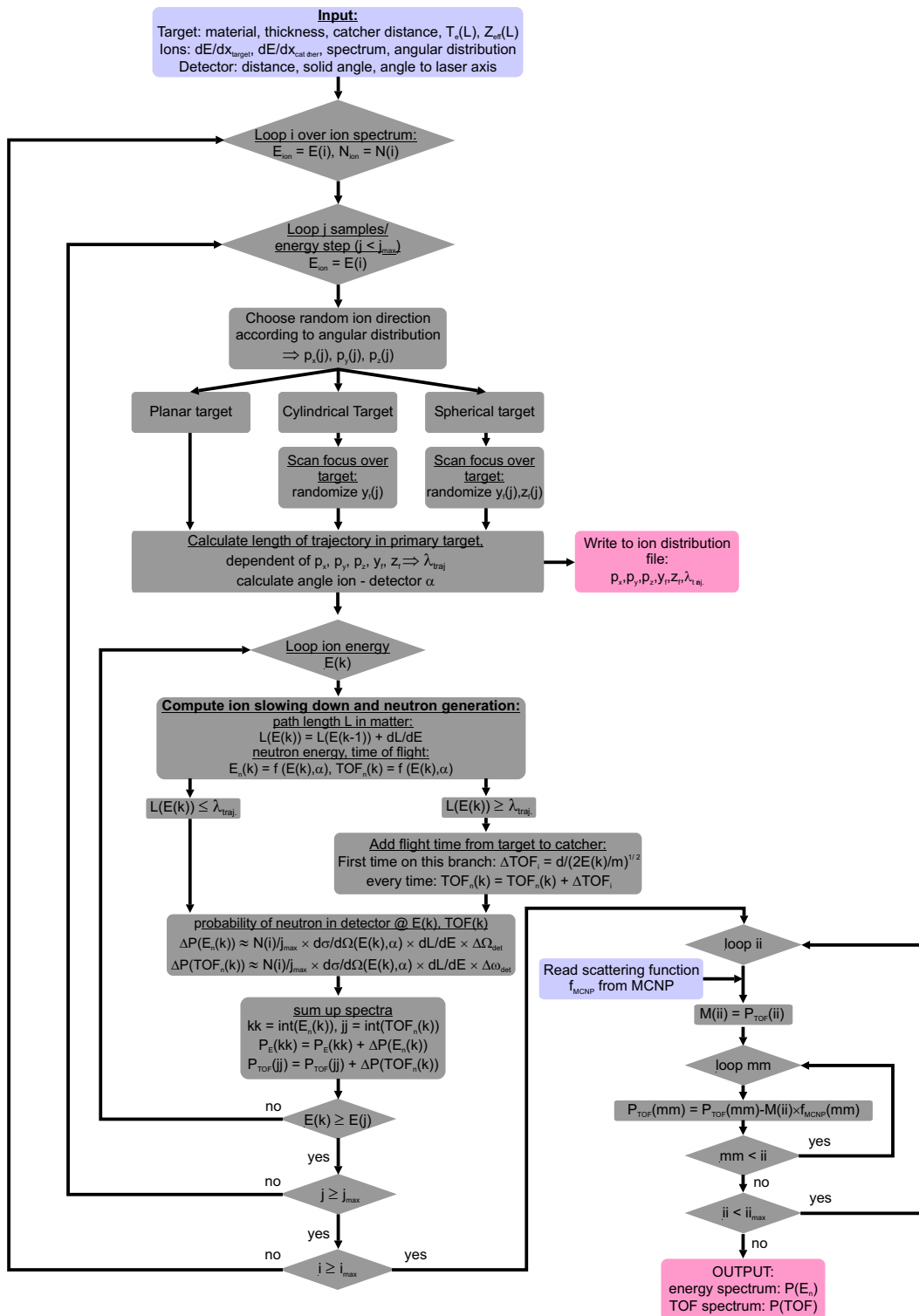
Figure 4.10: Flowchart of the main routine

given target boundary or plane are created, so that full record over the simulation is available.

4.4.5 Example

The following example illustrates the neutron spectral characteristics for different ion distributions. The experimental geometry was assumed to be very similar to the last experiments done with the ATLAS laser. The target was modeled to be a 500-μm thick CD_2 plastic disk irradiated under 45°. Two detectors are placed at a distance of 375 cm under an angle of 45° and 135°, respectively. The ion
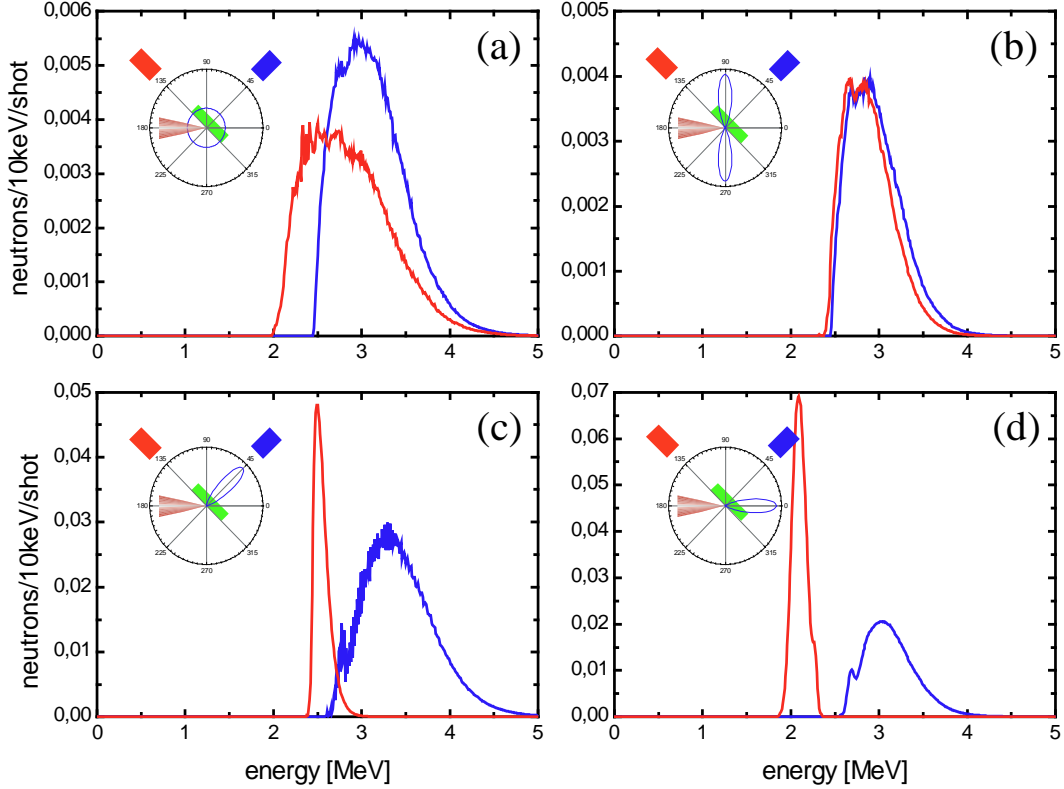
Figure 4.11: Neutron spectra for different ion emission characteristics. The modeling setup along with the ion distributions are shown in the insets. Blue corresponds to the detector under 45°, red to the one at 135°. The ion spectrum was assumed to be exponential with a slope of 250 keV.

emission pattern in these cases were assumed to be axially symmetric, with the symmetry axis lying in the incidence plane of the laser. It can be rotated with regard to the laser axis by an arbitrary angle. The ion temperature was assumed to be constant for all angles, so only the angular distribution is changed. In Fig. 4.11 the following cases were modeled:

1. **Isotropic ion emission into 4π:** The simplest case assumes a point-like Coulomb explosion of the ions in the laser spot into all directions. The spectra shown in Fig. 4.11(a) reveal that the detector under 135° (red), which

looks parallel to the target surface, sees a rather broad energy distribution. Because this detector sees equally many ions approaching and departing, the kinematic shift goes from minimal to maximal values at this ion temperature. The 45° (blue) detector sees blueshifted neutrons, since only the ions approaching it run into the target and trigger fusion.

2. **Radial ion emission from the laser axis:** This case corresponds to the case of a deep hole-boring into the plasma. Ions are emitted radially from the laser axis. The two detectors in Fig. 4.11(b) observe the neutrons under almost symmetrical viewpoints. The symmetry is only broken by the 45°-rotated target, which is responsible for the slight asymmetry in the spectra. Also here, only the ions running into the target fuse and hence cause a blue-shift in both detectors.

3. **Ion acceleration perpendicularly into the target:** This case corresponds to a very steep preplasma gradient and a corresponding 1-D-like ion acceleration (see Fig. 4.11(c)). For simplicity, the ion beam divergence was assumed to be 0.1 radians. Therefore the 45° detectors sees a strong blue-shift. For the 135° detector, the angle of detected neutrons and their generating ion is very close to 90°, which leads to a very narrow, 2.45 MeV-centered neutron spectrum.

4. **Ion acceleration along the laser axis:** Although this does not correspond to any of the cases described, some forward emission might exist even at 45° incidence angle (see Fig. 4.11(d)). This leads to slightly less energy under 45°, since the beam is not pointing straight at the detector. Under 135°, the neutron energy is even more reduced, since most ions have a velocity component directed away from it.

Keeping in mind Fig. 4.1, this behaviour becomes easily plausible. Understanding the neutron spectra is easy, if the following points are kept in mind:

1. The neutron emission cross-section in the laboratory frame is maximal in the direction of the fusing deuteron. From that follows:

    (a) Ions moving towards the observer cause blue-shifted, those moving away red-shifted neutrons.

    (b) From the width of a measured neutron peak follows the longitudinal ion temperature along the detector's line of sight. By measuring the neutron spectra from three or more (out-of-plane) directions, in principle

a tomogram of the ion distribution can be obtained. For azimuthally symmetric ion distributions, even two directions are sufficient.

(c) The shift of the neutron peak yields information on a predominant longitudinal velocity component

2. The neutron peak can be shifted by a nonuniform plasma line density along the line of sight.

With these few simple rules, it is not hard to infer general ion characteristics showing up in an experiment. By playing with the simulation parameters like ion temperature, angle distribution, amount of preplasma formation(providing fusion partners for ions emitted out of the target surface) in accordance to PIC simulations, it is possible to find a best set of parameters. In the current version of the software, this cannot yet be done automatically in an iterative process.

With the theory and modeling capabilities described in this chapter, sufficient background is laid to understand the experimental findings described in the next chapters.

4.5 Error Treatment

In contrast to high-precision experiments in other fields of laser physics and quantum optics, the experiments presented here are plagued with huge error bars. This problem is partially caused by the novelty of the research field and the lack of specially designed detectors for intense, pulsed radiation with sufficient energy resolution and accuracy. Existing detectors suffer from the harsh environment of a laser-plasma experiment and large shot-to-shot fluctuations of the plasma interaction. The experiments described in the following chapters generally exhibit very large systematic and statistic errors, the latter of which increase from extracting neutron numbers from the spectra over the determination of the ion temperature to the final estimate on the ion numbers. This is due to the nature of the neutrons as secondary particles, whose precise counting is difficult in many cases for reasons of laser stability. The precision of the experimental results presented here therefore decreases in three steps for the following quantities:

- **Neutron Numbers:** As directly measured particles, the neutrons are subject to systematic errors of the detection efficiency and statistical counting errors. The latter usually are negligible compared to the systematic errors.

These are not only determined by the uncertainty of the detector calibration as presented in Section 3.2.1, but also by fluctuations of the laser power and/or focusing conditions during an experimental run. For instance, if the rotating target plane in the ATLAS experiments (see Fig. 5.1) is not exactly perpendicular to the rotation axis, the resulting wobble causes shifts of the target surface in relation to the focal position. This leads to fluctuations in neutron yield for individual shots, and to an apparent reduction in overall efficiency. The same effect, but even more pronounced, occurs in the Jena experiment, where only a fraction of the droplets are actually hit by the laser, and even among hits exists a broad distribution of neutron yield. This reduced the time-averaged yield so much that the usually quite accurate silver activation detector did not detect a measurable signal anymore.

- **Ion Temperatures:** The dependence of the neutron TOF- or energy peak width is only a weak function of the ion temperature distribution, and also depends on the the detection direction (From Fig. 4.1 is evident that the energy shift of the neutron is large for angles of $0°$ between ion and neutron, whereas for angles close to $100°$ it is nearly zero), ion angular distribution and precise spectral shape, where the latter two are generally unknown. Any result given for the ion temperature therefore has to be based on certain assumptions about these two quantities, which are usually taken from 3D-PIC simulations. Generally and for simplicity, as an input for the modeling we used a single-temperature Boltzmann-like ion spectrum, if not otherwise stated. In most cases, this is a good approximation in terms of neutron spectral shape for the two-temperature exponential ion spectrum with a high energy cutoff seen in most experiments. Only for fusion of rear-side accelerated ions as shown in Chapter 7 the determination of ion temperatures is more accurate due to the large temporal separation of prompt and delayed neutrons, where the delay time equals the ion time-of-flight from the primary to the secondary target.

- **Ion Numbers:** The steep dependence of neutron numbers on the ion temperature (which is subject to rather large errors) makes determination of the ion numbers by matching the modeled neutron output to the absolutely calibrated experimental yield very uncertain. Direct measurement of ion numbers is difficult for hydrogen isotopes because of the low sensitivity of CR-39 for those species and calibration problems for x-ray film and RCF. Measurements of the ion charge are plagued by the unknown charge state distribution of the beam. Therefore, only order-of-magnitude estimates or more accurate relative numbers for the ion population can be given here.

Within these limits, the order-of-magnitude numbers derived from neutrons and from direct ion measurements agree quite well.
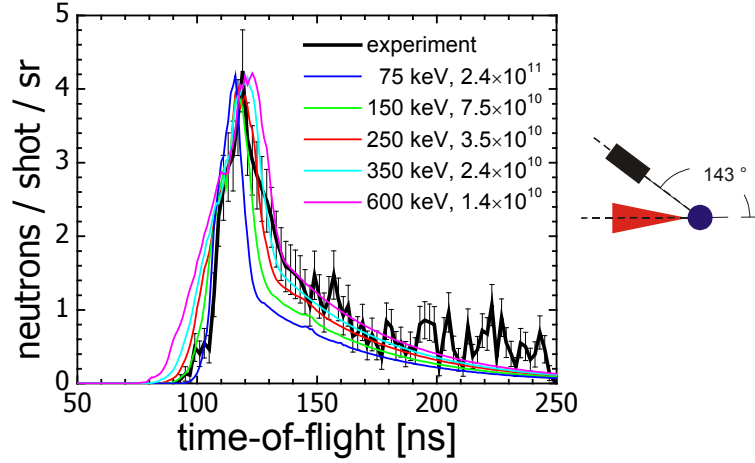
Figure 4.12: Comparison of modeled spectra with different ion temperatures to the measured one. This shows the approximate error margin in determining the ion temperature and ion numbers.

Because of the large magnitude of the errors and the complicated treatment, only an example of an error analysis shall be given here. A classical error propagation analysis is impractical, since the neutron spectrum cannot be written in a closed expression and due to the large number of parameters. All experiments described in this work exhibit similar errors if not otherwise stated, which are mostly governed uncertainty due to shot-to-shot fluctuations of the laser energy. The example
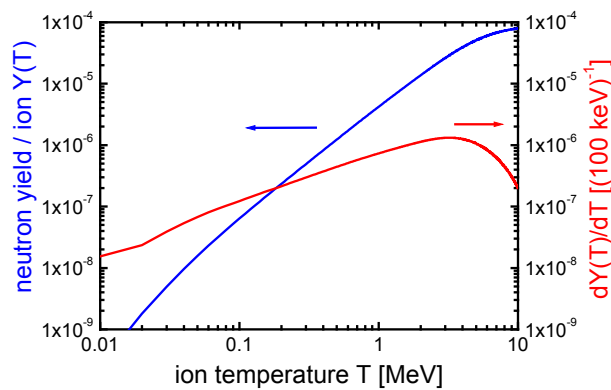
Figure 4.13: (blue) Neutron yield $Y(T)$ of the d-d fusion reaction as a function of ion temperature T. (red) Differential yield error $dY(T)/dT$ as a function if T.

spectrum analyzed here is taken from the Jena campaign, as described in detail in Chapter 7. In this case, the angle of the detector to the laser axis was 143°, with would, according to Fig. 4.1, correspond to the almost worst case in terms

of neutron energy spread if the ions were all forward directed. Since they are, according to PIC, rather directed sideways, a certain sensitivity of the spectral shape on ion temperature is indeed given here. Thus, the ion distribution modeled here is radially peaked (see Fig. 7.5), but for an isotropic distribution the results are very similar. Fig. 4.12 shows the results of the MCNEUT simulation for various ion temperatures overlaid with the experimental spectrum, and the necessary ion numbers to explain the neutron yield are given in the legend. This picture shows that in practice, the ion temperature can be determined to be somewhere between 150 keV and 350 keV with a best match at 350 keV. The according ion numbers vary by a factor of three, from 4.7×10^{10} to 1.5×10^{11}. This result is generalized in Fig. 4.13, where for the example of the d-d fusion reaction the neutron yield $Y(T)$ is plotted versus the Boltzmann-like ion temperature T. The derivative $dY(T)/dT \cdot \Delta T$ evaluated at T gives the yield uncertainty ΔY for a given temperature error ΔT.

Chapter 5

Neutron Yield and Spectroscopy at ATLAS

5.1 Experimental Setup

In the following chapter, the experimental apparatus for generating the neutrons and obtaining the neutron spectra will be discussed. The ATLAS laser at the Max-Planck-Institut für Quantenoptik was used for these experiments, especially the ATLAS-10 upgrade, incorporating a new final amplifier module and adaptive optics. The laser system and the development of the upgrade are described in detail in Appendix A, since the development and commissioning of the adaptive optics system was a major part of this work and of crucial importance for the success of the neutron experiments. However, some important results on the contrast ratio and preplasma conditions will be given in this chapter. At first, the experimental setup and the data aquisition system will be described, while experimental results of the neutron experiments are presented in the second part of this chapter. Most of the results are also compared to model calculations.

5.1.1 The ATLAS System

The ATLAS-10 Ti:Sapphire laser is currently capable of delivering 700-mJ, 160-fs pulses at a center wavelength of 790 nm and 10-Hz repetition rate to the target in an evacuated target chamber. The pulses therefore have a power of 4.3 TW, and thanks to an adaptive optics system, are focusable to an intensity of $2 \times 10^{19} \text{W/cm}^2$ averaged over the size of an Airy disk of the corresponding ideal beam. The adaptive optics system only became available in a number of steps during the last

2 years of this work. Early experiments were performed at considerable lower intensity $< 10^{18}\mathrm{W/cm^2}$, which was stepwise increased to the current level. The same holds true for the maximum beam energy. Before the installation of the adaptive optics system the maximum energy was limited to approx. 300 mJ. The laser and its optimization are described in greater detail in Appendix A.

5.1.2   Target Chamber Setup

After discussing the properties of the laser beam, the actual experimental setup in and outside the target chamber will be described in the following section. In Fig. 5.1, a schematical overview of the target chamber setup and the detector arrays is depicted.
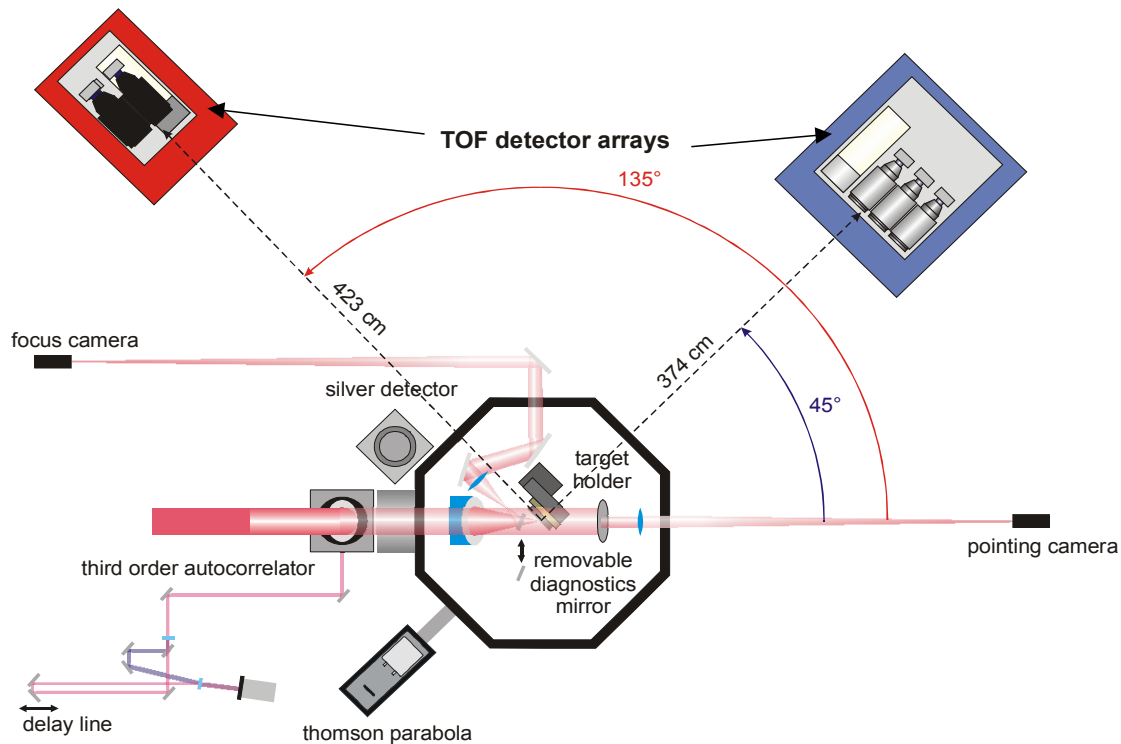
Figure 5.1: Setup of the ATLAS target chamber including all diagnostics.

Target Chamber

The wavefront corrected laser pulse is propagated to the target chamber through an evacuated tube system equipped with selected mirrors of high quality (typ. $\lambda/10$), in order to maintain the flat wavefront along the whole beamline. In the chamber, it is focused using a dielectrically coated $f/2.3$ off-axis parabola onto

the target surface. Since due to the short focal ratio the focal spot quality is very sensitive to pointing errors of the laser beam with respect to the parabola axis, a part of the beam leaking through the last turning mirror is coupled out and serves as a pointing diagnostics. Additionally, a small pickup mirror can be slid into the beam just before the parabola focus, which deflects the beam off through an $f/2$ imaging lens onto a CCD camera. This focus diagnostics has a magnification of 50 and serves as an online check of the focal quality. The prepulse detection unit is also sketched in Fig. 5.1.

Target

The target for the neutron generation experiments consisted of solid CD_2, which was first fabricated by hot-pressing commercially available CD_2-powder in a hydraulic press onto the surface of a 5cm diameter aluminum disk. This technique yields a very uneven, grainy CD_2 layer of a few 100-μm thickness, and flakes tend to fall off during laser irradiation. Fortunately, for later experiments a big piece of solid CD_2 plastic was obtained from Lawrence Livermore National Laboratory, and a number of 5-cm diameter target disks were be fabricated from it. The targets were mounted on a rotating and shifting target holder, where the laser beam draws a spiral trace on the target surface. Approximately 6000 shots could be made on one target. After irradiating the disks, they were leveled on a lathe and reused.

5.2 Prepulse Level and Plasma Gradient

As was discussed in Chapter 2, the amount and scalelength of the preplasma formed by laser light preceding the main pulse plays an important role for the characteristics of the laser-plasma interaction, and for the processes that can take place. Especially the ion emission characteristics depend critically on the preplasma conditions, as will be shown in Section 5.3.2. Since in the experiment the conversion of laser light into fast particles mainly takes place at the (relativistic) critical density $n_{crit,rel} > n_{crit}$, it is desirable to get as precise a knowledge about the plasma conditions there as possible. A well-established method for determining the plasma density gradient is interferometry with $2\omega_L$ laser light shortly before the main interaction. Since $n_{crit,2\omega} = 4n_{crit,\omega}$, this would in principle allow to probe the plasma up to $n_{crit,\omega}$ and higher. However, since $n_{crit,rel} > n_{crit}$, and due to light diffraction at the parts of the target surface that are out of focus

for the interferometry optics, this cannot be achieved in practice. The maximum density that can realistically be probed is around 0.5 $n_{crit,\omega}$. Thus, and because of its complexity, in this work an interferometry setup was not implemented, but the prepulse level was measured very carefully instead. One has to rely on model calculations to derive the plasma conditions from this measurement, but in all this method should be able to get a pretty good estimate of the real plasma conditions.

The two main sources of laser light before the main pulse are:

1. **Amplified Spontaneous Emission (ASE):** Every laser medium emits a certain amount of spontaneously emitted light as soon as it is pumped. Since a small fraction of this light always travels along the mode volume of the laser light, it can be amplified downstream and reach the target before the main pulse. Since this light is not chirped, it is not compressed by the compressor and is emitted as as long as the medium is pumped. The oscillator is pumped continuously and the amplifiers a few ns before the main pulse, so these components are the primary sources of ASE.

2. **Short Prepulses:** In the ATLAS laser as in many other CPA laser systems a regenerative amplifier (RGA) is used to amplify the oscillator pulses by a factor of $10^6 - 10^7$ over $\sim 10 - 20$ round-trips in a resonator. After having completed these round-trips, the pulses are switched out of the RGA by a Pockels cell and subsequent polarizer. Since this Pockels cell-polarizer combination allows some leakage of light even in the "off" state, pulses from the earlier round-trips can leak out of the RGA before the main pulse. Moreover, reflection off any plane component in the RGA might even constitute a separate cavity with one of the end mirrors or even send pulses through the RGA in the reverse direction. All these pulses with various round-trip times may leak out of the RGA and cause short (chirped) prepulses.

To detect the ASE level, the fast photodiodes mentioned in Appendix A were used. They were placed on both outputs of a beam-splitter, and the light reaching one of them was attenuated by a factor of $\sim 10^4$. This diode was not saturated by the laser pulse and acted as a reference calibration, while the other diode recorded faint prepulse and ASE light. Since the readout-time of the diodes was on the order of 650 ps, the signal of the main pulse has to be corrected for the difference of pulse duration and readout width. The results are plotted in Fig. 5.2:

The ASE level is below 10^{-7} of the main pulse intensity, which is an excellent value for such a laser system. However, at a peak intensity of 3×10^{19} W/cm^2
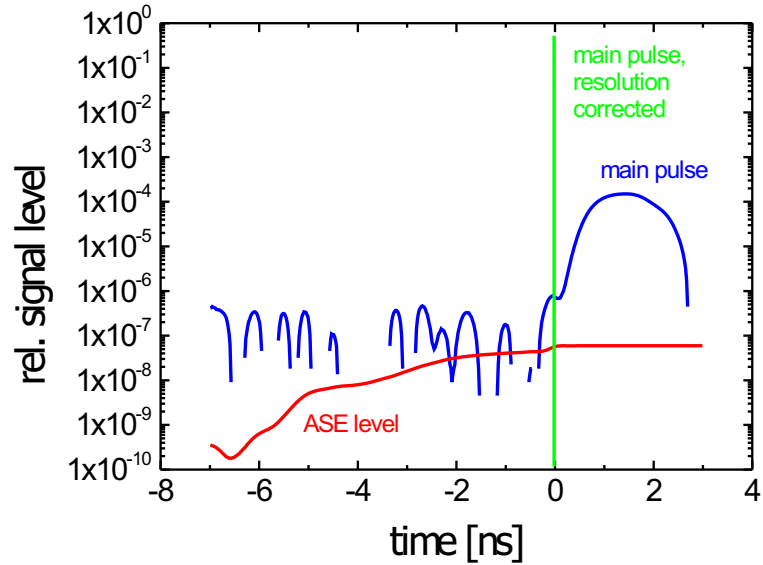
Figure 5.2: ASE level as measured with the diode setup. The red curve is the signal of the unattenuated diode, whereas the blue curve represents the main pulse signal. The green line represents the main pulse, corrected for detector timing resolution. Note that no large, short prepulses are present, which would show up in the red curve as early peaks (early blue peaks are readout noise).

this level of ASE means that for more than 4 ns before the main pulse arrives, the on-target intensity is of the order of 10^{12} W/cm^2, far above the plasma formation threshold.

Short, weak prepulses containing only a small amount of energy cannot be detected by this method. Therefore, a present third-order autocorrelator modified by incorporating a 2-m long delay line was coupled to the target chamber in order to detect these short pulses. The delay was varied in 5 cm steps and the autocorrelator was scanned over a 5 cm region for each step. Thus the whole 2-m delay range was sampled. In Fig: 5.3, these results are shown superimposed on the ASE measurement.

This measurement shows a large amount of prepulses at different times, leading to a strong preplasma formation. Since such an uncontrolled "jungle" of prepulses is disastrous for doing reproducible experiments, we tried to track down the source of these pulses. It turned out that the Pockels cell inside the RGA was aligned precisely perpendicular to the laser mode, so that the various crystal and window surfaces caused unwanted reflections of laser light into the mode volume of the RGA resonator, leading to a multitude of counterpropagating pulses in the RGA with different round-trip times. After twisting the Pockels cell by a small angle, these pulses all vanished. The resulting temporal structure of the ATLAS pulse is
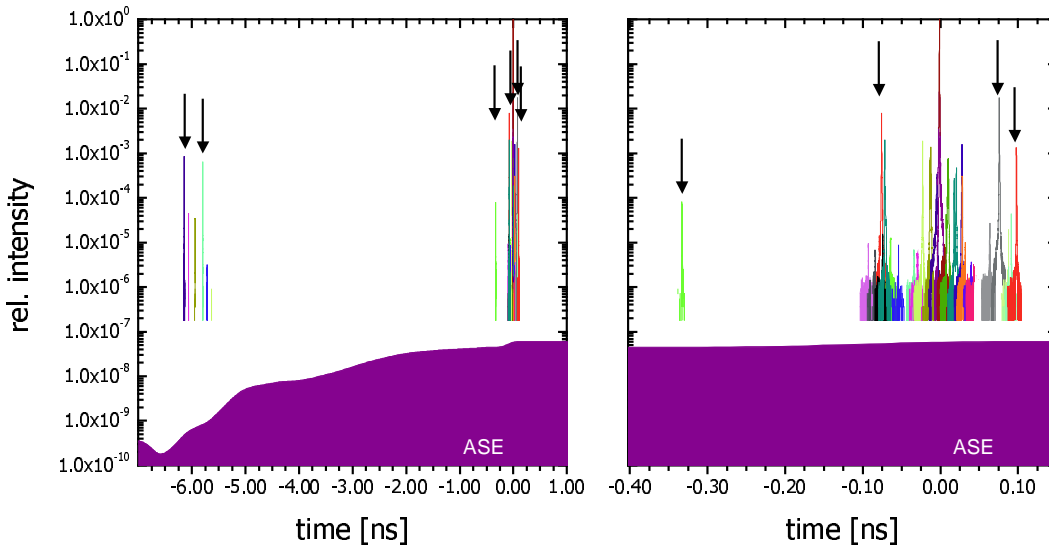
Figure 5.3: Short pre- and afterpulses as measured with the 3rd order autocorrelator for the whole delay range (left) and zoom into the last 400 ps before the main pulse (right). Most pulses around the main pulse are artifacts from the beamsplitters in the autocorrelator itself, or echos from afterpulses. The "real" pre- and afterpulses are marked with arrows. As one can see, the dynamic range of the autocorrelator measurement was close to 10^6, so the ASE level is by a factor of < 10 below the detection threshold of the autocorrelator.

shown in Fig. 5.4:
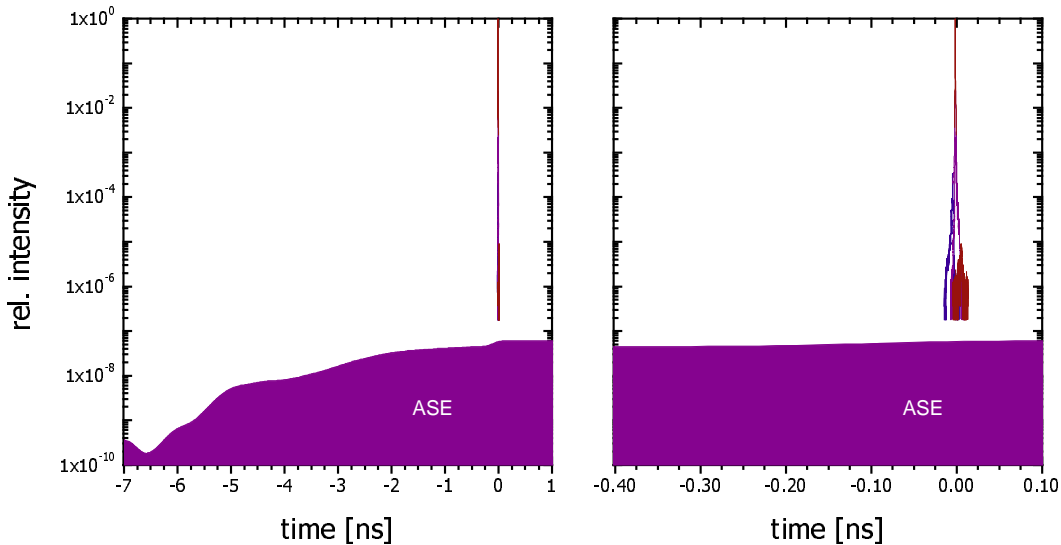
Figure 5.4: ATLAS prepulse level after fixing the RGA problem. Only the main pulse remains and the ASE level is $< 10^{-7}$.

To get an estimate of the preplasma gradient at the critical surface, Dr. Eidmann performed one-dimensional (1-D) simulations with the hydrodynamics code

MULTI-fs [62]. He modeled various laser intensity scenarios representing the cases measured above, namely a long ns-pedestal with 10^{11}W/cm^2 and 10^{12}W/cm^2, and a short fs-prepulse 400 ps before the main pulse, reaching 10^{17}W/cm^2. The pedestal corrresponds to different ASE-levels, while the fs-prepulse models one of the leakthrough pulses from the misaligned RGA. Fig. 5.5(a) shows the results. While a relatively long underdense preplasma is evident for both cases with and without a prepulse, the plasma scalelength at the relativistic critical surface is between 4 and 7.5 μm. The model considers only a pure 1-D expansion of the plasma, which yields too large a value as soon as the plasma expands to distances greater than the focus diameter, because lateral expansion will occur. Therefore, the slope is further increased and the plasma scalelength is reduced to $\approx$1.5 μm if one takes into account full 3-D expansion into 2π of the plasma plume (Fig. 5.5(b)). The true value may lie somewhere in between. For performing the 3-D PIC calculations presented below and in chapter 2, plasma gradients in this range were used.
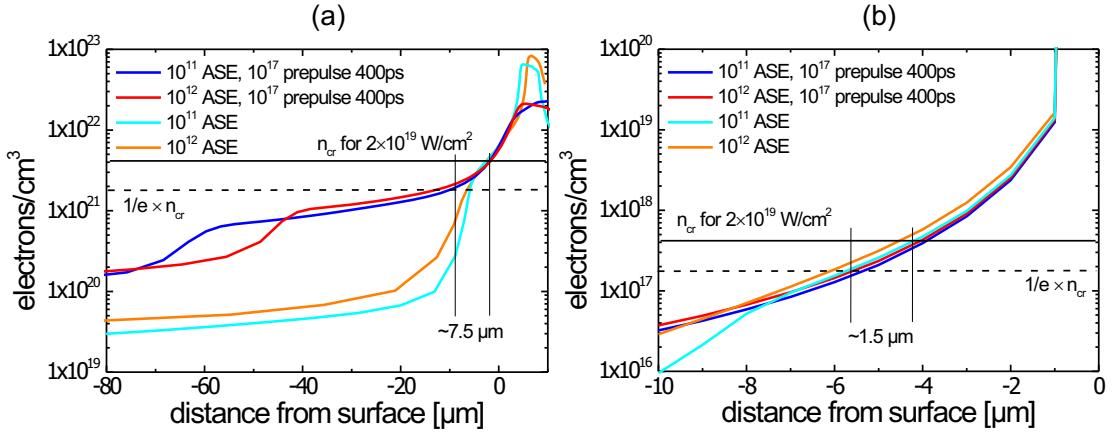
Figure 5.5: Behaviour of the electron density of the preplasma for 10^{11}W/cm^2 and 10^{12}W/cm^2, 8-ns ASE pedestals and an additional 10^{17}W/cm^2 fs-prepulse 400 ps before the main pulse. 1-D case from Multi-fs (a) and quasi- 3-D treatment from the Multi-fs results (b).

It is evident that the ASE pedestal dominates the generation of the preplasma, but an additional fs-prepulse can increase the plasma density close to the critical surface.

These results now can serve as a basis for simulations of the ion emission characteristics, as will be shown in Section 5.3.2.

5.3   Experiments and Results

5.3.1   Neutron Yield Optimization

The first set of experiments performed at the ATLAS laser was aimed at reproducing Pretzler's results [12] obtained with 200 mJ, 1×10^{18}W/cm^2 laser pulses from ATLAS-2. The maximum yield that could be achieved with this laser was 800 neutrons/shot, still not enough to get good statistics for neutron spectra in a reasonable time. This was only a slight improvement over Pretzler's yield of 140 neutrons/laser shot. In a first step, by commissioning ATLAS-10 and increasing the laser energy to 500mJ while keeping the intensity, the neutron yield could be raised to 5000 neutrons/shot in this work. This sharp rise is somewhat surprising given an only 2.5-fold increase in laser energy and a nominal equal intensity. From the ponderomotive scaling 2.17 and the related ion energy scaling 2.24, one would expect an equal ion temperature for the two cases and a linear dependence of the ion number on the laser energy due to the linear increase in spot area. The strongly nonlinear behaviour possibly indicates self-focusing of the laser pulse in the prepulse blow-off plasma in front of the target, which would lead to a much higher intensity at the critical surface. Regardless of the mechanism, these numbers are high enough to permit neutron spectroscopy with sufficient statistics. A further increase in neutron yield to ∼15000-25000 neutrons/shot could be achieved by implementing the adaptive optics system on ATLAS-10. On the one hand, this permitted to propagate the full laser energy to the target and, on the other hand boosted the intensity to 2×10^{19}W/cm^2. In Fig. 5.6 the neutron yield of different runs is plotted versus the laser energy. The scaling law of $n_n(E) \propto E^{2.8}$ extracted from the data is purely empirical at that point and cannot be explained by a physical model, since important input parameters like the intensity were not measured at that time. As is evident from the data points, the reproducibility from run to was very poor, which can be attributed to bad and irreproducible focusability of the laser without adaptive optics. However, the data points taken with adaptive optics show much less fluctuations than those without.

The large yield fluctuation for a given energy can be partly attributed to the difficulty to prepare an absolutely even CD$_2$ target, so the target surface shifts in and out of the focal plane randomly. Also at the time this data was taken, the adaptive optics system did not contain the closed loop optimization, so the corrections had to be applied by hand, a procedure taking a few hours. Due to temperature changes in the laser room, this optimization was only stable for a
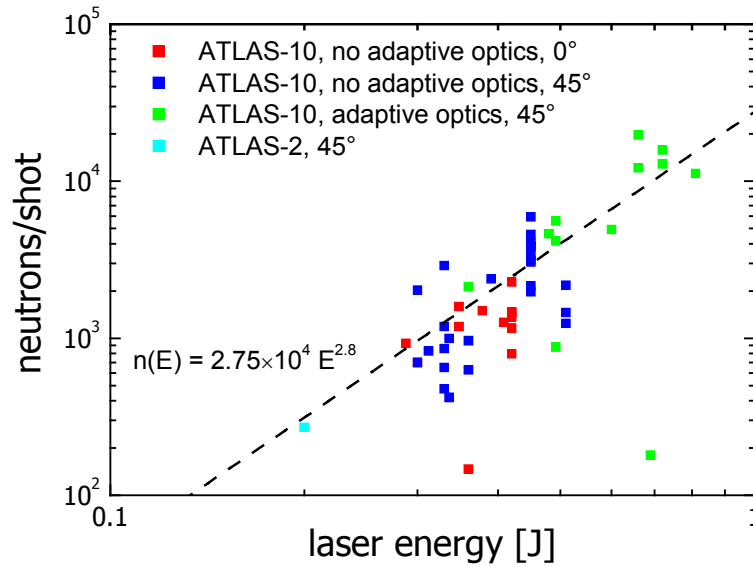
Figure 5.6: Neutron yield/shot from the ATLAS experiments. The data points are sorted according to the laser incidence angle (0° or 45°) and the laser development stage (ATLAS-2, ATLAS-10 with and w/o adaptive optics). The data points can be fitted by a power law with an exponent of 2.8.

few more hours, so some luck had to be involved in order to achieve good reproducibility. With the routine operation of the closed loop system at the end of this thesis, the laser performance became much more stable and the neutron yield was quite reproducible at around 15000-25000 neutrons/shot. Since this yield was the upper limit that could be achieved with ATLAS, the next step was to look for a possible application of these neutrons. The most promising prospect was the possibility to use the neutrons for plasma diagnostics. Since charged particles are strongly slowed down in the target or are deflected by the large electromagnetic space-charge or laser fields, neutrons are the only probe that can carry information about fast particles running into the target unaffected.

5.3.2 Directionality of Ion Emission

Neutron time-of-flight spectroscopy was used to determine the neutron energy spectrum. The setup shown in Fig. 5.1 was slightly modified in a way that the detectors were moved to various directions, and the laser incidence angle on the target was switched from 45° to 0° to change the polarization conditions (see Fig. 5.9). The laser was polarized in the plane of incidence (p-polarized) in the case of oblique incidence. A typical neutron time-of-flight spectrum and a scattering-corrected neutron energy spectrum is shown in Fig. 5.7, where the laser was inci-

dent under 45° to the target normal.
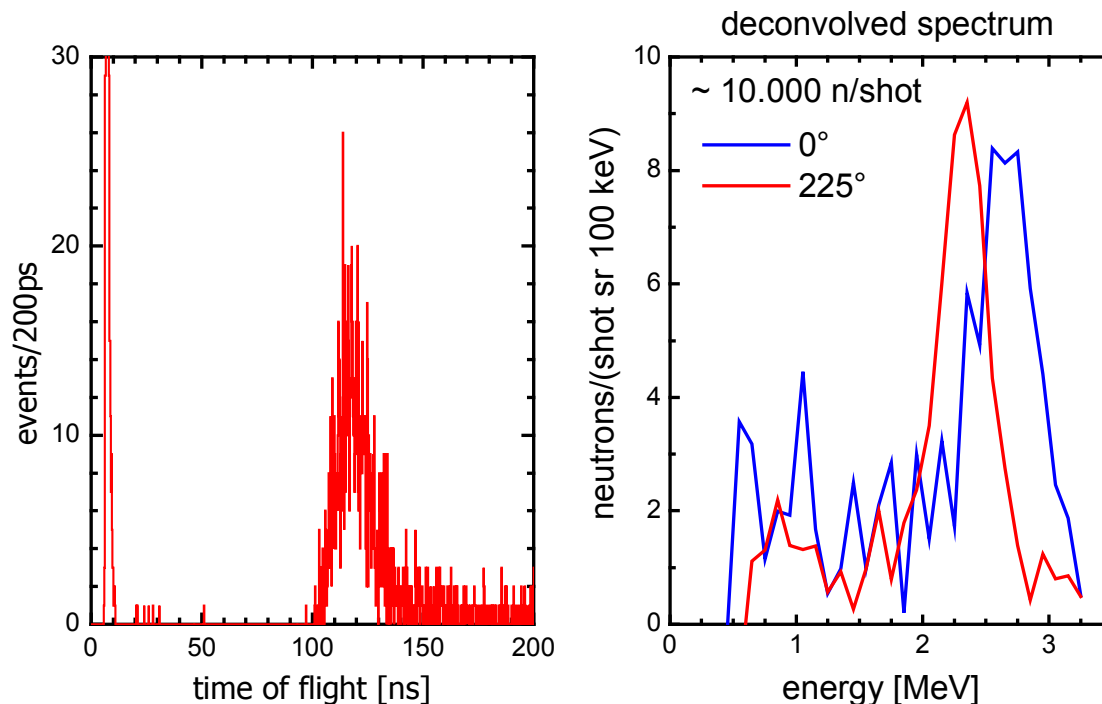
Figure 5.7: Neutron time-of-flight spectrum from a single detector (left). The separation between the prompt γ-peak and the delayed neutron signals is a measure for their energy. Right: Energy for two angles of the neutron detector arrays with respect to the target normal. The low energy cutoff is determined by the time window for the neutron detection.

The two energy spectra on the right side of Fig. 5.7 clearly exhibit a peak, which occurs at different energies for different detector directions. This kinematic shift away from the 2.45 MeV center-of-mass energy reflects the ion kinematics, as discussed in Chapter 4. The low energy tail is typical for these spectra and is caused by incomplete treatment of neutron scattering or by excess neutrons from the $^{12}C(d,n)^{13}N$ reaction. A comparison with model calculations is shown in Fig. 5.8, where an isotropic ion emission from the laser focus with an exponential energy spectrum with a slope of 75 keV was assumed.

The model curves represent the experimental data quite well. For other shots the temperature lay a bit higher, and a typical value for these laser conditions is 75-100 keV. The total number of accelerated ions based on that temperature estimate is approximately 3.5×10^{11}, which corresponds to a coupling efficiency of laser light to fast ions of ∼1.75%.

For a larger number of experimental runs, in Fig. 5.9 the peak position in the neutron energy spectrum is plotted versus the laser energy for different detection
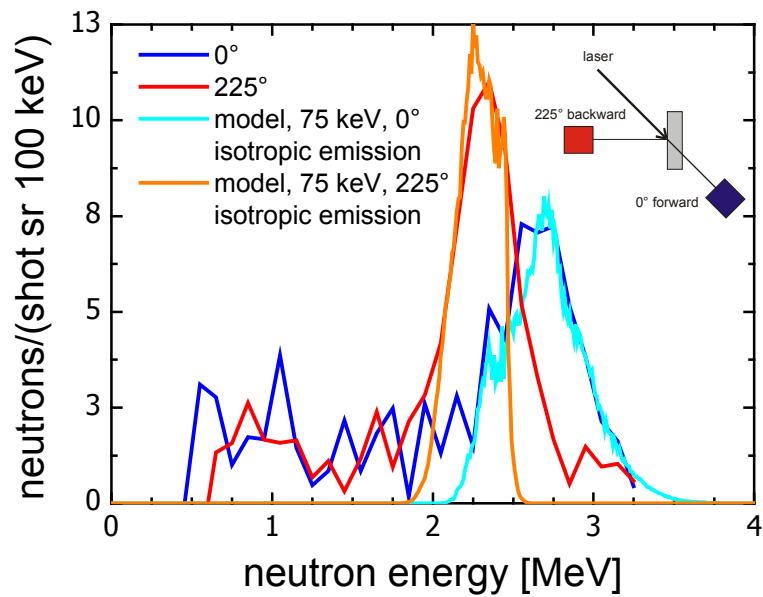
Figure 5.8: The neutron spectrum from Fig. 5.7 compared to model calculations with MCNEUT. The model parameters and results are explained in the text.

directions and laser incidence angles.
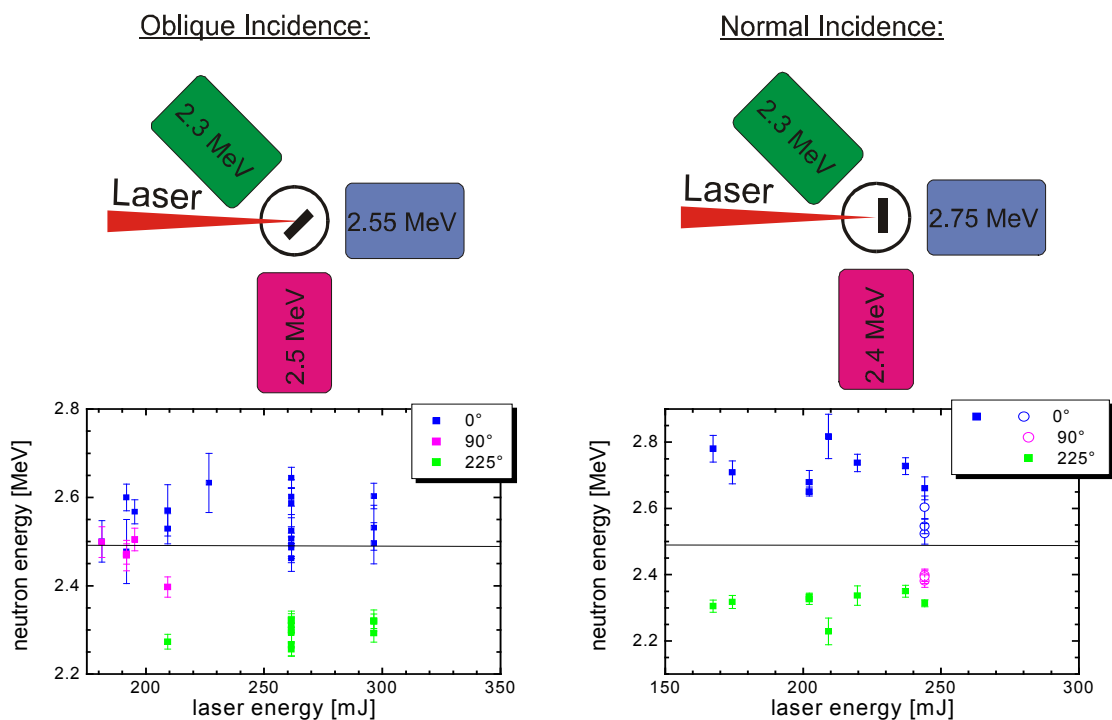
Figure 5.9: Position of the kinematically shifted neutron energy peak plotted against the laser energy for 0° and 45° laser incidence direction under various detection directions.

From this data, the following conclusions can be drawn:

1. **Oblique (45°) incidence (p-polarized):**

   (a) The two detectors placed symmetrically behind the target (0° and 90°) measure the same blue shift (i.e. a peak at energies higher than 2.45 MeV).

   (b) The detector at 225° measures redshifted neutrons.

2. **Normal (0°) incidence (s-polarized):**

   (a) The detector at 0° sees a strong blue shift.

   (b) The detector at 90° measures unshifted neutrons.

   (c) The detector at 225° measures redshifted neutrons.

From 1(a) it follows that the ion motion is symmetrical to the target normal. Points 1(a) and 1(b) implicate either isotropic emission, where the red-and blueshift are caused by the difference in plasma density inside and in front of the target, or by a overall velocity component directed symmetrically into the target. The same general picture is valid for case 2, so the ion emission is not related to the laser direction, but either to the target orientation or isotropic. In figure 5.10 the ion momentum space from 3-D PIC calculations is plotted for a number of preplasma scalelengths which are within the range determined by the estimate in section 5.2. These simulations represent four different cases:

- Acceleration into and out of the target even for an obliquely incident laser occurs at short preplasma scalelengths (Fig. 5.10 (c)). A steep density gradient belonging to a small scalelength corresponds to quasi 1-D situation with target normal acceleration.

- When the plasma scalelength is large (Fig. 5.10 (a)), hole boring becomes possible favoring ion acceleration in the radial direction normal to the laser axis.

- At intermediate scalelengths, a transition between the two extreme cases is observed (Fig. 5.10 (b)).

- A more isotropic acceleration occurs at even longer scalelengths when the focus is large (Fig. 5.10 (d)). Here the divergence of the ion beam is broader because of the "softer" plasma boundary and goes roughly into 2π. This situation would also explain the results from Fig. 5.9, and is in good agreement with the neutron spectrum in Fig.5.8. Since this scenario calls for a less
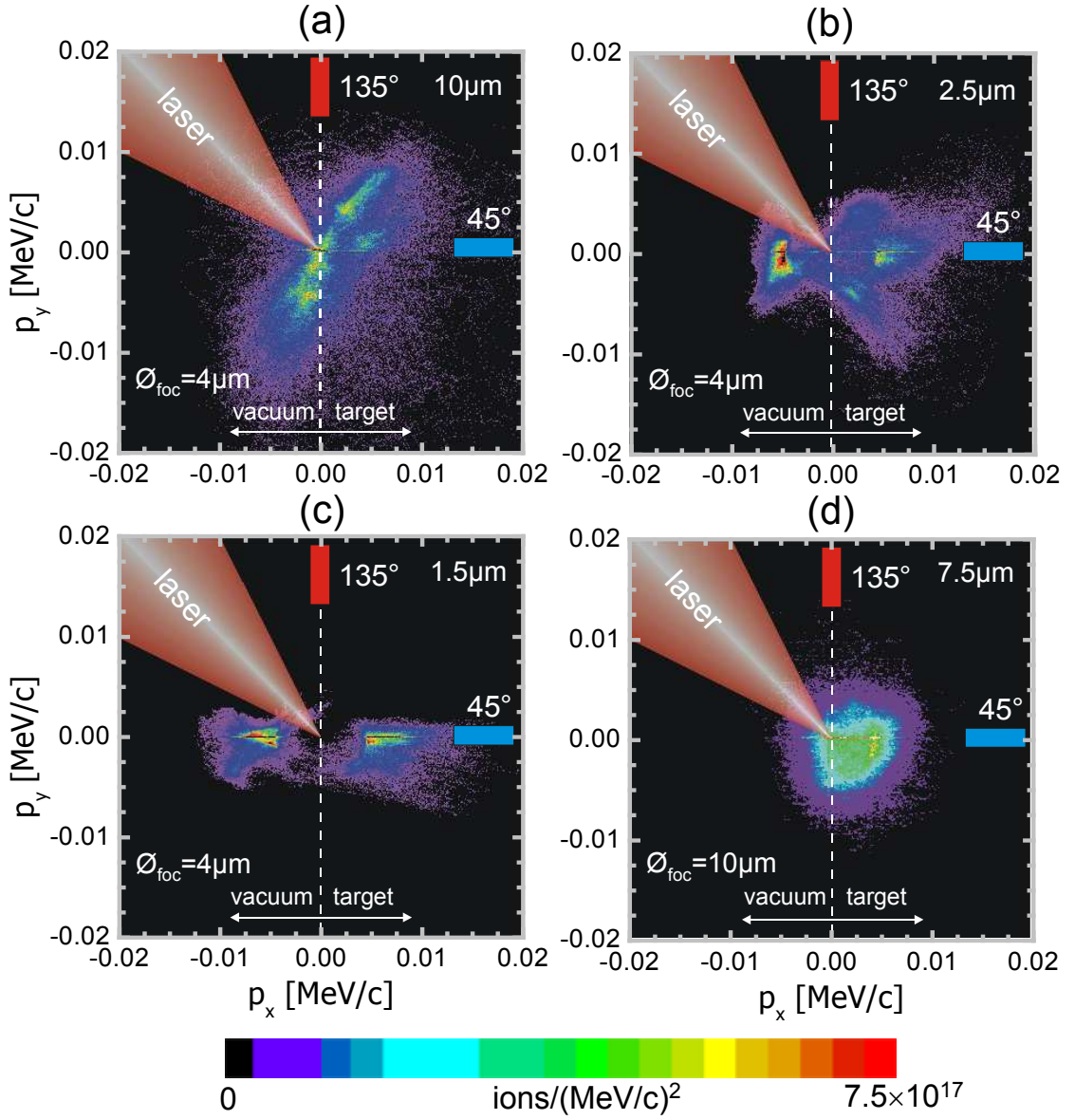
Figure 5.10: Projection of the ion momentum space on the px-py-plane for varying pre-plasma scalelengths and focal spot sizes. Spot size 4μm, 2×10^{19}W/cm^2: (a) Scalelength l=10μm, (b) l=2.5μm and (c) l=1.5μm. (d) Spot size 9μm, 5×10^{18}W/cm^2, scalelength l=7.5μm. The pulse duration was 158fs, and the snapshots were taken 40 fs after the pulse maximum. For orientation, the laser direction and target surface position in space coordinates is marked. Although the plots are momentum space, this gives an impression where the ions move. The simulation box was x=19.2μm $\times$ y=64μm $\times$ z=16μm in size and the laser was obliquely incident onto the target. The neutron detector directions are given for the following experiments (sections 5.3.3 and 5.3.4)

steep density gradient, it is more likely that the real emission characteristics is broad.

A comparison of p- and s-polarized laser pulses allows to rule out that the Brunel mechanism (see chapter 2, section 2.1.2) dominates the electron acceleration in our case. Since the Brunel mechanism works only for p-polarized light, one would expect a difference in the number and energy of the fast electrons for the two cases, which in turn would result in different ion and neutron energies and numbers. This difference is not seen in the experiment.

Taking into account the PIC results, this interpretation of the experimental data looks quite conclusive.

1. Due to the large focus the ions are accelerated either in a quasi 1-D geometry in a direction into and out of the target surface or are emitted completely isotropic. The neutron diagnostic is not able to clearly distinguish between these two cases.

2. The interaction takes place in a plasma with a gently density gradient, because obviously the Brunel mechanism plays no role for fast-electron generation.

5.3.3   Laser Energy Variation

After the installation of the two deformable mirrors, the laser focusability became much better, but still lacking the closed loop system the reproducibility had to rely on the skill of the laser operator. Nevertheless, an attempt was made to record a series of neutron spectra and yield for variable laser energy. The detectors were now and for all the following experiments placed under 45° and 135° at a distance of 3.75 m and 4.23 m from the target, respectively (see Fig. 5.1), and the laser hit the target under 45° with p-polarized light.

The focal spot size varied between runs, but it was monitored at the beginning of each run. Therefore it was possible to calculate the intensity for each run from the spot size and the laser energy. The measured yield can now be compared with a model based on the scaling laws describes in chapter 2. To estimate the total yield for runs with varying laser energy, E_L, equation 4.3 can be rewritten as:

$$N(T_p) \quad = \quad \int_{E=0}^{E_{max}} \int_{E_j=E_i}^{0} n_i(E_i, T_p) \, \sigma(E_j) \, \frac{dx}{dE}(E_j) \, dE \, dE_j \qquad (5.1)$$

$$\text{with}$$

$$n_i(E_i, T_p) \quad = \quad N_0 \frac{E_L}{k_B T_i} \, \exp\left(-\frac{E_i}{T_i}\right). \qquad (5.2)$$
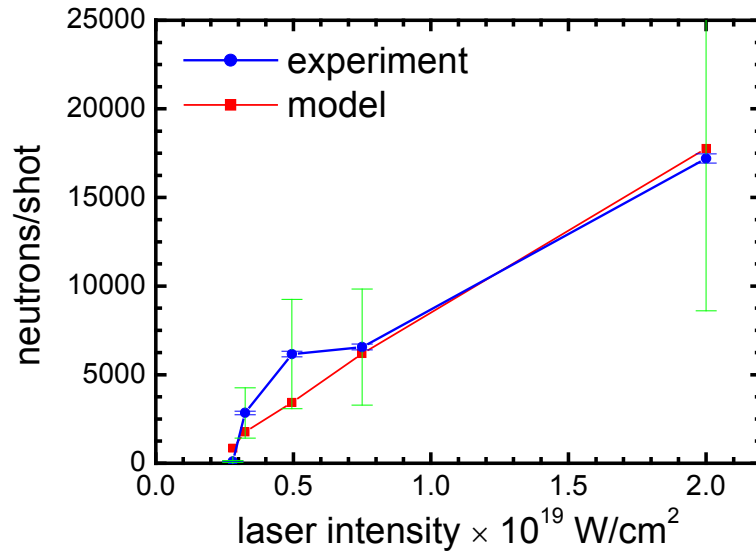
Figure 5.11: Experimental and theoretical neutron yield plotted versus the laser intensity. The intensity was varied by adjusting the laser energy to values of 200 mJ, 420 mJ, 560 mJ, 700 mJ and 840 mJ, respectively. The blue error bars include only the statistical error, while the green ones also include the systematic error. The model prediction assumes a scaling of the number of accelerated ions with $2.6{\times}10^{11} \cdot \sqrt{10^{19}W/cm^2/I_L}$ ions/J of laser energy.

Here, T_p is the ion temperature from equation 2.24 for a given laser intensity, k_B is the Boltzmann constant, E_i is the starting energy of each ion i in the spectrum and E_j is the momentary energy along the ion trajectory which can be calculated from cumulatively substracting the inverse of the differential range dx/dE from the starting energy E_i. The factor E_L/T_i in the definition of the ion spectrum takes into account that the energy content of the ion beam scales linearly with the laser energy, but a higher temperature is distributed among less ions.

The result of the experiment is compared to the model prediction in Fig. 5.11. The strong excess at lower intensities might be partially due to reduced pile-up error at low countrates, and maybe by a better overall hit rate at the lower intensities. Otherwise, the experiment is in good agreement with the model within the error bars. In Fig. 5.12 the neutron spectra of this measuring campaign is presented. The positions of the neutron peaks do not shift strongly with the laser energy/intensity, corresponding to a point-like ion source instead of the planar one in the experiments with large focus. However, the high-energy tail is much more pronounced at higher laser energies, showing that the ion temperature increases with laser energy. This is also confirmed by the increasing neutron yield. The typical ion temperature at the highest achievable intensities was determined to be around 200 keV.
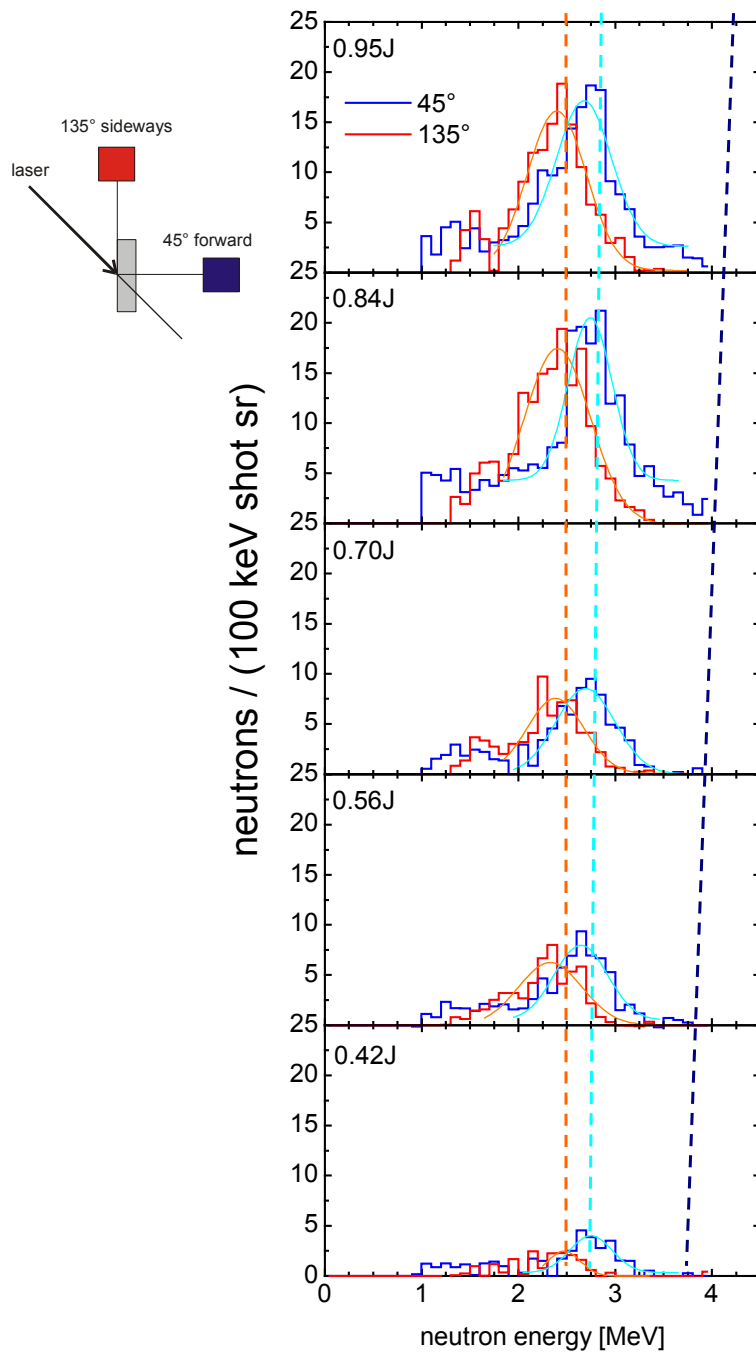
Figure 5.12: Deconvolved neutron spectra for a series of varying laser energy. The detectors were placed at 45°(blue line) and 135°(red line). A gaussian fit of each peak is also plotted.

5.3.4   Variation of the Preplasma Gradient

As already mentioned in section 5.3.2, the ion emission characteristics depend strongly on the preplasma gradient. Therefore, a comparison of neutron spectra
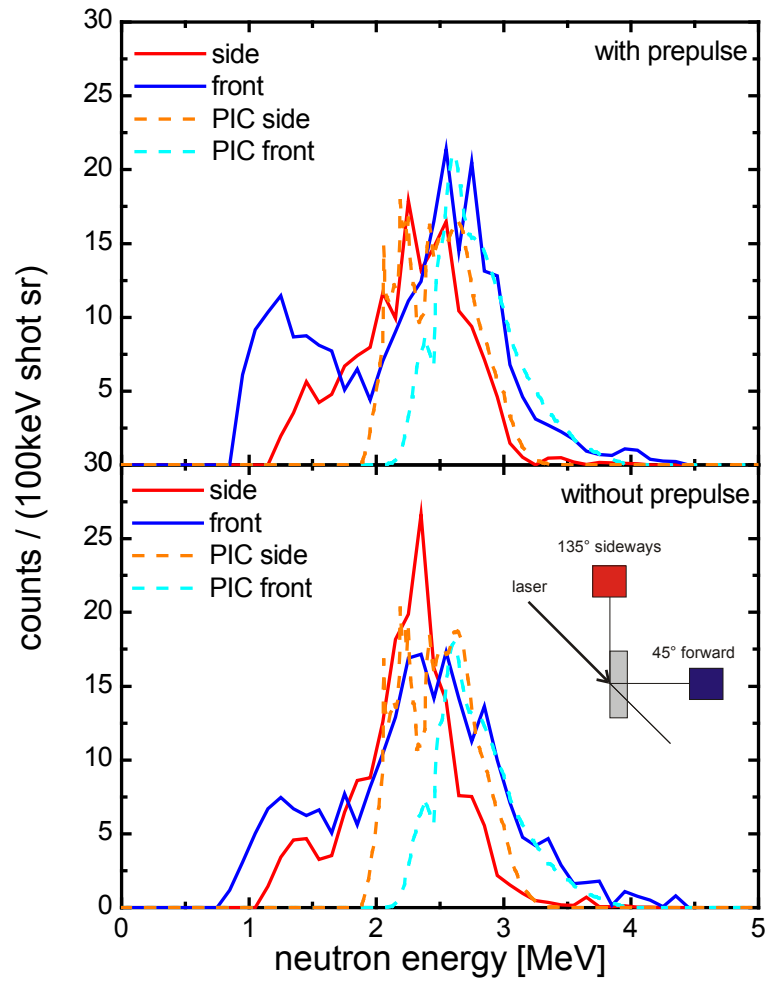
Figure 5.13: Neutron spectra with (top) and without (bottom) artificial prepulse. The neutron spectra derived from the 10-μm gradient PIC ion distribution of Fig. 5.10 are also plotted as dashed lines for the two detector positions.

with and without an artificially added prepulse was performed. Before this experiment was made, the contrast ratio of the ATLAS laser was carefully measured and prepulses caused by a misaligned regenerative amplifier were removed (see section 5.2). This resulted in a contrast ratio of $> 10^{-7}$ on the ns-scale, but at a peak intensity of 10^{19}W/cm^2 the intensity of the ASE background is still in the $10^{11} - 10^{12}$W/cm^2-range, sufficient for noticeable plasma creation. An artificial prepulse with an energy and intensity content of 1% of the main pulse can be added 400 ps before the main pulse. Neutron spectra were recorded with and without this prepulse. The result of this experiment is shown in Fig. 5.13. In this figure, the sum of all runs with and without artificial prepulse from the measurement campaign. Also plotted is the modeled neutron spectrum, which is based on the PIC calculation for a 10-μm plasma gradient, as shown in Fig. 5.10. The resulting experimental spectra exhibit small, but distinct differences.

These can be realized most clearly by comparing them to the PIC results. While the model curve agrees quite well with the experiment in the case with prepulse (the large discrepancy at neutron energies below 2 MeV is due to scattered neutrons), no close match can be achieved for the high contrast case. In the following, we will discuss the differences for both detector locations separately.

1. **Forward (45°) emitted neutrons:** For high contrast, the low-energy slope of the forward detected neutron peak is far more red-shifted than in the runs with prepulse. This is quite surprising, since redshifted neutrons can only be caused by ions streaming away from the target surface (and hence from the detector) into the coronal plasma, where they undergo fusion. Fig. 5.5 suggests a higher preplasma density for the case with prepulse, and consequently one would expect more red-shifted neutrons in this case. Since the experimental findings are the exact opposite of that, something must be wrong with this simple model; however, a conclusive solution to this problem is not yet found. A possible reason for the observed result may be a snow-plow effect of the prepulse, in the sense that the prepulse creates a void in the preplasma in front of the critical surface. This effect cannot be observed in 1-D hydrodynamic or PIC calculations, since here the plasma cannot move laterally out of the focal region. In 3-D, the prepulse could act in a similar way as the main pulse to create a density depression in the focus, since the time for the plasma to move is quite long. However, at prepulse intensities of 10^{17}W/cm^2, the relativistic effects are rather small, so this explanation is just a hypothesis. It cannot be tested in 3-D PIC simulations, since a 400 ps time interval between the pre- and main pulses are a factor of 1000 too long to treat in reasonable computing time, and a 3-D hydrodynamics code that can resolve the fs-prepulse does not exist to my knowledge.

2. **Sideways (135°) emitted neutrons:** The predominantly radial emission of ions with respect to the laser axis in the 10-μm gradient case (see Fig. 5.10) causes a relatively broad neutron spectrum in the sideways direction. This agrees well with the experiment for the low contrast case with prepulse. In the high-contrast case, as expected from the steeper gradient, the ion emission is more forward directed, leading to a narrower sideways peak.

These result of that last experiment shows that the dynamics of the laser-plasma interaction is still far from being fully understood, leaving enough room for further interesting research. Especially the effects of fs-prepulses acting on a long-pulse generated preplasma seem to be not yet completely described.

All in all, in this chapter, the first steps toward neutron spectroscopy taken in this thesis were described. We could show that by a moderate increase in pulse energy by a factor of 4 and simultaneously rising the laser intensity by a factor of 20, the neutron yield could be pushed by nearly two orders of magnitude, which can be mainly attributed to the steep increase of the d-d reaction cross-section with ion energy. Now enough neutrons can be generated to perform neutron spectroscopy. First results in this field show that, contrary to Pretzler's suggestion [12], the ion emission characteristics is either normal to the target or isotropic, which together with PIC simulations hints at an ion origin close to the critical density. The spectra can be modeled to determine approximate ion temperatures and numbers. If the laser energy is varied while the focusability is maintained, the variation of the neutron yield can be explained by the ponderomotive scaling law for the ion temperature and a fixed conversion efficiency of laser light into ions. The neutron spectra also show an increase in ion temperature. The preplasma scalelength does have an influence on the neutron spectra, but it cannot yet be fully modeled and understood.

Chapter 6

Transfer to High Laser Energy at LULI

6.1 Experimental Setup

During a four-month stay for a laser-electron acceleration experiment at the Lawrence-Livermore National Laboratory, which to some extent bridged the time to the first commissioning of the ATLAS-10 upgrade at Garching, I came into contact with a group led by Tom Cowan and Markus Roth. They planned to investigate ion acceleration at the LULI-100 TW laser and formed an international collaboration between the Gesellschaft für Schwerionenforschung Darmstadt, Germany (GSI), General Atomics, San Diego, USA (GA), Laboratoire pour l'Utilisation des Lasers Intenses, Palaiseau, France (LULI) and our institute at Munich. This was a unique opportunity to scale the techniques and results from the ATLAS to a laser with 50 times its energy in single-shot operation. After having shown that, at least in the case of d-d fusion, the neutron yield increases sharply with laser energy, a large increase in neutron yield was expected. Since the main goal of this collaboration was to investigate proton and heavy ion acceleration and their applications, the neutron measurements were also done having in mind their use as a plasma diagnostics. The experiments were performed in a series of campaigns from June, 2000 till January, 2002. With the much higher ion energies achievable with this laser (up to 25 MeV protons and 100 MeV fluorine ions) [36, 37], it became possible to efficiently explore other neutron source reactions with higher threshold, but also higher cross-section. The maximum neutron yield of 0.8×10^8 neutrons / shot could be achieved with the ^{9}Be(p,n)^{9}B reaction. This per-shot yield translates to 10^7 neutrons per Joule, more than two orders of magnitude more than with

ATLAS. Having proved the feasibility of neutron TOF techniques in a high-power laser environment in the experiments at ATLAS, another task was to transfer that skill to a laser with not only more than one order of magnitude higher energy, but also operating in single-shot mode. This transfer was highly successful, so for the first time neutrons from different source reactions could be distinguished by their spectra. Moreover, a direct comparison of deuterons accelerated from both target surfaces was carried out by means of TOF neutron spectroscopy. The latter experiment is described in chapter 7, since it matches very well to the physics described there.

6.1.1   The Luli 100 TW Laser

For the experiments, the LULI 100 TW hybrid Nd:glass / Ti:Sapphire laser was used, which amplifies pulses from a Ti:Sapphire oscillator and regenerative amplifier running at 1054 nm in a mixed Nd:silicate/phosphate-glass power amplifier chain.The details of this system are described in [63], so only the main parameters shall be mentioned here.
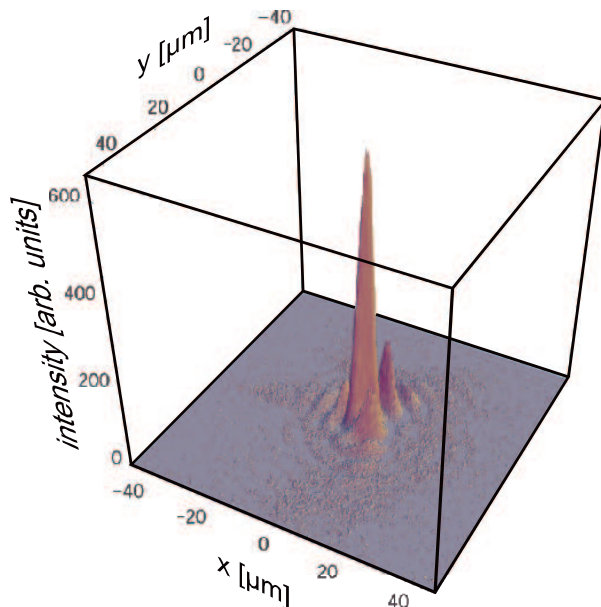
Figure 6.1: 3D plot of the intensity distribution in the focus of the LULI laser for a typical shot ($E_{laser} \simeq 15$ J). The dynamic range of the camera was only 650, so in the subsequent analysis all background pixels were set to 0 or 1 for an upper or lower limit in the intensity calibration.

The laser delivers pulses with an energy of up to 30 J on target, a duration of 450 fs, a pulse repetition rate of one shot/20 min. Most shots were done at a
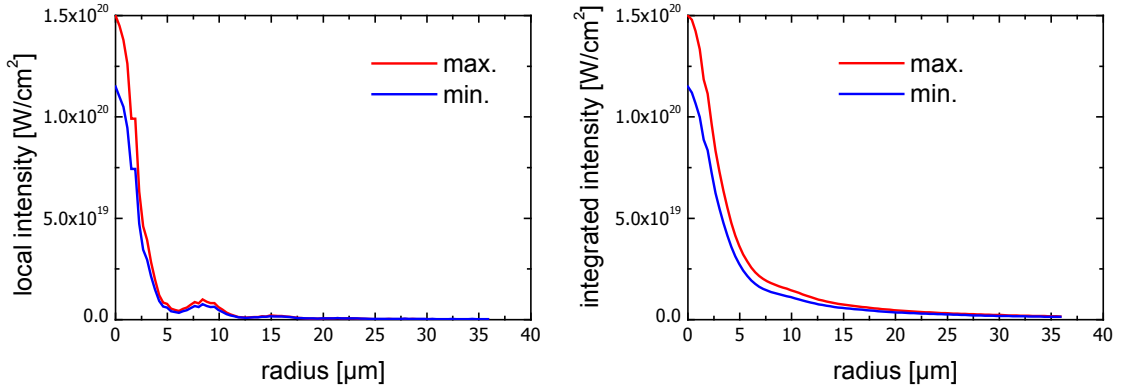
Figure 6.2: Radial dependence of local intensity $I_{loc.}$ and averaged intensity $I_{av.}$ up to the radius r for the upper limit (background = 0, red line) and lower limit (background = 1, blue line) case. The average intensity is calculated by evaluating $I_{av.}(r) = 1/(2\pi r) \int_0^r 2\pi I_{loc.}(r) \, r \, dr$. An averaged intensity at the radius of the airy disk (5 μm) of approx. 3×10^{19} W/cm^2 can be extracted from the right plot.

somewhat lower energy of around 15-20 J on target to reduce the damage risk of the compressor gratings. The focused intensity reaches 7×10^{19} W/cm^2 (Fig. 6.1 and Fig. 6.2). Although not equipped with an adaptive optics system, this laser achieves a focal quality close to the theoretical limit, because it is not plagued by a poor quality of the amplifying medium. Nevertheless, the installation of such as system has begun in order to suppress the thermal lensing effect of the amplifier glass and thus increase the shot rate.

6.1.2 Target Setup

The great variety of experiments carried out during the five experimental campaigns demanded many different target types. All of them were solid, thin films of various composition and thickness as for the ion generation experiments. All targets were irradiated under normal incidence. To get rid of surface contamination with proton-rich materials, either the target was resistively heated or irradiated on its back surface with a 100 mJ, 6 ns heating laser at intensities below the plasma formation threshold some milliseconds before the main shot. In the neutron generation experiments, depending on the reaction to be investigated either unheated gold and aluminum targets of 20 or 50 μm thickness were used to accelerate protons, or deuterium-compound coated 20 μm aluminum targets or CD_2 foils were employed for deuteron acceleration. In most cases, the latter targets were laser-heated to maximize the energy coupling into deuterons.

6.1.3   Neutron Time-of-Flight Diagnostics

As a primary diagnostics, two TOF plastic scintillation detectors were placed be-hind 15 cm of lead under 65° to the laser axis in the June 2001 campaign, 25° in October 2001, and under 180° degrees in the January 2002 campaign. The distance to the target was 240 cm in June, 245 cm in October and 174.5cm in January. The detectors were a modified version of the ones described in chapter 3, section 3.2.2. One of the detectors consisted of a 10 cm dia. by 2 cm thick BC 412Q disk with a decay time of <1 ns and low sensitivity, while the other one used a 11 cm dia by 2 cm thick disk of standard NE110 with ∼2.5 ns decay time and a higher sensitivity. Both were coupled to standard fast 2" Hamamatsu type E2979-500 phototubes. They were read out by a Tektronix TDS 540 1-GHz storage oscilloscope and the waveforms were stored on a floppy disk for further treatment. The oscilloscope was triggered by an unshielded cable attached to an empty channel on the oscilloscope that picked up the electromagnetic pulse (EMP) noise from the laser. This method is quite inaccurate in timing, but has got the advantage to be insensitive for all low-energy test shots, in contrast to the standard method of a trigger signal from a fast photodiode. The accurate timing can be inferred later from the gamma flash. Neutron scattering in the target chamber and the lead shielding was estimated from MCNP calculations and included in the model calculations.

6.1.4   Silver Activation Detector

Two silver activation detectors of the same type as described in chapter 3, section 3.2.1 were placed under 90° and close to 0° to the laser axis, just outside the target chamber. At 10 Hz, where the countrate during the irradiation is much higher than the counts caused by neutron capture events, the number of ^{108}Ag and ^{110}Ag atoms is slowly growing to an equilibrium, and decays after switching off the laser. In contrast to that, in the present experiment a single shot produces enough neutrons in a very short time to produce a perfect exponential decay signal in the detector (Fig. 6.3), and the area under the curve directly gives the number of produced radioactive nuclei. The detector signal was fed directly into a multichannel scaler.
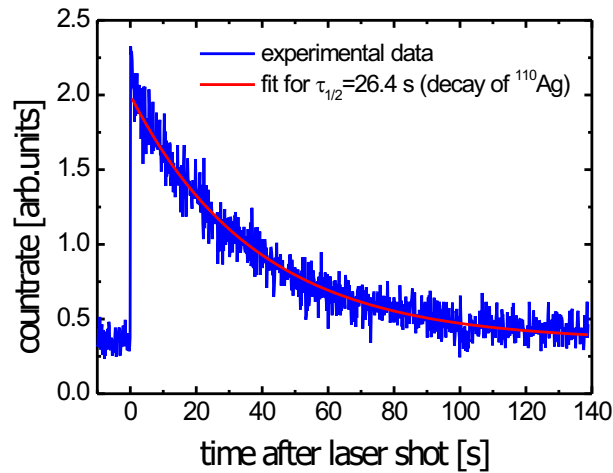
Figure 6.3: Silver activation decay signal from a single shot

6.1.5 Additional Diagnostics

Since the main scope of the experimental campaign was ion acceleration, we will quickly describe the main diagnostics used for ion detection. Although they play no direct role in the neutron experiments reported here, they are mentioned as the source of a broad spectrum of additional information used for understanding the neutron experiments.

Radiochromic Film

To image the transverse profile of the forward emitted ion beam for different energy intervals, a filter wheel was placed behind the target holder, loaded with 4 stacks of Radiochromic Film (RCF), consisting of 4-8 layers each. Radiochromic film consists of two layers of radiation dose sensitive dye embedded in a sandwich of polyethylene foils. The total thickness of the RCF sheets was 252 μm, including two 110 μm thick outer layers of polyethylene. Only protons with energies higher than 2.5 MeV can penetrate the first polyethylene layer and reach the dye. By layering a number of RCF sheets it is possible to image the proton beam at different energies, since protons with different energy range out in different layers. From these measurements, a typical beam divergence was determined to be between 15° and 20°.

Magnetic Spectrometers and Thomson Parabolas

In the ion acceleration experiments, the main energy-sensitive diagnostics consisted of two two proton spectrometers and two Thomson Parabola spectrometers. They were were connected to vacuum ports under -6°, 0° and 13° to the laser axis in different configurations. One of the Thomson Parabolas was developed in this work, and the other one was copied from the first with some minor modifications. A description of it is given in Appendix B. Both instruments are not ideally suited to measure the proton-vs. deuteron content of the emitted ion beam. The proton spectrometer provides no separation between the two isotopes, while the CR-39 detector sheets in the Thomson parabolas are largely insensitive to hydrogen isotopes above a few MeV because of the small specific energy loss of those ions. Replacing the CR-39 by X-ray film circumvents this problem, but the latter is hard to calibrate absolutely for different energies and species. Thus, these diagnostics were only treated as sources of supplementary information.

6.2   Neutron Yield from Various Targets

On the ATLAS and Jena lasers, the typical per shot yield was in the range of 15000-30000 neutrons. While these numbers are sufficient for plasma diagnostics applications when accumulating over many laser shots, as a source the yield falls short by several orders of magnitude. The main aim in the first set of experiments at the Luli laser therefore was to look at the scaling of the neutron yield for much higher laser energies. Although a laser delivering an energy of several tens to hundreds of joules with high repetition rate is not yet available, lasers like this are already in the planning and early commissioning stage, for instance the POLARIS project in Jena. Since the TNSA mechanism is much more prominent at higher laser energies, various neutron generation schemes including TNSA accelerated protons and deuterons are investigated in order to determine the source properties and to optimize the yield. Due to the limited number of available shots, it was not possible to carry out detailed parameter studies for all the different schemes, so one has to rely on a number of shots with rather random energies. However, with careful data analysis quite a conclusive picture can be obtained. First of all, all shots relevant for neutron generation are summarized and the corresponding number and properties of the neutrons are listed in Table 6.1.

Here, Ti:H and Ti:D refer to titanium loaded with hydrogen or deuterium, respectively, and CD and CH refer to an amorphous hydrocarbon or deuterated

Table 6.1: Shot number, laser energy, target material, target thickness, back surface treatment, catcher material and neutron yields.

shot number	laser energy	target material	target thickness	back surface	catcher material	neutron yield
	[J]		[μm]			
05310153	20.2	$(CD_2)_n$	5000	–	–	4.01×10^6
05312235	20.6	$(CD_2)_n$	5000	–	–	1.81×10^7
06010000	16.8	$(CD_2)_n$	30	laser heated	$(CD_2)_n$	1.85×10^7
05302302	22.6	Al	30	CD (100 nm)	$(CD_2)_n$	4.36×10^7
05312140	21.8	Al	30	CH (100 nm)	$(CD_2)_n$	4.37×10^7
06011614	18.7	Ti:D	50	laser heated	$(CD_2)_n$	1.09×10^7
06012033	24.4	Ti:D	50	laser heated	Ti:D	3.71×10^6
06011923	26.6	Ti:H	50	laser heated	Ti:D	2.96×10^7
06011850	25.1	Au	20	–	Aerogel	2.95×10^7
06012133	16.3	Au	20	–	Be cube	8.20×10^7

hydrocarbon layer with a carbon fraction of about 0.8. Laser heated targets were heated on their rear surface by a ns-Nd-YAG laser to remove contaminants immediately before the shot, as described in Section 6.1.2.
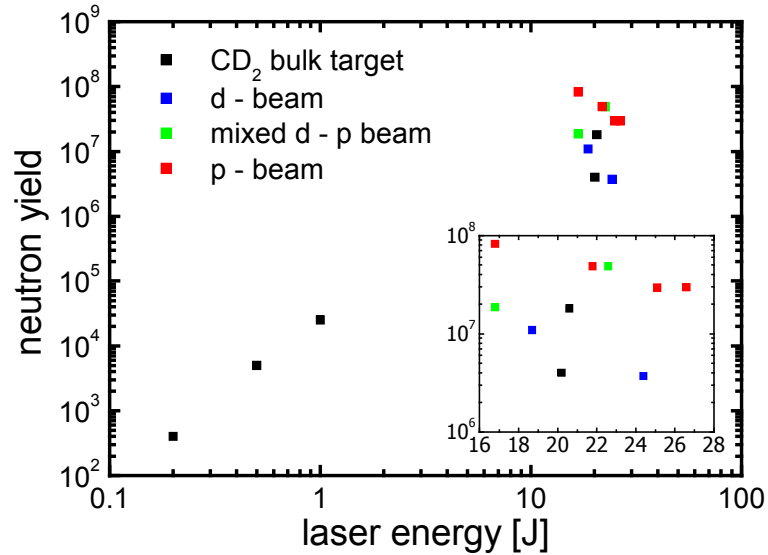
Figure 6.4: Comparison of total neutron yields for different ions and catcher targets as achieved at ATLAS and the 100 TW LULI laser.(Inset: Enlargement of the parameter space for the LULI shots)

In Fig. 6.4 these results are plotted in comparison to neutron yields obtained with different laser energies at ATLAS using solid CD_2-Targets. In general, it

can be stated that with ion temperatures achievable at a 100 TW class laser, the highest neutron yields can be reached with protons instead of deuterons, despite of the latter's higher cross-section at low energies.
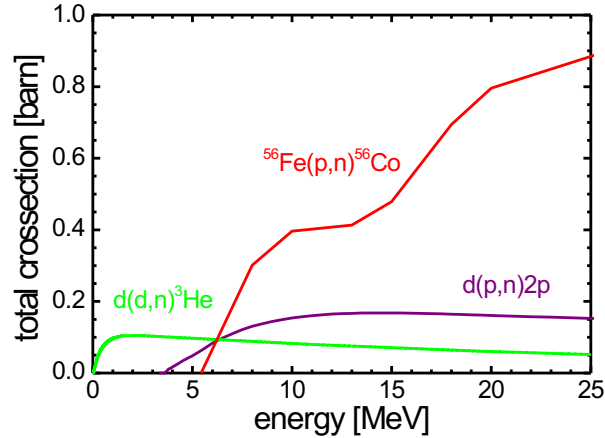
Figure 6.5: Neutron production cross-section for the reactions $d(d,n)^3He$, $d(p,n)2p$ and $^{56}Fe(p,n)^{56}Co$.

As can be seen from Fig. 6.5, using Fe as an example for most heavy elements, the threshold for the (p,n) reaction lies between 3 and 6 MeV, while the cross-section for this reaction at higher energies is much larger than for d-d or d-t fusion. Additionally, in the presence of protons on the back surface the accelerating fields get shielded from protons outrunning the deuterons, so that the latter can extract less energy from the field than protons can. This leads to a less efficient coupling of the laser energy into deuterons, making them less favorable for efficient neutron generation. In summary, with very high power lasers protons seem to be the more promising ion species to produce secondary neutrons than deuterons, at the expense of the lost neutron monochromaticity. In the following sections, a closer look into the various reaction mechanisms will be taken.

6.2.1 Bulk $(CD_2)_n$ Targets and Frontside Accelerated Deuterons

In order to establish a direct scaling of the ATLAS experiments to higher laser energies, the same bulk $(CD_2)_n$-targets were irradiated at the LULI laser to measure the neutron yield and the TOF spectrum. As can bee seen from Table 6.1, even with almost identical laser energy in the two shots the neutron yield differs strongly, indicating the bad reproducibility in high-power laser plasma experiments. Neutrons from these shots were caused by deuterons accelerated at the

frontside of the target by charge separation fields, as described in chapter 2 and observed in the ATLAS experiments. This makes it interesting to look at the neutron spectrum and maybe get some information on the ion temperature in analogy to the ATLAS experiments. The TOF spectrum in Fig. 6.6 exhibits a prominent fusion peak, which can be modeled by a deuteron temperature of several MeV.
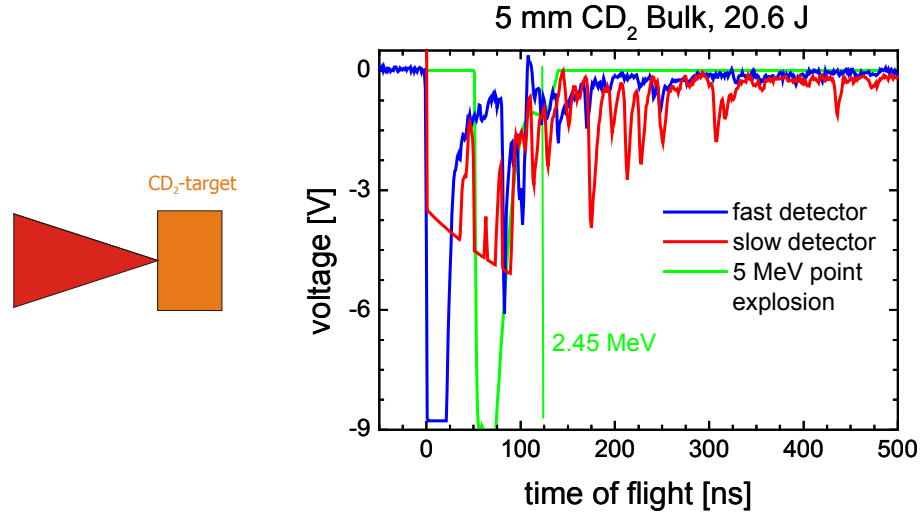
Figure 6.6: Oscilloscope traces of shot 05312235 on a bulk CD_2 target. Blue is the small fast detector, and red is a more efficient, slower detector. An exponential decay from the γ-flash was substracted from the red curve, hence the shape of the saturation line. A strong neutron peak is evident in the TOF spectra between 50 and 100 ns.

While the quality of this spectrum is not sufficient to extract a precise quantitative information about the ion temperature, the d-d fusion origin of a large part of the neutrons is proven by the fusion peak.

6.2.2 TNSA Accelerated Deuterons and Protons

The previous experiment was a direct scaling of the ATLAS conditions and was therefore based on ion acceleration in the laser focus. The main result of the LULI campaign from the direct ion spectroscopy measurements was the existence of a strong component of TNSA accelerated ions. Hence it was only natural to use these ions in a next step to generate even more neutrons. The first attempt used an aluminum target coated with an amorphous, 1-μm thick $C_{0.8}D_{0.2}$ on the rear surface, in order to replace some protons in the beam by deuterons. For comparison, a second shot was made onto a nearly identical target, but this time with an amorphous CH coating on the back. The parameters of all shots described here can be found in table 6.1. The ion beam interacted with a CD_2 secondary

target (catcher) placed 5 cm behind the coated Al-foil. The neutron TOF spectra are shown in Fig. 6.7.
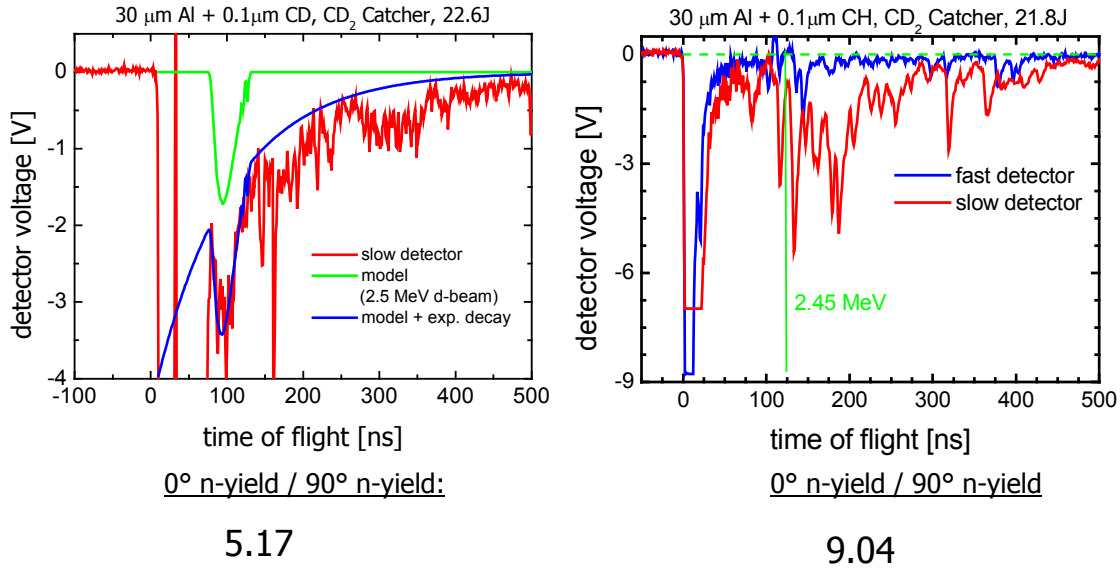
Figure 6.7: (left) Oscilloscope trace of shots 05302302 (CD coated aluminum). The green curve is a model spectrum for a 2.5-MeV ion beam off the target rear surface, which is fusing in the catcher. The blue curve is a fit to the exponential decay of the measured gamma signal added to the green curve. (right) Oscilloscope trace of shot 05312140 (CH-coated aluminum).

The laser energy and the neutron yields of the two shots are nearly identical, with the latter being as high as 5×10^7. From the left picture, it is evident that the first measured peak is at the same time (and therefore neutron energy) as predicted by the model for d-d fusion. However, at later times a large number of low-energy neutrons is visible, which are caused by deuteron breakup induced by high-energy protons. The same late neutrons are present in the right picture, caused by protons alone. Although the differential cross-section of the deuterium breakup reaction d(p,n)2p could not be found in the commonly available databases, it is interesting to look at the ratio of neutrons detected in beam direction and perpendicular to it by the silver activation counters. While this ratio for pure d-d fusion should be close to unity, in the left picture it is 5.17 and in the right one 9.04. This indicates that a different reaction is causing the most neutrons, and also hints at a strong anisotropy of the breakup cross-section. The result of these two shots shows that it is not possible to fully replace the protons in the beam by just preparing a deuterated rear surface layer. Obviously, enough proton-rich contaminants are absorbed at the surface before the shot to make up for a dominant proton component.

The conclusion drawn from this problem is that the proton contaminants must be removed prior to the shot to generate an ion beam containing a desired species. A very successful method to do this is heating the target to ≈1000°C, so the contaminants are boiled off the surface. Unfortunately this does not work for preparing a deuteron beam, because all deuteron containing compounds known to me decompose at much lower temperature and therefore are boiled away as well. The only method that worked reasonably well for deuterons was heating the target rear surface with a ns-pulsed Nd:YAG laser about 1 ms before the main shot. In this case, the CD-coated aluminum foil was replaced by a deuterium-loaded titanium foil, where deuterons are embedded in the bulk metal. This time the catcher was made from the same material. The TOF-spectrum is shown in Fig. 6.8.
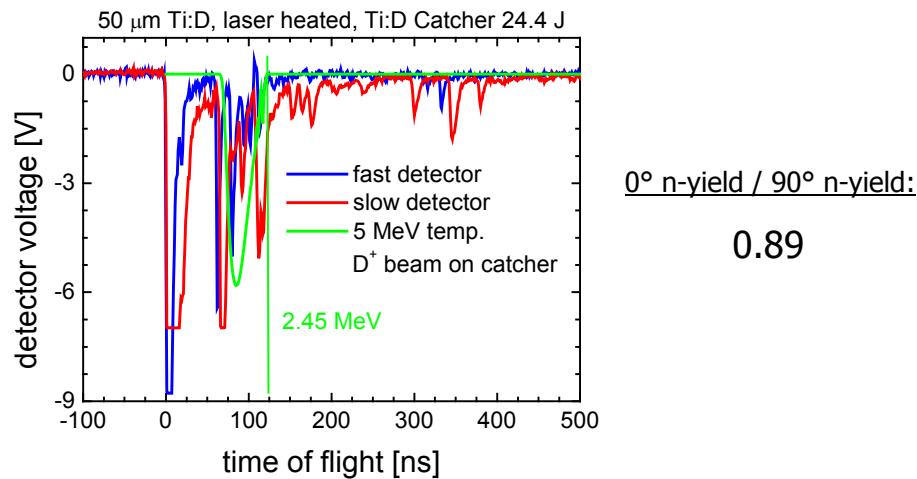
Figure 6.8: Shot 06012033 .

The exponential decay of the gamma signal is gone because of a reduced detector voltage. Now, the most neutron signals cluster around an energy of >2.45 MeV, with only few late signals. This is an indication of a reduced proton content in the beam. The ratio of neutrons in forward and sideways direction drops to 0.9, which is somewhat below the expected value for pure d-d fusion. The neutron yield for this shot was only 3.7×10^6, with an even higher laser energy than for the two unheated shots. The identical yield for those two shots can be explained by the fact that obviously the total efficiency for neutron production from d-d fusion is much smaller than from proton breakup. While the cross-section (see Fig. 6.5) of the p(d,n)2p-reaction is higher only at energies above 6 MeV, the main factor leading to this difference is the much higher efficiency for proton acceleration.

On the other hand, this comparison shows that laser heating the rear surface actually can remove protons to a certain degree. The cleaning is not perfect, as

shown in spectra of the Thomson parabola, but enough to make a difference for the neutron spectra.

As it became clear that the most neutrons are in fact generated by reactions between protons and the secondary target, mainly due to the more efficient proton acceleration, the gate to even higher neutron yields opened up. A reaction with a high cross-section is $^9\mathrm{Be}(p,n)^9\mathrm{B}$, with a threshold as low as 1.67 MeV, making this a promising candidate for achieving even higher yields. In order to prevent Be-contamination of the target chamber, a beryllium cube of 5 cm sides was mounted in an aluminum case, which had a 50-μm thick aluminum foil covered opening on one side. The protons transmitted through this cover can trigger neutrons in the beryllium cube. The primary target was a 20 μm gold foil, from which a strong proton beam had already been demonstrated. Although the laser energy was an only moderate 16.3 J on this shot, the neutron yield was 8.2×10^7, setting a new record for that laser. The neutron spectrum is shown in Fig. 6.9 along with the results of the matching simulation.

	measured:	calculated:
0° yield:	6.52×10^6 n/sr	6.48×10^6 n/sr
90° yield:	2.43×10^6 n/sr	2.44×10^6 n/sr
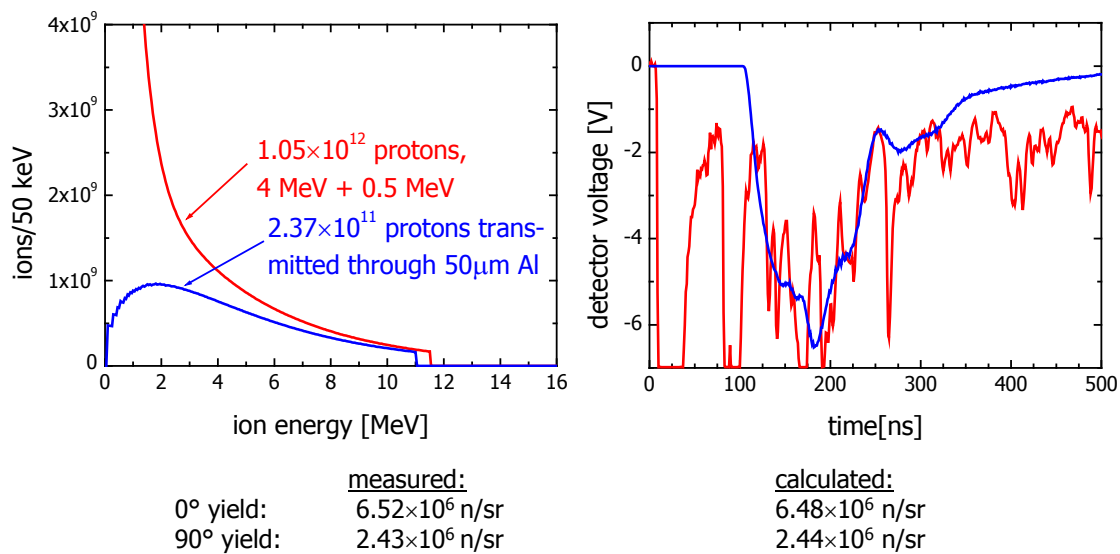
Figure 6.9: (left) Assumed proton spectrum from the primary target (red) and after the 50 μm aluminum cover (blue). The temperature of the hot component is 4 MeV in agreement with other shots done with similar targets and laser energy. The cold component is almost totally absorbed in the cover and plays no role for the simulation result. (right) Neutron TOF spectrum (red) and modeled spectrum (blue) for the ion beam shown on the left side. (below) The neutron emission into forward and sideways direction as measured by the silver activation counters is in perfect agreement with the model.

From this picture we can see that the measured neutron spectrum qualitatively can be identified as being caused by the $^9\mathrm{Be}(p,n)^9\mathrm{B}$ reaction, since it closely follows

the model curve, with the exception of an unexplained prompt peak. Of course the statistics in the TOF counters prevent an exact reproduction of the model curve. By comparing the predicted and measured neutron emission into different directions extracted from the model and the silver activation counters, respectively, it can be demonstrated that despite of the large systematic error in the efficiency calibration the relative accuracy of these counters is very good. The deviation from the model is on the order of one percent. This is not surprising because of the high number of activated silver nuclei, which was on the order of a few 10^4.

These results prove that it is possible to use neutron spectroscopy in a high-energy, single-shot laser environment to identify certain aspects of neutron production processes in a laser -plasma interaction. While the results are not very quantitative in terms of spectral shape and deduced ion energies, they nevertheless indicate that with more powerful lasers the goal of really doing plasma physics and diagnostics might be achieved in the near future with a higher neutron yield and hence better statistics. On the other hand, the yields achieved so far are high enough to think of first applications provided a laser is developed that delivers this kind of energy with high repetition rate. POLARIS laser being built in Jena is a promising candidate. A further experiment done at LULI will be described at the end of Chapter 7, since its physics is very similar to the experiments in Jena described there, and the LULI result acts as a good example of scaling these physics to high-energy lasers.

Chapter 7

Acceleration Processes Revealed by Neutrons

7.1   Introduction

A main result of the LULI campaign was that in the presence of protons the TNSA ion acceleration mechanism becomes inefficient for the acceleration of deuterons and heavier ions. This "proton poisoning" effect is caused by the fact that protons with their maximal charge-to-mass ratio outrun heaver ions and shield the accelerating fields. It is not yet clear how strong this effects influence the ponderomotive charge separation acceleration. Nevertheless, preparing a proton-free target surface most likely will maximize the heavy ion yield. Under the bad vacuum conditions available at typical laser facilities, this requires heating the target to temperatures of ~ 900 °C to get rid of proton-rich surface adsorbants. Unfortunately, by this treatment deuterons are removed from the target equally efficient, preventing deuteron acceleration off the surface. An obvious solution to this problem is the preparation of a fresh target surface prior to irradiation, in order to prevent adsorbants from building up. One way to achieve this is using a heavy water jet or droplet target. The development of such water jet source would have taken a prohibitively long time so close to the end of the thesis. When I was invited by Prof. Sauerbrey and his group in Jena to participate in an experiment on neutron generation from heavy-water droplets as part of their program of investigating laser-plasma-interaction with mass-limited targets, this was the perfect opportunity to circumvent this difficulty. At that time, the results from LULI with rear-side accelerated ions were still very present in the daily discussions at MPQ. Therefore, also here a catcher target was placed behind the droplet target in the

hope of increasing the neutron yield by using some of these rearside ions for fusion. Very soon it turned out that adding the catcher target produced a clearly separated second peak in the neutron TOF spectrum that can be attributed to ions fusing in the catcher. Now it was clear that this effect deserved to be further investigated, and we could show for the first time simultaneous ion acceleration from both the ponderomotive and TNSA acceleration scheme. The results of the Jena experiments are summarized in a paper submitted to Physical Review Letters, which is attached to the end of this thesis.

While the experiments at the ATLAS used only ions accelerated in the laser focus for neutron production, it was demonstrated from the LULI campaign and several other experiments [18, 64] that ions can be accelerated at the back surface of thin foils by the TNSA mechanism [33]. However, since the geometry of a round jet or spherical droplets is fundamentally different from a planar foil, the expected properties of the ion beams are different from the latter case, and also the data modeling is a bit more complex. Since small ($\sim 10\mu$m size) droplets are midway in size between clusters [14] and solid targets, these experiments can also be seen as a parameter study on target size.

7.2   Experimental Setup

The experiments were carried out at the Jena 10-TW Ti:Sapphire laser. The major difference to the ATLAS system discussed in chapter 5 is the shorter pulse duration of 80fs at 10-Hz repetition rate. This laser is capable of focusing 950 mJ of laser energy to an intensity of 10^{20} W/cm^2, using an f/2, 45° off-axis parabola. The spot is approximately 3 μm in size (FWHM) and contains 30% of the total energy. In the present experiment, the laser operated at a reduced energy of 650 mJ on target to prevent damage to the optical components. Since focusing was not checked after each run, an intensity of 3-4 $\times$ 10^{19} W/cm2 is a more realistic guess for these measurements.

The target irradiated by the laser was a (D_2O) jet with a nozzle size of 10 μm and a backing pressure of 50 bar. The nozzle orifice was modulated with a frequency of 1 MHz by a piezo ceramic element, which caused the jet to break up into a well ordered, linear chain of droplets of 20-μm diameter, spaced by 80 μm. The laser was not synchronized to the droplets, but was allowed to run freely at 10 Hz repetition rate. As a consequence of this and a random movement of the focal spot, not every laser pulse hit a droplet and the ones that did hit a random spot

on the droplet surface. As can be deduced from the number of gamma events recorded in the detectors and the total number of shots, about 1/10th of all shots hit the target well enough to produce gamma radiation. Therefore the number of gamma signals was used as a reference for the determination of the neutron yield per shot. Ions accelerated from the laser focus (as opposed to the ones from TNSA at the back surface) are able of triggering fusion reactions inside the droplet itself, leading to prompt fusion neutrons.

On some runs, an additional catcher target consisting of an array of seven 50 mm × 7 mm $CD_{(2(n))}$ disks was placed behind the target in laser direction at various distances (8.3 cm, 14.8 cm and 23.3 cm)(see Fig 7.1). Deuterons accelerated from the droplet and hitting the catcher produced fusion neutrons with a time delay corresponding to the ion time of flight from the droplet to the catcher.
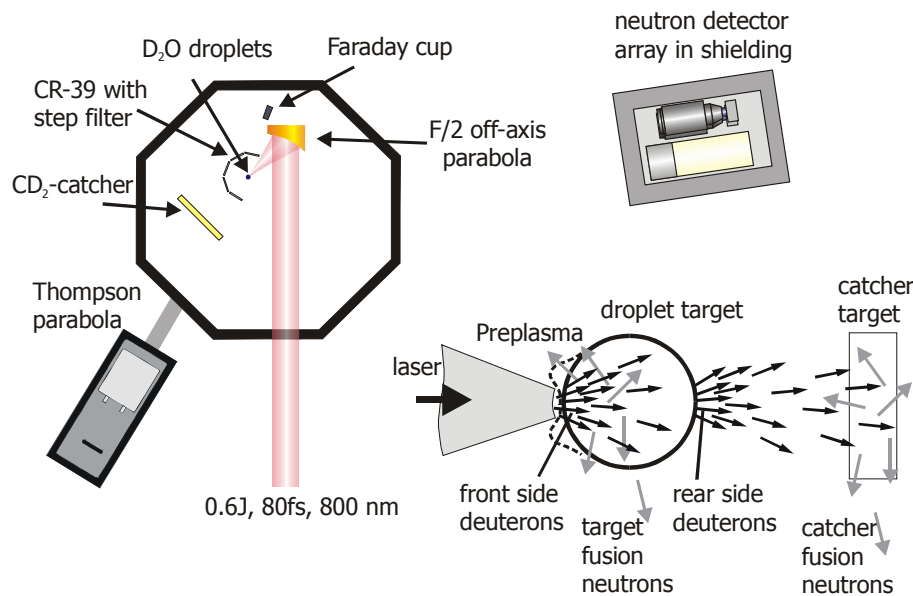
Figure 7.1: Experimental setup and schematics of ion generation and propagation

The fusion neutrons from laser accelerated deuterons were counted in an array of three fast scintillation detectors, one using 10-cm thick liquid NE213 as an active material and two using NE110 plastic disks of 2-cm thickness(Fig 7.1). The detector array was placed at a distance of 240 cm to the jet and at an angle of 143° to the laser axis. The detector solid angle was $\Delta\Omega$ =1.7 msr. The signals were counted and analyzed by standard NIM and Camac electronics, as described in Chapter 5, Section 3.2. The time resolution of the whole system is approximately 1 ns for gamma signals and 1.5 ns for neutrons. The detectors were placed in a lead housing of 9-cm wall thickness to the front and 10 cm to the sides to shield against the gamma burst from the laser interaction. Since in the experiment the neutron yield of many shots was high enough to produce multiple hits in the thick
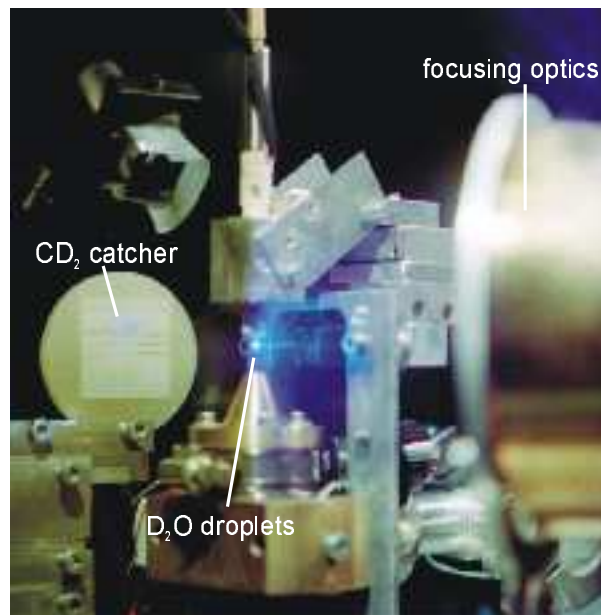
Figure 7.2: Photo of the experiment. The off-axis parabola used for focusing can be seen far right, the plasma emission from the droplet is visible in the middle, and the CD_2 catcher is placed behind the droplet at the left side.

liquid scintillator, the spectra recorded by this detector are distorted because of the under-representation of late signals.

This high yield was not anticipated, but fortunately in the thin detectors the count rate was sufficiently low. By increasing the total number of shots it was possible to get good statistics with the small detectors as well. All spectra presented in the following chapter were recorded as the sum of 30,000-60,000 shots and therefore represent an average over fluctuations in the laser energy, focus position on the droplet and preplasma conditions. All conclusions made are only valid under these assumptions.

As an additional diagnostics, a Thomson parabola was placed under 10° to the laser axis to analyze the forward accelerated ions. To measure the angular distribution of ions, five CD-39 sheets covered with a step filter made out of layers of 2-μm Mylar foil were arranged on a half circle around the target. Finally, a Faraday cup placed under 150 degrees to the laser axis provided information about the slow-ion component from the thermal plasma expansion.

To quantify the neutron spectra, the code MCNEUT was used in conjunction with 3-D PIC simulations from the VLPL code, as described in chapter 2.

7.3 Experimental Results

In a first experiment, the droplet jet was irradiated by the laser and the catcher target was placed 14.8 cm behind the jet. The catcher was covered by 250 μm of Mylar foil, stopping virtually all ions. The objective of these runs was to provide reference data without catcher, but with the same amount of neutron scattering material as in the following runs with catcher. The resulting spectrum, accumulated from 45,000 shots, is plotted in Fig. 7.3(a). A single neutron TOF peak is obvious. It has to be caused by ions from the laser focus fusing inside the droplet. The long tail of late signals can be mainly explained by neutron scattering, but a few neutrons from deuterium photofission and $^{12}C(d,n)^{13}N$ may also be included in this tail. However, the cross-section of these reactions is not known well enough to make a quantitative estimate.
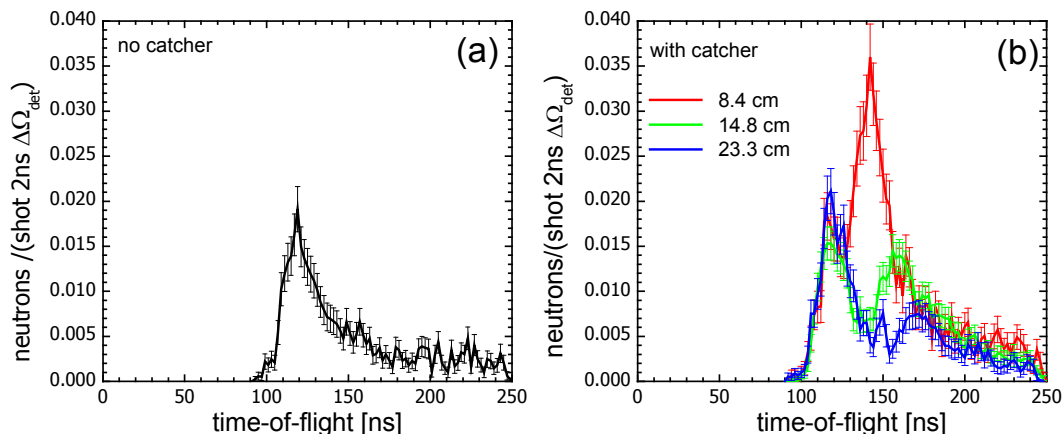
Figure 7.3: Neutron TOF spectra for runs with (a) covered catcher and (b) exposed catcher at different distances: 8.3 cm, 14.8 cm and 23.3 cm.

In Fig. 7.3(b), the mylar foil was removed from the catcher target, which was now placed at distances of 8.3 cm, 14.8 cm and 23.3 cm. Two clearly separated neutron time of flight peaks are evident, with the first still at the same position as in the run without catcher. Moving the catcher further away from the target, the second peak shifts to later times and broadens. This behaviour can be explained by fusion neutrons generated in the catcher by ions originating from the water droplet. In this scenario, the shift arises from the time the ions need to reach the catcher, and the broadening is due to the increasing time-of-flight dispersion of a non-monochromatic ion beam. As we will see later, this peak cannot be consistently explained by ions from the laser focus penetrating the droplet and hitting the catcher, but has to originate from a second ion population, which causes no fusion neutrons in the droplet itself.

The Thomson parabola data was plagued by electric field breakdowns due to bad vacuum conditions caused by a broken turbomolecular pump, but nevertheless it was possible to extract a spectrum of the fast deuterons emitted under 15° to the forward laser direction, albeit with a 30% uncertainty in the energy scaling. The spectrum is shown in Fig. 7.4 and exhibits a temperature of T = 320 keV. The high-energy cutoff lies at 1.2 MeV, while the low-energy cutoff is caused by the finite size of the CR-39 sheet. This spectrum represents a sum of ions from the front surface penetrating the target and ions from the back surface and can be regarded as an order-of-magnitude estimate of the ion energies involved.
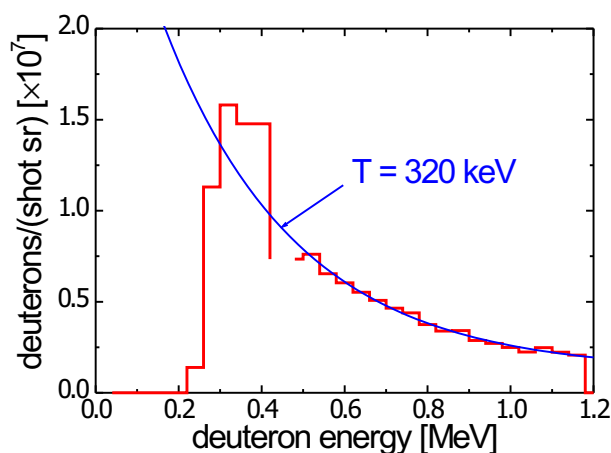
Figure 7.4: Thomson parabola spectrum of deuterons emitted from the droplet in forward direction, 15° to the laser axis.

The CR-39 sheets placed around the target could not be analyzed quantitatively, since the regions not covered by the 2-μm thick mylar foil were saturated, while deuterons penetrating one layer of mylar were difficult to count quantitatively due to the small size and depth of the craters they cause. Qualitatively, a slightly enhanced deuteron yield in laser direction and perpendicular to it could be detected.

7.4   Data Analysis and Comparison with Theory

In order to understand the spectra, we will first focus on the explanation of the first peak. Recalling equation 4.3 from chapter 2, the only unknown quantities are the ion energy and angular distribution $N_i(E_i, \theta)$ and the ion stopping power dE/dx in plasma.

7.4.1 Modeling of the First Peak

Modeling the Ion Distribution:

As described in equation 2.24 from chapter 2, section 2.2, the mean ion energy gain from planar ponderomotive charge separation is ~0.8 MeV for a laser intensity of $I = 3 \times 10^{19} \text{W/cm}^2$. Since this only holds true for a pure 1-D situation, this formula is not reliable for three dimensions. To get an idea of the ion energy *and* their angle distribution, VLPL-3D PIC simulations were performed. A laser pulse with Gaussian temporal and spatial profile (80-fs duration and 4-μm diameter) was incident from the left side onto a simulation box of $19 \times 16 \times 16 \mu\text{m}^3$ onto a preformed plasma of 4-μm scalelength followed by a uniform bulk density of $16 n_{\text{cr}}$. The simulation was performed under 0° and 45° (p-polarized) angle of incidence with very similar results; hence, only the 0°-calculation is shown here. The pulse bores rather deeply into the plasma before it reaches the critical surface, so the ion acceleration is predominantly radial to the laser axis, regardless of the target surface orientation. This situation is similar to the one described by Pukhov for relativistic channels in underdense plasmas [32]. It means that the position of the focal spot on the droplet has little influence on the ion distribution. Fig. 7.5 (a) shows the ion spectra recorded in different angle intervals to the laser axis; the light blue curve in Fig. 7.5 (b) plots the product of ion energy and number of ions per 10 keV versus the angle to the laser axis. The plot shows that the most and fastest ions are emitted under large angles to the laser axis. The angle-integrated ion spectrum consists of $\sim 10^{11}$ ions with a two-temperature exponential type spectrum with $T_{\text{i,cold}}$ ~100 keV and $T_{\text{i,hot}}$ ~350 keV. Note that the most energetic ions are emitted at a large angle and therefore cannot be seen in the Thomson parabola.

Putting this distribution into MCNEUT (with correction for target heating, as described below) results in a neutron TOF spectrum shown in Fig. 7.6, which fits quite reasonably to the measured one. However, by increasing the spread of the ion emission (inset of Fig. 7.6), an even better match can be achieved. This larger spread might be due to residual effects of the laser incidence angle at the target surface. This angular distribution is in qualitative agreement with the CR-39 data.

The same distribution was also used to fit the first peak in the spectra recorded with catcher. The number of ions needed to explain the neutron spectra is on the order of $2.5 - 5 \times 10^{10}$, depending on the precise temperature. The detailed shape of the angular and energy distribution is of small influence on the neutron spec-
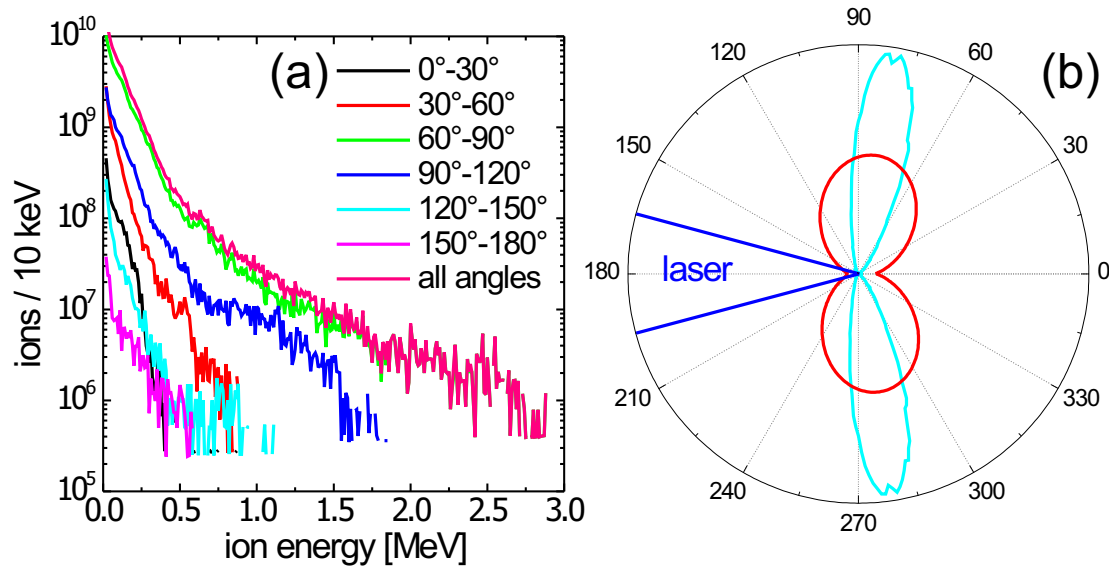
Figure 7.5: PIC results: ion spectra at different angles from the laser axis and sum spectrum (a). Distribution of ion angles to the laser axis (b) from the PIC output (light blue) and modified distribution for best match with the experiment (red).
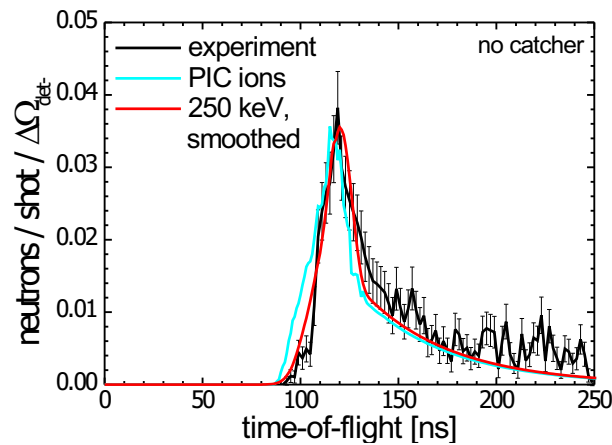
Figure 7.6: Experimental and modeled neutron TOF spectrum for the run without catcher. The PIC output (light blue) and the optimized (red) angular distributions are shown in the inset

trum. An isotropic ion angular distribution with a somewhat lower temperature (250 keV) would also explain the measured droplet neutrons, but according to the PIC calculations would require a much larger laser focus to occur.

Influence of target heating

As already described in chapter 2, section 4.2, the influence of electron target heating on the spectral shape of the neutrons is small (see Fig. 4.6. The assump-
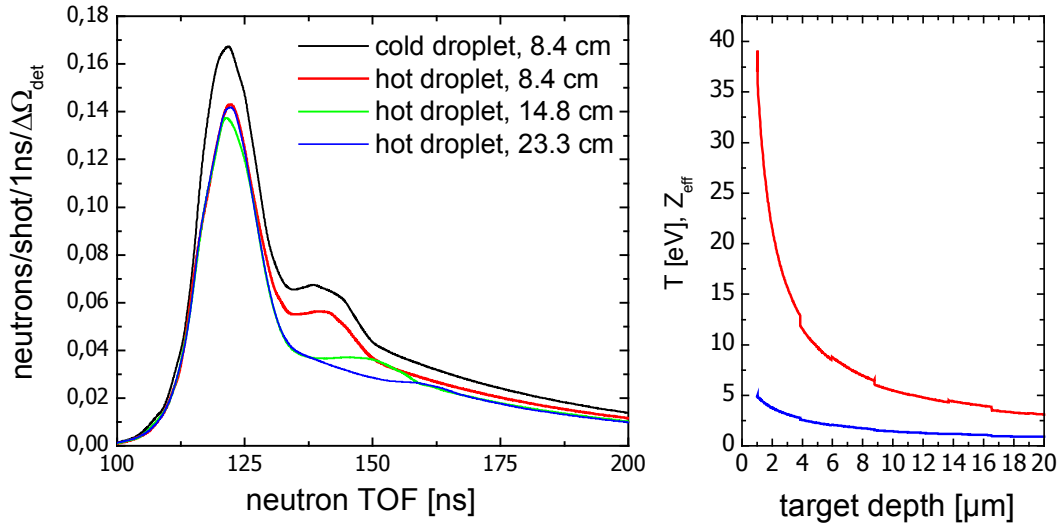
Figure 7.7: Simulated neutron spectra, assuming only front accelerated deuterons, for different catcher distances. The stopping is treated for cold and hot matter (left). The calculated temperature inside the droplet as derived from our simple model is shown right.

tion of 20% laser energy conversion into fast electrons (T_{hot}=1.47 MeV given by ponderomotive scaling), which are streaming into the target under 2π solid angle, leads to a target temperature of 40 eV close to the focus dropping to 3 eV at the target rear surface. In Fig. 7.7 the calculated neutron spectra for a 250 keV ion temperature are shown for heated and unheated targets and varying catcher distance. Only ions from the laser focus are taken into account.

7.4.2 Modeling of the Second Peak

Having ruled out above that ions accelerated in the laser focus can penetrate the droplet and induce a significant amount of neutrons in the catcher target, we can now confirm that the second peak cannot be caused by these ions, but is due to a second, different ion population. They have to be accelerated off the droplet rear surface by large electric fields, most likely caused by the TNSA mechanism (see Chapter 2, Section 2.2.4). We will now investigate whether this mechanism can explain our findings. According to TNSA, hot electrons from the laser focus penetrate the target and exit at the rear surface. They cannot escape into vacuum due to the charging-up of the droplet and form an electron cloud at the surface of the target. It extends approx. one Debye length into vacuum and sets up a strong field ($\sim$1 TV/m) at the rear surface:

$$E_{stat} \approx kT_{hot}/e\lambda_D \quad , \quad \lambda_D = (\epsilon_0 kT_{hot}/e^2 n_{e,hot})^{1/2}. \tag{7.1}$$
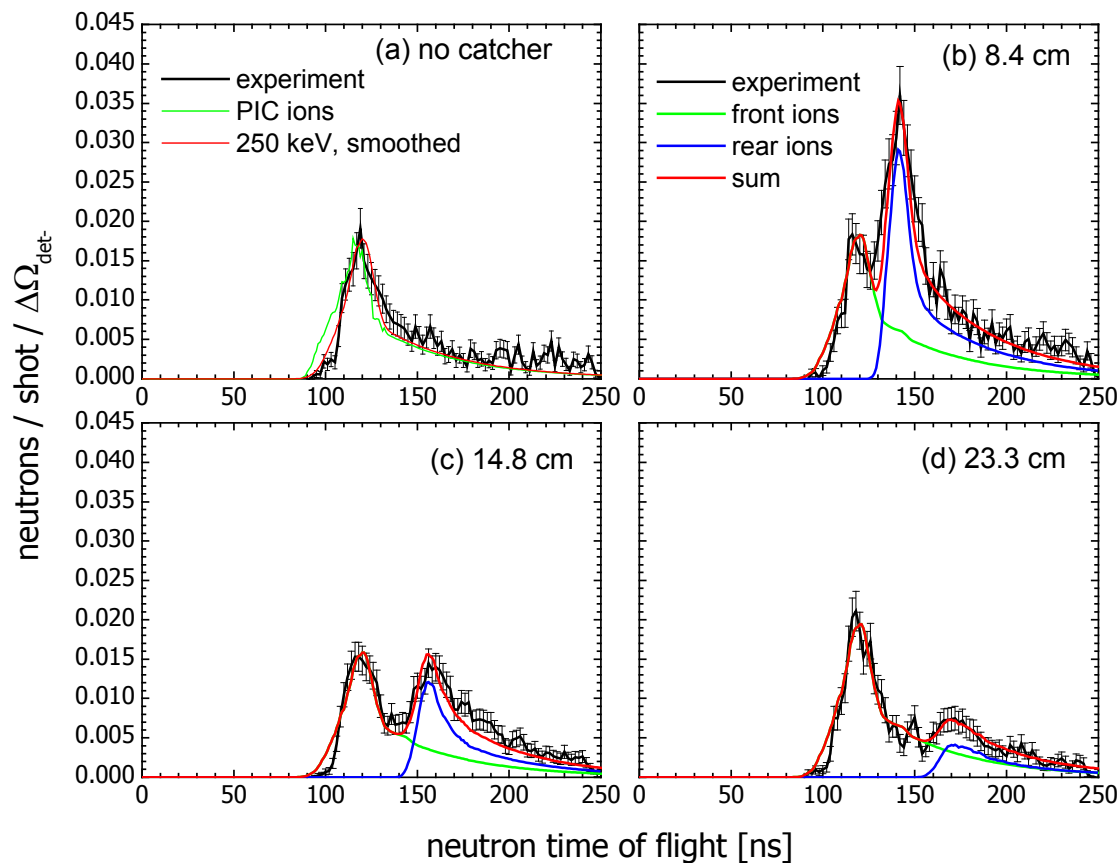
Figure 7.8: Neutron TOF spectra without catcher (a) and different catcher distances (b) 8.4 cm, (c) 14.8 cm, and (d) 23.3 cm. The smooth lines show simulations for ion emission of and T_i,=350 keV from the front (green) (see Fig. 7.6) and T=100 keV (b,c) or T=110 keV (d) off the rear surface (blue). The sum spectrum is plotted red.

The lateral spread of the cloud depends on the divergence and the transport of the electron beam passing the target, which are not well known. The droplet is isolated from the environment and electrons are bound to it by space charge fields, so they distribute quickly around the surface. Thus a more or less uniform electron halo forms around the droplet. This would lead to a 4π (quasi-rear surface) acceleration.

Assuming an ion acceleration into 4π, we can now use MCNEUT to calculate the catcher fusion spectrum for different ion temperatures. The resulting spectra are shown in Fig. 7.8(b,c,d), together with the model curves for the first peak and the sum spectrum, compared to the experimental results from Fig. 7.6.

The position of the second peak is plotted versus the catcher distance in Fig. 7.9. The experimental values agree well with a temperature of the rear side ions of 100 ± 30 keV. The numbers of ions hitting the catcher which are needed to explain the neutron signals for the three runs are 9.5×10^{10} (8.4 cm distance),
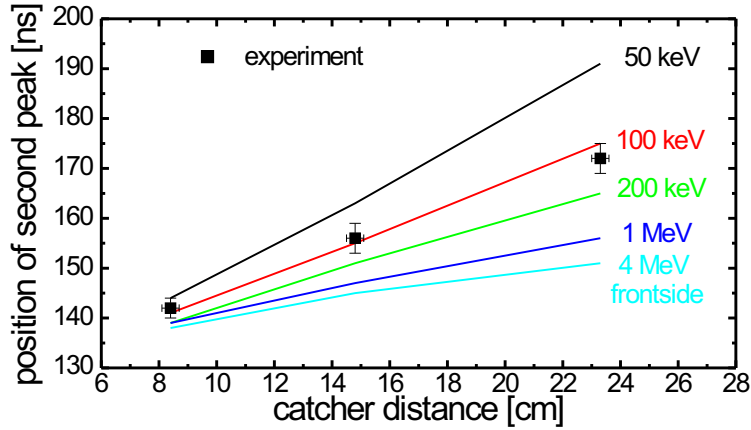
Figure 7.9: Position of the catcher peak for different ion temperatures (model) and experimental data points.

4×10^{10} (14.8 cm), and 1.8×10^{10} (23.3 cm), corresponding to a total number of surface accelerated ions in 4π of 7.5×10^{11}, 9×10^{11}, and 8.5×10^{11}, respectively. Since these values are remarkably close for the three runs, we may conclude that the acceleration into a large solid angle is consistent with our neutron data. The 100-keV temperature seems to be quite low in comparison with other experiments in which TNSA ions were also observed. This discrepancy becomes feasible by heuristically scaling the calculations reported by MacKinnon et al. [65]. For 20-μm planar targets and 100-fs, 10-J, 1×10^{20}-W/cm^2 laser pulses, the velocity of the rear surface was 0.05c, corresponding to $T_i =$1.15 MeV. The accelerating field for TNSA scales with $\sqrt{n_{e,hot}}$, which is the density of hot electrons from the laser focus reaching the target rear surface. For a fixed conversion efficiency of laser light into electrons, the total number N_e of electrons scales with

$$N_e \propto \frac{E_\mathrm{L}}{T_{hot}}. \tag{7.2}$$

.

These electrons reach the rear surface over a time of $\sim \tau_l$ in a circle of diameter $\sim$ target thickness (d_t) in the planar case, leading to an electron density of

$$n_{e,hot} \sim \frac{N_e}{\tau_l \ c \ \pi \ d_t^2}. \tag{7.3}$$

For droplets, the electrons are spreading over the whole surface and the density is reduced to approximately one forth. Overall, this leads to a factor of 9 reduction in accelerating field strength for the Jena parameters as compared to the JanUSP

conditions. Assuming the field duration is the approximately the same under both conditions, this leads to an ion energy of 125 keV, which is reasonably close to the observation.

From the MCNEUT calculations, the number of ions needed to model the measured spectra can also be deduced. The results are listed in table 7.1.

Table 7.1: Ion numbers N_x, temperatures T_x and energy transfer E_x into ions for $x \in (front, rear)$ as determined by the fits to the neutron spectra from Fig 7.8.

d_{catch} [cm]	N_{front} in 2π $\times 10^{11}$	T_{front} [keV]	E_{front} [mJ]	N_{rear} in beam $\times 10^{11}$	T_{rear} [keV]	E_{rear} [mJ]	E_{total} [mJ]
no	0.37	250	1.5	n/a	n/a	n/a	n/a
8.4	0.4	250	1.6	7.5	100	12	14
14.8	0.32	250	1.3	9	100	14	16
23.3	0.4	250	1.6	8.5	110	16	17

It is obvious from the relative numbers that the coupling efficiency of laser light into ions from the rear surface is greater than for ions accelerated in the laser focus in forward direction. The total coupling efficiency into ions within the conditions mentioned above is on the order of 2.5%.

For the first time, this experiment has been able to distinguish between ions accelerated from *both* target surfaces in a *single* measurement. It proves that both acceleration processes take place independently. From the recorded neutron spectra, a quantitative estimate of the ion numbers and temperatures can be inferred in both cases. The output of 3D-PIC simulation postprocessed with MCNEUT is close to the experimental findings for the front surface acceleration.

7.5   Scaling to LULI Conditions

The last campaign at the LULI laser took place in January 2002, a few weeks after the first campaign in Jena. Hence, the double-peak issue was already known, and an attempt was made to get similar results from LULI. The experimental setup was very simple. We focused the laser onto a 30-μm thick $(CD_2)_n$-foil as a primary target. No heating laser was available at the time of this experiment. The catcher made from an array of 5-cm diameter, 6-mm thick $(CD_2)_n$ plastic discs was placed

at 53 cm distance in laser direction. The detectors were located at an angle of 180°
to the laser axis (i.e. in backward direction) to fulfill the following requirements:

1. **Maximize the temporal spacing between the γ-flash and the target
   and catcher neutron signals.** Under 180°, the time-of-flight for ions from
   target to catcher and the neutron TOF from catcher to the detector add up
   fully.

2. **Minimize the effect of angular spread on the spectral shape.** Since
   no ions flying into the detector direction are expected to fuse, only negative
   longitudinal ion velocity components lead to neutrons. For these, the energy
   spread is very narrow.

3. **Minimize the γ-flash for a given shielding** Electrons and γ-rays are
   emitted predominantly in forward direction

The setup is shown on the left side of Fig. 7.10, and the neutron TOF spectrum
on the right side.
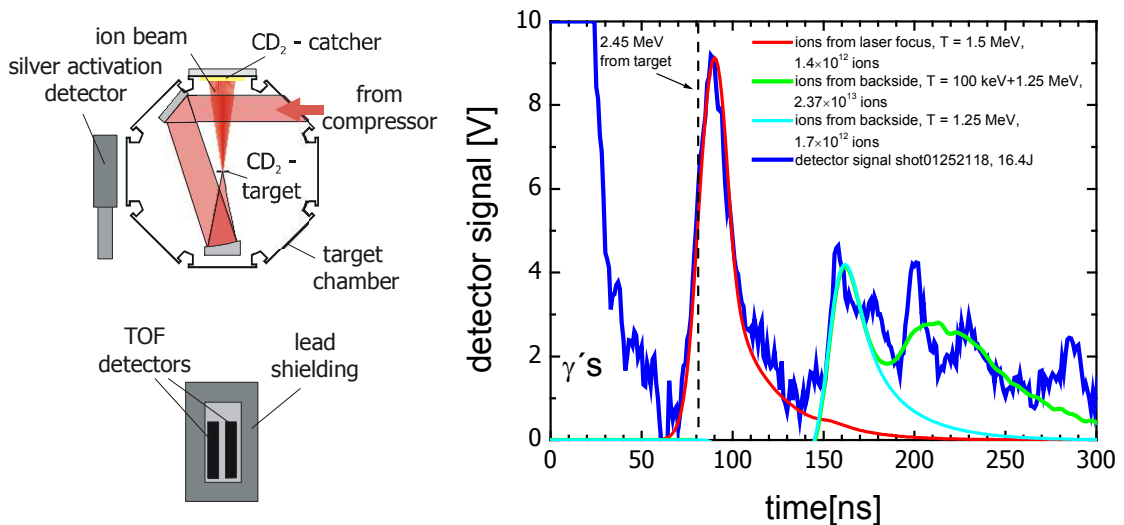
Figure 7.10: (left) Experimental setup for the front- and rear surface acceleration
experiment. Note that the target was unheated, so proton inhibition was a problem.
(right) Neutron TOF spectrum and model calculations.

Analog to the Jena experiment, three main features are evident.

1. A prompt γ-flash is prominent and dominates the spectrum at t=0.

2. An early neutron signal at approx. 90 ns stems from fusion reactions in the
   target itself.

3. A late neutron signal (or a group of peaks) from fusion reactions in the catcher by ions from the rear surface.

These peaks can be modeled with MCNEUT in the following way:

1. **Frontside ions - fusion in the target** The best match for the frontside ion component is achieved with a exponential ion spectrum with a temperature of $T_{hot} = 1.5\pm0.5$ MeV. Unfortunately, the shape of the model spectrum is quite insensitive to the ion temperature, so these numbers are only a rough estimate. Since the total number of ions needed to explain these spectra is a steep function of the ion temperature, its determination is also quite inaccurate. Due to the higher temperature more ions can penetrate the target than in Jena, but the bigger distance of the catcher and its smaller solid angle lead to a negligible signal from those ions fusing in the catcher. Also the effect of target heating is of only minor importance (see section 4.2.2, Fig. 4.6)

2. **TNSA-accelerated ions - catcher neutrons** The second peak exactly matches a 1-MeV deuteron temperature, while the later ones can be described by a 100-keV deuteron component. These values seem low in comparison to typical proton temperatures, but the shot was made without laser heating the target surface, so proton poisoning was certainly an issue. Consequently, the late neutrons could also be caused by protons breaking up the catcher deuterons. For this reaction, no differential cross-section is available, so a modeling is not possible. The spectrum-integrated total cross-section is of the same order of magnitude as the d-d fusion cross-section (see Fig. 3.2, so the neutron numbers are plausible.

For those best-match temperatures, the modeling parameters are as follows.

If the spectra are described by the formula

$$N(E) = \frac{E_{tot}}{kT_{hot}} \cdot e^{-\frac{E}{kT_{hot}}} = N_{hot} \cdot e^{-\frac{E}{kT_{hot}}}, \qquad (7.4)$$

where E and kT are the individual ion energy and hot temperature in MeV, E_{tot} is the total energy content of the ion population, and N_{hot} is the number of hot ions, one needs $N_{hot} = 1.5\times10^{12}$ ions with T_{hot}=1.5 MeV and to explain the target fusion peak. This assumes a broad emission angle of $60°\pm25°$ to the laser axis, which is justified by the PIC simulation for the Jena case, and also by

the fact that there is a certain amount of blue-shifted neutrons in the spectrum (the time-of-flight for 2.45 MeV neutrons is marked in Fig. 7.10) which stem from ions with a velocity component in detector direction. The numbers stated above correspond to an energy content in the frontside hot ion population of 360 mJ, which translates to a conversion efficiency of 2.1%. This value is very similar to the ATLAS result, whereas in the Jena case the low efficiency of 0.5% might be caused by a discrepancy of hits which emit γ-rays and good hits for ion acceleration. Unfortunately, it was not possible to perform 3D-PIC calculations analogue to the Jena case for the LULI laser parameters, since the computing time requirement would be excessive because of the comparatively long pulse duration and large focus diameter. This is, nevertheless, a very interesting task for the future, when more computing power will be available.
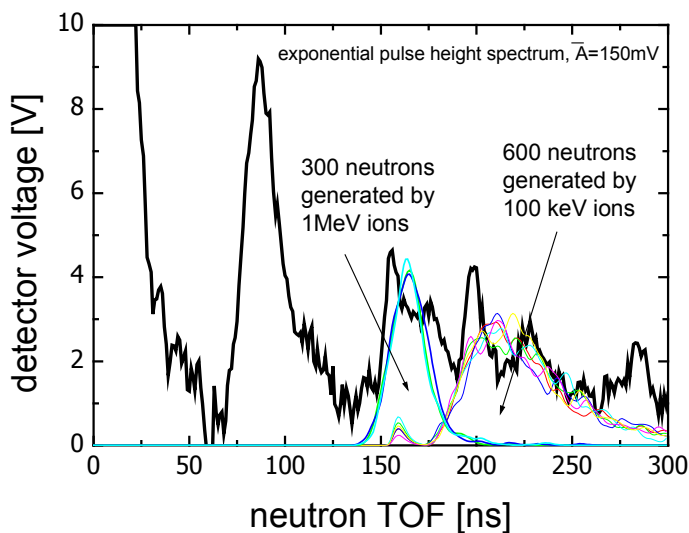
Figure 7.11: Model calculations of the rear TNSA accelerated ions. For each neutron hitting the detector, a pulse shape corresponding to a single neutron hit with a statistical pulse height following exponential pulse height distribution is added to the simulated spectrum. This was done for a number of times. The statistical fluctuations are much smaller than the features of the experimental spectrum.

For modeling the rear surface acceleration a two-temperature spectrum is necessary where the low-temperature component accounts for the late signals. A total of $N_{hot} + N_{cold} = 4.74 \times 10^{13}$ ions in a cone of 17° opening angle with T_{hot}=1.25 MeV and T_{cold}=100 keV (or protons) is necessary to explain the tail of neutrons at late times (green curve in Fig. 7.10). Recalling that this shot was made with an *unheated* $(CD_2)_n$ plastic target, the protons quench much of accelerating fields for the deuterons. Therefore, the temperature is much lower than for pure protons (see [37]). The 17° are derived from RCF measurements of proton beam divergences from other shots. Of course, if the divergence angle is greater than the solid

angle of the catcher, it affects the total number of ions needed to explain the data. The hot component alone amounts to $N_{hot} = 7.5 \times 10^{10}$ ions and yields the light blue curve in the spectrum without the 100 keV component. Note that in this case also much more ions are accelerated from the rear surface, while having a lower temperature than the front component. But since on this shot proton inhibition was certainly an issue, the lower energy at the rear surface should not be taken literally. It is therefore necessary to repeat this experiment with a clean target rear surface.

The apparently statistics-dominated low-energy tail of the time-of-flight spectrum poses the question whether this result and its analysis are significant. To clarify this point, the single-neutron response of the TOF-detector was measured at ATLAS to be approx. 150 mV in 6-7 ns pulses, leading to a total charge of approx. 20 pC per neutron. From that (and from neutron yields calculated with reasonable numbers of deuterons in the beam) follows that the features in the spectrum consists of several hundred neutrons. With this knowledge, a second simulation can be made taking into account the neutron statistics and the spectral modulation arising from that. The result is shown in Fig. 7.11 and shows that the statistical fluctuations are much smaller than the measured features, which therefore may indeed be real and represent structures in the ion beam. They loosely remind of structures found in the film-recorded proton spectra taken with the magnetic spectrometers. While it is perhaps too early to make a firm claim based on one shot that the peaks in the neutron spectrum are closely related to a corresponding structure in the ion population, it is certainly justified to scrutinize this phenomenon in future experiments. Nevertheless, the energy peaks in the neutron spectrum are interesting because they may contain information on the ionization dynamics of the expanding Debye sheath in the frame of the TNSA model (for more information, please refer to M. Hegelich's PHD thesis [37]).

Comparing the LULI and Jena results quantitatively is difficult because of three factors:

- Proton inhibition and differences in target shape (see 7.4.2) lead to difficulties in comparing the rearside ion temperatures.

- The frontside ion temperature can only be determined with a large error, especially in th LULI case, due to uncertainties in ion beam divergence. This severely restricts the accuracy of any statement made for the ion numbers.

- The true beam divergence and possible beam inhomogeneities are hard to measure, which strongly affects the total number of rear side accelerated

ions.

The following analysis therefore is based only on neutron yields and the parts concerning parameters of the ion beam are based on the best estimates.

For getting a rough estimate for the efficiency of the both acceleration mechanisms, it is instructive to look at the neutron yields per Joule detected in the LULI vs. the Jena case for both populations separately. In Fig. 7.12, these numbers are plotted versus the laser energy.
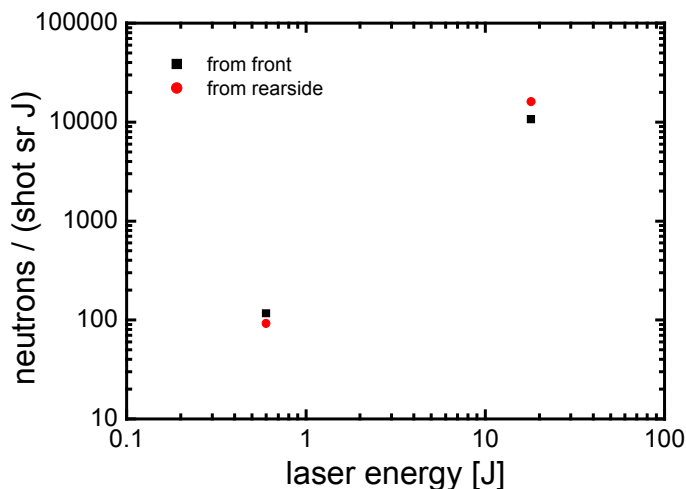
Figure 7.12: Comparison of the neutron yields per shot for front- and rearside accelerated ions in the Jena and LULI cases.

Whereas in Jena more neutrons in were produced by the frontside component, in LULI the situation reverses and the neutron yield for the rearside component dominates. This is understandable, because in LULI the ratio of catcher solid angle and beam solid angle was larger, but also hints at a more efficient TNSA-acceleration (at least in the forward direction).

Comparing the hot temperature of the front side ions, the difference amounts to a factor of 5. This cannot be explained by the small difference in intensity between the two cases, because according to the ponderomotive scaling law the temperature scales only with $\sqrt{I_{Laser}}$. The best estimate temperature at LULI is well explained by equation 2.24 for intensities of $6 \times 10^{19} \mathrm{W/cm^2}$ and $\alpha < 1$, whereas the temperature measured at Jena is far below that. A probable reason for this is already described in Section 2.2.1. Since the double layer at the critical surface needs a finite time to form, very short laser pulses like at Jena might not be able to fully reach the double-layer regime, and the pulse is already decaying when the layers start to form. However, this is just a speculation, which will be clarified as soon

as 3D-PIC calculations for long ($\sim$400 fs) pulses can be performed. Nevertheless, it fortifies the basis for a future new theory, which takes into account not only the ion energies and temperature, but also their total numbers in dependence of the laser energy and pulse duration.

Chapter 8

Conclusion and Outlook

Various aspects of generation and spectroscopy of high-intensity laser produced neutrons were studied in this work. As a whole, they answered many questions about the neutron yield expectations, production mechanisms and underlying plasma phenomena like ion acceleration. On the other hand, they left some new open questions and opportunities for further research.

The first and most fundamental result of this work was the first demonstration of high neutron yields (several 10^4 n/shot) from a table-top laser. Only by this achievement enough neutrons were generated to enable further research like neutron spectroscopy to clarify the neutron production mechanisms. The key to this success lay in our laser development efforts, mainly the installation of an adaptive optics system at the ATLAS-10 laser, which pushed the laser intensity from 10^{18}W/cm² to 2×10^{19}W/cm² in $\sim$700 mJ, 160 fs pulses. Only after completing this work, it was possible to do systematic and reproducible studies of laser-driven neutron generation, whereas before that, the results were quite unstable. Moreover, due to the higher intensities reached with the better focusing, the neutron yields could be improved by a factor of 3-5.

8.1 Neutron Source

Complementary to current reactor- or radioisotope- based neutron sources, a laser driven neutron source offers a number of unique features that make it potentially interesting for a number of applications. In contrast to the former, it is inherently safe and can be switched on and off with no further complications. Moreover, when using front accelerated ions, the source size is only given by the range of fast ions

in the target material folded by size of the focal spot (($\sim 10\mu m^3$,) and its duration is governed by the time the ions need to stop folded with the laser duration ($\sim$ps). This makes these laser plasmas the most brilliant fast neutron source built so far in the laboratory. Especially the small source size might substantially increase the resolution in fast neutron radiography and/or tomography. The short neutron pulses emitted by our source open new opportunities for investigating dynamic processes, and the possibility for triggering them by firing the laser at any chosen time further facilitates their successful use for special applications. We found that with laser energies between 500 mJ and 700 mJ, up to 25000 n/shot could be generated by focusing the laser onto a deuterated plastic target or heavy water droplets. This yield to our knowledge is the highest so far measured with a table-top laser, and is substantially higher than other experiments done at slightly lower laser energy [66, 14]. The difference can be understood from the laser parameters, especially the focusability or the use of an entirely different target in the case of [14]. From experiments and also from theory, it became quite clear that for our laser and the d-d fusion reaction this yield is the maximum that can be expected. 10^4 neutrons/laser are enough for doing neutron spectroscopy by accumulating many shots, but for any kind of source application the yield has to be improved by at least 3-4 orders of magnitude. The LULI-experiments proved that these numbers can be achieved with a moderate increase in laser size and the measured yield indeed almost reached the desired 10^8 neutrons/per shot. In comparison to the ATLAS experiments, the specific neutron yield (neutrons/laser energy) obtained at LULI was higher by 1-2 orders of magnitude.

It is difficult find a good scaling law at even higher laser energies and/or intensities, since the experimental data is sparse, and the PIC calculations could not be performed for longer pulses than for the ATLAS. The existing analytical models only make a very vague statement about the achievable ion energies, and exclude all pulse duration and laser energy scaling related effects. Most of them are one-dimensional and hence make no statement at all about the angular divergence of the ion beam, and conversion efficiencies are mostly not included. In the case of ions from the target rear side, the situation is even worse. The only available analytical model focuses on the ion energy only, while numerical models taking into account the actual laser-plasma interaction are scarce.

This situation was improved by combining the experimental, numerical and analytical results from this thesis. For short pulses, 3-D PIC calculations can quite well describe the ion acceleration mechanism in the laser focus, while for longer pulses and/or laser energy they are restricted by computing power. In

those cases the analytical model by Wilks and Pukhov [27, 28, 23] might give quite good results as indicated by the ion temperatures measured at LULI. The model delivers the ion energy, while the numbers are given by the fact that the laser energy conversion into ions is fairly constant above a certain intensity threshold. The angular divergence of the ions in very intense laser-plasma interaction seems to be more radially directed because of the deep hole-boring action. All these factors together now allow a fairly accurate prediction of neutron yields achievable with *front-side* accelerated ions at petawatt class lasers. As an example, we consider the following cases:

laser system	pulse energy [J]	pulse duration [fs]	spot size [μm]	focus intensity [W/cm^2]	ion temp. [MeV]	ion number
ATLAS	0.6	160	5	1.91×10^{19}	0.25 (exp.)	3×10^{11}
LULI	20	400	9	7.86×10^{19}	1.94	1.94×10^{12}
VULCAN	50	600	9	1.31×10^{20}	2.5	3.75×10^{12}
PW	500	600	10	1.06×10^{21}	7.11	1.32×10^{13}

The values for pulse energy, duration and the spot size are chosen in order to represent the properties of the example systems. From that the focus intensity can be easily calculated, and using equation 2.24 for absorption α=1 yields the corresponding ion temperature (in the case of ATLAS the experimentally determined temperature is used, since it does not obey the scaling of equation 2.24). Assuming 2-3% conversion efficiency of laser light into fast ions, from the total available laser energy and the ion temperature we can estimate the number of fast ions. By calculating the thick-target neutron yield for an exponential ion spectrum from equation 5.1, the average neutron yield per ion for various ion beam temperatures can be determined. These functions are plotted at the left side of Fig. 8.1 for a number of relevant neutron production reactions. Using their value for the above determined ion temperatures and multiplying it with the number of fast ions provides the desired neutron yields for the different laser systems, as shown on the right side of Fig. 8.1.

It becomes clear that the d-t fusion reaction would be the ideal candidate for achieving high yields at low laser energies and intensities, but the radioactivity of tritium makes this source difficult to handle. Moreover, due to the pronounced low-energy peak in its cross-section the advantage of d-t is melting down at high laser intensities and hence high ion temperatures. With d-t, a neutron source
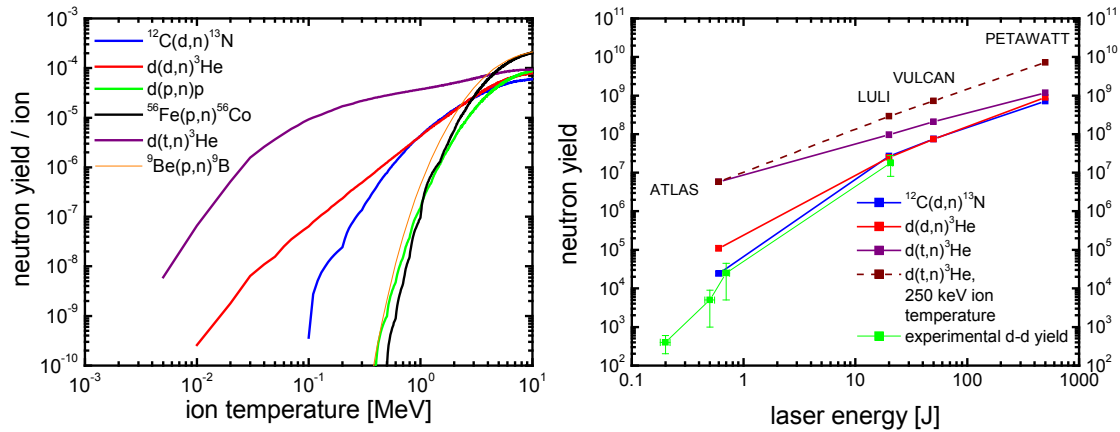
Figure 8.1: (left) Neutron yield per ion for different ion beam temperatures and source reactions. (right) Scaling of the expected neutron yield for frontside ion acceleration for different laser parameters as given in table 8.1. For comparison, the experimentally achieved yields from the d-d fusion reaction from frontside accelerated ions in bulk solid targets is also plotted here.

delivering 10^8 neutrons/s could be built already now with state-of-the-art, 10Hz, few-J Ti:Sapphire lasers. Since the slope of the d-t curve is quite shallow, simply upgrading the laser energy does and keeping the tight focusing only moderately improves the neutron yield. By deliberately defocusing the laser to keep the intensity and hence the ion temperature low, almost one order of magnitude in neutron yield can be gained, as is shown in Fig. 8.1. With a future 10 Hz Petawatt laser, a neutron source with 10^{11} neutrons/s can be envisioned. D-T also offers the advantage of high neutron energy at low ion energies, which leads to a relatively small kinematic spread of the neutron time-of-flight, therefore maintaining a short neutron pulse duration over a relatively long flight distance.

With other neutron production reactions than d-t, the expected yields have to be reduced by one to two orders of magnitude for the same laser energy.

Unfortunately, for *rearside* accelerated ions no good model exists up to date, but the experimental results from both LULI and Jena suggest that even higher neutron yields can be expected from them. Since it is difficult to accelerate pure deuteron beams from the rear surface of solid targets, proton-induced reactions offer perhaps the best prospects for achieving high yields. Especially for high energy protons, some reactions exhibit exceptionally high cross-sections, like $^{56}Fe(p,n)^{56}Co$ and $^9Be(p,n)^9B$. However, these neutrons are not monoenergetic.

All in all, many roads lead to Rome, which is perhaps the best way of describing the great variety of possible laser driven neutron source configurations. Relying

on front-side accelerated ions yields the smallest possible source sizes and durations, whereas the rear-surface accelerated ion beams have the greater potential for reaching high yields, while their source volume and duration are given by the lateral and temporal spread of the beam on its way to the catcher. The next step to realizing such a source is to build the necessary laser capable of delivering a few 10 J pulses with a repetition rate of 10 Hz, and find reliable ways of generating pure deuteron beams, which may include the development of a planar, 20-50μm thick heavy water jet target.

Hopefully in the meantime the neutron user community will devise new applications for such a laser source. As already mentioned, the source size offers intriguing possibilities for radiography applications, and especially the d-t reaction delivers the ideal neutron energy for damage-testing fusion reactor materials. However, the mainstream of neutron research today is done with thermal neutrons. Fast neutrons, in contrast, are able to penetrate large volumes of material, making them ideally suited for investigating thick samples of matter. Here, the problems lie more on the detector side, since highly temporal and spatially resolved fast neutron detectors are not yet developed, and with some hope in the next years more research will be devoted to these problems.

8.2 Plasma Diagnostics

As mentioned above, only the achievement of considerable neutron yields with a table-top laser enabled the application of neutron spectroscopy to get information on the laser-accelerated ion population, and therefore on the basic acceleration processes in the laser-plasma interaction. These results were compared with current theories and provided important input for their modification. Despite of the large uncertainties in absolute neutron yield, relative measurements helped to clarify some important points concerning the laser ion acceleration mechanism.

The directionality of ions accelerated in the laser focus was investigated in a number of experiments, and strong hints were found that the ratio of the focal spot to the preplasma scalelength determines the preferred ion emission direction. In the case of a large laser focus and hence low prepulse intensity, the ion emission seems to be directed into the target or at least isotropic, because the laser exerts its push onto a fairly large area and a steep density gradient, generating a quasi-1-D situation. As focal spot diameter is reduced, the laser intensity increases, and the laser bores deeply into the now more pronounced preplasma. Now the neutron

spectra can be better explained by assuming a radially directed ion acceleration from the walls of the hole-boring channel dug into the overdense preplasma. This picture is confirmed by 3-D PIC simulations performed for the laser parameters encountered in the experiment. It may be of some importance for optimizing the neutron yield in a particular direction for source applications, and agrees qualitatively with results from Disdier [13]. Varying the preplasma scalelength instead of the laser focus diameter should in principle cause the same effects. Hence an experiment was performed to investigate its influence on the spectra, which gave results that are not yet fully understood, but may hint at a snow-plough action of a fs-prepulse sitting on top of a long ASE background, in a sense that the short prepulse actually removes the preplasma generated by ASE instead of creating more of it.

In the experiments performed at the LULI-laser, it soon became clear that the most efficient ion acceleration under these laser conditions takes place at the rear side of thin foil targets, and that proton and heavy ion beams of up to several ten MeV maximum energy were created with intriguing characteristics [36, 37, 64]: Very low emittance, full space charge compensation, high directionality. These beams are very interesting for neutron production. Because of their high energy, one is not restricted to the low threshold of the d-d or d-t fusion reactions, but can employ other source reactions as well. It was demonstrated that the highest neutron yields could be achieved by stopping this proton beam in a secondary target, and that the obtained time-of-flight spectra could be modeled by the Monte-Carlo code in cases where the differential (p,n) cross-section of the secondary target material was known. Here the strong enhancement of the neutron yield compared to the ATLAS laser enabled us to obtain neutron spectra in a single shot. The angle-resolved yield measurement also showed that the d(p,n)p reaction exhibits a particularly strong forward peak of the emitted neutron distribution, making this reaction interesting for source applications as well as to determine the proton content in a mixed proton-deuteron beam. These mixed deuteron-proton beams were the main obstacle to achieve quasi-monoenergetic neutrons from the d-d-fusion reaction, since protons from surface contaminants are accelerated predominantly off the rear target surface and quench the accelerating field for deuterons.

The output of the PIC simulations were postprocessed by a newly developed 3-D Monte-Carlo neutron production code to prove their general agreement with the experimental data. Alternatively, this code was used to tailor arbitrary ion distributions for best match with the experiment.

8.3 Future Experiments

The success in operating the neutron spectrometers at a number of different high-intensity laser environments makes confident that laser-generated neutrons will be used as a routine diagnostics tool for relativistic laser-plasma interactions in the future. A number of open questions can be addressed only by neutrons:

- **Determination of the preplasma conditions in the overdense region:** As mentioned in Chapter 5, the preplasma scalelength might have an influence on both the ion acceleration mechanism and the subsequent neutron production by means of providing fusion partners for outgoing deuterons. Especially for understanding the details of the frontside ion acceleration mechanism the knowledge about the plasma gradient is an important piece of information. The scalelength in the overdense region can neither be directly measured nor modeled adequately in three dimensions. Neutron spectroscopy might be able to experimentally determine is value. By simultaneously measuring the outgoing ion spectra under different angles and the neutron spectrum in line-of-sight perpendicular to the target plane, the column density of the preplasma along this line can be determined. By assuming an exponential density slope, this yields the plasma gradient. (See Fig. 8.2)
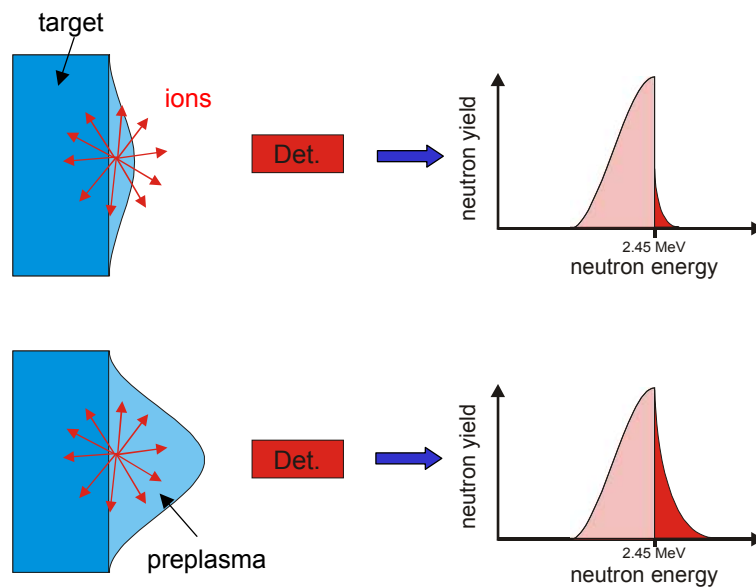
Figure 8.2: A long, dense preplasma will generate neutron events with a blueshifted energy for the indicated detector and target positions.

- **Determination of bulk ion acceleration [67]:** As indicated in chapters 4, 6 and 7, the electron transport in insulator targets is not yet well un-

derstood. The high current density of the electrons penetrating the target material may lead to anomalous electron stopping phenomena like magnetic and space-charge mediated inhibition. Especially the latter mechanism results from the building up of large space charge potentials by the large uncompensated charge moving inside the non-conducting target, which hinders further current flow. These space charge fields can grow so high that they in turn can field ionize and accelerate bulk ions deep inside the target itself. Since these ions are inaccessible to any other spectroscopy method, they have to be characterized in situ. Neutrons are a perfect tool for that task, since they would witness every fast-moving deuteron inside a deuterated plastic target. The experiment can be done by putting a sufficiently thick protective layer of non-deuterated material on top of the deuterated plastic in order to ensure that no deuterons are accelerated in the laser focus itself. Any measured fusion neutron yield can such be attributed to ions accelerated in the bulk of the target. It would also be very interesting to look for a kinematic shift of these neutrons in order to determine whether the bulk acceleration is directed of not.

- **Theoretical Work:** In addition to giving impulse to new experiments, this work has also triggered questions about the precise mechanism of frontside ion acceleration and its comparison to the rearside ion component. Since for both of them the theoretical description is far from being complete (neither analytical solutions for the laser energy and pulse duration dependence nor three-dimensional numerical results for long pulses are available), a combination of experimental efforts by to scale the front-rearside comparison presented here to higher laser energies and/or different pulse durations and theoretical studies is needed to understand all details of laser-induced ion acceleration. In the theoretical part, especially a series of full-3D PIC simulations is necessary to establish a reliable scaling of the ion beam parameters in dependence of the laser parameters. It certainly is interesting to look further into the pulse duration scaling of the frontside acceleration, especially for ultrashort pulses, where the double layer formation is not the dominant mechanism. Since most experiments today are done with single-shot lasers that exhibit large pulse-to-pulse fluctuations, systematic parameter studies of the phenomena described here are scarce. The missing knowledge has to be retrieved from numerical studies, which certainly will benefit from the steadily increasing computational power available to the scientist.

Appendix A

ATLAS Development

A.1 The ATLAS System

ATLAS is a Ti:Sapphire short-pulse, high-power laser system capable of delivering infrared 150-fs duration pulses of up to 7-TW peak power ([68]. The active medium used in this type of lasers is a titanium doped sapphire crystal. This material is is characterized by its very broad amplification bandwidth from approx. 650 - 1050 nm, supporting the amplification of pulses as short as less than 10 fs, and its broad absorption band in the visible, making it suitable to a wide variety of pump sources. Due to its high quantum efficiency and good heat conductivity, relatively high repetition rates are possible at substantial energy. At the very high light fluxes achievable with the stored energy and supported pulse durations of this material, problems arise due to nonlinear effects upon propagation in matter. Self-phase-modulation (SPM) modifies the spectral composition and leads to a lengthening of the pulse whereas small-scale selffocusing (SSSF) gives rise to hot spots destroying optical components. Only the invention of the so called Chirped-Pulse-Amplification (CPA) - technique by Strickland and Mourou ([1]) has avoided these problems and lead to an excursive increase in available laser power.

This is achieved by a combination of temporal stretching and recompression of the pulse before and after amplification. The pulse is generated with low energy and a duration of 100 fs, gets stretched by a factor of 10^4 to 10^5 and only then is amplified and transported though transmissive components, now having a duration as in a classical "long-pulse" - laser. At the end of the amplifier chain and behind all transmissive components, the pulse is recompressed temporally and is then available as an energetic, high-power pulse.

This scheme is employed in the ATLAS system. A COHERENT Mira-900 master oscillator pumped by an Argon ion laser delivers a pulse train consisting of 100-fs pulses at a central wavelength of 790 nm, a bandwidth of 8 nm and an energy of approx. 2.5 nJ with a repetition rate of 86 MHz. These pulses are stretched to a duration of 200 ps in a grating stretcher. This device consists of two antisymmetrically oriented gratings between which two confocal positive lenses are placed. The distance of one grating to its nearest lens is below the focal length of the lens. Each frequency component of the pulse is sent through the stretcher along different trajectories. This makes the red part of the pulse spectrum leave the stretcher before the blue part, leading to a temporal stretching of the pulse, without changing its spectral shape. In principle, by passing these stretched pulses through the compressor consisting just of two parallel gratings and exhibiting a dispersion exactly opposite to that of the stretcher, it is possible to fully recompress the pulse to its original duration. In reality, the amplification slightly changes the spectral composition of the pulse as well as its wavefront, so that a full recompression is not achieved in real systems.

Having generated the train of stretched pulses with a few nJ energy in each pulse, amplification to higher energies is achieved by an amplifier chain. Before that, the repetition rate is reduced from 86 MHz down to 10 Hz by a system of two Pockels cells and three polarizers. The first amplifier in the chain consists of a regenerative amplifier (RGA) in form of a linear cavity. The pulses are coupled in and after 13 round trips out of the resonator by a Pockels cell and two polarizers at a well defined time. Amplified to an energy of approx. 10 mJ, the pulse is then cleaned from unwanted prepulses by two more Pockels cells. The prepulses arise in the amplifier from light leaking out of the cavity after the 11th and 12th pass, and would lead to an unwanted preplasma formation at the target surface. After the RGA the pulses are fed into the first bow-tie multipass amplifier (MPA), where they are intensified in four passes in a 18-mm Ti:Sapphire crystal to approx. 360 mJ. This crystal is pumped by twin 800-mJ frequency-doubled green Nd-YAG laser pulses of 6-ns duration generated in two Coherent Powerlite pump lasers. The pulse is then recompressed to a duration of approx. 130 fs by a grating compressor with a transmission efficiency of 70%. Together with an energy of 250 mJ after compression this yields a 2-TW laser pulse at 10-Hz repetition rate. Due to its high intensity of close to 100 GW/cm^2, the pulse has been transported in a vacuum beam line to the target chambers in order to avoid serious degradation in beam quality arising from SSSF and SPM. The laser described so far is called the ATLAS-2 laser and represents the low-power version of the ATLAS system. Since the power of 2 TW is only sufficient to see a few neutrons, most of the

experiments were carried out using the high-power version of ATLAS. It has an additional multi-pass amplifier that was still under construction at the beginning of this work. In the following section, this so called ATLAS-10 amplifier stage will be described in some detail along with some problems encountered during operation.

A.1.1 ATLAS-10
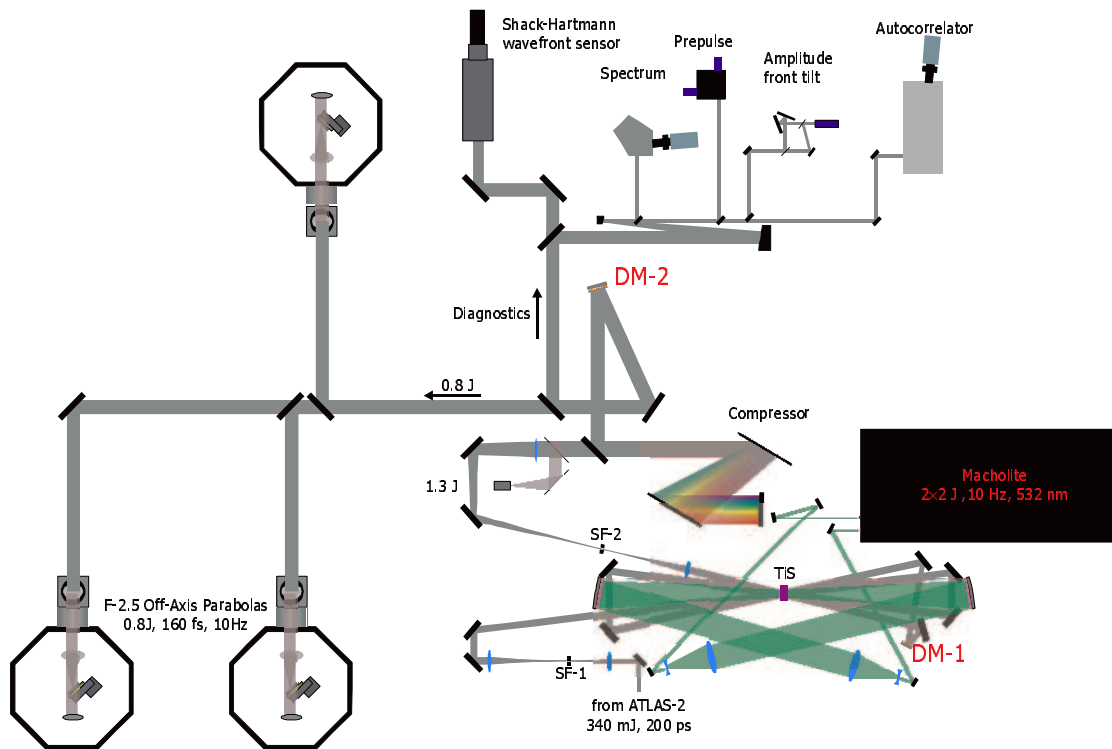
Figure A.1: ATLAS-10 amplifier, beam diagnostics and target chamber setup

The 360 mJ pulses from the first multi-pass amplifier, instead of being recompressed and used for experiments, can be further amplified in a second multi-pass amplifier using four passes in a 40-mm Ti:Sapphire crystal to an energy of around 1,3 J, and compressed in a second vacuum compressor with gratings of 25-cm diameter. After cleaning the incoming pulse of high-order aberrations in a vacuum spatial filter, the beam is enlarged to 18-mm diameter before it is amplified in the same bow-tie setup as in the first multi-pass amplifier. This stage is pumped by twin 2-J, 532-nm, 6-ns long green pulses at 10 Hz from a Coherent Nd-YAG laser. The pump profile (as in the first stage) is smoothed by honeycomb integrating mirrors in order to get a homogeneous pump flux in the crystal. Unfortunately, the crystal exhibits severe defects due to a poor growth process, which strongly

reduces the optical quality of the crystal even when not pumped. This situation worsens when the crystal is pumped due to thermal lensing and birefringence causing severe wavefront aberrations already after the third pass. A few meters downstream from the last pass, the near field intensity distribution shows two intense hot spots, endangering optical elements downstream. Even after expanding the beam to 65 mm through a second vacuum spatial filter, the large and expensive compressor gratings with a damage threshold of only 120 mJ/cm^2 are at risk, since the maximum flux of the near field in the grating plane amounts to 300 mJ/cm^2 at an energy of 1.3J. (Fig. A.2 a). The problem could not be resolved by cooling
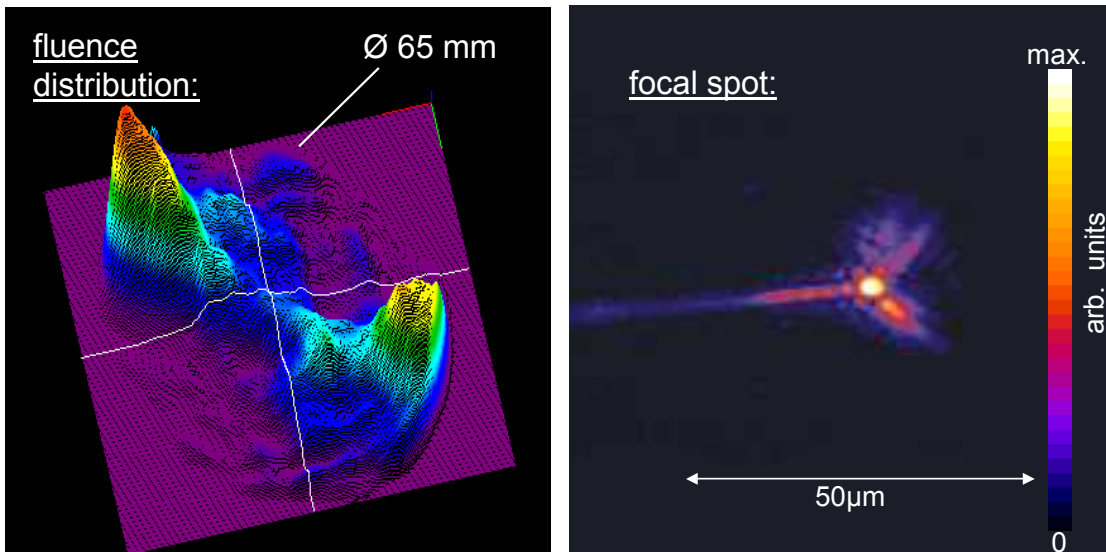
Figure A.2: Intensity distributions of ATLAS-10 beam at full energy without adaptive optics: (a) near field (b) far field

the crystal to -30 °C, so the energy in the beam had to be kept as low as 600 mJ at the compressor entrance, translating to an output energy of 360 mJ (only at a measured throughput of 60%). Due to the strong wavefront aberrations, the focusability of this beam turned out to be poor. Focused intensities of 10^{18} W/cm^2 could not be exceeded(Fig. A.2 b). However, even with less intensity compared to ATLAS-2, just by increasing the beam energy by about 50%, the neutron yield could be increased by about an order of magnitude in first experiments with this laser.

A.1.2   Adaptive Optics

To cure the relatively poor performance of the ATLAS-10 upgrade, an adaptive optics system was developed and installed at the ATLAS facility [68], since the
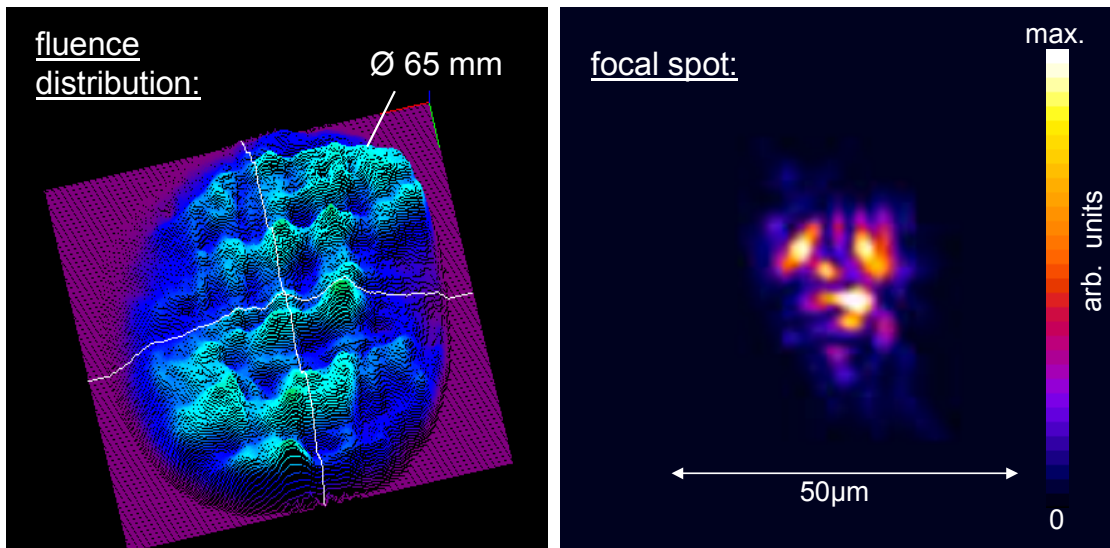
Figure A.3: Intensity distributions of ATLAS-10 beam at full energy with first deformable mirror operating: (a) near field (b) far field

delivery time and conditions for a new crystal proved prohibitive. A large part of the work done in this thesis was related to get this system up and running, so I will give a brief introduction to it, pointing out the main differences and novelties compared to other, existing systems. The work was done in collaboration with Dr. Kudryashow's group at the Laser Research Center of the Russian Academy of Science, who delivered the hardware and software for the system. Mr. Baumhacker and Prof. Pretzler of our group designed the system in close collaboration with the russian group and the PHD students working at ATLAS-10. Initially the hope was to be able to correct for the wavefront and the near field profile errors by a single 30-mm diameter bimorph deformable mirror with 17 electrodes and a dielectric coating placed closely to the source of the aberration, i.e. the crystal, but in a simple four pass bow-tie geometry it is only possible to insert the mirror into one arm. If the wavefront curvature radius is on the order of one pass, the mirror is no longer close to the source of the aberration, but in propagation from the crystal to the mirror will pick up intensity fluctuations. Fig. A.3 shows the intensity distribution in the grating plane with correction by this first adaptive mirror in comparison to Fig. A.2. The peak beam loading at a beam energy of 1.3 J drops from 300 mJ/cm^2 to 90 mJ/cm^2, which can be safely transmitted through the compressor. Fortunately, the correction voltages that have to be applied on the electrodes can be found by trial and error rather quickly and and remain stable for many weeks to months. With this single mirror, it is now possible to use the full energy of the ATLAS-10 laser, but as expected the wavefront modifications introduced by its operation further deteriorates the focusability of the beam (Fig. A.4). This made
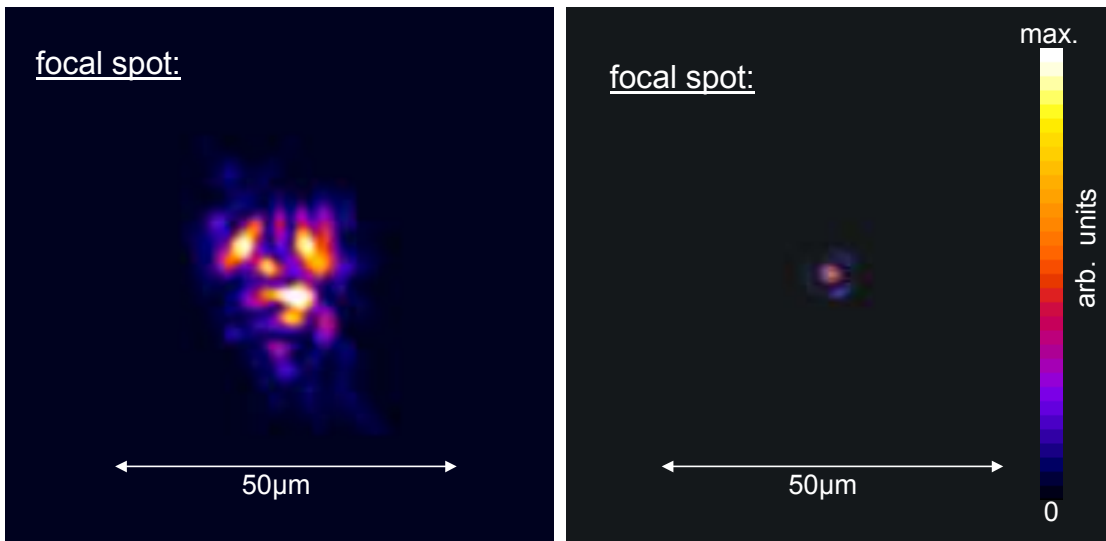
Figure A.4: 2D and 3D Intensity distributions of ATLAS-10 beam at full energy with both deformable mirrors operating: (a) Only first mirror in operation, the 2nd mirror is idle. (b) Both deformable mirrors are in operation with the 2nd mirror controlled by the closed loop.

necessary the installation of a second deformable mirror (bimorph, 80-mm diameter, 33 electrodes, dielectric coating) to take care of the wavefront deformation close to the compressor plane at the compressor exit. Having achieved a good near field distribution in that plane, by flattening the wavefront a high quality, parallel beam is generated that can be transported through the vacuum tube system to the target chambers. It turned out that the correction voltages required for the second mirror can be found by trial and error as well, but since there are 33 voltages to choose that procedure takes a few hours. Unfortunately, the correction does not remain as stable as for the first mirror and is very sensitive to changes in beam pointing, so that after a few hours the correction has to be redone. That circumstance hinders a fruitful operation of the laser system to a great extent, so that a closed loop system based on a Shack-Hartmann-sensor was developed in collaboration with the manufacturer of the mirrors. In principle, this sensor consists of a microlens array in front of a CCD camera, which splits the beam into many individual beamlets. Detecting the position of each beamlet's focal spot in the CCD plane is a direct measurement of the local pointing across the beam profile and, since the beam pointing is always perpendicular to the wavefront, a measurement of the local wavefront slope. By comparing the positions of these many beamlets with their positions from a reference plane wavefront, the wavefront aberrations are absolutely measured. For an automatic correction of these aberrations, it is necessary to know the response function of the bimorph mirror

for a each electrode. Therefore with the startup of the system for each electrode, a defined voltage is applied and the change in the position of the beamlets is recorded. Using a matrix algorithm with the measured wavefront as an input and the reference wavefront together with the response functions as parameters [69], it is now possible to correct the wavefront aberrations after a few iterations and to achieve a beam quality of $\lambda/5$ or better. In total, this procedure takes about five minutes and ensures a routine operation of the laser with only a minimum of alignment work. Images of the focal spot taken in the target chambers show a very good focusability with a Strehl Ratio of approx. 0.7-0.8. (Fig. A.4, Fig. A.5). The images showing the focal spot were obtained by taking a series of 8-bit exposures through different filters and replacing the overexposed parts of images with less attenuation with the scaled information of more filtered images. Thus it is possible to obtain a dynamic range equivalent to 14-bit resolution with only an 8-bit camera. Since for safety reasons, the second mirror is placed behind the
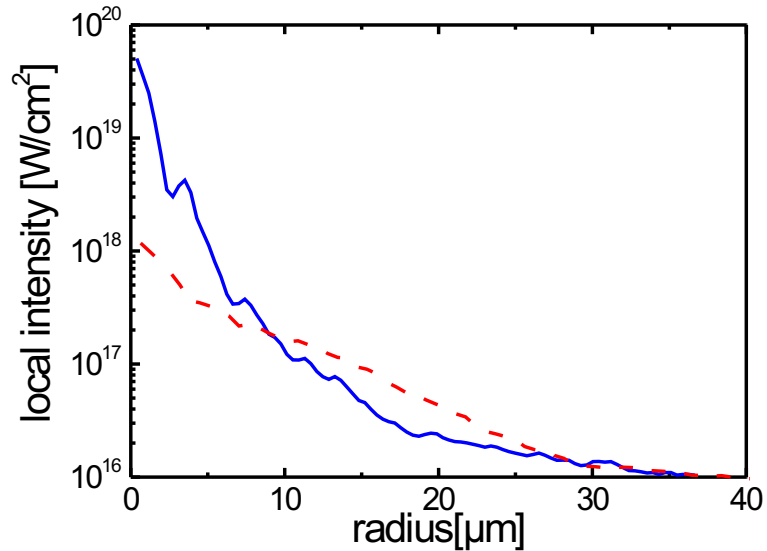
Figure A.5: Radial intensity distribution in the focus of an f 2.2 off-axis parabola without (dash) and with (solid) closed loop working. The radius of the Airy disc is 2.6 microns, which translates to a peak intensity of 7×10^{19} W/cm^2 for an ideal beam. The maximum intensity of ATLAS-10 reaches 7×10^{19} W/cm^2, corresponding to a Strehl Ratio of 0.7

compressor, care has to be taken in propagating a non-planar wavefront through the compressor. A more complete treatise of this problem is given in [70, 71], so here the main aspects are briefly discussed only. The following considerations were suggested by Prof. Pretzler [72].

Three main aberrations arise from passing the compressor with an aberrated wavefront. For the sake of simplicity, the locally curved wavefront is modeled by

a converging beam of the same wavefront curvature(Fig. A.6).
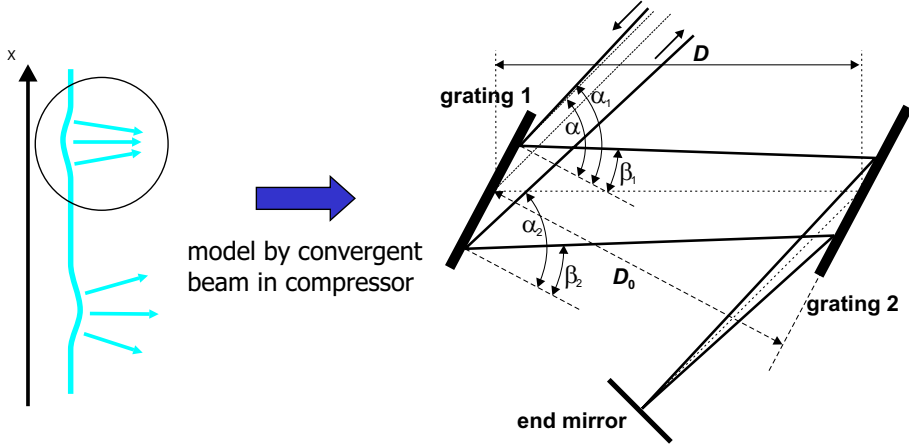
Figure A.6: Illustration of incomplete recompression fidelity: A beam entering the compressor with an angle α_1, which deviates from the optimum angle α by $\Delta\alpha_1$, exits under an angle $\alpha_2 = \alpha - \Delta\alpha_2$. Due to the nonlinear dependence of incidence and reflection angle (see Fig. A.8) upon reflection on a grating, $\Delta\alpha_1 \neq \Delta\alpha_2$. This leads to the introduction of higher-order dispersion terms for the compressor and hence to an incomplete recompression.

The first effect of a convergent wavefront passing through the compressor is an incomplete recompression of the beam. Since the beam is no longer parallel, different parts of the beam enter the compressor at different angles, leading to a nonuniform compression across the beam diameter. The effect on pulse duration is shown in Fig. A.7, and is of only minor importance with curvature radii occurring on ATLAS ($r_{curvature} \geq 15$m). An angular spread of the incoming beam has different consequences in a plane parallel to the grating grooves and in one perpendicular to them. In the parallel plane, reflection angle equals incidence angle, whereas in the perpendicular plane the direction of the reflected beam is governed by diffraction, and a change in incidence angle yields a nonequal change in reflection angle, as can be seen from Fig. A.8.

This leads to two focal lines parallel and perpendicular to the groove plane. Their distance x is only a function of the compressor geometry and independent of the beam divergence. It is given by

$$x = 2\,\mathrm{D} \cdot \left(1 - \frac{\cos^2 \alpha}{\cos^2 \beta_0}\right), \tag{A.1}$$

where D is the grating separation along the beam and α and β_0 are the angle of the incoming and reflected beams, respectively. For a parallel beam, the two focal lines are shifted to infinity, so no astigmatism shows up in the beam, but for

For $\Delta a = 3$ mrad: $\Delta t = 1$ fs
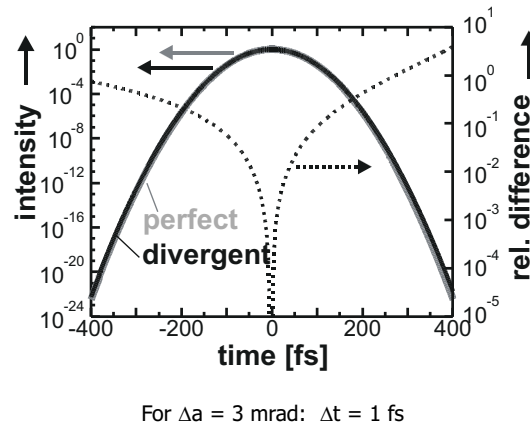
Figure A.7: Change in pulse duration and contrast due to a convergent wavefront in the compressor. The intensity profile of a parallel gaussian pulse is shown in grey, whereas the profile of a convergent beam is depicted in black. The dashed line shows their relative intensity difference (right scale).
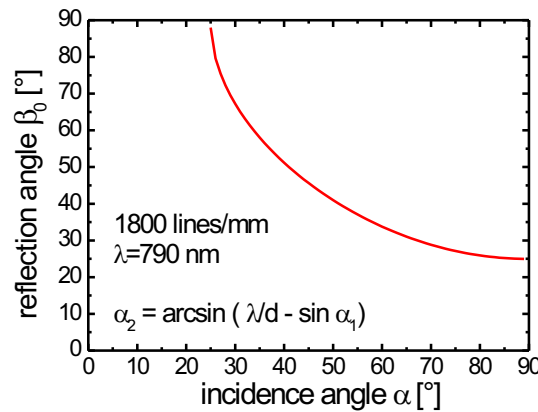
Figure A.8: Dependence of the reflection angle of a 1800 lines/mm grating on the incidence angles.

curved wavefronts it becomes visible. It can in principle be corrected for by the deformable mirror.

Since the compressor dispersion leads to different pathlengths for different colors, a convergent beam also leads to a chromatic aberration. This can be intuitively understood from Fig. A.9, where without restricting universality the blue beam comes to focus on the end mirror and the red one due to its longer path does not. This means that for both colors the beam waist is situated at different distances from the final focusing optics, which is equivalent to a different object distance with respect to it. Therefore, also the image distance varies with color, which causes a chromatic aberration that cannot be corrected for by the adaptive mirror. It has to be kept smaller than the diffraction limit, thus restricts the maximum allowable wavefront curvature radius to ≥ 15m for our system.
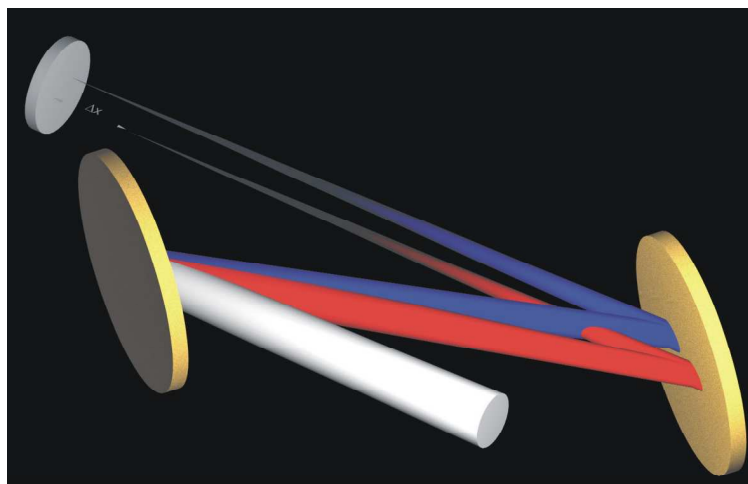
Figure A.9: Illustration of chromatic aberration introduced by a non-parallel beam in the compressor.

A.1.3   Beam Diagnostics

Apart from focusability, various other beam properties have a strong influence on the laser interaction with the target. To characterize and quantify them, a separate laser table hosts the ATLAS-10 beam diagnostics suite. It can be activated by sliding a movable mirror into the beamline, delivering the laser pulses to the various diagnostics. Additionally, a mirror in front of the compressor can be replaced by a wedge, which serves as an attenuator upon reflection on an uncoated glass surface. Both are placed on a sliding stage and are aligned to precisely the same plane. This setup reduces the beam energy by a factor of 100, so the fully amplified beam can be handled by all the diagnostics. Besides the wavefront sensor, a second-order autocorrelator to measure the pulse duration, a spectrometer to measure the bandwidth, an interferometric field autocorrelator to measure the phase front tilt and two fast photodiodes for diagnosing prepulses are installed. The beam energy is measured by a pyroelectric detector on the main laser table. To check the prepulse level of the beam and look for leaking pulses out of the regenerative amplifier an existing 3rd order autocorrelator was modified with a 1 m long delay line, so it is possible to detect short prepulses up to 6 ns before the main pulse.

A.1.4   Cleaning of Compressor Gratings

Upon the last reflection on the compressor gratings the laser is temporally fully compressed, implying maximum laser power and intensity in the unfocussed beam. This leads to a laser field strength on the grating surface of the order of 10^9 V/m,

which is orders of magnitude higher than the field emission threshold. Even more enhanced by the groove structure of the grating surface, this leads to massive field emission of electrons out of the tips of structure. These electrons, in turn, ionize and split carbon containing molecules in the residual vacuum (pump oil, sweat, CO_2 etc...), causing carbon to deposit on the grating surface. After typically $\sim 10^5$-10^6 laser shots, a dark coating on the last grating surface is built up, which represents the beam intensity distribution and severely affects the grating reflectivity and thus the compressor efficiency. Drops in overall efficiency from 60% to 30% have been measured, indicating a drop in reflectivity of the last grating from $\sim 92\%$ to $\sim 46\%$. Prolonged exposure to high intensity laser light might even result in physical damage of the grating structure itself due to increased absorption. In this work, for the first time a complete cleaning of the grating surface by reactive ion etching in a hydrogen or oxygen plasma was proposed and experimentally verified. After the grating surface had aquired the carbon coating, it was to taken to the Institut für Plasmaphysik's Surface Physics Group for cleaning. They exposed the grating to a electron-cyclotron-resonance-(ECR)- generated hydrogen plasma for a time of up to an hour, which completely removed the carbon deposit without affecting the gold coating. After this treatment the grating surface regained its full reflectivity. When the treatment was done in a conventional discharge plasma, the treated surface showed some residual fogging resembling the carbon deposit, which had no measurable effect on the grating efficiency, but nevertheless was visible by eye. It is unclear if this fogging is due to damage of the gold layer from the higher plasma ion temperature as compared to the ECR plasma, or was caused by the laser imprint itself. In conclusion, this treatment produces very satisfactory results and is practised by a number of laboratories around the world in the meantime, and several groups have already installed an in-situ ion etching apparatus into the compressor chamber.

Appendix B

Development of a Thomson Parabola Spectrometer

A Thomson parabola spectrometer was constructed to obtain spectra of laser generated ions of different mass and charge state. The ions are entering the spectrometer through a small pinhole aperture and propagate through a region with parallel electric and magnetic fields. They are deflected according to their velocity v

$$R_{mag} = \frac{m_i v}{qeB} \tag{B.1}$$

by the magnetic field and to their energy

$$R_{el} = \frac{m_i v^2}{qeE} \tag{B.2}$$

by the electric field. Here the radius of deflection due to the magnetic or electric fields is denoted as $R_{mag,el}$, the ion mass is m_i , its charge state q and the magnetic and electric field B and E. The two Thomson Parabolas are operated at a common magnetic field of 0.6T and an electric field of 15 kV/cm or 30 kV/cm, respectively. Given the deflection from both fields as $x_{mag,el} = l^2/R$ for small deflections (l is the length of the field region), it is easy to see that for any given velocity the E-field deflection x_{el} scales with the B-field deflection x_{mag} as

$$x_{el} = \frac{m_i \; E}{l^2 \; q \; e \; B^2} x_{mag}^2, \tag{B.3}$$

which means that ions with the same q/m, but different energies (velocities) end up on parabolic curves in the detector plane (see Fig. B.1(a)) . A Thomson parabola produces a spectrum for each value of q/m, thus providing discrimination between different ion species. The magnetic field was measured in a the middle plane
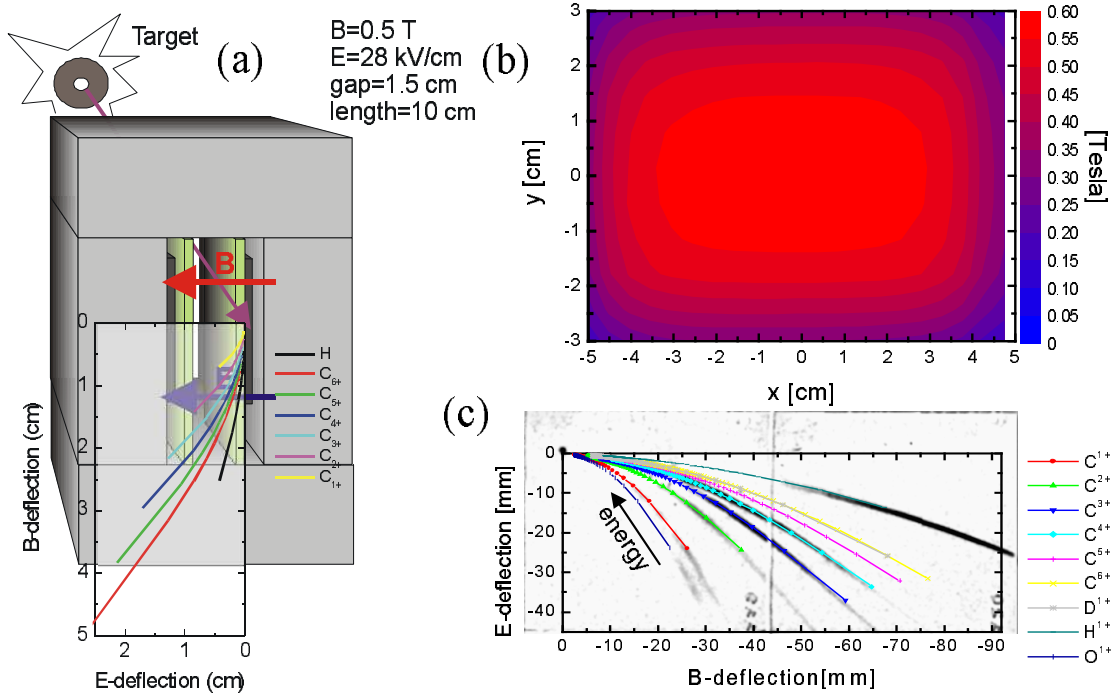
Figure B.1: (a) General setup of the Thomson parabola spectrometer. (b) Map of the magnetic field strength in the middle plane of the magnet. (c) Comparison of measured ion traces (grayscale scan) with simulation results from SIMION (colored lines).

between the magnets and 6 mm left and right of it. The result (middle plane) is shown in Fig. B.1(b).

In order to quantify the spectra, the electrode and magnet geometry was modeled with the particle tracing code SIMION 3D [73], which was set to reproduce the measured field distribution within an error of 5% at all points. The electric field distribution could not be measured, but can be modeled fairly accurately using SIMION's field solver. The result of this modeling is compared with a scan of an irradiated CR-39 sheet in Fig. B.1(c), and shows a good agreement. The sequence of different charge states is reproduced very accurately.

Ions of different species, but equal q/m cannot be separated in a Thomson Parabola alone. As a detector exclusively sensitive to ions with high spatial resolution, CR-39 nuclear track sheets were used in the Thomson parabolas. They are sensitive for all ion species except high-energy hydrogen isotopes, which is due to the low damage density the latter cause while they are stopped in matter. CR-39 is a polymer that gets damaged by ionizing radiation passing through it, and is etched after irradiation to enlarge the damage zones stemming from the incident particle, so little craters in the surface are created. These craters can be counted under a microscope. For protons with an energy below ∼100 keV, the craters are

Figure B.2: Photograph of two Thomson parabola spectrometers (in the foreground) attached to the LULI 100TW target chamber.

too shallow to yield a sufficient contrast under the microscope. Ions with different energy deposition density cause different shapes and size of craters, making it possible to distinguish two different ion species with the same q/m in one parabolic trace. Due to this unique property of CR-39, it is possible (with some restrictions) to separate and obtain spectra from all ion species and charge states entering the detector.

Without a fixed energy point, the parabolic traces can be scaled by a constant factor in both axes without changing the picture. Fortunately, such a fixed energy point exists. For high energy protons, the etched craters in CR-39 vanish above 6-8 MeV because of the small energy loss of such protons. However, protons at 10 MeV can penetrate the CR-39 and cause craters on the back surface of the sheet. The penetration point only depends upon the thickness of the sheet and the absolute field values, and therefore can be used to absolutely calibrate the energy along a trace.

The irradiated CR-39 slides are etched and scanned in a microscope equipped with an x-y table and an image recognition system to produce a data file which contains information on the location, diameter, excentricity, and central brightness of each pit. This file can be processed to set cuts onto unwanted ion species, dirt and background signal, and to obtain an absolutely calibrated ion spectrum. In Manuel Hegelich's PHD thesis [37], this system is described in detail.

Appendix C

Publication List

1. * [1] **S. Karsch**, S. Düsterer, H. Schwoerer, F. Ewald, D. Habs, M. Hegelich, G. Pretzler, A. Pukhov, K. Witte, and R. Sauerbrey: *High-intensity laser induced ion acceleration from the target front and rear sides*, submitted to PRL, 2002

2. M. Roth, M. Allen, P. Audebert, A. Blazevic, E. Brambrink, T.E. Cowan, J. Fuchs, J.C. Gauthier, M. Geissel, M. Hegelich, **S. Karsch**, J. Meyer-ter Vehn, H. Ruhl, T. Schlegel and R.B. Stevens: *The generation of high-quality, intense ion beams by ultra-intense lasers*, Plasma Physics and Controlled Fusion **44** 1-10 (2002)

3. * M. Hegelich, **S. Karsch**, G. Pretzler, D. Habs, K. Witte, W. Guenther, M. Allen, A. Blazewic, J. Fuchs, J.C. Gauthier, M. Geissel, P. Audebert, T. Cowan and M. Roth: *MeV Ion Jets from Shortpulse-Laser-Plasma Interaction with thin Foils*, PRL **89**, 085002-1 (2002)

4. M. Roth, T.E. Cowan, J.C. Gauthier, M. Allen, P. Audebert, A. Blazevic, J. Fuchs, M. Geissel, M. Hegelich, **S. Karsch**, J. Meyer-ter Vehn, A. Pukhov and T. Schlegel: *The dependence of intense laser-accelerated ion beams on target properties*, Physical Review Special Topics - Accelerators and Beams **5**, 061301 (2002)

5. * H. Baumhacker, G. Pretzler, K.J. Witte, M. Hegelich, M. Kaluza, **S. Karsch**, A. Kudryashov, V. Samarkin and A. Roukossouev: *Correction of strong phase and amplitude modulations by two deformable mirrors in a in a multistaged Ti:sapphire laser*, Optics Letters **27**, 1570-1572 (2002)

---

[1]Publications marked with * are attached to this work

6. **S. Karsch**, D. Habs, T. Schätz, U. Schramm, P.G. Thirolf, J. Meyer-ter-Vehn and A. Pukhov: *Particle Physics with Petawatt-Class Lasers*, Laser and Particle Beams **17** 565-570 (1999)

Bibliography

[1] D. Strickland and G. Mourou, *Compression of amplified chirped optical pulses*, Opt. Commun. **56**, 219 (1985).

[2] M. D. Perry and G. Mourou, *Terawatt to petawatt subpicosecond lasers*, Science **264**, 917 (1994).

[3] M. D. Perry, D. Pennington, B.C. Stuart, G. Tietbohl, J.A. Britten, C. Brown, S. Herman, B. Golick, M. Kartz, J. Miller, H.T. Powell, M. Vergino and V. Yanovsky, *Petawatt Laser Pulses*, ol **24**, 160 (1999).

[4] I.N. Ross, P. Matuossek, M. Towrie, A.J. Langley and J.L. Collier, *The prospects for ultrashort pulse duration and ultrahigh intensity using optical parametric chirped pulse amplifiers*, oc **144**, 125 (1997).

[5] M. Nisoli, S. Stagira, S. De Silvestri, O. Svelto, S. Sartania, Z. Cheng, M. Lenzner, Ch. Spielmann and F. Krausz, *A novel-high energy pulse compression system: generation of multigigawatt sub-5-fs pulses*, Appl. Phys. B **65**, 189 (1997).

[6] A. Pukhov and J. Meyer ter Vehn, *Relativistic Magnetic Self-Channeling of Light in Near-Critical Plasma: Three-Dimensional Particle in Cell Simulation*, Phys. Rev. Lett. **76**, 3975 (1996).

[7] M. Borghesi, A.J. MacKinnon, L. Barringer, R. Gaillard, L.A. Gizzi, C. Meyer, O. Willi, A. Pukhov and J. Meyer ter Vehn, *Relativistic Channeling of a Picosecond Laser Pulse in a Near-Critical Preformed Plasma*, Phys. Rev. Lett. **78**, 879 (1997).

[8] H. Alfvén, *On the Motion of Cosmic Rays in Interstellar Space*, Physical Review **55**, 425 (1939).

[9] F. Floux, D.Cognard, L.-G. Denoeud, G. Piar, D. Parisot, J.L. Bobin, F. Delobeau and C. Fauquignon, *Nuclear Fusion Reactions in Solid Deuterium Laser-Produced Plasma*, Phys. Rev. A **3**, 821 (1970).

[10] J. Lindl, *Development of the indirect drive approach to inertial confinement fusion and the target physics basis of ingnition and gain*, pop **2**, 3933 (1995).

[11] P.A. Norreys, A.P. Fews, F.N. Beg, A.R. Bell, A.E. Dangor, P. Lee amd M.B. Nelson, H. Schmidt, M. Tatarakis and M.D. Cable, *Neutron production from picosecond laser irradiation of deuterated targets at intensities of $10^{19} W/cm^2$*, Plasma Phys. Controlled Fusion **40**, 175 (1998).

[12] G. Pretzler, A. Saemann, A. Pukhov, D. Rudolph, T. Schätz, U. Schramm, P. Thirolf, D. Habs, K. Eidmann, G.D. Tsakiris, J. Meyer ter Vehn and K. Witte, *Neutron Production with 200mJ ultrashortlaser pulses*, Phys. Rev. E **58**, 1165 (1998).

[13] L. Disdier, J-P. Garconnet, G. Malka and J-L. Miquel, *Fast Neutron Emission from a High-Energy Ion Beam Produced by a High-Intensity Subpicosecond Laser Pulse*, Phys. Rev. Lett. **82**, 1454 (1999).

[14] T. Ditmire, J. Zweiback, V.P. Yanovsky, T.E. Cowan, G. Hays and K.B. Wharton, *Nuclear fusion from explosions of femtosecond laser-heated deuterium clusters*, Nature **398**, 489 (1999).

[15] J. Zweiback, R.A. Smith, T.E. Cowan, G. Hays, K.B. Wharton, V.P. Yanovsky and T. Ditmire, *Nuclear Fusion Driven by Coulomb Explosion of Large Deuterium Clusters*, prl **84**, 2634 (2000).

[16] T.E. Cowan, private communication, 2002.

[17] J. Zweiback, T.E. Cowan, R.A. Smith, J.H. Hartley, R. Howell, C.A. Steinke, G. Hays, K.B. Wharton, J.K. Crane and T. Ditmire, *Characterization of Fusion Burn Time in Exploding Deuterium Cluster Plasmas*, prl **85**, 3640 (2000).

[18] R.A. Snavely, M.H. Key, S.P. Hatchett, T.E. Cowan, M. Roth, T.W. Phillips, M.A. Stoyer, E.A. Henry, T.C. Sangster, M.S. Singh, S.C. Wilks, A. MacKinnon, A. Offenberger, D.M. Pennington, K. Yasuike, A.B. Langdon, B.F. Lasinski, J. Johnson, M.D. Perry, and E.M. Campbell, *Intense High-Energy Proton Beams from Petawatt-Laser Irradiation of Solids*, Phys. Rev. Lett. **85**, 2945 (2000).

[19] A. Maksimchuk, S. Gu, K. Flippo, V.Y. Bychenkov and D. Umstadter, *Forward Ion Acceleration in Thin Films Driven by a High-Intensity Laser*, Phys. Rev. Lett. **84**, 4108 (2000).

[20] J. Meyer ter Vehn, A. Pukhov and Zh.-M. Sheng, in *Atoms, Solids, and Plasmas in Super-Intense Laser Fields*, edited by D. Batani, C.J. Joachain, S. Martellucci and A.N. Chester (Kluwer Academic / Plenum Publishers, New York, 2001), pp. 167–192.

[21] P. Mora and T.M. Antonsen, *Kinetic modeling of intense, short laser pulses propagating in tenuous plasmas*, Phys. Plasmas **4**, 217 (1997).

[22] B. Quesnel and P. Mora, *Theory and simulation of the interaction of ultraintense laser pulses with electrons in vacuum*, Phys. Rev. E **58**, 3719 (1998).

[23] S.C. Wilks, W.L. Kruer, M. Tabak and A.B. Langdon, *Absorption of Ultra-Intense Laser Pulses*, Phys. Rev. Lett. **69**, 1383 (1992).

[24] T. Tajima and J.M. Dawson, *Laser Electron Accelerator*, Phys. Rev. Lett. **43**, 267 (1979).

[25] C. Gahn, G. D. Tsakiris, A. Pukhov, J. Meyer ter Vehn, G. Pretzler P. Thirolf, D. Habs and K. J. Witte, *Multi-MeV Electron Beam Generation by Direct Laser Acceleration in High Density Plasma Channels*, Phys. Rev. Lett. **83**, 4772 (1999).

[26] F. Brunel, *Not-So-Resonant, Resonant Absorption*, Phys. Rev. Lett. **59**, 52 (1987).

[27] A. Pukhov, *Three-Dimensional Simulations of Ion Acceleration from a Foil Irradiated by a Short-Pulse Laser*, Phys. Rev. Lett. **86**, 3562 (2001).

[28] N. Izumi, Y. Sentoku, H. Habara, K. Takahashi, F. Ohtani, T. Sonomoto, R. Kodama, T. Norimatsu, H. Fujita, Y. Kitagawa, K. Mima, K.A. Tanaka and T. Yamanaka, *Observation of neutron spectrum produced by fast deuterons via ultraintense laser plasma interactions*, Phys. Rev. E **65**, 036413 (2002).

[29] J. Denavit, *Absorption of High-Intensity Subpicosecond Lasers on Solid Density Targets*, Phys. Rev. Lett. **69**, 3052 (1992).

[30] A. Pukhov and J. Meyer ter Vehn, *Relativistic laser-plasma interaction by multi-dimensional particle-in-cell simulations*, Phys. Plasmas **5**, 1880 (1998).

[31] K. Krushelnick, E.L. Clark, Z. Najmudin, M. Salvati, M.I.K. Santala, M. Tatarakis, A.E. Dangor, V. Malka, D. Neely, R. Allott and C. Danson, *Multi-MeV Ion Production from High-Intensity Laser Interactions with Underdense Plasmas*, Phys. Rev. Lett. **83**, 737 (1999).

[32] A. Pukhov, Z.-M. Sheng and J. Meyer ter Vehn, *Particle acceleration in relativistic laser channels*, Phys. Plasmas **6**, 2847 (1999).

[33] S.C. Wilks, A.B. Langdon, T.E. Cowan, M. Roth, M. Singh, S. Hatchett, M.H. Key, D. Pennington, A. MacKinnon, and R.A. Snavely, *Energetic proton generation in ultra-intense laser-solid interactions*, Phys. Plasmas **8**, 542 (2001).

[34] S.P. Hatchett, C.G. Brown, T.E. Cowan, E.A. Henry, J.S. Johnson, M.H. Key, J.A. Koch, A.B. Langdon, B.F. Lasinsky, R.W. Lee, A.J. MacKinnon, D.M. Pennington, M.D. Perry, T.W. Phillips, M. Roth, T.C. Sangster, M.S. Singh, R.S. Snavely, M.A. Stoyer, S.C. Wilks and K. Yasuike, *Electron, photon and ion beams from the relativistic interaction of Petawatt laser pulses with solids targets*, Phys. Plasmas **7**, 2076 (2000).

[35] E.L. Clark, K. Krushelnick, J.R. Davies, M. Zepf, M. Tatarakis, F.N. Beg, A. Machacek, P.A. Norreys, M.I.K. Santala, I. Watts and A.E. Dangor, *Measurements of Energetic Proton Transport through Magnetized Plasma from Intense Laser Interactions with Solids*, Phys. Rev. Lett. **84**, 670 (2000).

[36] M. Hegelich, S. Karsch, G. Pretzler, D. Habs, K. Witte, W. Guenther, M. Allen, A. Blazewic, J. Fuchs, J.C. Gauthier, M. Geissel, P. Audebert, T. Cowan, and M. Roth, *MeV Ion Jets from Shortpulse-Laser-Plasma Interaction with thin Foils*, submitted to Phys. Rev. Lett. **89**, 085002 (2002).

[37] M. Hegelich, Dissertation, Ludwig-Maximilians Universität München, 2002.

[38] *Handbook on photonuclear data for applictions (IAEA-TECHDOC-draft No.3* (International Atomic Energy Agency (IAEA), Vienna, 2000).

[39] *Evaluated Nuclear Data Files W^3 Retrieval System, Evaluated Nuclear Data Library* (Brookhaven National Laboratory, http://www.nndc.bnl.gov/nndc/endf/, 2002).

[40] G.F. Knoll, *Radiation Detection and Measurement, Chapters 14, 15 and 19* (Wiley & Sons, New York, 1989).

[41] D.R. Slaughter and W.L. Pickles, *A highly sensitive silver-activation detector for pulsed neutron sources*, Nuclear Instruments and Methods **160**, 87 (1979).

[42] unknown, WinCamda Camac Data Aquisition System, 1997.

[43] L. Gremillet, Dissertation, Ecole Polytechnique, 2001.

[44] G. Schatz and A. Weidinger, *Nukleare Festkörperphysik* (Teubner, Stuttgart, 1992), S. 300.

[45] M. Drosg, *Drosg2000 Neutron Source Reactions* (International Atomic Energy Agency, www.iaea.org, ADDRESS, 2000).

[46] J.F. Ziegler and J.P. Biersack, SRIM 2000 stopping tables and computer code, www.srim.org, 2000.

[47] G. Belyaev, M. Basko, A. Cherkasov, A. Golubev, A. Fertman, I. Roudskoy, S. Savin, B. Sharkov, V. Turtikov, A. Arzumanov, A. Borisenko, I. Gorlachev, S. Lysukhin, D.H.H. Hoffmann and A. Tauschwitz, *Measurement of the Coulomb energy loss of fast protons in a plasma target*, Phys. Rev. E **53**, 2701 (1996).

[48] J.D. Jackson, *Classical Electrodynamics* (Wiley & Sons, New York, 1975).

[49] S. Augst, D. D. Meyerhofer, D. Strickland and S. L. Chin, *Laser ionization of noble gases by Coulomb-barrier suppression*, J. Opt. Soc. Am. B **8**, 858 (1991).

[50] J. H. Posthumus, A. J. Giles, M. R. Thompson and K. Codling, *Field-ionization, Coulomb explosion of diatomic molecules in intense laser fields*, J. Phys. B: At. Mol. Opt. Phys. **29**, 5811 (1996).

[51] U. Mohideen, M. H. Sher, H. W. K. Tom, G. D. Aumiller, O. R. Wood II, R. R. Freeman, J. Bokor and P. H. Bucksbaum, *High intensity above-threshold ionization of He*, Phys. Rev. Lett. **71**, 509 (1993).

[52] L. Gremillet, F. Amiranoff, S.D. Baton, J.-C. Gauthier, M. Koenig, E. Martinolli, F. Pisani, G. Bonnaud, C. Lebourg, C. Rousseaux, C. Toupin, A. Antonicci, D. Batani, A. Bernardinello, T. Hall, D. Scott, P. Norreys, H. Bandulet, and H. Pepin, *Time-Resolved Observation of Ultrahigh Intensity Laser-Produced Electron Jets Propagating through Transparent Solid Targets*, Phys. Rev. Lett. **83**, 5015 (1999).

[53] Y. Sentoku, K. Mima, Z.M Sheng, P. Kaw, K. Nishihara and K. Nishikawa, *Three-dimensional particle-in-cell simulation of energetic electron generation and transport with relativistic laser pulses in overdense plasmas*, Phys. Rev. E **65**, 046408 (2002).

[54] M. Honda, J. Meyer ter Vehn and A.Pukhov, *Collective Stopping and Ion Heating in Relativistic-Electron-Beam Transport for Fast Ignition*, Phys. Rev. Lett. **85**, 2128 (2000).

[55] V.T. Tikhonchuk, *Interaction of a beam of fast electrons with solids*, Phys. Plasmas **9**, 1416 (2002).

[56] F. Pisani, A. Bernardinello, D. Batani, A. Antonicci, E. Martinolli, M. Koenig, L. Gremillet, F. Amiranoff, S. Baton, J. Davies, T. Hall, D. Scott, P. Norreys, A. Djaoui, C. Rousseaux, P. Fews, H. Bandulet, and H. Pepin, *Experimental evidence of electric inhibition in fast electron penetration and of electric-field-limited fast electron transport in dense matter*, Phys. Rev. E **62**, 5927 (2000).

[57] S. P. Lyon and J. D. Johnson, SESAME Equation-of-state tables, 1992.

[58] R.M. More, in *Handbook of Plasma Physics* (North-Holland, Amsterdam, 1991), S. 70.

[59] Ed. J.F. Briesmeister, *MCNP - A general Monte Carlo N-Particle Transport Code* (Los Alamos Tech. Pub. LA-12625-M (4B), ADDRESS, 1997).

[60] U. Teubner, I. Uschmann, P. Gibbons, D. Altenbernd, E. Förster, T. Feurer, W. Theobald, R. Sauerbrey, G. Hirst, M.H. Key, J. Lister and D. Neely, *Absorption and hot-electron prodution by high intensity femtosecond uv-laser pulses in solid targets*, Phys. Rev. E **54**, 4167 (1996).

[61] J.A. Koch, M.H. Key, R.R. Freeman, S.P. Hatchett, R.W. Lee, D. Pennington, R.B. Stephens and M. Tabak, *Experimental measurement of deep directional columnar heating by laser-generated relativistic electrons at near-solid density*, Phys. Rev. E **65**, 016410 (2002).

[62] K. Eidmann, J. Meyer ter Vehn, T. Schlegel and S. Hïler, *Hydrodynamic simulation of subpicosecond laser interaction with solid-density matter*, Phys. Rev. E **62**, 1202 (2000).

[63] J.C. Gauthier, F. Amiranoff, C. Chenais-Popovics, G. Jamelot, M. Koenig, C. Labaune, E. Leboucher-Dalimier, C. Sauteret and A. Migus, *LULI activities in the field of high-power laser-matter interaction*, Laser and Particle Beams **17**, 195 (1999).

[64] M. Roth, T.E. Cowan, J.C. Gauthier, M. Allen, P. Audebert, A. Blazevic, J. Fuchs, M. Geissel, M. Hegelich, S. Karsch, J. Meyer ter Vehn, A. Pukhov and T. Schlegel, *Energetic ions generated by laser pulses: A detailed study*

on target properties, Phys. Rev. Special Topics - Accelerators and Beams **5**, 061301 (2002).

[65] A.J. MacKinnon, Y. Sentoku, P.K. Patel, D.W. Price, S. Hatchett, M.H. Key, C. Andersen, R. Snavely and R.R. Freeman, *Enhancement of Proton Acceleration by Hot Electron Recirculation in Thin Foils Irradiated by Ultraintense Laser Pulses*, Phys. Rev. Lett. **88**, 215006 (2002).

[66] D. Hilscher, O. Berndt, M. Enke, U. Jahnke, P.V. Nickles, H. Ruhl and W. Sandner, *Neutron energy spectra from the laser-induced $D(d,n)^3He$ reaction*, Phys. Rev. E **64**, 016414 (2001).

[67] P. Norreys, private communication, 2002.

[68] H. Baumhacker, A. Böswald, H. Haas, M. Fischer, W. Fölsner, G. Keller, U. Andiel, X. Dong, M. Dreher, K. Eidmann, E. Fill, M. Hegelich, M. Kaluza, S. Karsch, G. Pretzler, G. Tsakiris and K.J. Witte, *Advanced Titanium Sapphire Laser ATLAS*, MPQ-Report **272**, (2002).

[69] K. Akaoka, S. Harayama, K. Tei, Y. Maruyama and T. Arisawa, *Closed loop wavefront correction of Ti:sapphire Chirped Pulse Amplification laser beam*, SPIE Proceedings **3265**, 219 (1998).

[70] H. Baumhacker, G. Pretzler, K.J. Witte, M. Hegelich, M. Kaluza, S. Karsch, A. Kudryashov, V. Samarkin and A. Roukossouev, *Correction of strong phase and amplitude modulations by two deformable mirrors in a in a multistaged Ti:sapphire laser*, Optics Letters **27**, 1570 (2002).

[71] Z. Wang, Z. Xu and Z.-Q. Zhang, *A New Theory for the Treatment of a Pulsed Beam Propagating Through a Grating Pair*, IEEE. J. Quantum. Electron. **37**, 1 (2001).

[72] G. Pretzler, private communication, 2001.

[73] D.C. McGilvery and D. Dahl, SIMION 3D 7.0 Ion and Electron Optics Program, 2001.

High-intensity laser induced ion acceleration from the target front and rear sides

S. Karsch[1,2], S. Düsterer[3], H. Schwoerer[3], F. Ewald[3], D. Habs[2],

M. Hegelich[1,2], G. Pretzler[4], A. Pukhov[4], K. Witte[1], and R. Sauerbrey[3]

[1] *MPI f. Quantenoptik, 85748 Garching, Germany*
[2] *Universität München, 85748 Garching, Germany*
[3] *Friedrich-Schiller-Universität Jena, 07740 Jena, Germany*
[4] *Universität Düsseldorf, Düsseldorf, Germany*
(Dated: November 6, 2002)

Fusion neutrons from a heavy water droplet target irradiated with laser pulses of 3×10^{19} W/cm^2 and from a deuterated secondary target are observed by a time-of-flight (TOF) neutron spectrometer. The observed TOF spectrum can be explained by fusion of deuterium ions simultaneously originating from two different sources: ion acceleration in the laser focus by ponderomotive charge separation and target-normal sheath acceleration (TNSA) off the target rear surface. The experimental findings are in agreement to 3-D particle-in-cell (PIC) simulations.

PACS numbers: 52.38.Kd, 29.30.Hs, 52.65.Rr, 52.65.Pp

In recent years, high-intensity femtosecond (fs) lasers [1] have been used to study the new area of relativistic laser-plasma interaction. In this context, one of the most dynamic topics is the acceleration of particles to very high energies over sub-mm distances. Electrons, protons and heavy ions have been accelerated to > 50 MeV using large fs glass lasers (e.g.[2–4], but even smaller Ti:Sapphire tabletop fs lasers are capable to accelerate electrons and ions to several MeV and higher [5–7]. Much research is directed towards the development of compact particle sources with a well-characterized emission. However, the physics of laser particle acceleration is far from being understood. In previous experiments, powerful ultrashort laser pulses were focused onto thin foil targets. Intense ion beams were detected behind the foil in laser direction. Two mechanisms of ion acceleration are presently under discussion. First, the ponderomotive charge separation at the front surface induces a double layer and the resulting static fields accelerate ions into the target [6, 8, 9]. Secondly, the laser-heated electrons propagate through the target, build up a space charge at the rear surface and extract ions by the target-normal sheath acceleration (TNSA) mechanism [4, 10, 11]. Multi-dimensional PIC simulations [10, 12] suggest that both mechanisms are active and work simultaneously but independently. With standard experimental techniques, it is hard to distinguish between these two mechanisms. The species predominantly accelerated are protons from oil or water contaminants present on both target surfaces, and the interaction takes place in a tiny volume of the order of 100 μm^3. In this paper, deuterons were used for separating the front and rear surface acceleration contributions. Deuterons are not naturally found in surface contaminants and are able to trigger fusion reactions such as d(d,n)^{3}He at very low energies ($E_D \gtrsim 20$ keV), when using deuterated target material. The resulting fusion neutrons with their center-of-mass energy of 2.45 MeV can be used to obtain information

on the incident deuteron energy and angular distribution [9, 13–15] by measuring their kinematic shift. In this report, we use neutron TOF spectroscopy to get a clear distinction between front and rear surface accelerated deuterons and to determine the number and temperature of both species. Furthermore, the results are compared to PIC calculations. The experiments (Fig. 1)
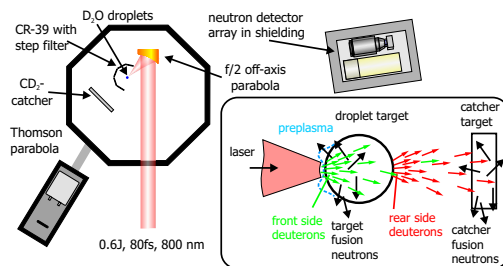
FIG. 1: Experimental setup: Laser pulses are focused onto D$_2$O droplets. Deuterons from the laser focus create prompt fusion neutrons in the droplet, while deuterons from its back side cause delayed fusion reactions in the deuterated catcher target. A sketch of the two ion populations and the subsequent neutron production is shown in the inset.

were carried out at the Jena TW Ti:sapphire laser, delivering τ_L= 80 fs, 10 Hz, E=600 mJ pulses at $\lambda_L = 0.8\mu$m. They were focused by an f/2 off-axis parabola to a spot size of 3 μm FWHM, leading to a focused intensity of $I = 3\times10^{19}$ W/cm^2 = $30 \times I_{18}$. The target consisted of well defined 20-μm diameter D$_2$O droplets produced by a piezoelectrically modulated 10-μm diameter nozzle [16]. In spite of the difference in geometry from planar targets, the main acceleration mechanisms work also in droplets with minor modifications. A secondary catcher target consisting of a 7-mm thick (CD$_2$)$_n$ disk (diameter 15cm) was placed behind the droplet in laser direction (see Fig.1) at distances of 8.4 cm, 14.8 cm or 23.3 cm, covering 1.6, 0.7 or 0.3 sr, respectively. The fusion neutron
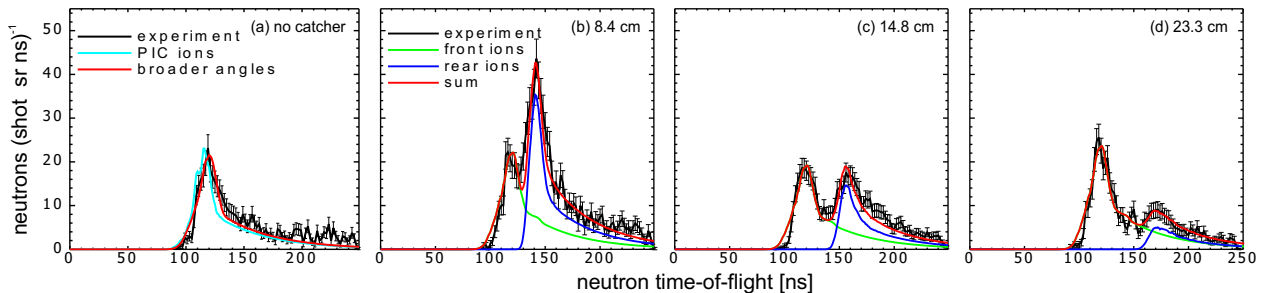
FIG. 2: Neutron TOF spectra without catcher (a) and different catcher distances (b) 8.4 cm, (c) 14.8 cm, and (d) 23.3 cm. The green, red and blue lines show simulations for ion emission of $T_{i,cold}$=100 keV and $T_{i,hot}$=350 keV from the front (see Fig. 3) and T=100 keV (b,c) or T=110 keV (d) off the rear surface.

TOF spectra were recorded by two NE110 plastic scintillation detectors. The time resolution of the whole system is ∼1.5 ns and the detector efficiency was ∼0.2. The detectors were placed at a distance of 240 cm to the focus at an angle of 143° to the laser axis inside a lead housing of 9 cm wall thickness to shield against the gamma burst from the laser interaction. In order to suppress errors in the spectral shape from pile-up, the count rate was kept low (∼ 0.25 detected neutrons / laser shot). The presented spectra were accumulated during ∼40.000 laser shots.

The neutron TOF spectra in Fig. 2 show the variation in spectral shape for different catcher distances. The spectrum in Fig. 2(a) was taken without catcher target and exhibits only a single peak from fusion neutrons created inside the droplet. With the catcher in place, a second peak appears in the spectrum (Fig. 2(b-d)), indicating fusion in the catcher by deuterons accelerated from the droplet. When the catcher distance is enlarged, the second peak shifts to later times and gets broader. The distance between the two peaks corresponds to the ion TOF from the target to the catcher, whereas the broadening reflects the TOF dispersion of the ion spectrum. When the catcher was covered with a 200-μm thick undeuterated plastic foil, a spectrum similar to the one shown in Fig. 2(a) was obtained for every catcher position which rules out that the second peak might be due to neutrons created in the droplet and scattered by the catcher.

The energy distribution of deuterons ejected from the droplet was determined by a Thomson parabola spectrometer under 15° to the laser axis and exhibits a maximum energy of ∼ 1.2 MeV and an ion temperature of 200–400 keV for different runs. CR-39 detector sheets placed around the target detected an almost isotropic ion emission with slight enhancement in 0° (laser direction) and 90° (perpendicular). This combination of data from different detectors contains enough information for clearly separating the processes involved.

First we concentrate on ion acceleration at the front

surface [9, 12, 17]. The laser pulse propagates up to the critical electron density, where it is partially absorbed (absorption coefficient α) and reflected. The light pressure $P = (2 - \alpha)I/c = (2 - \alpha)I_{18} * 3.3$ GBar displaces electrons into the dense plasma and a double layer is produced. The generated electrostatic field $\mathbf{E_s}$ accelerates ions. It is counterbalanced by the laser ponderomotive force $F_p = e\langle \mathbf{v} \times \mathbf{B_L}\rangle/c$, where $\mathbf{B_L}$ is the laser magnetic field, $\mathbf{v}$ is the electron quiver velocity and $\langle...\rangle$ means averaging over one laser period. For relativistically intense lasers, we take $|\mathbf{v}| \approx \mathbf{c}$, and estimate $\mathbf{E_s} \approx \mathbf{E_L}/2$, where $\mathbf{E_L}$ is the laser field. The characteristic ion energy can be found from the recession velocity u_r of the laser-plasma interface [9, 12, 17]: $(u_r/c)^2 = (1 - \alpha/2)m\overline{Z}n_{cr}I_{18}/(1.37Mn_r)$, where $n_r \approx n_{cr}\sqrt{1 + I_{18}/2.74}$ is the plasma density at the reflection point and n_{cr} is the usual critical density. M and m denote the ion and electron mass and $\overline{Z}$ the mean ion charge. The ion energy associated with this velocity is $E_{ion} = Mu_r^2/2 \approx (1 - \alpha/2)mc^2\overline{Z}\sqrt{I_{18}/2.74} \simeq 0.84$ MeV for $\alpha = 1$, $\overline{Z} = 1$. Peak ion energies can be up to 4 times this value due to the reflection from the running shock front [12, 18]. Our analytical model is one-dimensional (1D). However, in a real laser focus, the ponderomotive pressure acts in all directions, so the double layer forms in a nearly spherical geometry around the head of the pulse. This leads to a broad energy and angular spectrum of accelerated ions in agreement to our data.

To refine this coarse picture and to get an idea of the energy and angle distribution of ions from the laser focus, we performed simulations with the 3D PIC code VLPL [19]. A laser pulse with Gaussian temporal and spatial profile (80 fs duration and 4 μm diameter) was incident from the left side onto a simulation box of $19\times16\times16\mu m^3$ onto a preformed plasma of 4-μm scalelength followed by a uniform bulk density of $16n_{cr}$. The simulation was performed under 0° and 45° (p-polarized) angle of incidence. The pulse bores rather deeply into the plasma before it reaches the critical surface, so the ion accelera-

tion is predominantly radial to the laser axis, regardless of the target surface orientation. This means that the position of the focal spot on the droplet has little influence on the ion distribution. Fig. 3 (a) shows the ion spectra recorded in different angle intervals to the laser axis, and the light blue curve in Fig. 3 (b) plots the product of ion energy and number of ions per 10 keV versus the angle to the laser axis. The plot shows that the most and fastest ions are emitted under large angles to the laser axis, and the angle-integrated ion spectrum consists of $\sim 10^{11}$ ions with a two-temperature exponential type spectrum with $T_{i,cold} \sim 100$ keV and $T_{i,hot} \sim 350$ keV. Note that the most energetic ions are emitted at a large angle and therefore cannot be seen in the Thomson parabola.
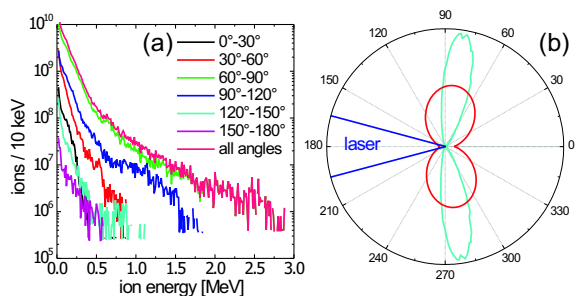
FIG. 3: PIC results: ion spectra at different angles from the laser axis and sum spectrum (a). Distribution of ion angles to the laser axis (b) from the PIC output (light blue) and modified distribution for best match with the experiment (red).

To simulate the measured neutron TOF spectra and correlate them to ion distributions, the Monte Carlo neutron production code MCNEUT was developed. The code tracks individual deuterons of a given distribution through the target, catcher and detector geometry in 3D. The ions are slowed down according to their energy loss in plasma, while their fusion probability is determined by the differential cross-section taken from the DROSG2000 tables [20]. The energy of the produced neutrons is calculated from two-body reaction kinematics. For each energy step, the probabilities are summed up in a TOF spectrum. The contributions of scattered neutrons are included by MCNP [21] neutron transport calculations for the chamber and detector geometry. The resulting scattering function was implemented in MCNEUT. Experimental laser pointing fluctuations which lead to different ion path lengths inside the droplet were modeled by moving the ion origin randomly across the droplet. When using the deuteron distribution from the PIC-simulation as input, the resulting neutron TOF-spectrum is in reasonable agreement with the experiment [see Fig. 2(a)]. An even better match is achieved with a broader angle distribution [see Fig. 3 (b)], but the same ion temperature as from PIC.

We will now rule out that these front side deuterons are able to penetrate the target in large numbers and cre-

ate the second peak as well. For calculating the fraction of ions penetrating, target heating by fast electrons must be regarded, since the ion energy loss dE/dx is different in solid matter and plasma. In plasma, the stopping is enhanced for fast ions. But for slow ions, whose velocity v_i is smaller than the electron thermal velocities v_{th}, dE/dx drops drastically, leading to an enhanced transmission. We assumed that 20% of the laser energy is converted into fast electrons (T_{hot}=1.47 MeV given by the ponderomotive scaling). They stream into the target in a 2π solid angle and deposit their energy by collisional stopping. The local temperature can then be determined from SESAME equation-of-state tables [22], and the effective charge state is estimated from a Thomas-Fermi model [23]. These values are put into our stopping model, which treats the contribution of bound target electrons by the SRIM tables [24] and that of free electrons by a low-energy extension of the plasma energy loss from [25]. With these tools, we calculated the fusion neutrons produced in the catcher target by deuterons from the front which have penetrated the droplet target. The results are presented in Fig. 4. No agreement with the measurements in Fig. 2(b-d) is observed. It is also evident that the overall effect of target heating on the neutron spectra is small.
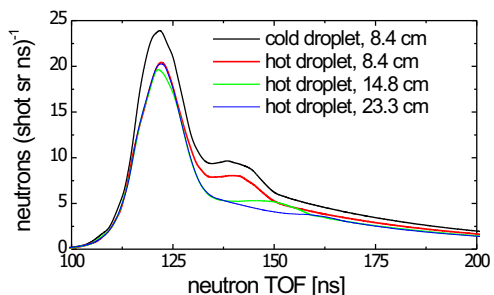
FIG. 4: Simulated neutron spectra, assuming only front accelerated deuterons, for different catcher distances. The stopping is treated for cold and hot matter.

This calculation proves that the second peak in the measured TOF spectra cannot be explained by front side ions. Therefore, a second deuteron population is postulated, which does not interact in the droplet and therefore is accelerated at the droplet rear surface by the TNSA mechanism: according to TNSA, hot electrons from the laser focus penetrate the target and exit at the rear surface. They cannot escape into vacuum due to the charging-up of the droplet and form an electron cloud around the target surface. It extends approx. one Debye length $\lambda_D = (\epsilon_0 kT_{hot}/e^2 n_{e,hot})^{1/2}$ into vacuum and sets up a strong field at the rear surface: $E_{stat} \approx kT_{hot}/e\lambda_D \sim 1$ TV/m. Here, $n_{e,hot}$ is the density of hot electrons from the laser focus after reaching the target rear surface. The lateral spread of the cloud depends on the divergence and the transport of the electron beam through the target. The

droplet is isolated from the environment and electrons are bound to it by space charge fields, so they distribute quickly around the surface and an almost uniform electron halo forms around the droplet. The TNSA mechanism responsible for the directed ion acceleration from the rear side of foils therefore accelerates ions into 4π in our case as found experimentally by the CR-39 detectors. Assuming ion acceleration into 4π, we can put these TNSA-ions into MCNEUT to calculate the TOF spectra of fusion neutrons from the catcher target. By varying the ion temperature we can find the best match to the experiment. These spectra are shown in Fig. 2(b,c,d) together with the measurements. According to the calculation, the second neutron peaks in the three runs were caused by 1.9×10^{11} (8.4 cm distance), 8.1×10^{10} (14.8 cm), and 3.6×10^{10} (23.3 cm) ions hitting the catcher. Taking into account the catcher solid angles at different distances this corresponds to a total number of surface accelerated ions of 1.5×10^{12}, 1.8×10^{12}, and 1.7×10^{12}, respectively. Since these numbers are in good mutual agreement, we conclude that the assumption of an isotropic ion acceleration is indeed consistent with our neutron data.
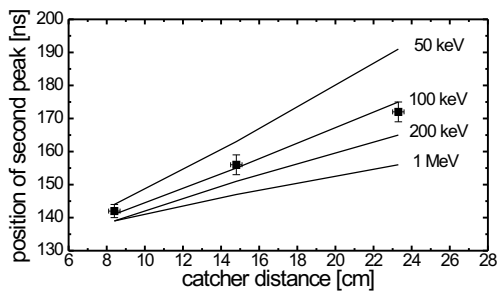
FIG. 5: Position of the second peak for different ion temperatures as predicted by MCNEUT and experimental data.

The position of the second peak is plotted against the catcher distance in Fig. 5. It can be seen that the experiment agrees well with a temperature of the rear side ions of 100 ± 30 keV. In absolute numbers, this is low compared to other experiments, but it can be explained by the laser parameters and geometry. MacKinnon et al. [26] report that for 20-μm thick planar targets and 100 fs, 10J, 1×10^{20} W/cm^2 laser pulses, the expansion velocity of the rear surface was 0.05c, corresponding to $T_i = 1.15$ MeV. The accelerating field for TNSA scales with $\sqrt{n_{e,hot}}$. For a fixed conversion efficiency η of laser energy E into electrons, the total number $N_{e,hot}$ of electrons scales with $\eta E/T_{hot}$. These electrons reach the rear surface within $\sim \tau_L$ in a spot of radius $\sim r_t$ (r_t= target thickness/2) in the planar case, leading to an electron density of $n_{e,hot} \sim N_{e,hot}/(\tau_L\ c\ \pi\ r_t^2)$. For droplets, the electrons spread over the whole surface and the density is reduced to one forth. Altogether, this leads to a factor of 9 reduction in acceleration-field strength for the Jena parameters as compared to the JanUSP conditions. Assuming the field duration is similar in both experiments, this leads to a mean ion energy of 125 keV, reasonably close to the observation.

In conclusion, we reported a plasma diagnostics application of deuterium ions accelerated by a table-top 10-Hz multi-terawatt-laser. The use of deuterated secondary and primary targets and fusion neutron TOF spectroscopy made it possible for the first time to distinguish between ions accelerated from both target surfaces in a single experiment. We identified two different acceleration mechanisms, namely acceleration in the laser focus by ponderomotive charge-separation fields and acceleration off the droplet surface by the TNSA mechanism. The measurement proves that both acceleration processes are working independently at the same time and show that under our conditions, much more ions originate from the rear surface, albeit at lower energies, as from the front. Going to higher laser energies, and therefore a higher $n_{rme,hot}$, the rear-surface ion population should become even more dominant. Although the absolute ion temperatures are rather low, the laser-to-ions energy conversion is high: We arrive at an energy content of $\sim$3 mJ for the frontside component and $\sim$25 mJ for the surface accelerated ions, leading to a total conversion efficiency into fast ions of about 5%.

[1] D. Strickland et al., Opt. Commun. **56**, 219 (1985).
[2] D. Gordon, et al., Phys. Rev. Lett. **80**, 2133 (1998).
[3] S. Hatchett, et al., Phys. Plasmas **7**, 2076 (2000).
[4] M. Hegelich, et al., Phys. Rev. Lett. **89**, 085002 (2002).
[5] C. Gahn, et al., Phys. Rev. Lett. **83**, 4772 (1999).
[6] A. Maksimchuk, et al., Phys. Rev. Lett. **84**, 4108 (2000).
[7] H. Schwoerer, et al., Phys. Rev. Lett. **86**, 2317 (2001).
[8] E. Clark, et al., Phys. Rev. Lett. **84**, 670 (2000).
[9] N. Izumi, et al., Phys. Rev. E **65**, 036413 (2002).
[10] S. Wilks, et al., Phys. Plasmas **8**, 542 (2001).
[11] R. Snavely, et al., Phys. Rev. Lett. **85**, 2945 (2000).
[12] A. Pukhov, Phys. Rev. Lett. **86**, 3562 (2001).
[13] D. Hilscher, et al., Phys. Rev. E **64**, 016414 (2001).
[14] L. Disdier, et al., Phys. Rev. Lett. **82**, 1454 (1999).
[15] S. Karsch, et al., Laser and Part. Beams **17**, 565 (1999).
[16] S. Düsterer, et al., Appl. Phys. B **73**, 693 (2001).
[17] S. Wilks, et al., Phys. Rev. Lett. **69**, 1383 (1992).
[18] J. Denavit, Phys. Rev. Lett. **69**, 3052 (1992).
[19] A. Pukhov et al., Phys. Plasmas **5**, 1880 (1998).
[20] M. Drosg, *Drosg2000* (www.iaea.org, 2000).
[21] J. Briesmeister et al., Los Alamos LA-12625-M (1997).
[22] S. Lyon et al., Los Alamos LA-UR-3407 (unpub.) (1992).
[23] R. More, *in: Handbook of Plasma Physics* (North-Holland, 1991).

[24] J. Ziegler et al., *SRIM 2000* (www.srim.org, 2000).

[25] J. Jackson, *Classical Electrodynamics* (Wiley, 1975).

[26] A. MacKinnon, et al., Phys. Rev. Lett. **88**, 215006 (2002).

MeV Ion Jets from Short-Pulse-Laser Interaction with Thin Foils

M. Hegelich,[1,2] S. Karsch,[1,2] G. Pretzler,[1,2] D. Habs,[2] K. Witte,[1] W. Guenther,[3] M. Allen,[4] A. Blazevic,[5] J. Fuchs,[6] J. C. Gauthier,[6] M. Geissel,[5] P. Audebert,[6] T. Cowan,[4] and M. Roth[5]

[1]*MPI für Quantenoptik, 85748 Garching, Germany*
[2]*Universität München, 85748 Garching, Germany*
[3]*Universität Siegen, 57068 Siegen, Germany*
[4]*General Atomics, San Diego, California 92121*
[5]*GSI Laboratory, 64291 Darmstadt, Germany*
[6]*LULI, Ecole Polytechnique, 91128 Palaiseau, France*
(Received 27 December 2001; published 2 August 2002)

Collimated jets of carbon and fluorine ions up to 5 MeV/nucleon (~ 100 MeV) are observed from the rear surface of thin foils irradiated with laser intensities of up to 5×10^{19}W/cm^2. The normally dominant proton acceleration could be surpressed by removing the hydrocarbon contaminants by resistive heating. This inhibits screening effects and permits effective energy transfer and acceleration of other ion species. The acceleration dynamics and the spatiotemporal distributions of the accelerating E fields at the rear surface of the target are inferred from the detailed spectra.

For over 25 years, energetic protons and ions have been generated by focusing $\sim$ns pulses from large Nd:glass and CO$_2$ lasers ([1] and references therein) on solid targets at intensities of 10^{14}–10^{16} W/cm^2. The ions emerging from the coronal plasma are emitted into a large solid angle. They exhibit strong trajectory crossing and a broad energy spectrum with typical ion temperatures of $\sim$100 keV/nucleon. These unspectacular characteristics have prevented major applications. This scenario is totally different when the ion acceleration is caused by femtosecond (fs) laser pulses. When these are focused on thin foils targets ($\sim$ 50 μm) at intensities of $> 10^{19}$ W/cm^2, proton beams are observed which exhibit new features [2–4]: (i) 10^{11}–10^{13} well collimated ($< 20°$) protons with 5 to 50 MeV are generated, (ii) they come from the *rear surface* and move in the laser direction, and (iii) they form a dense, charge-neutralized bunch of $\sim$1 ps duration. These proton beams have already been applied for the diagnostic of high-density plasmas [5] and suggested for fast ignition [6]. Application in isotope production for positron emission tomography might follow soon.

Hatchett and Wilks [7,8] attribute the above mentioned characteristics of the proton beam to the so-called target-normal sheath acceleration mechanism (TNSA), the notion being that relativistic electrons with density, n_e, and temperature, T_e, created at the target front side penetrate the foil and by extending past the rear surface produce a strong space-charge field:

$$E \approx k_B T_e/e\lambda_D, \qquad \lambda_D = (\epsilon_0 k_B T_e/e^2 n_e)^{1/2}. \qquad (1)$$

Typical values of $k_B T_e \sim 2$ MeV and $n_e \sim 2.5 \times 10^{19}$ cm^{-3} yield $\lambda_D \sim 2$ μm (distance over which the electric field E decays) and $E > 10^{12}$ V/m. A few monolayers of atoms at the rear surface experience field ionization by barrier suppression (FIBS) [9] and are accelerated normal to the surface by E. The most energetic electrons always extend farther out into vacuum, maintaining the accelerating field as long as the electron temperature is high. This is fundamentally different from the long-pulse case, in which bulk effects and collisional ionization by thermal electrons in the coronal plasma are the dominant mechanisms. In the fs case, however, the ion generation and acceleration mechanisms are decoupled from the *stochastic* laser-plasma interaction, which offers many advantages for producing well-controlled ion beams. The decoupling and the rapid rear-surface acceleration are the reasons why the protons appear in a highly laminar, low emittance ps bunch inside which no trajectory crossing occurs. So far, mainly protons have been observed from the rear side. This is attributed to contaminations of hydrocarbon and H$_2$O layers adhered to the target. Because of its low ionization potential and high charge-to-mass ratio hydrogen is among the first ion species produced and most effectively accelerated, thereby screening the space-charge fields for all other ion species.

In this Letter, we present the first experimental study demonstrating that besides protons also high-brightness, high-energy ($\sim$ MeV/nucleon) ion beams can be accelerated from the *rear surface* of thin foils. These ions are effectively accelerated only if the hydrogenous surface contaminants are removed. We obtain absolutely calibrated high-resolution energy spectra of different ion species and charge states. These provide additional information, not in the proton signal, about the spatiotemporal evolution of the accelerating field and the origin of the observed ions. We show for the first time that it is possible to control the accelerated ion species by choosing a target composed of a front-side interaction material and a rear-side ion source layer. The high-energy ions out of these prepared source layers unambiguously prove the existence of an effective rear-surface acceleration mechanism. For our experimental conditions, we thereby resolve the long-standing

controversy as to whether the high-energy (> 10 MeV) protons come from the rear surface and are accelerated by the TNSA mechanism [6,10–12] or stem from the front surface and are accelerated by the charge-separation field in the laser plasma [3,13]. The electric field deduced from the ion spectra can explain the high-energy protons (> 25 MeV [4]) in our experiments. This result also constitutes a major difference to long-pulse experiments, where rear-surface acceleration was a minor effect only, that vanished almost completely when either the contaminating hydrocarbons were removed [14] or foils thicker than a few μm were used [15]. With the new capability to accelerate ion species at will and indications that beam focusing [4], spectra and charge state control might be feasible, applications such as laser accelerators are becoming realistic. Also the transport of a dense charge-neutralized ion beam in plasmas and solids, enabling isochoric heating of macroscopic volumes ($\sim 10^5$ μm^3) to > 300 eV, could now be studied.

Our experiments were performed with the 100-TW laser at the Laboratoire pour l'Utilisation des Lasers Intenses (LULI). The laser pulses (~ 30 J, ~ 300 fs, 1.05 μm) were focused at normal incidence on target to an intensity of up to 5×10^{19} W/cm^2. The contrast, i.e., the peak-to-pedestal intensity ratio, amounts to $\sim 10^7$ at $t = 1.5$ ns. As targets we used 50 μm thick Al and W foils coated on the rear side with 1 μm carbon or 0.3 μm CaF$_2$, respectively. The accelerated particles were investigated by three complementary diagnostics: (a) a stack of radiochromic films (RCF) 5 cm behind the target to record the angular distribution of the emitted proton beam [7,16], (b) a magnetic proton spectrometer [17] at 13° to the target normal with a Kodak DEF x-ray film to measure the proton energy spectra, and (c) two Thomson parabola spectrometers ($B = 0.65$ T, $E = 1.3$ MV/m) with CR-39 track detectors at 0° and 6° at a distance of about 1 m (solid angle $\sim 5 \cdot 10^{-8}$ sr) to obtain the ion energy spectra. CR-39 is sensitive to single ion events but insensitive to electromagnetic radiation and electrons. An ion striking a CR-39 plate destroys the polymer matrix along its path and causes nm-scale damage sites. These are transformed into cone- or bowl-shaped craters when the CR-39 is etched in NaOH solution. Each individual track is analyzed by optical microscopy with custom pattern recognition software [18] yielding position and track size parameters, from which the absolute ion energy spectra are then obtained. Because the optical density is not simply proportional to the number of pits, only "single-track counting" yields correct results for the areal ion density, whereas optical scanning may lead to erroneous results.

To remove the hydrogenous contaminants, we tried radiative, laser, and resistive heating and found the latter the most effective (see also [19]). We heated Al and W foils up to ~ 600 K and ~ 1200 K, respectively. Already the partial removal of hydrocarbons strongly enhanced the acceleration of carbon ions, as shown in Fig. 1. The proton spectrometer yielded typically $\sim 10^{11}$ protons of up to 25 MeV,

for unheated targets. For heated Al targets, the number of protons is reduced to $\sim 10^{10}$ with energies of up to 3 MeV. The energy of the carbon ions is increased by a factor of ~ 2.5 and the number by 2 orders of magnitude to $\sim 2 \times 10^{11}$, corresponding to a laser-to-ion energy conversion of 0.5%. Acceleration is most efficient for C^{4+} ions, with a cutoff energy of ~ 1 MeV/nucleon at the high-energy end. In all spectra the high-energy cutoff is dependent on the charge state, ruling out recombination as a dominant effect in our experiments. This is confirmed by the low number of neutral atoms (~ 1%) forming the pinhole image on the CR-39. This behavior is fundamentally different from that observed in the carbon spectra in long-pulse experiments [20], where all charge states had a similar cutoff and the *rear-surface* ion signal almost vanished for heated targets [19]. Using W targets, the higher heating temperatures resulted in a complete removal of hydrocarbons. The proton spectrometer as well as the CR-39 did not show any protons, while strong fluorine ion tracks are observed originating from the CaF$_2$ layer at the target rear side (Fig. 2). Since only the target rear surface is coated with either C or CaF$_2$, the carbon and fluorine ions originate unambiguously from the *rear surface* of the targets. The acceleration of heavier ions was again increased considerably: F^{7+} was accelerated up to 100 MeV (> 5 MeV/nucleon) at > 5% energy conversion. The RCF confirmed this by showing a narrow spot in the first layer, which, in the absence of protons, indicates fluorine ions of energies above 4 MeV/nucleon. The analysis of the lower charge states
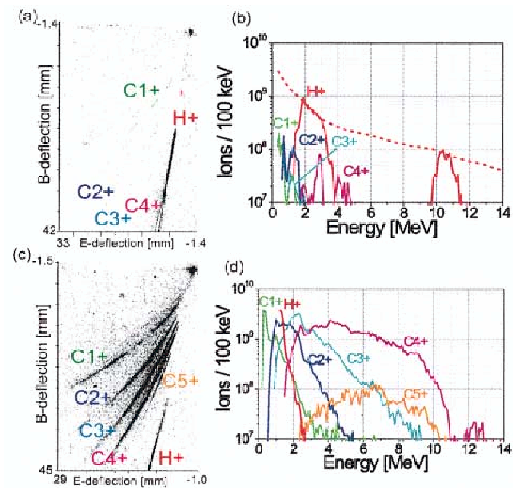
FIG. 1 (color). (a) Ion traces (on CR39) from an unheated Al | C target and (b) corresponding spectra. The gap in the proton signal is due to the CR-39 detector which is optimized for heavier particles. The dotted line illustrates the H$^+$ spectra as obtained with the proton spectrometer. (c) Ion traces from a heated Al | C target and (d) corresponding spectra. The ion signals are strongly enhanced. The spot in the upper right corner of (a),(c) is the pinhole image formed by neutral atoms.
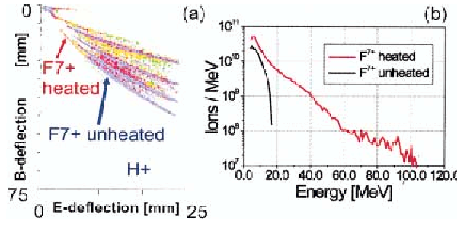
FIG. 2 (color). (a) Overlayed signals of heated (orange) and unheated (blue) W | CaF$_2$ targets: The proton signal vanishes for heated targets; the fluorine signals (especially F^{7+}) go up to much higher energies. (b) Corresponding F^{7+} spectra: F^{7+} ions achieve more than 100 MeV (5 MeV/nucleon).

proves to be more difficult due to overlapping of F and Ca traces with similar charge-to-mass ratios.

Long-pulse experiments showed that ion spectra can be used to identify the ionization and acceleration mechanisms, e.g., isothermal expansion (with $T_{e,\mathrm{hot}} \sim$ 10–100 keV) and collisional ionization up to the highest

charge state (e.g., C^{6+}), followed by recombination to the lower charge states in the drift phase ([1,20] and references therein). In short-pulse experiments, however, FIBS in the strong transient space-charge field dominates because of the fs timescale and high electron temperature ($\sim$ MeV). We can rule out ionization by the laser pulse or by a shock front by simultaneous target interferometry. The laser pulse is completely absorbed in the preplasma and the target thickness is chosen to prevent prepulse-caused shock breakout until $\sim$10 ns after the main pulse. Collisional ionization is estimated from [21]:

$$\nu_{\mathrm{col}} \approx n_e v_e 4\pi a_b^2 (U_H^2/U_k k_B T_e) \ln(k_B T_e/U_k), \quad (2)$$

where a_b is the Bohr radius, v_e is the electron velocity, and U_k and U_H are the ionization potentials of the ionized species and hydrogen, respectively. We also considered the influence of heating by possible return currents with a temperature $k_B T_e^{\mathrm{ret}} \sim 50$ eV [22], which must balance the hot electron flow, i.e., $n_e^{\mathrm{ret}} v_e^{\mathrm{ret}} \simeq n_e^{\mathrm{hot}} v_e^{\mathrm{hot}} \Rightarrow n_e^{\mathrm{ret}} \sim 2.5 \times 10^{21}$ cm^{-3}. We estimated the field ionization rate from the ADK model [23]:

$$\nu_{\mathrm{ADK}} \approx 6.6 \cdot 10^{16}(Z^2/n_{ef}^{4.5}) \exp[-(2Z^3/3n_{ef}^3)(E_{\mathrm{at}}/E)][10.87(Z^3/n_{ef}^4)(E_{\mathrm{at}}/E)]^{2n_{ef}-1.5}, \quad (3)$$

where $E = 2$ TV/m [from Eq. (1)] is the ionizing field, $E_{\mathrm{at}} = 0.51$ TV/m is the atomic electric field, Z is the charge of the created ion, and $n_{ef} = Z/\sqrt{U_k/U_H}$. The various ionization frequencies are listed in Table I. Other analytical models yield similar results and the exact numerical rates are even higher [23]. For all models field ionization dominates by orders of magnitude over the collisional processes for our set of parameters and for charge states up to He-like. For C^{5+}, $\nu_{\mathrm{col}}^{\mathrm{hot}}$ is larger than ν_{ADK}, which may explain the different spectral shape and lower numbers for this charge state. Assuming detailed balancing [24], we estimate recombination rates of $\sim$1% consistent with our measured data.

Having established that the ion spectra are linked to the accelerating E fields, we can now extract information such as the field strength which is not available from the proton data. With FIBS as the dominant ionization process, the

$k+$-ionic state will be created as soon as the electric field is above the threshold

$$E_k = U_k^2 \varepsilon_0 \pi/eZ. \quad (4)$$

We can use E_{k+1} as an upper limit for the electric field strength that a $k+$ ion has experienced. By integrating the equations of motion for an ion in a field rising in time with the laser pulse to E_k, staying at this value for a time τ_k^{min} and then decaying exponentially, τ_k^{min} defines a lower limit for the acceleration time, required to achieve the observed maximum ion energy for a given charge state (see Table I). The acceleration length, l_k^{min}, is the distance traveled by an ion during τ_k^{min} and is therefore a measure for the minimal spatial extension of the fields. The ultra-high-field region turns out to be of the duration of the laser pulse and of short length (≤ 500 fs, ≤ 5 μm). Only the C^{4+} ions see these

TABLE I. Calculated field and ionization parameters for carbon. U_k is the ionization potential of the kth ionic charge state and E_k is the corresponding field strength [Eq. (4)]. E_k^{max} is the maximal E field, τ_k^{min} is the minimal field duration, and l_k^{min} is the minimal acceleration length for a given k. ν are the ionization frequencies due to the hot electrons ($k_B T_e^{\mathrm{hot}} \sim 2$ MeV, $n_e^{\mathrm{hot}} \sim 2.5 \times 10^{19}$ cm^{-3}), the return current ($k_B T_e^{\mathrm{ret}} \sim 50$ eV, $n_e^{\mathrm{ret}} \sim 2.5 \times 10^{21}$ cm^{-3}), and the field ionization ($E_f = 2$ TV/m). Because $\tau_4^{\mathrm{min}} \sim \tau_{\mathrm{laser}}$, E_4^{max} is lower than the theoretically possible value of $5.3 \cdot 10^{12}$ V/m.

k	U_k (eV)	E_k (V/m)	E_k^{max} (V/m)	τ_k^{min} (ps)	l_k^{min} (μm)	$\nu_{\mathrm{col}}^{\mathrm{hot}}$ (ps^{-1})	$\nu_{\mathrm{col}}^{\mathrm{ret}}$ (ps^{-1})	ν_{ADK} (ps^{-1})
1	11.2	2.2×10^{10}	5.2×10^{10}	60	230	2.53×10^{-2}	2.13	5.93×10^4
2	24.4	5.2×10^{10}	1.3×10^{11}	10	48	1.1×10^{-2}	0.68	2.65×10^5
3	47.9	1.3×10^{11}	1.8×10^{11}	4.3	25	5.29×10^{-3}	0.21	1.46×10^6
4	64.5	1.8×10^{11}	1.75×10^{12}	0.35	3	3.28×10^{-3}	0.11	4.62×10^6
5	392	5.3×10^{12}				5.29×10^{-4}	$\cdots$	8.5×10^{-5}
6	490	7.0×10^{12}				4.14×10^{-4}	$\cdots$	7.03×10^{-9}
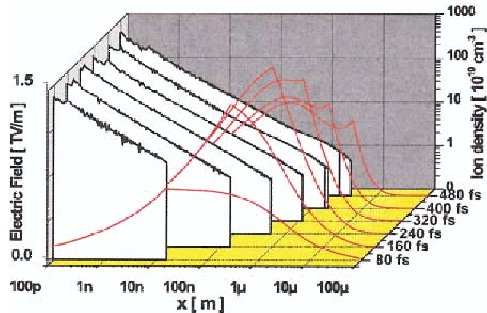
FIG. 3 (color). Space-time history of the accelerating electric fields (red curves) and the C^{4+}-dominated ion distributions (white curves) as calculated by our model: The field maximum moves out into the vacuum. Already during the pulse there exists an ion distribution on a μm scale.

highest fields, while the lower charge states are accelerated by lower fields of up to 2 orders of magnitude longer duration, which is not explainable by the static TNSA model.

In order to get a better understanding of how the ion energies and charge state distributions develop in space and time, we have developed a 1D-numerical model which calculates the electron dynamics behind the target, assuming a Boltzmann equilibrium for the electron energy spectrum and a current distribution which follows the laser pulse. We include the ionization process (FIBS), the acceleration of different ion species, and screening effects on the potential. In each time step, we solve Poisson's equation for the given charge distribution, check for ionization events, advance the different ion species, and solve again Poisson's equation for the new charge distribution. When the first laser-heated electrons enter the vacuum behind the target, they create the space-charge field E, albeit in a highly dynamic way, much more complex than in the simple TNSA model. When more and hotter electrons pass through the surface, the field increases until $E = E_1$. Now FIBS sets in and the produced ions and electrons decrease the field at the surface. An equilibrium between the growing external field and the surface ionization rate keeps the field at the surface always at E_1. The created ions are accelerated into the vacuum while the freed electrons are pushed into the target. Whereas the field close to the target is shielded by the ions, the unshielded field in vacuum keeps increasing. The maximum of the electric field moves outwards into vacuum, ionizing the outermost ions further (see Fig. 3). The model reproduces the measurements for protons and the high charge states. As long as there is a source of hot electrons, nearly all ions are sequentially ionized to C^{4+}. As seen in the experimental data, the lower charge states require 2 orders of magnitude longer time scales and possibly a 3D treatment to allow for low fields in the fringe regions. To explain the long acceleration times the electron recirculation model of [10] may prove useful. Another approach is to envision the individ-

ual charge states in separately lined up bunches each with a charge neutralizing electron cloud lagging a bit behind, thereby setting up an effective field for the next lower charge state bunch. A model to completely explain the acceleration dynamics is currently developed. The evaluation of the fluorine shot shown in Fig. 2 shows that $E \sim 2$ TV/m active over $\tau_7^{min} \sim 350$ fs is necessary to accelerate F^{7+} ions up to 100 MeV over a scale length of $l \sim 10$ μm. The inferred fields would accelerate H^+ up to ~ 25 MeV, as typically observed with unheated targets.

In summary, by using high-intensity laser pulses we achieved efficient ($> 5\%$ energy conversion), directed ion acceleration to more than 5 MeV/nucleon from the *rear surface* of thin-foil targets. High-resolution energy spectra measured for different ionic charge states yield detailed information on the spatiotemporal behavior of the accelerating fields. They show that FIBS is the dominant ionization mechanism while recombination and collisional ionization are negligible except for C^{5+}. A 3D-TNSA model including dynamic fields and multiple ion species is needed to correctly describe the acceleration process.

[1] S. Gitomer *et al.*, Phys Fluids **29**, 2679 (1986).
[2] R. Snavely *et al.*, Phys. Rev. Lett. **85**, 2945 (2000).
[3] E. Clark *et al.*, Phys. Rev. Lett. **84**, 670 (2000).
[4] M. Roth *et al.*, Phys. Rev. ST Accel. Beams **5**, 061301 (2002).
[5] M. Borghesi *et al.*, Phys. Rev. Lett. **88**, 135002 (2002).
[6] M. Roth *et al.*, Phys. Rev. Lett. **86**, 436 (2001).
[7] S. Hatchett *et al.*, Phys. Plasmas **7**, 2076 (2000).
[8] S. Wilks *et al.*, Phys. Plasmas **8**, 542 (2001).
[9] S. Augst *et al.*, J. Opt. Soc. Am. B **8**, 858 (1991).
[10] A. Mackinnon *et al.*, Phys. Rev. Lett. **88**, 215006 (2002).
[11] Y. Murakami *et al.*, Phys. Plasmas **8**, 4138 (2001).
[12] A. Mackinnon *et al.*, Phys. Rev. Lett. **86**, 1769 (2001).
[13] A. Maksimchuk *et al.*, Phys. Rev. Lett. **84**, 4108 (2000).
[14] F. Begay *et al.*, Phys. Fluids **25**, 1675 (1982).
[15] G. Tsakiris *et al.*, Phys. Rev. Lett. **46**, 1202 (1981).
[16] E. Clark *et al.*, Phys. Rev. Lett. **85**, 1654 (2000).
[17] T. Cowan *et al.*, Phys. Rev. Lett. **84**, 903 (2000).
[18] G. Rusch *et al.*, Nucl. Tracks Radiat. Meas. **19**, 261 (1991).
[19] F. Begay *et al.*, J. Phys. D **13**, L29 (1980).
[20] C. Joshi *et al.*, Appl. Phys. Lett. **34**, 625 (1979).
[21] V. Tikhonchuk, Phys. Plasmas **9**, 1416 (2002).
[22] L. Grémillet *et al.*, Phys. Rev. Lett. **83**, 5015 (1999).
[23] D. Bauer *et al.*, Phys. Rev. Lett. **75**, 4622 (1995).
[24] L. Oster, Am. J. Phys. **38**, 754 (1970).

Correction of strong phase and amplitude modulations by two deformable mirrors in a multistaged Ti:sapphire laser

H. Baumhacker, G. Pretzler, K. J. Witte, M. Hegelich, M. Kaluza, and S. Karsch

Max-Planck-Institut für Quantenoptik, Hans-Kopfermann-Strasse 1, D-85748 Garching, Germany

A. Kudryashov, V. Samarkin, and A. Roukossouev

Adaptive Optics for Industrial and Medical Applications Group, Institute on Laser and Information Technology of the Russian Academy of Science (ILIT RAS), Svyatoozerskaya Street 1, Shatura, Moscow Region, 140700 Russia

We describe a novel scheme consisting of two deformable bimorph mirrors that can free ultrashort laser pulses from simultaneously present strong wave-front distortions and intensity-profile modulations. This scheme is applied to the Max-Planck-Institut für Quantenoptik 10-TW Advanced Titanium-Sapphire Laser (ATLAS) facility. We demonstrate that with this scheme the focusability of the ATLAS pulses can be improved from 10^{18} to 2×10^{19} W/cm^2 without any penalty in recompression fidelity. © 2002 Optical Society of America

OCIS codes: 010.1080, 140.3590, 220.1000.

In high-power multistage Nd:glass and Ti:sapphire (TiS) laser systems, wave-front aberrations (WFAs) that result in deterioration of beam quality are common. These WFAs originate from imperfections in the many optical components that are present in the beamline as a result of optical figure errors, pump-induced thermal distortions in the amplifiers, and the third-order nonlinear n_2 effect. In TiS lasers, cooling the crystals to the temperature of liquid nitrogen can essentially eliminate pump-induced distortions.[1–3] A more versatile approach, however, is to use adaptive optics, which can counteract each of the three WFA sources, regardless of whether they occur individually, in pairs, or all together simultaneously. This was demonstrated in Refs. 4–7 by use of just a single deformable mirror (SDM).

In the SDM concept, only the WF of the pulse is corrected, not the intensity profile. This scheme works well as long as the WF perturbing action of each individual optical element is so weak that the shortest local radius of curvature, R, of the WF of the exiting pulse is many times the distance to the adaptive mirror. In addition, the pulse should not pick up strong intensity modulations, e.g., by nonuniform amplification. However, when an optical element such as a multipass amplifier causes a single-pass WFA with an associated R value of the order of the pass-to-pass propagation distance, the pulse intensity profile becomes increasingly modulated from pass to pass. On further propagation, these modulations may get even worse. If one stays with the SDM concept, the beam loading would then have to be reduced so that the optical components placed downstream from the amplifier are not damaged. In chirped-pulse amplification laser systems, the compressor gratings are then particularly endangered because of their low damage threshold. The system efficiency is thereby decreased considerably, too.

In this Letter we study this heavy-perturbation case, which to our knowledge has not been investigated experimentally before and is characterized here by the simultaneous presence of strong phase and amplitude modulations. We show that by invoking two DMs one can cancel the modulations without any sacrifice

in beam loading. In our concept, the compressor is placed between two DMs and thus has to be operated with a distorted WF. For this situation, we present conditions that, when met, maintain the pulse recompressibility and focusability within reasonable limits.

The two-DM concept has also been investigated for applications in areas others than the one studied here, so far only theoretically. These other applications include beam shaping for high-power laser beams in laser photochemistry and material processing[8] as well as delivering a high-quality pulse on a remote target after propagation through turbulent atmosphere.[9] In astronomy, the use of two DMs may enable one to overcome turbulence-induced phase and amplitude modulations for widely enlarged fields of view (Refs. 10 and 11, and references therein). The algorithms developed in Refs. 8–11 for control of the DM surfaces are not applicable to our situation because of the presence of the gratings between the two DMs, which limits beam loading.

The heavy-perturbation case that we are confronted with arises in the final disk amplifier of our Advanced Titanium:Sapphire Laser (ATLAS) facility (Fig. 1). The front end of the laser[12] delivers a 300-mJ pulse that is centered at 790 nm and stretched from 100 fs to 200 ps with a smooth intensity profile and a well-behaved WF. After four passes, the fluence pattern of the pulse inside the compressor is heavily modulated (Fig. 2, left) due to crystal-growth defects (Fig. 3) and pump-induced aberrations. At a pulse energy of 1.3 J at the compressor entrance, the peak fluence reaches 0.3 J/cm^2 on the first grating, far beyond its damage threshold of 0.15 J/cm^2. Under these loading conditions, the energy that is transmittable through the compressor is limited to only 0.5 J. Because of the simultaneous presence of WFAs and intensity modulations, the SDM concept is no longer applicable. To increase the amount of energy that is transportable through the compressor, we must first smooth the fluence profile. This is achieved with deformable mirror DM1 (17 electrodes, 30-mm diameter, bimorph),[13] which replaces the plane mirror in the beamline before the pulse makes its final transit through the amplifier
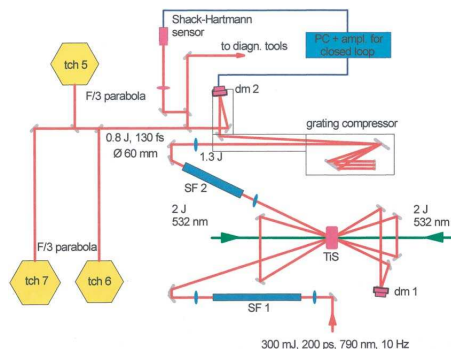
Fig. 1. Setup of the final amplifier in the ATLAS facility with two deformable mirrors, DM1 and DM2, closed loop, and three target chambers (TCH5–TCH7). The TiS crystal of 40-mm outer diameter is pumped from two sides. The TiS pulse provided by the front end passes through the crystal four times and is thereby amplified from 0.3 to 1.5 J. The pulse then runs through spatial filter SF2, and the pulse diameter increases from 18 to 63 mm. The pulse is then recompressed to 130 fs in an evacuated compressor chamber that houses two holographic gold gratings and is connected to the target chambers by evacuated tubes.

(Fig. 1). The best electrode voltage settings for DM1 can be found manually with a few iterations by use of a real-time beam-profile analyzer.   For the same energy of 1.3 J as before, the peak fluence of the smoothed profile is then reduced to 90 mJ/cm^2 so that the 1.3-J energy can be safely transmitted through the compressor.   At constant voltage settings, the smoothed beam profile remains stable over weeks and changes little on propagation inside the compressor and a few meters downstream.

The action of DM1 modifies the WFAs originating in the amplifying crystal but does not generate a plane WF. A plane WF is generated with a second deformable mirror, DM2 (33 electrodes, 80-mm diameter, bimorph).[13] DM2 is placed behind the compressor so that it is able to compensate for the optical figure errors of the gratings and to ensure that highly peaked intensity patterns that might occur when DM2 is optimized cannot damage the gratings. The compressor is thus fed with a chirped pulse whose WF is distorted. In this situation, which was investigated theoretically in Ref. 14, the following three effects are of major importance: loss of compression fidelity, astigmatism, and chromatic aberration. For an estimate of the level of WFAs that are tolerable without too high a loss in beam quality, the rigorous theory[14] is not needed. It is sufficient to replace the real pulse with a spherical WF whose curvature is chosen to be equal to the maximum local curvature in the real distorted WF.   The focus of the model WF is downstream DM2.

From measurements, we find that the recompression fidelity in terms of pulse duration and contrast is hardly affected as long as any local radius of curvature of the WF exceeds 15 m. The condition is met in the ATLAS for pulse energies of up to 1 J after compression.

The originally spherically convergent beam turns astigmatic when it leaves the compressor, leading to the occurrence of two focal lines instead of a single point focus because the beam behaves differently in the dispersion and nondispersion planes of the compressor. With $R \geq$ m, the compressor-induced astigmatism turns out to be weak and is hence easily correctable with DM2, since the necessary displacement is ≤ 1 μm. The compensation of the original beam convergence is not a problem, either.

The chromatic aberration originates from the different path lengths of the individual spectral components on their way through the compressor. When they are exiting, the individual spectral beam components still have the same cone angle, but at a fixed position in space the radii of curvature are different. This effect cannot be compensated for with DM2. The beam emerging from DM2 will hence be parallel for the spectral component near λ_0 but divergent for the components with $\lambda < \lambda_0$ and convergent for those with $\lambda > \lambda_0$. The focus of such a beam is hence no longer pointlike but exhibits longitudinal spreading, with each spectral component having its own focus located at a different position. This spreading is tolerable when the foci of all colors inside the spectral range $4\Delta\lambda_{FWHM}$ lie within the Rayleigh length of the spectral beam component at λ_0. For the ATLAS, this criterion requires $R > 15$ m, which is met. The theoretical analysis reveals that $R \propto \Delta\lambda_{FWHM}$. Very short pulses with $\Delta\lambda_{WFHM} \geq 50$ nm thus need to be rather well collimated if one wishes to avoid intensity degradation in the focus. This conclusion is in fair agreement with the results of the rigorous theory.[14]
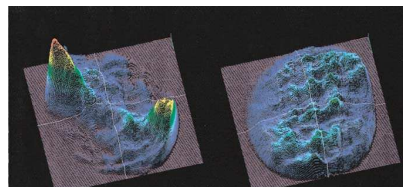
Fig. 2. Fluence patterns in the plane of the first compressor grating. Left, DM1 is replaced with a plane mirror; peak fluence, 300 mJ/cm^2. The double-peak pattern is due to the coarse two-half structure of the WFAs shown in Fig. 3. Right, DM1 is optimized; peak fluence reduced to 90 mJ/cm^2. The remaining fluence modulation arises from the fine structure of the WFAs (Fig. 3). The very high spatial frequencies, which carry little energy, are lost on propagation through the spatial filter SF2 (Fig. 1).
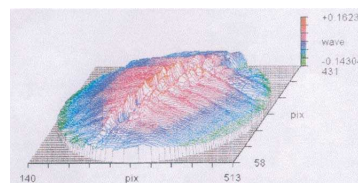
Fig. 3. WFAs that are due to growth defects in the final disk amplifier of 40-mm diameter, 17-mm thickness, and $\alpha l = 2.3$ at 532 nm.
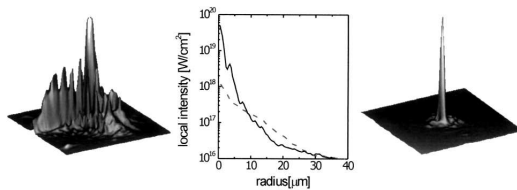
Fig. 4. Fluence profile in the focus of the $F/3$ off-axis parabola. Left, DM1 and DM2 are on, but DM2 acts as a plane mirror. Middle; local intensity as a function of radius for the fluence profiles shown to the left (- - -) and right (——). Right, DM1 and DM2 are on, but DM2 is locked to operation for minimal WFAs.

We generate a parallel beam with DM2 by comparing the actual WF as measured with a Shack–Hartmann sensor that has a 12×12 lenslet array with a reference WF obtained from a diode laser running at 790 nm and expanded to a parallel beam of 63-mm diameter. Edge points with an intensity of less than 10% of the maximal intensity are disregarded. The reference WF is stored in the computer for subsequent use. The voltage settings to be assigned to the electrodes of DM2 then have to be found so that the WF of the ATLAS pulse matches the reference WF as closely as possible. This is achieved by application of a closed loop. The algorithm employed for this purpose is the same as that developed in Ref. 5. The deviations between the actual and the reference WFs are minimized by use of the peak-to-valley optical-path difference as a criterion. Usually, approximately five iterations are needed to decrease the peak-to-valley value from the original 10λ to $\lambda/4$. The voltage settings corresponding to minimal WF distortion are stored. They can be used for hours because of the high thermomechanical stability of the ATLAS and the correspondingly low shot-to-shot fluctuations of the WF. For routine operation of the ATLAS, the closed loop is no longer needed once the WF correction is complete. We can then remove the beam splitter feeding the Shack–Hartmann sensor from the beam line to keep the B integral low. In case of performance deterioration, e.g., because of thermal drift, the whole WF correction procedure, which takes $\sim$15 s, has to be redone.

We check the quality of the corrected WF in each target chamber by measuring the fluence patterns in the foci of the $F/3$ off-axis parabolas, using an 8-bit CCD camera and a set of calibrated filters. This combination provides an effective dynamic range of $>10^4$. The focus is viewed at $50\times$ magnification. Because of the 1-mm-diameter pinhole SF2, there can be no energy outside the sensor chip (6 mm $\times$ 4 mm). Hence, the amount of energy that can possibly be hidden in the pixels showing no direct response is at most 10% of the total pulse energy. In each chamber, we obtain the same result for thousands of shots. With DM1 on and DM2 acting as a plane mirror, we find the multiple-peak fluence pattern depicted in the left-hand part of Fig. 4. The Strehl ratio (for its definition, see Ref. 15) is only $\sim$0.04. However, when DM2 is locked to operation for minimal WFA, we find

a dramatic improvement (Fig. 4, right). A single peak appears that contains 65% of the pulse energy within the diffraction-limited diameter. The mean intensity inside the diffraction-limited diameter is raised by a factor of $\sim$20 from $\sim$10^{18} to 2×10^{19} W/cm^2. The Strehl ratio increases to 0.7. The Strehl ratio estimated from the corrected WF with a peak-to-valley optical path difference of $\lambda/4$ is 0.8. The difference in the two ratios is attributed to the fact that the real WF has higher-order abberrations that are not measurable with our Shack–Hartmann sensor and are not correctable with our adaptive optics.

We have shown that a combination of two DMs can free ultrashort laser pulses from simultaneously present heavy phase and amplitude modulations without any penalty in recompression fidelity and focusability.

References

1. G. Erbert, L. Bass, R. Hackel, S. Jenkins, K. Kanz, and J. Paisner, in *Conference on Lasers and Electro-Optics*, Vol. 10 of 1991 OSA Technical Digest Series (Optical Society of America, Washington, D.C., 1991), pp. 390–391.
2. M. Pittmann, J. Rousseau, L. Notebaert, S. Ferré, J. Chambaret, and G. Cheriaux, in *Conference on Lasers and Electro-Optics*, Vol. 56 of OSA Trends in Optics and Photonics Series (Optical Society of America, Washington, D.C., 2001), p. 83.
3. S. Backus, R. Bartels, S. Thompson, R. Dollinger, H. Kapteyn, and M. Murnane, Opt. Lett. **26,** 465 (2001).
4. B. Van Wonterghem, J. Murray, J. Campbell, D. Speck, C. Barker, I. Smith, D. Browning, and W. Behrend, Appl. Opt. **36,** 4932 (1977).
5. K. Akaoka, S. Harayama, K. Tei, Y. Marayuma, and T. Arisawa, Proc. SPIE **3265,** 219 (1997).
6. F. Druon, G. Cheriaux, J. Faure, J. Nees, M. Nantel, A. Maksimchuk, J. Chanteloup, and G. Vodvin, Opt. Lett. **23,** 1043 (1998).
7. J. Chanteloup, H. Baldis, A. Migus, G. Mourou, B. Loiseaux, and J. Huignard, Opt. Lett. **23,** 475 (1998).
8. K. Nemoto, T. Fujiti, and N. Goto, Proc. SPIE **2119,** 155 (1994).
9. G. Roger, J. Phys. Colloq. **41,** 399 (1980).
10. K. Li You, Q. C. Dong, and W. D. Xiang, High-Power Laser Particle Beams **12,** 665 (2000).
11. A. Tokovinin, M. Le Louarn, E. Viard, N. Hubin, and R. Conan, Astron. Astrophys. **378,** 710 (2001).
12. K. Yamakawa, P. Chin, A. Magano, and J. Kmetec, IEEE J. Quantum Electron. **37,** 2698 (1994).
13. DM1 and DM2 were produced in the mainframe of Max-Planck-Institut–ILIT RAS collaboration. See also J. Dainty, A. Koryabin, and A. Kudryashov, Appl. Opt. **37,** 4663 (1998).
14. Z. Wang, Z. Xu, and Z.-Q. Zhang, IEEE J. Quantum Electron. **37,** 1 (2001).
15. W. J. Smith, *Modern Optical Engineering*, 2nd ed. (McGraw-Hill, New York, 1990), p. 337.

Danksagung

An dieser Stelle möchte ich allen, die zum Gelingen dieser Arbeit beigetragen haben, ein herzliches Dankeschön aussprechen.

Ich danke Herrn Prof. Dr. Dieter Habs für die bereitwillige Übernahme der Doktorvaterschaft für einen an der TU heimatlos gewordenen "Hochintensitätslaserverrückten", und für die großzügige Unterstützung mit Rat, Tat, Reise- und Sachmitteln während der gesamten Arbeit.

Genauso möchte ich Herrn Prof. Dr. Klaus Witte danken, der mir die Anfertigung dieser Arbeit in der Laser-Plasma-Gruppe als externem, aber doch bald voll integriertem Mitglied ermöglicht hat. Er hat mir durch seinen sehr verständnisvollen und angenehmen Führungsstil die engagierte Mitarbeit in seiner Gruppe zu einem eigenen Anliegen gemacht. Besonders für das mir entgegen gebrachte Vertrauen, mir nach anfänglichen "Katastrophen" viel Verantwortung bei der Weiterentwicklung des Lasers zu überlassen, möchte ich mich bedanken. .

Prof. Dr. Georg Pretzler bin ich für die fundierte Einführung in mein Arbeitsgebiet und die stets ermunternde Betreuung und Diskussionsbereitschft auch in "schwierigen Fällen" besonders dankbar.

Den Herren Dr. George Tsakiris, Dr. Klaus Eidmann, Dr. Ernst Fill, Dr. Ulrich Schramm und Dr. Peter Thirolf danke ich für die vielen kleinen und großen Denkanstöße und ihre stetige Diskussionsbereitschaft.

Ein großes Dankeschön an Horst Baumhacker für sein Vertrauen und seine Einweisung an "seinem" ATLAS-10 und für seine wertvolle Hilfe und ein immer offenes Ohr.

Besonders möchte ich auch Prof. Dr. Alexander Pukhov für die Zurverfügungstellung seines 3-D PIC-Codes VLPL und die tatkräftige Online-Hilfe danken.

Prof. Dr. Markus Roth, Dr. Thomas Cowan und Dr. Patrick Audebert gilt mein Dank für die Aufnahme in die berühmte GSI-LULI-GA-MPQ-Kollaboration und